

Study of the training effect in exchange bias using the domain state model

Andreas Biternas

A Thesis submitted for the degree of Doctor of Philosophy

THE UNIVERSITY *of York*

Department of Physics

December 2009

Abstract

The most common product of the storage industry is the well known hard disk, based on the magnetic recording and reading of data. The research of magnetic materials is enhanced by the establishment of hard disks as a recording media. Given the current trend toward nanostructured materials and complex materials design, the understanding of the origins of magnetic phenomenology at the atomistic level has become necessary. In this thesis, we focus on the aging effects of magnetic materials. The systems that are investigated are bilayer thin films comprised of two materials with different magnetic order. The so called exchange bias systems are comprised of a ferromagnetic layer in contact with an antiferromagnetic layer. Exchange bias systems are part of the current read-heads, which utilise the phenomenon of Giant Magnetoresistance discovered by A. Fert and P. Grünberg, who were awarded a Nobel prize in 2007 for this discovery. The most well-known characteristic of the exchange bias systems is the shift of the hysteresis loop along the horizontal axis. The reduction of this shift with consecutive hysteresis cycles is called the training effect.

The current research focused on the dependence of the training effect on various exchange bias system parameters using the well established domain state model. A novel analysis was developed for the study of the antiferromagnet during consecutive hysteresis loops. A special focus was given to the response of training effect on temperature. Several characteristics of the system were varied to investigate the physics of the training effect, such as the antiferromagnetic thickness and dilution with non-magnetic defects. The reversal modes of the ferromagnet were also investigated varying the anisotropies of the system as well the angle of the magnetic field.

New characteristics were added to the domain state model increasing the realism of this model. The interface roughness was introduced in the model, as more representative of realistic exchange bias systems. Furthermore, different crystallographic structures such as body-centered cubic and hexagonal-close packed, were investigated as in these structures the coupling between the ferromagnet and the antiferromagnet increases. In these structures, in addition to the interface roughness, the enhance coupling is shown to give rise to complex trends of the exchange bias and the training effect.

Contents

List of Figures	5
List of Tables	11
Acknowledgments	12
Author's Declaration	13
1 Introduction	14
1.1 Magnetism in materials: Ferromagnets, antiferromagnets and hysteresis loops	15
1.2 Exchange bias phenomenon and the training effect	17
1.3 Applications of exchange bias systems	19
1.4 Related phenomena	21
1.5 Important quantities of exchange bias systems	23
1.6 Experimental findings and system behaviour	24
1.6.1 Exchange bias systems	24
1.6.2 Exchange bias and coercivity	25
1.6.3 Training effect	28
1.7 Motivation	29
1.8 Thesis Outline	30
2 Models of exchange bias	31
2.1 Macroscopic models	31
2.1.1 The ideal model	31
2.1.2 The Meiklejohn Model	35
2.1.3 Planar AFM Domain wall model-Néel's approach	36
2.1.4 Mauri model-Partial domain wall	37
2.1.5 Frozen canted interface spins-Kiwi model	39
2.1.6 Partial domain wall-Kim-Stamps approach	40
2.1.7 Hoffmann model-Training effect	41
2.1.8 Radu approach-The spin glass model	42
2.2 Mesoscopic models and micromagnetics	43
2.2.1 Non-interacting grained and thermal fluctuation aftereffect models	43
2.2.2 Interacting AFM grain model	46
2.2.3 Less-ideal models	47
2.3 Microscopic models	48
2.3.1 Spin flop - Koon's model	49
2.3.2 Various improved microscopic models	50
2.3.3 Domain state model	51
2.4 Multiscale models	53

2.5	Modelling nanoparticles and other structures	54
3	Theory of magnetism in solids	57
3.1	Magnetism in solids	57
3.2	The exchange interaction	59
3.3	The indirect exchange and the super-exchange	61
3.4	The anisotropy	63
3.4.1	Magnetocrystalline anisotropy	63
3.4.2	Shape anisotropy	64
3.5	Magnetostatic dipole interaction	66
3.6	Domains and Domain walls	67
4	Atomistic Model-Methodology and initial results	69
4.1	Modelling a FM	69
4.1.1	Investigation of trial step radius	70
4.1.2	Calculation of Curie temperature and hysteretic dependence on temperature	70
4.1.3	Exchange integral and coordination number dependence	71
4.1.4	Lateral size effect	73
4.1.5	Magnetocrystalline anisotropy dependence	73
4.2	Modelling a diluted antiferromagnet	75
4.2.1	Calculating the Néel temperature of a diluted antiferromagnet	76
4.3	The domain state model	76
4.3.1	First simulation: Cooling process dependence	79
5	Influence of the AFM and temperature on the training effect	80
5.1	Training effect and fitting laws	80
5.1.1	Hysteresis loops	80
5.1.2	Analysis of the training effect	83
5.2	Athermal and thermal training effect	85
5.3	Temperature dependence: Behaviour of the ferromagnet	86
5.3.1	Hysteresis loop of parallel and transverse component	87
5.3.2	Exchange bias field	88
5.3.3	Coercive fields	91
5.4	Temperature dependence: Behavior of the antiferromagnet	92
5.4.1	Irreversible magnetization of AFM interface	93
5.4.2	Spin and Domain types	95
5.4.3	Analysis of stable spins	96
5.4.4	Low temperature effects	101
5.5	Influence of the AFM thickness	104
5.5.1	Néel temperature	105
5.5.2	Exchange bias training effect	105
5.5.3	Coercive fields: The Type I and Type II training effect	107
5.6	Influence of the AFM dilution on training effect	108
5.6.1	Néel temperature	109
5.6.2	Exchange bias and coercive field training effect	109
5.6.3	Behavior of the AFM	111
5.7	Summary	114

6	Magnetocrystalline anisotropy dependence of the training effect	115
6.1	Training effect dependence on anisotropy types and parameters	115
6.2	Influence of angle between easy axis and magnetic field	122
6.2.1	Uniaxial FM anisotropy - Uniaxial AFM anisotropy (Group (I))	122
6.2.2	Uniaxial FM anisotropy - Biaxial AFM anisotropy (Group (II))	130
6.2.3	Biaxial FM anisotropy - Biaxial AFM anisotropy (Group (III))	135
6.2.4	Biaxial FM anisotropy - Uniaxial AFM anisotropy (Group (V))	140
6.3	Summary	143
7	Influence of the FM/AFM coordination number on the training effect	146
7.1	Interface roughness dependence of the training effect	146
7.2	EB systems with sc, fcc and bbc structure	149
7.3	A special case: A fully uncompensated interface	153
7.4	Hexagonal structured EB systems	155
7.5	Summary	157
8	Conclusions and further work	159
8.1	Model and analysis	159
8.2	Temperature effects	160
8.3	AFM characteristics effects	160
8.4	Anisotropy effects	161
8.5	Rough interface effects	162
8.6	Crystallographic structure effects	162
8.7	Outlook and future prospects	163
	Appendices	165
	A Heat-Bath Monte Carlo	165
	B Nomenclature	167
	Bibliography	171

List of Figures

1.1	The scale of things.	14
1.2	a) Ferromagnetic and antiferromagnetic order (ideal) in a bulk material. b) A ferromagnetic hysteresis loop.	16
1.3	a) The shifted hysteresis loop of the Co particles and b) The torque magnetization of a material with uniaxial anisotropy and of the $Co - CoO$	18
1.4	Consecutive hysteresis loops of a $Co - CoO$ system measured with torque balance.	19
1.5	Progress of read head sensor technologies.	20
1.6	a) A typical giant magnetoresistance. b) Structure of a spin-valve head.	21
1.7	Distribution of energy barriers to reversal in a AFM layer following two different methods of determining the blocking temperature.	23
1.8	Exchange bias hysteresis loop with the important quantities.	24
1.9	Exchange bias thin film, consisting of a FM and an AFM.	24
1.10	a) EB field and coercivity dependence on FM layer thickness for a $Fe_{80}Ni_{20}/FeMn$ bilayer. b) EB field and coercivity dependence on AFM layer thickness.	25
1.11	Exchange bias system with AFM having a) compensated spins and b) uncompensated spins on the interface.	26
1.12	Dilution dependence of absolute exchange bias field (a) and of coercivity (b) in the $Co_{1-x}Mg_xO$ layer for various temperatures.	28
1.13	Temperature dependence of the EB, coercivity, positive and negative coercive field of $NiO/Ni_{81}Fe_{19}$ bilayer.	29
2.1	Phenomenological model of EB.	32
2.2	Phenomenological model with the schematic view of the vectors and angles.	33
2.3	Meiklejohn model of EB with the schematic view of the vectors and angles.	35
2.4	The partial domain wall developed at the interface of the AFM, for a system with a thin FM film on a thick AFM substrate.	37
2.5	Magnetization curves for magnetic field applied parallel to the AFM easy axis for different values of the interface ratio.	38
2.6	Dependence of the normalized EB field h_{eb} (a) and coercivity h_c on the $(A_{12}/\xi)/2\sqrt{A_{AFM}K_{AFM}}$ ratio for several μ	39

LIST OF FIGURES

2.7	Spin configuration of the FM and the AFM layers.	40
2.8	Magnetization curve (a) and spin configuration (b) at three different points of the magnetic field.	41
2.9	Diagram of the Fulcomer-Charap model.	43
2.10	Comparison between experimental findings for a $Co - CoO$ system and Fulcomer-Charap model results.	44
2.11	Hysteresis loop of an EB system with and without AFM intergrain exchange coupling.	46
2.12	Formation and annihilation of a 360° domain wall (nucleation) in the FM.	47
2.13	Possible spin configurations for a non-ideal interface in an EB system.	48
2.14	EB with reversible cycling and a hysteresis loop without EB.	49
2.15	a) Schematic phase diagram of a three dimensional diluted AFM. b) Schematic illustration of Imry-Ma argument.	52
2.16	Spin configuration of an AFM.	54
2.17	a) Topographical representation of a smooth interface plane. b) Elliptical islands of a monoatomic layer. c) Topographical map containing overlapping islands.	55
2.18	a) Spin configuration of an equatorial cut of a nanoparticle. Spin configuration of Co nanoparticles embedded in CoO with b) uncompensated-parallel coupling and c) compensated- perpendicular coupling.	56
3.1	The Bethe-Slater curve.	61
3.2	a) Schematic representation of the spin arrangement of the Mn^{2+} ions in MnO . b) Dependence of indirect exchange integral on the separation between atoms.	62
3.3	Schematic representation of a) direct exchange, b) superexchange and c) indirect exchange.	62
3.4	Magnetization curves of magnetite for different crystallographic orientation.	63
3.5	a), b) Uniaxial , c), d) biaxial and e), f) cubic magnetocrystalline anisotropy.	65
3.6	Domains with a) Néel and b) Bloch domain wall in a FM.	67
3.7	a) Domain wall energy and b) width dependence on the film thickness for Bloch and Néel domain walls.	68
4.1	Dependence of characteristic time in Monte-Carlo steps on trial step radius.	70
4.2	a) Phase transition of a ferromagnet. b) Hysteresis loop temperature dependence.	71
4.3	Hysteresis loop dependence on a) the exchange integral and b) the form of nearest neighbors.	72

LIST OF FIGURES

4.4	Hysteresis loop dependence on lateral size of the thin film.	73
4.5	Hysteresis loops for different a) kinds of anisotropy, b) anisotropy constants (uniaxial) and c) angles between the easy axis and the applied magnetic field.	74
4.6	Phase transition of an AFM	76
4.7	The energy surfaces of a) uniaxial and b) biaxial anisotropy.	78
4.8	Cooling field effect on the EB field.	79
5.1	First and tenth hysteresis loop of the FM and the AFM interface of the parallel, transverse, in-plane component of magnetization.	81
5.2	First and tenth hysteresis loop of the bulk AFM of the a) parallel and b) transverse component of magnetization.	81
5.3	Snapshots of an EB system during the first two hysteresis loops	82
5.4	Training effect of exchange bias field and coercive field for several temperatures.	83
5.5	Two examples of the fitting laws for two different temperatures.	84
5.6	Numerical results and power law fits for three different temperatures.	86
5.7	Easy axes of an exchange bias system with biaxial AFM anisotropy.	87
5.8	Training effect of a) the exchange bias field and b) the coercivity for different temperatures and AFM thicknesses.	88
5.9	Temperature dependence of the training effect for several systems.	89
5.10	Temperature dependence of the training effect of the coercive fields for several systems.	91
5.11	Temperature dependence of the training effect for several systems.	94
5.12	AFM interfacial spin configuration snapshots of an uniaxial and a biaxial AFM in an EB system.	95
5.13	Distributions of reversal angles of the first reversal.	97
5.14	Training effect of the concentration of the stable spins.	98
5.15	Training effect of the magnetization of the stable spins.	99
5.16	Comparison of the magnetization of the stable interfacial spins ($M_{S.I.S.}$) and of irreversible domain state magnetization (M_{irr}).	100
5.17	Magnetization of the AFM interface of systems with a) uniaxial and b) biaxial AFM anisotropy.	101
5.18	First and tenth hysteresis loop of the AFM interface of the in-plane component of magnetization for biaxial AFM anisotropy.	102
5.19	a) Energy contour plot of a EB system with biaxial AFM anisotropy. b) One-dimensional representation of effective energy for AFM spins.	103
5.20	Distribution of the nearest neighbors for AFM interfacial spins.	104

LIST OF FIGURES

5.21	Distribution of the nearest neighbors for AFM interfacial spins for a) uniaxial and b) biaxial AFM anisotropy.	104
5.22	Néel temperature dependence on the AFM thickness.	105
5.23	Training effect of a) the exchange bias field and b) the coercivity for different AFM thicknesses at constant temperature.	106
5.24	AFM thickness dependence of the training effect.	106
5.25	Training effect of a) the concentration of stable spins in the AFM interface and b) their net magnetization.	107
5.26	a) AFM thickness dependence of the training effect of the coercive fields. b) Schematic representation of Type I and Type II training effect.	108
5.27	Néel temperature dependence on the AFM dilution.	109
5.28	Training effect of a) the exchange bias field and b) the coercivity for different AFM dilutions at constant temperature.	109
5.29	AFM dilution dependence of the training effect.	110
5.30	Training effect of a) the concentration of stable spins in the AFM interface and b) their net magnetization for different AFM dilutions.	112
5.31	a) Training effect of the reversible and irreversible domain state magnetization of the AFM interface as function of AFM dilution. b) Effect of different AFM dilutions on AFM interfacial hysteresis loop.	113
5.32	AFM interface spin configuration snapshots for a system with a) 40% and b) 20% AFM dilution.	113
6.1	Easy axes of an EB system with cubic and uniaxial anisotropy.	116
6.2	Training effect of a) EB field and b) coercivity for strong AFM anisotropy for several FM anisotropy constants and combinations.	117
6.3	Training effect of a) EB field and b) coercivity for intermediate AFM anisotropy for several FM anisotropy constants and combinations.	117
6.4	Training effect of a) EB field and b) coercivity for weak AFM anisotropy for several FM anisotropy constants and combinations.	118
6.5	FM consecutive hysteresis loops for $k_{FM} = 0.1J_{FM}$ and $k_{FM} = 0.02J_{FM}$	119
6.6	In-plane component of magnetization of the first and tenth hysteresis loop of the FM for $k_{FM} = 0.1J_{FM}$ for several combinations of anisotropy.	120
6.7	In-plane component of magnetization of the first and tenth hysteresis loop of the FM for $k_{FM} = 0.02J_{FM}$ for several combinations of anisotropy.	121
6.8	Different components of magnetization for several angles between magnetic field and FM easy axis.	123
6.9	FM spin configuration snapshots for systems with $k_{FM} = 0.1J_{FM}$ and $k_{FM} = 0.02J_{FM}$	125

6.10	Dependence of the training effect on magnetic field angle.	126
6.11	In-plane component of magnetization of the AFM for $k_{FM} = 0.1J_{FM}$ for several angles between magnetic field and FM easy axis.	127
6.12	In-plane component of magnetization of the AFM for $k_{FM} = 0.02J_{FM}$ for several angles between magnetic field and FM easy axis.	128
6.13	Angular dependence of the training effect of the concentration and of the magnetization ($M_{S.I.S.}$) of the stable spins.	129
6.14	Different components of magnetization for several angles between magnetic field and FM easy axis.	131
6.15	FM spin configuration snapshots for a system with $k_{FM} = 0.02J_{FM}$ for $\theta = 5^\circ$ and biaxial AFM anisotropy.	132
6.16	Dependence of the training effect on magnetic field angle for a) EB field and of b) coercivity for systems with $k_{FM} = 0.1J_{FM}$ and $k_{FM} = 0.02J_{FM}$	132
6.17	In-plane component of magnetization of the first and tenth hysteresis loop of the AFM for $k_{FM} = 0.1J_{FM}$ for several angles between magnetic field and FM easy axis.	133
6.18	In-plane component of magnetization of the first and tenth hysteresis loop of the AFM for $k_{FM} = 0.02J_{FM}$ for several angles between magnetic field and FM easy axis.	134
6.19	Angular dependence of the training effect of the concentration and of the magnetization ($M_{S.I.S.}$) of the stable spins.	135
6.20	Different components of magnetization for several angles between magnetic field and FM easy axis.	136
6.21	Dependence of the training effect on magnetic field angle for a) EB field and of b) coercivity for systems with $k_{FM} = 0.1J_{FM}$ and $k_{FM} = 0.02J_{FM}$	138
6.22	In-plane component of magnetization of the AFM for $k_{FM} = 0.1J_{FM}$ for several angles between magnetic field and FM easy axis.	139
6.23	In-plane component of magnetization of the AFM for $k_{FM} = 0.02J_{FM}$ for several angles between magnetic field and FM easy axis.	140
6.24	Different components of magnetization for several angles between magnetic field and FM easy axis.	141
6.25	Dependence of the training effect on magnetic field angle for a) EB field and of b) coercivity for systems with $k_{FM} = 0.1J_{FM}$ and $k_{FM} = 0.02J_{FM}$	143
6.26	In-plane component of magnetization of the AFM for $k_{FM} = 0.1J_{FM}$ for several angles between magnetic field and FM easy axis.	144
6.27	In-plane component of magnetization of the AFM for $k_{FM} = 0.02J_{FM}$ for several angles between magnetic field and FM easy axis.	145

7.1	A sketch of an EB system with rough interface.	147
7.2	Interface roughness dependence of the training effect for systems with a) 40% dilution and b) no dilution.	148
7.3	Interface roughness dependence of the training effect of the coercive fields for systems with a) 40% dilution and b) no dilution.	149
7.4	Snapshots of the FM before and during reversal.	149
7.5	Schematic representations of the EB systems that we used with a) bcc structure with the [110] crystallographic orientation along the interface and b) fcc structure with the [100] crystallographic orientation along the interface.	150
7.6	Interface roughness dependence of the training effect for systems with a) sc structure, b) bcc[110] structure and c) fcc structure.	151
7.7	Interface roughness dependence of the training effect of the coercive fields for systems with a) sc structure, b) bcc[110] structure and c) fcc structure.	152
7.8	Schematic representations of the EB systems that we used with bcc[100] structure.	153
7.9	Interface roughness dependence of the training effect a) of the EB field and of b) of the coercive fields for systems with bcc structure.	154
7.10	Schematic representations of the EB systems that we used with a) hcp structure and b) fcc structure with interface along the [110] crystallographic orientation.	155
7.11	Interface roughness dependence of the training effect for systems with a) hcp structure and b) fcc[110] structure.	156
7.12	Interface roughness dependence of the training effect of the coercive fields for systems with a) hcp structure and b) fcc[110] structure.	156
A.1	Schematic representation of the selection of the new spin for the trial step in a Monte-Carlo step.	166

List of Tables

4.1	Coordination number of crystal structures.	72
6.1	Anisotropy combinations	116

Acknowledgments

It is a great pleasure to have the possibility to thank the people, to whom I will be forever grateful, who have introduced me to the study of magnetism. Over four years the Ph.D. course at the University of York has proved to be an excellent and most rewarding intellectual exposure which has culminated in this dissertation.

Firstly, I would like to express my sincere gratitude to my two supervisors, Ulrich Nowak and Roy Chantrell, for the opportunity to work with them on this project, for their guidance and for providing me with the means to carry out this research. Their enthusiasm willingness to help have allowed me develop to be a more capable scientist. Their guidance and encouragement have truly defined for me what a supervisor should be like, and without them this work would never have been completed.

Furthermore, I must mention my coworkers in Computational Magnetism group, Denise Hinzke, Richard Evans, Jerome Jackson, Natalia Kazantseva, Margaret Clegg and many others, who have always be quite helpful and for providing a friendly and stimulating workplace. Through the discussions with them, they really helped me understand many concepts of my subject. Also, I would also like to thank Kevin O'Grady, Luis Eugenio Fernández Outón and Gonzalo Vallejo-Fernández for the very helpful discussions.

I am indeed grateful to European Union NEXBIAS Research Training Network (Contract No. HPRN-CT-2002-00296) but for whose generous support, this work could not have materialized. Also, the White Rose Grid Computational Recourses at University of York and Sheffield is gratefully acknowledged.

Of course mention must also be made of my friends and my basketball mates who have provided me psychological support, their friendship and an actual help with my thesis: Dimitris Kolovos, Eugenia Orfanou, Ioannis Klapaftis, Georgia Papadopoulou, Margaritis Voliotis, Alexandros Kostakis, Ioannis Korkontzelos, Chrisostomos Florakis, Sophie Manuel and many others.

Finally, I wish to deeply thank my parents, Maria and Georgio, and my brother, Ioannis, for the encouragement and love with which they have surrounded me during the Ph.D. years.

Author's Declaration

The work described in this thesis was carried out in the Department of Physics, University of York and has not been submitted for any other degree or diploma of any examining body. All the material described herein is the original work of the author, except where otherwise acknowledged. Parts of this work have been previously published by the author in a number of journals, international conferences and workshops.

A. Biternas

4th May 2010

Introduction

In recent years, material science has become one of the most dominant sciences in the commercial sector. New materials are being developed with amazing properties and capabilities. Using these materials in commercial products enhance their efficiency and reduce their volume. The miniaturization of the electronic, magnetic or mechanical parts of devices has reached the region of the nanoworld where DNA molecules or even single atoms can be manipulated, as shown in Fig. 1.1. The characteristics of nanostructures- especially their electronic and magnetic ones- are often significantly different from the same material in the bulk. Nanostructures are, in a sense, a unique state of matter with particular promise for new and potentially very useful products. Exploring the science of nanostructures has become a new theme common to many disciplines; Extensive studies and investigations are undertaken in the field of Condensed Matter Physics, as well as in Statistical Physics. The combination of descriptive theories with advanced experimental techniques leads to a deeper understanding of the materials' physics of the materials.

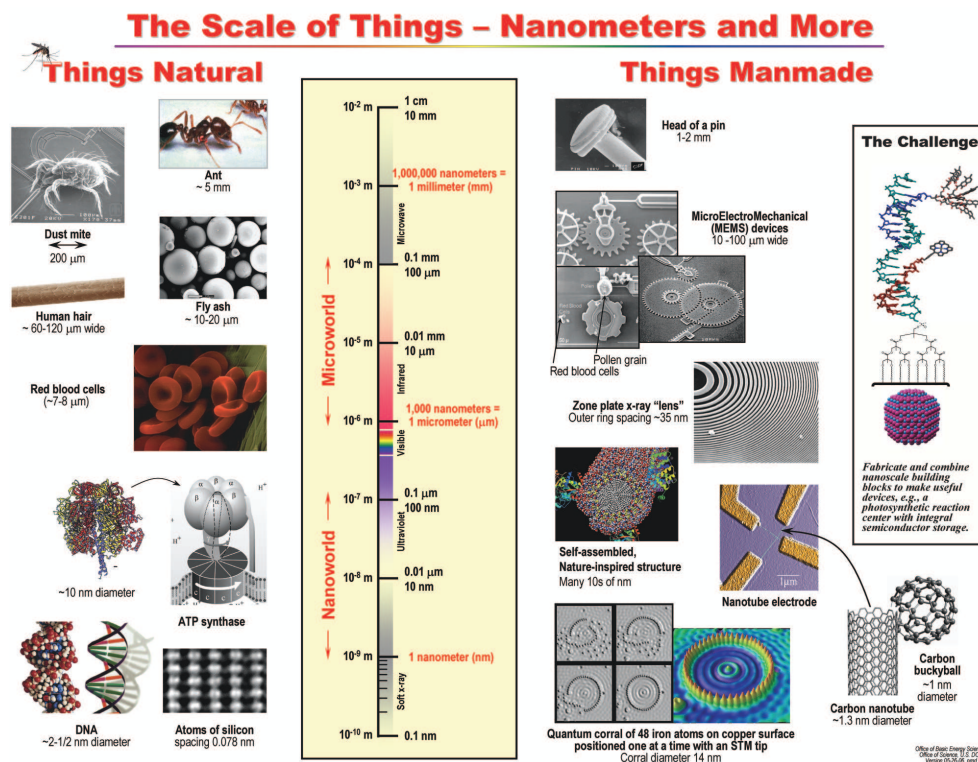


Figure 1.1: The scale of things.[1]

One of the fields that has taken advantage of material science is information technology. This discipline today includes every kind of computer as well as consumer electronic devices. The huge development of information technology has led to an exponential growth in the semiconductor and data storage industries. The latter especially continues to grow at a rapid pace, fueled by the explosion of content being created and consumed. The most common product of this industry is the well known hard disk based on the magnetic recording and reading of data.

In general, magnetic materials constitute a very important category in material science, which is an extremely well developed field. This is due to the huge commercial application, mainly, in storage of digital and analogue information as mentioned above; but also in the aviation industry, for the creation of strong motors and aviation sensors, as well as in the medical industry for the creation of diagnostic imaging devices e.g. magnetic resonance imaging (MRI). Also, superconducting magnets are used for the directioning of rays in the accelerators, as well as magnetic bottles used for the containment of plasma. Spintronics is a new field which exploits magnetic materials. It involves the development of integrated circuits using the flux of spins rather than the flux of the electric charge as in the case of electronics. More futuristic applications include trains that levitate above the train track, an application already used in the MAGLEV train route in Japan, and the creation of magnetic fields proper for shielding from cosmic rays, in possible space missions to other planets. A great effort is paid for the experimental and theoretical investigation of these applications.

The main purpose of the present research is the theoretical investigation of magnetic materials that can be used in industry for commercial applications. Especially, we investigate theoretically the properties of magnetic systems that consist of two materials with different magnetic order, called exchange bias systems. Atomistic simulations will be used to gain a theoretical understanding of the physics of these systems.

1.1 Magnetism in materials: Ferromagnets, antiferromagnets and hysteresis loops

According to Aristotle, the concept of magnetism was first discussed scientifically by Thales around 5th century BC. However, the existence and use of magnetism was known earlier by Indian and Chinese ancient scientists. Magnetism can be considered the attractive force between two bodies. When a magnetized body is dipped in iron filings, they align along the direction of the field created by it; these lines converge in places close to the ends of the body, called poles. The concepts of poles is useful for the definition of the two basic quantities of magnetism, the magnetic field and the magnetization.

The magnetic field \mathbf{H} may be defined in terms of magnetic poles: a unit of magnetic

field is the field produced from a magnetic unit pole in a length unit distance. A magnetic field may be produced by a current of electricity as well as by a magnet. The magnetization M may be defined the same way as the magnetic field: a unit of magnetization is the magnetization produced from a magnetic unit pole in a unit area or volume. Magnetization is a quantitative measure of the magnetic property in a material. In general, the root of the magnetization of a material arises from electric currents or moving electric charges (electrons orbital angular motion around the nucleus) and from the intrinsic magnetic moments (“spin”) of many particles (especially electrons). Materials can be categorized according to the ordering of the net magnetic moment of each atom as ferromagnetic and antiferromagnetic ordered materials (the most well known forms). In ferromagnetic materials, the magnetic moments are aligned in the same direction as each other and are named after iron with which have similar properties (nickel, cobalt). In contrast, in antiferromagnetic materials each magnetic moment is “anti-aligned” to its neighbors, as shown in Fig. 1.2a).

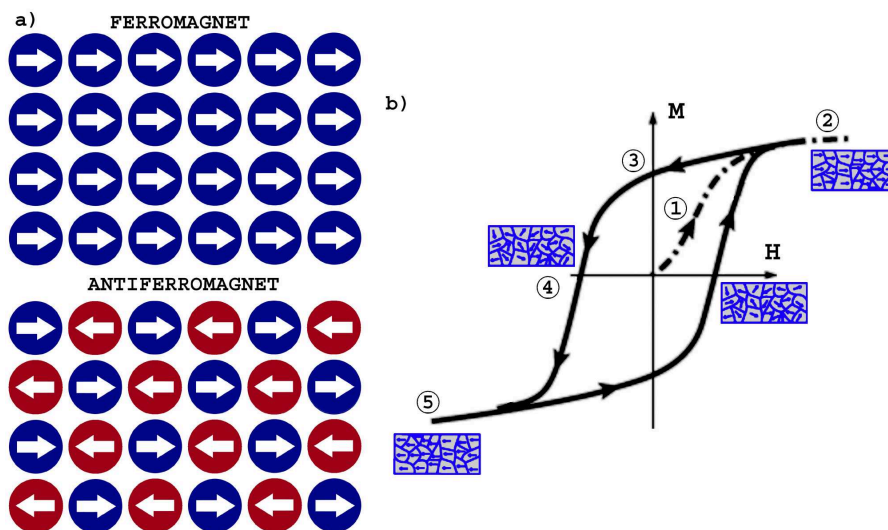


Figure 1.2: a) Ferromagnetic and antiferromagnetic order (ideal) in a bulk material. b) A ferromagnetic hysteresis loop. ① The material follows a non-linear magnetization curve beginning from zero field value. ② Material magnetized to saturation by alignment of the magnetic moments of atoms or of regions of atoms (“domains”). ③ When the magnetic field is zero, the material retains a considerable magnetization. ④ The magnetic field is now reversed and increased to a large value to drive the magnetization to zero. That actually means that the magnetic moments of the atoms or the domains have net magnetization zero. ⑤ Material magnetized to saturation in the opposite direction.

The behavior of a material can be described by its permeability curve and hysteresis loop. Permeability μ is the magnetization-magnetic field ratio (M/H) and represents the increase of flux caused by the presence of a magnetic material inside a magnetic field. Usually, a hysteresis loop can be generated from systems that have memory[2]. The hysteresis loop is a magnetization curve as function of magnetic field and shows the

“history dependent” nature of magnetization. As shown in Fig. 1.2, a hysteresis loop is created by first increasing the magnetic field from zero (point 1) to a high value (point 2) and then decreasing it to its opposite value (point 5). It is observed that the original curve is not retraced; the induction “lags behind” the field. When the material has been driven to its saturation value (maximum value of magnetization), the magnetic field can then be dropped to zero and the material will retain most of its magnetization (remembering its history). This general phenomenon is called hysteresis, it was originally named by Ewing. Hysteresis loops occur predominantly in ferromagnets but not in antiferromagnets as their magnetization is always zero.

1.2 Exchange bias phenomenon and the training effect

Exchange bias (EB) is the phenomenon in which the hysteresis loop of a system, consisting usually of two magnetic materials with different magnetic order, is shifted along the magnetic field axis. The most common EB system is a multilayer consisting of a ferromagnet (FM) in contact with an antiferromagnet (AFM). The term EB is established because the hysteresis loop is shifted with a bias field, in addition to the applied field, which is created from the exchange interaction[3, 4].

This phenomenon was first discovered in 1956 from Meiklejohn and Bean [5, 6, 7], in a system consisting of fine particles which have a core of Co and a shell CoO . The existence of this oxide layer surrounding the particles of Co was considered to be the cause of the displacement of the hysteresis loop. The Co is the FM and the CoO the AFM. They reported their discovery as new exchange anisotropy. The procedure they used was to firstly cool the system below the Néel temperature, T_N , of the AFM in an external magnetic field. The Néel temperature of an AFM material and the Curie temperature of a FM material is the temperature above which the magnetic materials is in a paramagnetic state. This cooling process begins above the Néel temperature of the AFM but below the Curie temperature of the FM. The final fixed temperature where we observe the EB phenomenon must be below the so-called blocking temperature T_B above which EB is not observed. The shift and width are quantified as the EB field and coercivity of hysteresis loop, respectively.

Initially, it was concluded that the shifted hysteresis loop was an effect created by the existence of an oxide layer surrounding the Co particles, implying that the magnetic interaction along the interface is responsible for this effect. So, being considered as an interfacial effect, the investigation of exchange bias are carried out on thin films, usually consisting of a bilayer structure with an AFM part in contact with an FM one.

The shift of the hysteresis loop of $Co - CoO$ particles is shown in Fig. 1.3a). The

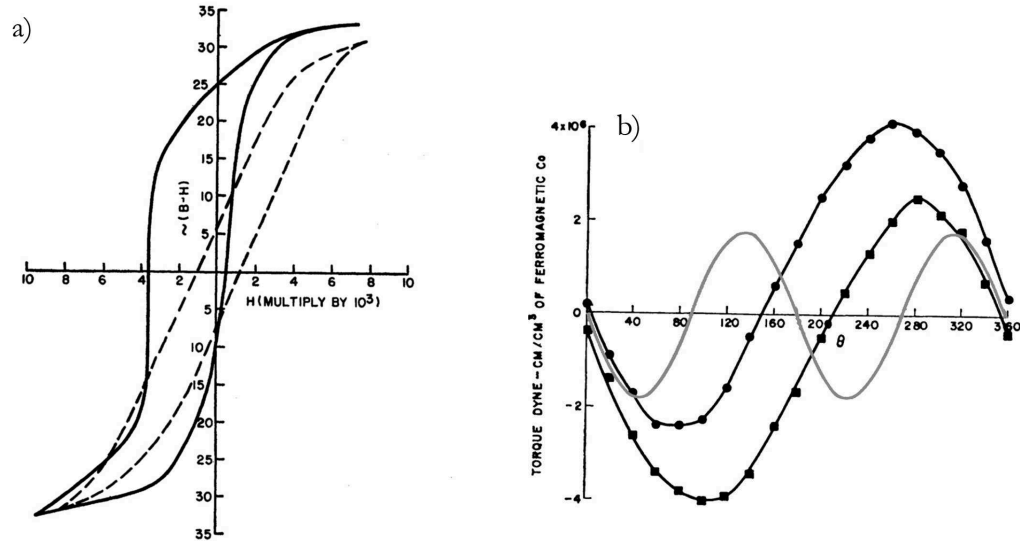


Figure 1.3: a) The shifted hysteresis loop of the Co particles at $77^\circ K$ after cooling in a field of $10kOe$ (solid line) and the hysteresis loop of Co particles after cooling in zero field (dashed lines) and b) The torque magnetization of a material with uniaxial anisotropy (grey line) and of the $Co - CoO$ with the unidirectional anisotropy as measured for decreasing (circles) and increasing (boxes) angle θ . [5, 6]

cooling process was started from room temperature, which is higher than the Néel temperature of the CoO , and decreased to $77^\circ K$. When the above procedure happens in zero field, the hysteresis loop is symmetrically centered around zero value of magnetic field, a behavior corresponding to FM materials. But, when a positive field is applied during the cooling process, the hysteresis loop is shifted to the left, even when very high magnetic fields were applied.

Fig. 1.3b) shows the torque curves of this system in comparison to a system with uniaxial anisotropy. In general, torque magnetometry is used to measure the magnetocrystalline anisotropy of ferromagnets. The anisotropy energy for the system of $Co - CoO$ particles is described from the term $K_d \cos^2 \beta$ rather than from $K_a \cos^2(2\beta)$ for uniaxial anisotropy, where β is the angle between the FM magnetization and the FM easy axis and K_a, K_d are the uniaxial and unidirectional anisotropy constants, respectively. This expression clearly shows that for 0° the particles are in a stable state. Typically, in a case of uniaxial anisotropy there are two stable states, one at 0° and the other at 180° angle.

In conclusion, the shift of the hysteresis loop is caused by the produced anisotropy of the system, called unidirectional anisotropy. Thus, instead of uniaxial anisotropy, where the magnetization is, energetically favorable to two opposite directions (easy axis), the net magnetization of an EB system is energetically favorable to only one direction. Meiklejohn and Bean [5, 6, 7] connected the loop shifting with the explanation for the unidirectional anisotropy.

The training effect is the decrease of the shift, coercivity and the change of the shape

of a hysteresis loop after several consecutive hysteresis loops for a fixed temperature. The training effect was discovered by Paccard *et al.*[8] in 1966 in three systems exhibiting FM-AFM coupling with uniaxial anisotropy. Fig. 1.4 shows the consecutive hysteresis loops of a $Co-CoO$ system. The first loop appears to be shifted more than the others. Also, this decrease in the shift is more significant on the left-hand branch of the loop than on the right hand, causing a decrease of the hysteresis loop's coercivity.

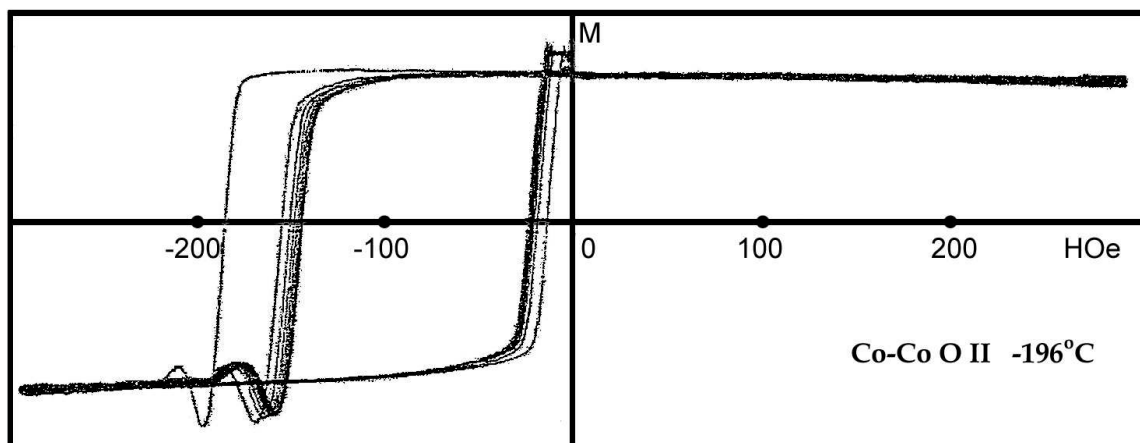


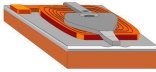
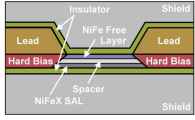
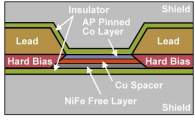
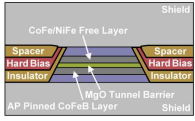
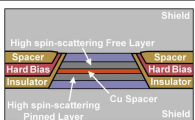
Figure 1.4: Consecutive hysteresis loops of a $Co-CoO$ system measured with torque balance. The observed overshoot is an instrumental effect.[8]

It is common for the training effect to be separated into two categories: the effect between the first and the second loop, and the other between consecutive hysteresis loops. Especially during the first cycle the system behaves in irreversible way, because of the non-equilibrium state of the AFM that is gained during the cooling process. The second type of training effect show that the shifting decreases with the increase of the number of consecutive hysteresis loops and follows a inverse power law, as proved by Paccard *et al.*[8]. The cause of this is suggested to be the reconfiguration of the spins or of the domain state of the AFM during the consecutive cycles, causing fluctuations in the FM-AFM coupling. Lastly, the importance of the training effect rests on the stability of exchange bias bilayer which is inside many devices.



1.3 Applications of exchange bias systems

Exchange bias systems are used in the read-head of the magnetic hard disk drives of personal computers for reading the stored information. The mechanism of the sensor is called Giant Magnetoresistance (GMR), discovered by A. Fert and P. Grünberg, who were awarded a Nobel prize in 2007 for this discovery. Despite the fact that the first commercial use of exchange bias was in the anisotropic magnetoresistance (AMR) used in IBM disk drive recording heads around the 1970s, it did not displace the inductive readback head until the 1990s, as shown in Fig. 1.5.

1.3. Applications of exchange bias systems

Year	Density (Gb/in ²)	Sensor Technology	Structure	MR Effect	Current Geometry
1979	0.01 Gb/in ²	Thin-film Inductive		N/A	N/A
1991	0.1 Gb/in ²	MR Sensor		Anisotropic MR	CIP
1997	2 Gb/in ²	Spin Valve		Giant MR	CIP
2006	100 Gb/in ²	Tunnel Valve		Tunneling MR	CPP
2011	1 Tb/in ²	CPP GMR		Giant MR	CPP

2007 Nobel prize

Albert Fert & Peter Grunberg

Figure 1.5: Progress of read head sensor technologies.[9]

A typical GMR is shown in Fig. 1.5, consists of a FM layer (free layer) separated by a non-magnetic spacer from an exchange biased bilayer (hard layer). The role of the free layer is to “read” the bit of the magnetic media, so it gains the magnetization of the trace field. The hard layer is used as a reference layer of the sensor, meaning that its magnetization is pinned to a specific direction. Consequently, this magnetization does not change its direction under the change of the trace field, as the one of the free layer does. The angle between the magnetization direction of the free layer and hard layer changes the resistance of the non-magnetic spacer, which causes the read signal. This sensing mechanism is called the GMR effect and was discovered by Baibich *et al.* in 1988 [10].

The above sensor is usually referred to as spin-valve and is mounted on a lever arm suspended some nanometres above a lubricant layer that covers the recording media. This sensor is shielded from the magnetic field of the bits other than the one being read. Fig. 1.5b) shows a cross-section TEM picture of a real read-head sensor. Other GMR-based applications include automotive and aviation sensors, non-volatile magnetic memory, solid state compasses as well as landmine detectors.

Another application of exchange bias is in recording media because of the increase of coercivity, without the decrease of saturation magnetization, caused by the AFM. The AFM acts as a domain stabilizer for the FM through the exchange interaction between the FM and the AFM, because some of the AFM spins are frozen to a specific direction after the cooling process. This leads the FM magnetization to stabilize in a desired direction. In

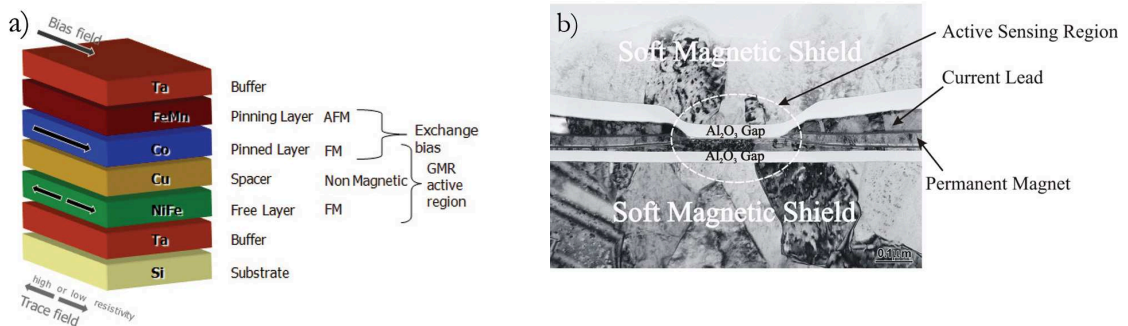


Figure 1.6: a) A typical giant magnetoresistance with the trace field pointing to the one or the opposite direction. b) Structure of a spin-valve head, similar to the ones used on hard disks.[11]

total, the interaction between the two materials induces an extra source of anisotropy to the FM, helping it to overcome the superparamagnetic limit[12]. The superparamagnetic limit is caused, in this case, by thermal fluctuations when the miniaturization of magnetic elements exceed a specific limit, leading to magnetization instability. The density of the recording media can be increased by decreasing the size of the magnetic elements without losing their stable magnetic state by implementing the exchange coupling with an AFM [12].

One of the most promising applications of the spin valve is the magnetic random access memory (MRAM), which will use an array of GMR elements or a tunnel magnetoresistance (TMR). The TMR is similar to the GMR except in the spacer which is replaced by an insulator. The advantages of MRAM are that there are no moving parts, no reading head and the ability to access information in a random way (random access).

Despite the many advantages, the applications of exchange bias systems are limited by the fact that the blocking temperature observed in most of the systems is much lower than room temperature. However, there is active research seeking new applications of exchange bias and it is very likely that GMR and TMR will find a large number of applications in the future due to their cost-effective sensing capabilities.

1.4 Related phenomena

EB systems also exhibit several other phenomena e.g. asymmetric reversal modes, enhanced coercivity, non vanishing rotational hysteresis, blocking temperature, memory and perpendicular exchange bias effect. The blocking temperature T_B of an EB system is the temperature above which the EB field vanishes.

The asymmetric reversal mode during a hysteresis loop observed in some exchange bias

systems is an important characteristic of these systems. It is usually observed directly as an asymmetry of the shape of the hysteresis loop, but many experimental investigations have obtained a more detailed view of the phenomenon using neutron scattering techniques[13] or polarized neutron reflectometry [14]. They show that the first reversal is a result of domain wall movement and the second reversal results from magnetization rotation.

Enhanced coercivity is another characteristic of exchange bias systems. More specifically, the coercivity of the FM in an exchange bias system is larger than when the FM is alone. This phenomenon is present even if the temperature is above the Néel temperature of the AFM[15].

By rotational hysteresis we mean the work done on rotating a specimen 360° in a magnetic field, as a result of the irreversible changes of magnetization. Usually, for systems of a single domain FM particle, the rotational hysteresis as function of magnetic field has a finite value for a range of magnetic field and zero elsewhere[7]. But for exchange bias systems, the rotational hysteresis has a finite value above a certain value of magnetic field[7, 5]. This feature is more general than the shifted hysteresis loop for these systems. Actually, a unidirectional anisotropy results in no hysteresis at any value of the magnetic field. The non vanishing rotational hysteresis was attributed to the irreversible changes of the magnetic state of the sample taking place during the rotation of the sample in the magnetic field. Such irreversible changes occurred in the AFM.

The memory effect[16, 17] is a characteristic that EB systems exhibit when they are heated above the initial temperature T_I , where T_I is the temperature at which the cooling process began. When the EB system is cooled from an T_I and then heated above the this T_I the EB phenomenon disappears, even though the blocking temperature T_B is greater than the initial temperature T_I . Usually when we make a temperature investigation of the EB, for every temperature we carry out the cooling process from the T_I to the temperature at which we desire to find the hysteresis loop shift each time. This is how the blocking temperature T_B is found. But when we only carry out the cooling process from the T_I once and then we increase the temperature, the system “remembers” this T_I and the hysteresis loop shift becomes zero at that temperature although this temperature is lower than the blocking temperature T_B .

As mentioned above the blocking temperature is the temperature at which exchange bias ceases to exist. The most common method for determining the blocking temperature is to measure the shift of hysteresis loop, increasing the temperature until the shift becomes zero and remains zero with further increases in temperature. For granular systems, each AFM grain has its own blocking temperature creating a distribution of blocking temperatures in the AFM. This can give false estimation of the blocking temperature due to thermal activation during measurement. An alternative method has been suggested [18] that the blocking temperature is defined when equal fractions of the AFM are oriented in

opposite directions, as shown in Fig. 1.7.

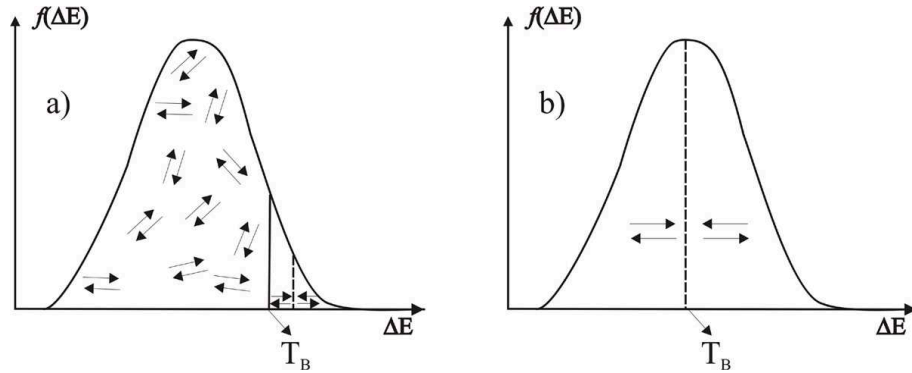


Figure 1.7: Distribution of energy barriers to reversal in a AFM layer a) following the common method of determining the blocking temperature and b) following the alternative method. [18]

Finally, by perpendicular exchange bias we mean the exchange bias phenomenon when a magnetic field is applied perpendicular to the plane of the system. Because of the reduced spin dimensionality, perpendicular exchange bias systems are considered easier to understand than conventional exchange bias systems. Their applications are expected to become important in future perpendicular recording and sensing devices[19].

1.5 Important quantities of exchange bias systems

Two important properties of EB systems are the exchange bias field and the coercivity. The coercivity H_c of a hysteresis loop is the distance between the two points of a hysteresis loop where the magnetization is zero, as shown in Fig. 1.8. Usually, these two points are referenced as the negative and positive coercive field or (H_{C_-}, H_{C_+}) respectively). So, the coercivity is $H_{eb} = (H_{C_-} - H_{C_+})/2$. The exchange bias field H_{eb} is the displacement of the hysteresis loop from zero magnetic field and it is used to quantify the intensity of the exchange bias. Thus, the EB field is $H_{eb} = (H_{C_-} + H_{C_+})/2$. In experiments and numerical simulations it is very difficult to have exact points for the two coercive fields (usually we have points which are very close to zero of magnetization). Often, we use an interpolation method (linear is satisfactory) between the two points where the magnetization goes from positive to negative and vice versa.

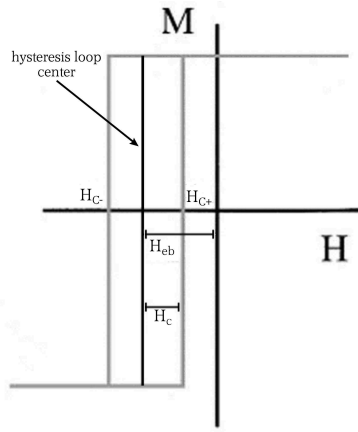


Figure 1.8: Exchange bias hysteresis loop with the important quantities.

1.6 Experimental findings and system behaviour

1.6.1 Exchange bias systems

There are several different systems where the exchange bias phenomenon is exhibited. It is usually observed in systems involving two different magnetic orders: a FM, a ferrimagnet or an AFM, with the most common system being that of AFM and FM. Also there is a great variety of materials where EB has been observed [3, 4]. The most common types are microfilms, nanoparticles and coated monocrystalline AFM which clearly have an AFM-FM interface. Microfilms are multilayers consisting usually of one layer of AFM and one layer of FM, as shown in Fig. 1.9, and nanoparticles are particles, the core of which is AFM and the shell is FM, like the system of Co/CoO , which Meiklejohn and Bean [5] investigated. Microfilms are also divided into two sub-categories: epitaxial films and sputtered films, the latter having granular structure. Coated monocrystalline AFM is a very unusual system where a single AFM crystal, cut in a specific crystallographic orientation, is coated with an FM material. Another category of EB systems is inhomogeneous materials in which there is no clear AFM-FM interface. Spin glasses are included in this category. Finally, inhomogeneous materials consist of metals like Fe, Co, Ni, Mn, Ag, Cu , oxidized metals and more occasionally sulfides, fluorides and nitrides.

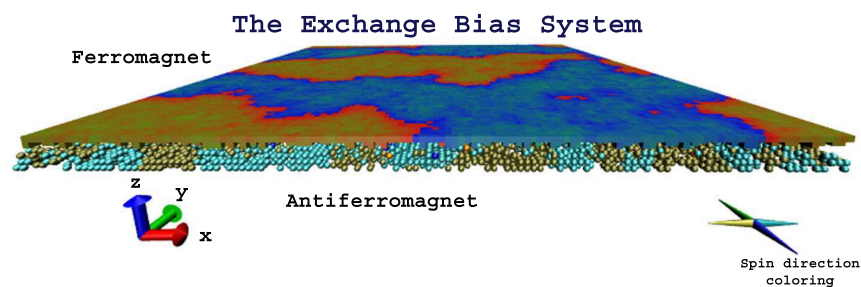


Figure 1.9: Exchange bias thin film, consisting of a FM and an AFM.

1.6.2 Exchange bias and coercivity

To better understand the behavior of an EB system, the dependence of EB field as well as coercivity is discussed, as measured by experimental apparatus. For the measurement of the EB field and coercivity a device such as semiconductor quantum interference device (SQUID) is used in order to get a hysteresis loop of a sample along the axis of the magnetization field. Torque magnetometry is also used to measure the anisotropy. Several other methods exist for the measurement of other properties of magnetic materials, which are useful for the investigation of EB systems [3, 4].

Obviously, EB field and coercivity decrease with increasing temperature of the system. The EB field decreases to zero at the blocking temperature T_B . The EB field trend on temperature and subsequently T_B changes with different system characteristics e.g. dilution with non-magnetic defects [20]. Furthermore, EB field and coercivity depend on the cooling field during the cooling process to the desired temperature. Experimentally it is observed that the EB field decreases with increasing magnetic cooling field[21] and in some systems becomes positive[22].

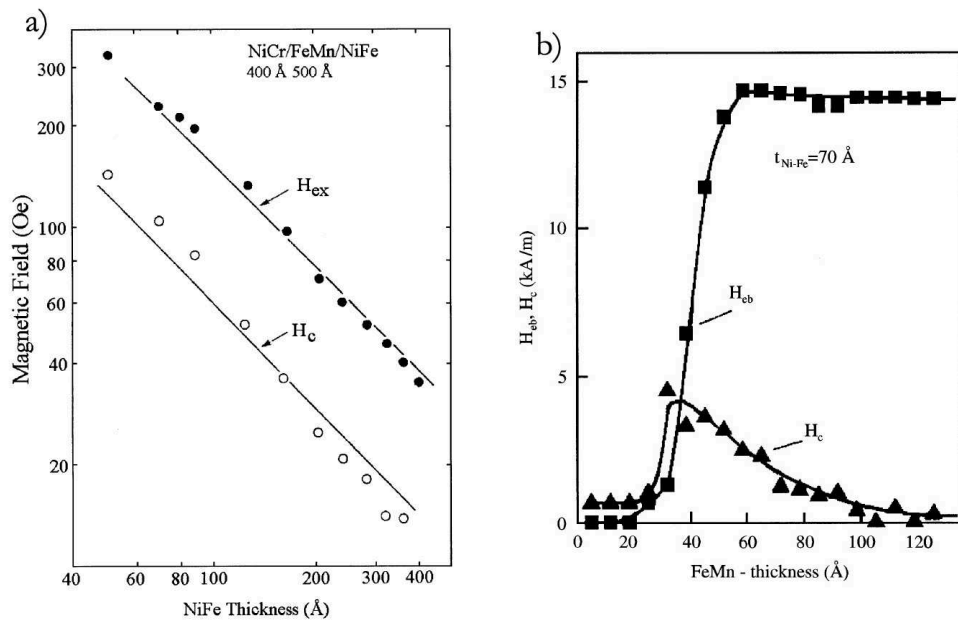


Figure 1.10: a) EB field (filled circles) and coercivity (open circles) dependence on FM layer thickness for a $Fe_{80}Ni_{20}/FeMn$ bilayer[23]. b) EB field (squares) and coercivity (triangles) dependence on AFM layer thickness for a $Fe_{80}Ni_{20}/FeMn$ bilayer[24].

The thickness of the two materials has a very important role. Firstly, the EB field and the coercivity are roughly inversely proportional to the thickness of the FM t_{FM} , for all the systems e.g. for a $Fe_{80}Ni_{20}/FeMn$ bilayer, as shown in Fig. 1.10a) [23]. This relation holds, as long as the thickness of the FM is bigger than the FM domain wall size, and this varies from system to system. Secondly, the dependence of EB field and coercivity on AFM thickness is non-monotonic and changes from epitaxial to grain structured systems.

In epitaxial systems the EB field decreases with increasing AFM thickness. On the other hand, for grain structured systems, with thick AFM layers, the EB field is independent of the AFM thickness. For thin AFM layers, the EB field is proportional to the thickness of the AFM, beginning from zero exchange bias field for a very thin AFM layer, as shown in Fig. 1.10b) [24]. This general behavior presents discrepancies with other experimental findings. Finally, another important effect in the behavior of the system is that the AFM thickness changes the Néel temperature of the AFM and consequently the blocking temperature of the system.

The spin orientation of the AFM is crucial for the configuration of the interface of the system. The orientation of AFM spin can be separated into two categories. Firstly, based on the compensation at the interface and secondly, on the plane where the AFM spins lie. In general, a compensated AFM interface is considered to exist when the total magnetization averaged over a microscopic length-scale is zero, as shown in Fig. 1.11a). On the other hand, when the spin configuration results in non-zero magnetization, the interface is uncompensated, as shown in Fig. 1.11b). Although it is expected that the spins pinning the FM self-cancel, giving rise to a net zero exchange bias field, this does not happen. It was found that all the exchange bias systems with compensated interfaces that were investigated experimentally, exhibit exchange bias. Especially, some of them exhibited very large hysteresis loop shifts, even larger than the uncompensated configurations of the same AFM material.

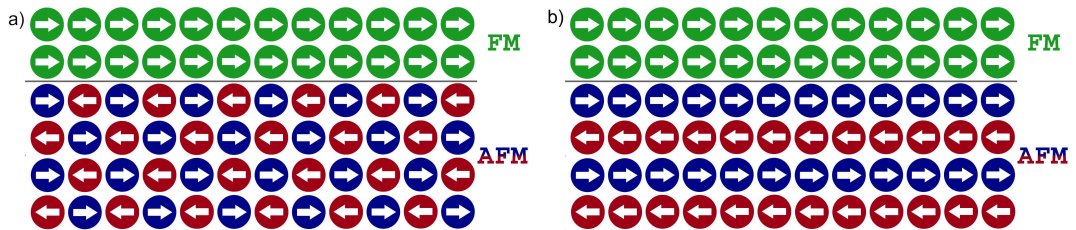


Figure 1.11: a) Exchange bias system with AFM having compensated spins on the interface, b) Exchange bias system with AFM having uncompensated spins on the interface.

In the second category, the spin configurations can be separated according to the plane of the pointing direction, so they can be in-plane or out-of-plane AFM spins. Usually, when the AFM spins are in the plane, EB field is maximum, but when they are out-of-plane, the EB field is zero. For an intermediate angle, the EB field is about half of the value for the case of in-plane spins. Finally, the shape anisotropy of the FM plays a crucial role in this dependence.

Also, the AFM spin configuration depends on the initial temperature T_I of the system before the cooling process[25] and on the dilution (non-magnetic defect concentration)[20] of the AFM material, as recently shown. The crystalline structure (e.g. fcc, bcc, etc.) and the magnetocrystalline anisotropy effects the behavior of the system e.g. for low AFM

anisotropy we have very low or zero EB field H_{eb} but increase in coercivity H_c [26].

Various structural factors can also affect the exchange bias field, e.g. interface roughness, crystalline structure, dilution of the AFM, grain size and crystallinity. Interface roughness is not very easy to quantify or measure experimentally. Many models [27] consider the percentage of FM spins inside the AFM interface layer to be related to interface roughness. Experimentally, interface roughness is quantified by considering the thickness of the mixed layers. In general, EB systems are sensitive to interface roughness with some of them having decreasing EB field with increasing roughness; however, in other systems the contrary occurs.

Secondly, the crystalline structure of the material, as well as its orientation in the interface plane plays an important role in EB systems. Usually, epitaxial systems have the same kind of crystalline structure i.e. an fcc AFM and fcc FM, but sputtered systems can have a different crystalline structure in each of the materials. There is strong dependence of EB field on crystalline structure because of the change in the number of neighbors of each spin in the bulk and interface of each material. The crystallographic orientation is connected with the structure of AFM spins on the AFM. For systems, where the spins are oriented along [001] or [110] directions, a larger training effect is seen compared with the [101] or [001] directions [26]. Blachowicz *et al.* [28] showed that exchange bias is dependent on the crystallographic symmetry of the two layers, the lattice mismatch between layers, the sequence of layers upon deposition and the quality (roughness) of the FM/AFM interface.

AFM dilution in the bulk, as well as in the interface, can enhance the exchange bias field and the coercivity. Dilution can be created by non-magnetic defects or vacancies in the AFM. As shown in Fig. 1.12, dilution can enhance the exchange bias and coercivity up to a limit, after which a decrease is observed. This trend is connected with the formation of volume domain walls, which prefer to pass through the defects [20].

Crystallinity is another important factor in the exchange bias systems. The crystallinity can be determined as the percentage of the volume of the material that is crystalline, compared with the volume that is amorphous. As expected, the increasing texture of the sample increases the exchange bias field, although there isn't a clear method measuring the crystallinity [29]. The crystallinity is connected with the grain size, although the role of grain size is complicated because it changes other parameters of the system, such as AFM anisotropy, spin structure, etc. EB is reported to increase with increasing grain size for some systems and with decreasing grain size in other systems.

Anisotropy is one the most important factors in the exchange bias systems. Although most investigations do not focus on FM anisotropy, experimental findings for the AFM anisotropy dependence of EB field show that it increases with larger AFM anisotropy [30, 31]. It is difficult to extract quantitative conclusions about anisotropy dependence due

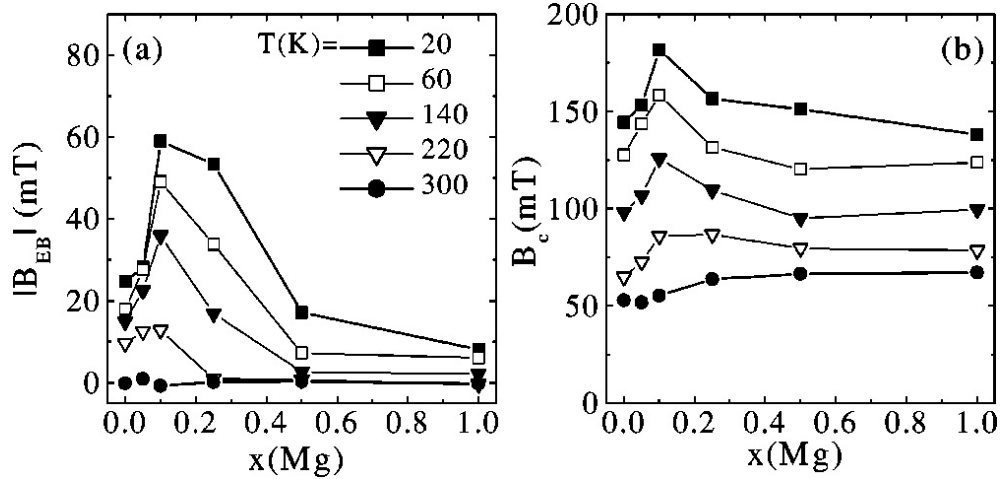


Figure 1.12: Dilution dependence of absolute exchange bias field (a) and of coercivity (b) in the $Co_{1-x}Mg_xO$ layer for various temperatures. The x denotes the percentage of the spins replaced by the non-magnetic Mg ions. [20]

to the lack of the absolute value of the anisotropy.

1.6.3 Training effect

The training effect is affected by the factors mentioned in the previous section like dilution and thickness of the AFM, and cooling field. Keller *et al.* [20] investigated the influence of dilution on the training effect in a $Co/Co_{1-x}Mg_xO$ system where x denotes the AFM dilution. They found that the magnitude of the relative training effect behaves non-monotonically with dilution. Furthermore, they found that the magnitude of the training effect and the exchange bias field are closely related to their dilution dependence. That means at optimum dilution the exchange bias is strongest with the smallest training effect, while at high and low dilution the exchange bias decreases with the training effect being increased.

Temperature is an important factor that influences the training effect. Khapikov *et al.* examined the temperature dependence of the exchange bias field and coercivity of a $NiO/Ni_{81}Fe_{19}$ bilayer for several consecutive hysteresis loops, as shown in Fig. 1.13. They showed that the EB and the training effect increases as the temperature decreases. At high temperatures both phenomena disappear. Also, the appearance of exchange bias is accompanied by a decrease of the equilibrium coercivity. The cooling field during the process of cooling to the desired temperature effects also the EB, coercivity and reversal modes training[25]. It is found that cooling in zero field results zero training effect.

The training effect is strongly influenced by the AFM thickness as showed by Zhang *et al.* [33] for $NiFe/IrMn$ bilayers. They separated the training effect into two types. Type I is when the hysteresis loop shrinks from both sides with the cycle of the applied field, meaning that the two branches of the loop move in opposite directions. Type II is when

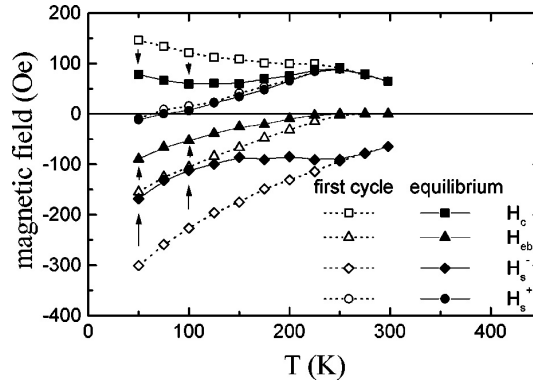


Figure 1.13: Temperature dependence of the first hysteresis loop and equilibrium values of the EB, coercivity, positive and negative coercive field of $NiO/Ni_{81}Fe_{19}$ bilayer. [32]

both branches move in the same direction towards the positive pinned direction. They found that the type of the training effect changes from type I to type II with increasing AFM thickness.

Another important factor that influences the training effect is the cooling field. Paul *et al.* [25] investigated the dependence of the training effect considering two different magnetic configurations. They considered a system in a remanent state without an external cooling field and a system which was field cooled. The first system did not exhibit a training effect while the second one showed a clear training effect.

Finally, a strong dependence of the training effect on a material's structure has been observed. More specifically, Fecioru-Morariu *et al.* [34] investigated the effect of crystalline structure on the training effect. They used [001] and [110] epitaxial samples for comparison it with a polycrystalline thin film. The training effect was found to be strongest in the polycrystalline sample. Manzoor *et al.* [35] compared the training effect for different sizes of grains in a polycrystalline thin film. They found that the smallest grains give rise to a larger training effect of the EB field due to the fact that larger AFM grain-volumes give rise to thermally stable bias fields and consequently smaller training effects.

1.7 Motivation

EB system is a very important part of the giant magnetoresistance device used as a reading head in hard disks. For the consistent operation of the giant magnetoresistance device, a thorough analysis of the aging effects of the EB systems is needed. The training effect is the most important aging effect of EB systems. In general, for the commercialization of an EB system, it is necessary to maximize the EB field and minimize the training effect. Thus, we have studied this effect, using the domain state model [36] and systematically varying different characteristics of the EB system.

The main focus is on the AFM characteristics and behavior, using a novel analysis of the

AFM to connect the AFM phenomenology with the training effect. The macroscopic AFM magnetization is compensated due to the balance of the magnetic spins in all sublattices. It is widely accepted that a break of the in-plane translational symmetry is needed to explain EB and the training effect. This break in symmetry can occur through defects, interface roughness, magnetic domains, granular structural or a combination of these four[37]. In this thesis, the dilution and the magnetic domain effects in th EB and the training effect will be investigated. Also, the effect of interface roughness will be investigated using a more general framework. The granular structure dependence will be investigated in the future.

1.8 Thesis Outline

The thesis can be separated into three parts. The first part has two chapters and discusses modeling EB systems. The second chapter gives a short review of the literature considering the model and simulations of exchange bias systems and the training effect. In this chapter the models are divided into five categories according to their scale and the structure they describe.

Chapter 3 will start with an introduction to theoretical description of magnetism in solids at the atomic level. A detailed analysis of the Hamiltonian used in magnetism will be given.

The second part consists of three chapters and will discuss the results using an ideal FM/AFM interface. In Chapter 4 first a thorough description of the domain state model, which is used in the current thesis, will be given. Also, will be presented the first results of the thesis.

Chapter 5 will present the dependence of the training effect on the AFM and temperature. A detailed analysis of the AFM spin behavior will be presented. Chapter 6 will then extend this work to investigate the effect of anisotropy of both materials in the training effect, using a large set of anisotropy combinations and constants.

The third part which consists of Chapter 7 will discuss the results using non-ideal AFM/FM interface. In this chapter, the dependence of the training effect on the interface coordination number (the number of closest-neighbors which belong to the other material) will be presented. This number is varied by changing the interface roughness of the system as well as the crystalline structure of the materials.

The thesis will then finish with a summary and conclusions, describing the main discoveries of the thesis and some future plans for developing even more realistic EB models.

Models of exchange bias

The modeling of EB systems was always causing contradiction between the experimentalists and the theoreticians of the field because of the controversial results. The main problem is that there is not a single model that can explain the whole range of the experimental results. So, although the EB phenomenon has been investigated for more than four decades the microscopic origins remain controversial and under investigation. The models used for the EB system can be separated into three categories according to their length scale of the area with the same magnetic moment: Macroscopic, mesoscopic and microscopic[3].

2.1 Macroscopic models

2.1.1 The ideal model

A very simple qualitative model can be derived using the macroscopic observation of the hysteresis loop shift due to unidirectional anisotropy[4]. A schematic of the model is shown in Fig. 2.1, where T_C is the Curie temperature of the FM layer, T_N is the Néel temperature of the AFM layer, below which AFM is on the long-range AFM state. EB system materials must satisfy the condition $T_N < T_C$ for a successful cooling process. At the beginning, the system is at temperature lower than the Curie temperature and higher than the Néel temperature ($T_N < T < T_C$). The AFM is in a paramagnetic state with the spins randomly oriented, while the FM spins are oriented according to the external magnetic field. The hysteresis loop is centered around zero magnetic field without being affected by the AFM.

The cooling process involves the application of a strong external magnetic field while decreasing the temperature to a desired value, which is smaller than the Néel temperature of the AFM. At the end of the cooling process, the AFM, due to the exchange interaction at the interface and the external magnetic field, will be in a long-range AFM state. This state will consist of uncompensated layers, anti-parallel each other, and with the interface layer to be aligned ferromagnetically or antiferromagnetically to the FM interface layer. The interface, being uncompensated, will lead to a finite net magnetization in this layer. Both the FM and the AFM are considered to be in the single domain state remaining like that during the whole hysteresis loop.

As the magnetic field reverses, the spins of the FM begin to rotate, as shown in Fig. 2.1.

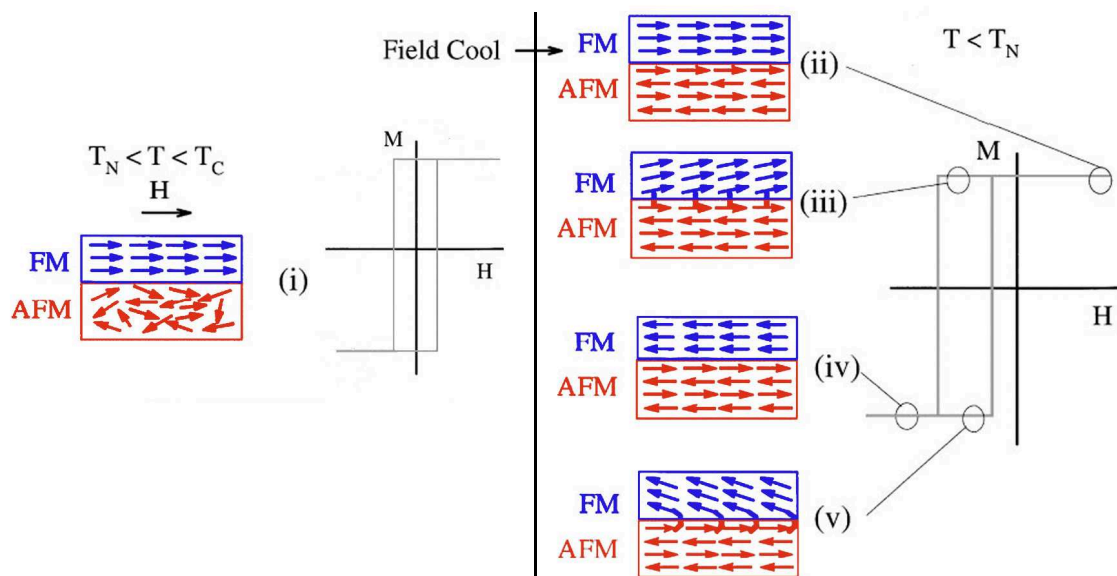


Figure 2.1: Phenomenological model of EB. [3] i) The EB system before cooling process, where the temperature is lower than the T_C of the FM and higher than the T_N of the AFM. The AFM layer is in a long-range paramagnetic state and the FM layer is in ordered phase. The hysteresis loop of this state is center around the zero value of the applied magnetic field. ii) The spin configuration of the EB system after the cooling process of the system below Néel temperature in a positive magnetic field. The interface spins of the AFM are considered uncompensated. iii) The FM begins to reverse after saturation at the negative fields. iv) The FM is fully reversed after an in-plane rotation of the FM spins. v) The spin configuration when the reverse process begin, for negative magnetic field.[4]

Due to the exchange coupling between the AFM and FM, the AFM, which is considered to be rigid, will exert a small torque on the spins of the FM, opposing to the change of the direction from their original position. Consequently, an extra magnetic field is needed to reverse the magnetization, meaning that only one direction is energetically favorable (unidirectional anisotropy). In terms of the hysteresis loop, the negative coercive field will be smaller than the one at temperatures higher than the Néel temperature. During the reverse process, the small torque is exerted on the spins of the FM helping them to change back to the original direction. So the positive coercive field will be smaller than the one at temperatures higher than the Néel temperature. Finally, the resulting hysteresis loop appears shifted to negative values of the magnetic field, with the shift called EB field and being negative.

Based on the phenomenology of the previous description, Meiklejohn and Bean[6] developed a model with the following assumptions:

1. The FM rotates coherently, and has uniaxial anisotropy with the easy axis in-plane.
2. The AFM also has uniaxial anisotropy with the easy axis in-plane.
3. The AFM's spins are rigid. They remain unchanged during the magnetization reversal of the FM.

2.1. Macroscopic models

4. The AFM layers are in uncompensated state, so the interface layer has a net magnetic moment.
5. The interface of the FM and AFM are considered perfectly smooth.
6. Single domain state is assumed for both the AFM and FM
7. At the interface, the AFM and the FM are coupled with an exchange interaction.

The initial model was based on the Stoner-Wohlfarth model [38], for coherent rotation of the FM magnetization. So the energy per unit area, before the cooling process can be written as:

$$\mathcal{H} = -\mu_o H M_{FM} t_{FM} \cos(\beta) + K_{FM} t_{FM} \sin^2(\beta), \quad (2.1)$$

where H is the applied magnetic field, M_{FM} is the magnetization of the FM spins during the reversal, t_{FM} is the FM's thickness, K_{FM} is the magnetocrystalline FM anisotropy constant and β is the angle between the FM magnetization and the anisotropy. The applied magnetic field is parallel to the easy axis of the FM. So, the first term describes the Zeeman energy of the system and the second term the uniaxial anisotropy. The above expression 2.1, using the stability condition give the familiar result for the coercivity: $H_c = 2K_{FM}/\mu_o M_{FM}$.

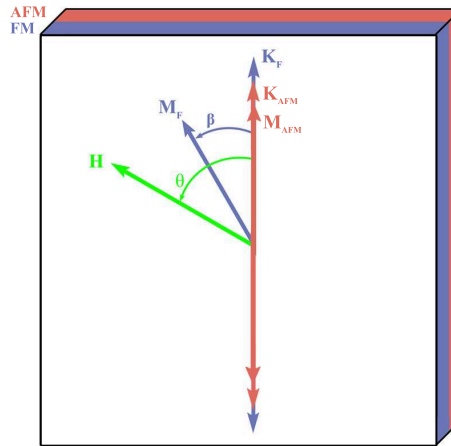


Figure 2.2: Phenomenological model with the schematic view of the vectors and angles. K_{AFM} and K_{FM} is the easy axes of the uniaxial anisotropy of the AFM and the FM, respectively. β is the angle between FM magnetization M_{FM} and the anisotropy easy axis K_{FM} . This angle is changing during the magnetization reversal. M_{AFM} is the sub-lattice magnetization of the AFM, which remains constant. The other sub-lattice magnetization is pointing to the opposite direction as showed. H is the applied magnetic field which for this model has direction parallel to the easy axis of the AFM and the cooling field ($\theta = 0$).

In this model, they introduced another term for the interface exchange coupling between the FM and the AFM. In Fig. 2.2 the EB system with the vectors involve in this model

2.1. Macroscopic models

is shown schematically. K_{AFM} and M_{AFM} is the easy axis for the uniaxial anisotropy and the sublattice magnetization of the AFM, respectively, β is the angle between the FM magnetization and anisotropy axis and θ the angle between the applied magnetic field and the easy axis of the AFM. It is assumed that the applied field is parallel to the easy axis of the AFM, meaning $\theta = 0$ and the AFM spins remain still with their orientation pointing along the easy axis of the AFM. Also, the applied field is parallel to the cooling field. So the energy per unit area, after the cooling process can be written as:

$$\mathcal{H} = -\mu_o H M_{FM} t_{FM} \cos(\beta) + K_{FM} t_{FM} \sin^2(\beta) - J_{INT} \cos(\beta), \quad (2.2)$$

where J_{INT} is the interfacial exchange coupling energy per unit area parameter. So, the last term describes the exchange coupling between the FM and the AFM. Using the stability condition $\partial\mathcal{H}/\partial\beta = 0$ and the condition for energy minimum $\partial^2\mathcal{H}/\partial^2\beta > 0$, there are two solutions: 1) $\beta = \cos^{-1}[(-\mu_o H M_{FM} t_{FM} - J_{INT})/2K_{FM} t_{FM}]$ for $-\mu_o H M_{FM} t_{FM} - J_{INT} \leq 2K_{FM} t_{FM}$ and 2) $\beta = 0, \pi$ for $\mu_o H M_{FM} t_{FM} + J_{INT} < 2K_{FM} t_{FM}$. The first one does not fulfill the energy minimum condition and has no physical significance. The second one corresponds to the energy minima of energy at that points. For finding the coercive fields, in which the magnetization of the FM is zero across the easy axis, $\beta = 0, \pi$ is taken:

$$H_{C-} = (2K_{FM} t_{FM} - J_{INT})/\mu_o M_{FM} t_{FM} \quad (2.3)$$

$$H_{C+} = (-2K_{FM} t_{FM} - J_{INT})/\mu_o M_{FM} t_{FM}. \quad (2.4)$$

Using the expression for the coercivity and EB field, we take:

$$H_c = 2K_F/\mu_o M_F \quad (2.5)$$

$$H_{eb} = -J_{INT}/\mu_o M_F t_F. \quad (2.6)$$

Compared to the initial Stoner-Wohlfarth model [38], the coercivity remains the same, but we take a shift along the negative x-axis. That means that the solution is the same as the case prior to cooling with the substitution of an effective field :

$$H' = H - J_{INT}/\mu_o M_F t_F \quad (2.7)$$

The Eq. 2.6 predicts correctly that the sign of the EB field is negative. The EB field sign is produced from the sign of the interface exchange coupling parameter. So positive EB can be reproduced by simply changing the sign of J_{INT} in Eq. 2.2 from positive to negative. Also, the real exchange coupling constant J_{INT} isn't evaluatable and as a real interface isn't atomically smooth, it is not known how this will affect this constant. As Kiwi [39] nicely labeled as "a hard nut to crack", the interface feature of EB systems is complex regarding structure and magnetic properties. So, in general, the exchange coupling

parameter is chosen to be equal with the exchange AFM constant (J_{AFM}). Using these values for the exchange coupling constant, the resulting EB field was several orders of magnitude larger than the experimental value. Finally, Eq. 2.6 predicts that the variation of the EB field is inversely proportional to the thickness of the FM, obeyed by a large number of experimental investigations, as mentioned in the previous chapter. A similar qualitative model was proposed by Goodman *et al.* [40], named the seven point model.

2.1.2 The Meiklejohn Model

A model was developed from Meiklejohn [7] based on the previous intuitive model. A new degree of freedom for the AFM magnetization was introduced in order to account for the measured non-vanishing rotational hysteresis at high fields. The AFM can rotate during the magnetization reversal, as shown in Fig. 2.3, without losing the generalization of rigid state of the AFM. This is because the AFM can rotate only as a whole.

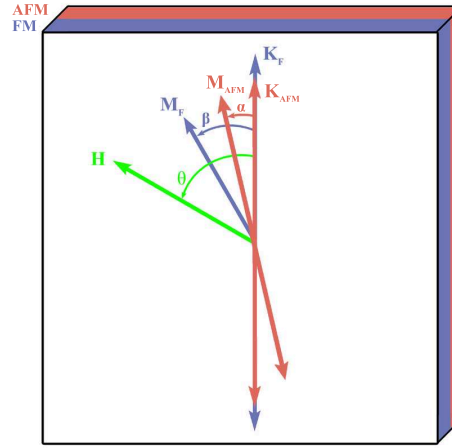


Figure 2.3: Meiklejohn model of EB with the schematic view of the vectors and angles. [7] K_{AFM} and K_{FM} is the easy axes of the uniaxial anisotropy of the AFM and the FM, respectively. β is the angle between FM magnetization M_{FM} and the anisotropy easy axis K_{FM} . This angle is changing during the magnetization reversal. M_{AFM} is the sub-lattice magnetization of the AFM. α is the angle between AFM magnetization M_{AFM} and the anisotropy easy axis K_{AFM} . The other sub-lattice magnetization is pointing to the opposite direction as shown. H is the applied magnetic field which for this model has a direction parallel to the easy axis of the AFM and the cooling field ($\theta = 0$).

So the energy per unit area, after the cooling process, for the previous model using the new assumption, can be written as:

$$\mathcal{H} = -\mu_o H M_{FM} t_{FM} \cos(\theta - \beta) + K_{FM} t_{FM} \sin^2(\beta) + K_{AFM} t_{AFM} \sin^2(\alpha) - J_{INT} \cos(\beta - \alpha), \quad (2.8)$$

where α is the angle between the AFM magnetization and the K_{AFM} uniaxial easy axis direction and t_{AFM} is the thickness of the AFM. The new term, in comparison to the previous model is the AFM anisotropy energy. It considered again that the reversal field is parallel to the AFM easy axis ($\theta = 0$). Also, the anisotropy of the FM was neglected ($K_{FM} = 0$) in the above model, so the resulting coercivity is due to the exchange interaction between the FM and the AFM. Using the stability conditions $\partial\mathcal{H}/\partial\beta = 0$ and $\partial\mathcal{H}/\partial\alpha = 0$ leads to a system of two equations. For finding the coercive fields $\beta = \theta + \pi/2$ is used, which gives $H_{C-} = H_{C+} = -J_{INT}/\mu_o M_{FM} t_{FM} \cos(\alpha - \theta)$. The EB is given by:

$$H_{eb}(\theta) = -J_{INT}/\mu_o M_{FM} t_{FM} \cos(\alpha - \theta). \quad (2.9)$$

For the case of $\theta = 0$, solution of the equations for the EB is calculated analytically and reads:

$$H_{eb} = \begin{cases} \frac{-J_{INT}}{\mu_o M_{FM} t_{FM}} \sqrt{1 - \frac{J_{INT}^2}{4K_{AFM}^2 t_{AFM}^2}} & K_{AFM} t_{AFM} / J_{INT} \geq 1 \\ 0 & K_{AFM} t_{AFM} / J_{INT} < 1 \end{cases} \quad (2.10)$$

This equation is inversely proportional to the thickness of the FM, but the additional term considers the characteristics of the AFM. More specifically, the EB is finite for $K_{AFM} t_{AFM} / J_{INT} \geq 1$ which means that during the magnetization reversal the magnetocrystalline anisotropy of the AFM is strong enough to hold the AFM order, although there can be small rotations of the angle α . For this case no coercivity is predicted. When $K_{AFM} t_{AFM} / J_{INT} < 1$ the EB phenomenon disappears. This is due to the strong interfacial coupling, meaning that the AFM spins follow the FM spins. An extended discussion of this model is carried by Radu[41] and a similar result was gained from a grained model by Fujiwara *et al.* (see Fig. 6a) in Ref.[42]), when the grains have the same anisotropy.

2.1.3 Planar AFM Domain wall model-Néel's approach

Since, the previous models predicted EB several orders of magnitude higher than the experimental values, and therefore new assumptions were made for this loss of coupling energy. A novel theoretical approach was made firstly by Néel [43] in which he introduced the concept of the planar domain wall in the AFM or FM layer, developed during the magnetization reversal. Particularly, he considered coupling of the FM with a low anisotropy AFM, leading to the creation of an AFM or a FM domain wall parallel to the interface. Thus, the planar domain wall will absorb a fraction of the interface exchange coupling energy, lowering the EB phenomenon. This is the so called Néel domain wall, having the form of a partial domain wall because of the weak coupling. The model is based in calculation of the orientation of magnetization of each layer through a differential equation, predicting a minimum AFM thickness for producing of hysteresis loop shift.

2.1.4 Mauri model-Partial domain wall

Based in the idea of a partial domain wall parallel to the interface in the AFM, Mauri *et al.* [44] introduced a macroscopic model for the description of this domain wall which is uniform in its volume, as shown in Fig. 2.4. As Néel's model, the motivation of this hypothesis was to explore a possible reduction of the EB field from Meiklejohn model. The basic difference in the assumptions of this model with the Meiklejohn model is that the AFM layer develops a domain wall parallel to the interface.

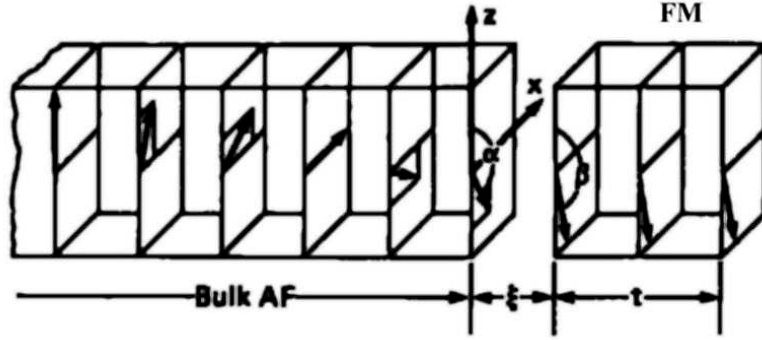


Figure 2.4: The partial domain wall developed at the interface of the AFM [44], for a system with a thin FM film on a thick AFM substrate. The magnetization of only one sublattice of the AFM is shown.

The AFM interface layer magnetization is oriented in different direction from the FM orientation making an angle α with the AFM anisotropy easy axis. The next AFM layers gradually form a magnetization perpendicular to the first one. Schematically in Fig. 2.4, only the one sublattice is depicted, with the magnetization of the other sublattice being oppositely oriented to complete the AFM order. It is assumed that the FM is at ξ distance. They used it in the energy expression for the description of the tail of a domain wall of the AFM, considering that the AFM is infinitely thick. The interfacial domain wall decreases the energy of equilibrium state of the magnetic configuration and it is a 90° domain wall. So the energy per unit area, after the cooling process, for the Meiklejohn model using the new assumption, can be written as:

$$\begin{aligned} \mathcal{H} = & \mu_0 H M_{FM} t_{FM} (1 - \cos(\beta)) + K_{FM} t_{FM} (1 - \sin^2(\beta)) \\ & + A_{12}/\xi (1 - \cos(\alpha - \beta)) + 2\sqrt{A_{AFM} K_{AFM}} (1 - \cos(\alpha)), \end{aligned} \quad (2.11)$$

where the fourth term represent the energy of the partial domain wall, which is parallel to the interface. The parameter A_{AFM} is the exchange stiffness of the bulk AFM and the A_{12} is the exchange stiffness of the AFM interface with J_{INT} defined as $J_{INT} = A_{12}\xi$. The difference in some of the expressions is due to the easy axis lying perpendicular to the applied magnetic field.

By numerical minimization of the energy Eq. 2.11, magnetization curves were calcu-

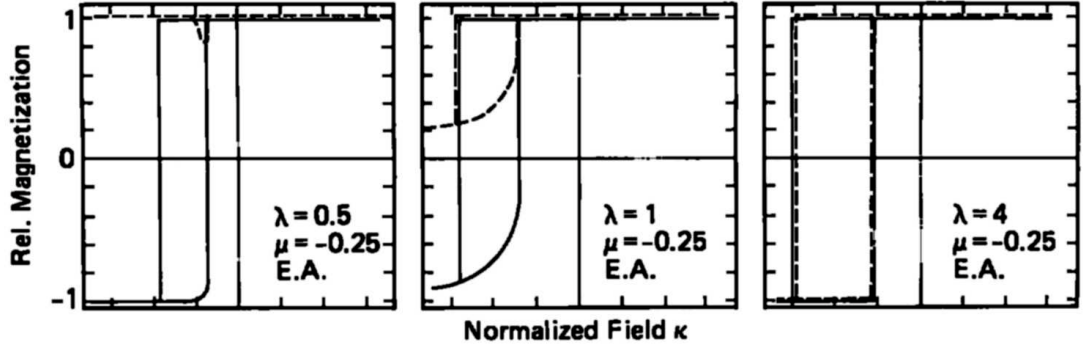


Figure 2.5: Magnetization curves for magnetic field applied parallel to the AFM easy axis for different values of the interface ratio λ . λ is denoted the $(A_{12}/\xi)/2\sqrt{A_{AFM}K_{AFM}}$ ratio and $\mu = K_{FM}t_{FM}2\sqrt{A_{AFM}K_{AFM}}$. The solid lines show the FM magnetization and the dashed lines show the AFM's interface magnetization.[44]

lated, considering different $(A_{12}/\xi)/2\sqrt{A_{AFM}K_{AFM}}$ ratio. As in the Meiklejohn model, a similar expression for the EB field was derived:

$$H_{eb} = \begin{cases} -(A_{12}/\xi)/\mu_0 M_{FM} t_{FM} & (A_{12}/\xi)/2\sqrt{A_{AFM}K_{AFM}} \ll 1 \\ 2\sqrt{A_{AFM}K_{AFM}}/\mu_0 M_{FM} t_{FM} & (A_{12}/\xi)/2\sqrt{A_{AFM}K_{AFM}} \gg 1 \end{cases} \quad (2.12)$$

When $(A_{12}/\xi)/2\sqrt{A_{AFM}K_{AFM}} \ll 1$, meaning for strong exchange interface coupling, the EB field is similar to the Meiklejohn model, with the exchange coupling parameter dependent on the distance ξ between the two materials. For weak coupling, the EB field is independent of the interfacial exchange coupling but it depends on the domain wall of the bulk AFM. Fig. 2.5 shows magnetization curves for three different values of the $(A_{12}/\xi)/2\sqrt{A_{AFM}K_{AFM}}$ ratio. When the ratio has a value of four, the steady state of the system is reached with the EB field reaching a maximum value according to Eq. 2.12. Also, the AFM's interface magnetization is totally reversed, meaning that 180° domain walls were created in the AFM.

Geshev [45] used the Mauri *et al.*[44] model considering analytical and numerical derivation for the EB field and the coercivity. The results show discrepancies with the results of Mauri model but excellent agreement with the experimental results. These quantitative discrepancies are claimed to result from the energy minimization methodology used in each publication. The analytical derivation gave five different sets of expressions for the hysteresis loop shift and coercivity.

The dependence of EB field as well as coercivity, obtained numerically for several values of $\mu = -K_{FM}t_{FM}2\sqrt{A_{AFM}K_{AFM}}$ are depicted in Fig. 2.6. All curves of coercivity versus exchange coupling ratio exhibit minima, which become deeper and sharper with increasing FM uniaxial anisotropy (μ). On the other hand, EB field curves versus exchange coupling ratio exhibit maxima which become similarly more pronounced for higher FM

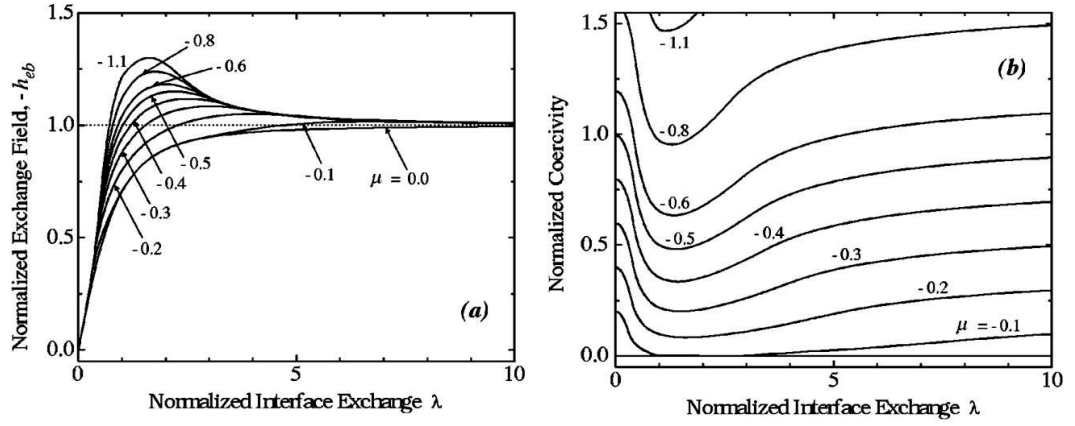


Figure 2.6: Dependence of the normalized EB field h_{eb} (a) and coercivity h_c on the $(A_{12}/\xi)/2\sqrt{A_{AFM}K_{AFM}}$ ratio for several $\mu = -K_{FM}t_{FM}2\sqrt{A_{AFM}K_{AFM}}$. [45]

anisotropy. For weak and strong interface coupling ratio ($(A_{12}/\xi)/2\sqrt{A_{AFM}K_{AFM}} < 1$ and $(A_{12}/\xi)/2\sqrt{A_{AFM}K_{AFM}} > 4$), all the EB field curves coincide.

Xi *et al.* [46, 47] developed a model similar to Mauri's model where they consider that a helical structure (planar domain wall) is developed as the AFM moments at the interface try to follow the magnetization of the FM during reversal. Specifically, when the AFM moments at the interface reach the AFM hard axis, the helical structure becomes unstable and the AFM moments rotate into the opposite direction. So the moments settled down to a new stable state which still contains some twisted moments. This irreversible motion was predicted by Mauri's and Néel's model.

Morosov *et al.* [48, 49, 50] presented a model based on Mauri's but with uncompensated AFM interface. Also, they considered rough and smooth interface using an analytical expression for its description. It is the only EB model found in the literature that used strictly analytical methods. For flat AFM interfaces they found similar domain wall behavior as Mauri's model and for rough AFM interfaces they found that EB field is caused by static spin vortices at the interface.

2.1.5 Frozen canted interface spins-Kiwi model

Kiwi *et al.* [51, 52, 53, 39] introduced a new model for EB systems. This model is based on the assumption that the AFM interface is fully compensated and freezes into a canted spin state after the cooling process, keeping the AFM order, as shown in Fig. 2.7. Also, the magnetization of the FM is orthogonal to the AFM easy axis. So the energy per unit

area, after the cooling process, can be written as:

$$\begin{aligned}
 \mathcal{H} = & -J_{AFM}M_{AFM}t_{AFM}\cos(\alpha_1 - \alpha_2) - K_{AFM}(\cos^2(\alpha_1) + \cos^2(\alpha_2)), \\
 & -\mu_oHM_{AFM}t_{AFM}(\cos(\alpha_1) + \cos(\alpha_2)) \\
 & -J_{INT}(\cos(\beta + \gamma - \alpha_1) + \cos(\beta + \gamma - \alpha_2)) \\
 & -J_{FM} \sum_i^{N-1} M_iM_{i+1}\cos(\beta_i - \beta_{i+1}) - \sum_i^N [K_{FM}(\cos^2(\beta_i - \gamma) + \mu_oHM_i\cos(\beta_i))].
 \end{aligned} \tag{2.13}$$

where $J_{AFM} < 0$ is the AFM coupling between the two AFM sublattices, α_1 and α_2 are the angles between the AFM easy axis and the first and second sublattice, respectively and M_{AFM} is the magnetization of the AFM. M_i is the magnetization of the i layer of the FM, with β_i the angle of the magnetization of this layer with the FM easy axis. γ is the angle between easy axis of the FM and the AFM, where in this case is equal to 90° and β is the angle of the net FM magnetization from the FM easy axis. They found that the energy is stored in an incomplete domain wall within the FM but no domain wall is developed in the AFM. Specifically, an exchange-spring magnet results, with EB effect and enhancement of the coercivity consistent with experimental results, as is claimed.

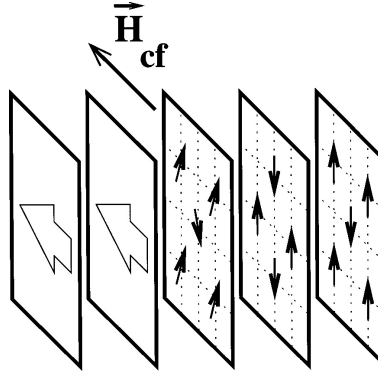


Figure 2.7: Spin configuration of the FM and the AFM layers. The AFM spins are canted relatively to the cooling field H_{cf} . [52]

2.1.6 Partial domain wall-Kim-Stamps approach

Kim and Stamps [54, 55, 56, 57, 58, 59, 60] using the previous assumptions of Néel, Mauri *et al.* and Kiwi *et al.*, they introduced the concept of the partial domain wall. More specifically, they used a bilinear and a biquadratic term for the description of exchange coupling, a spin-flop configuration in the AFM interface. They investigated compensated, partially compensated and uncompensated interfaces. A structure similar to that of Kiwi *et al.* with canted spins is found.

The calculated magnetization curve for the FM/AFM system is shown in Fig. 2.8, with the corresponding spin structure at three different values of the magnetic field. A partial domain wall in the AFM twists as the FM rotates, an effect more favorable energetically

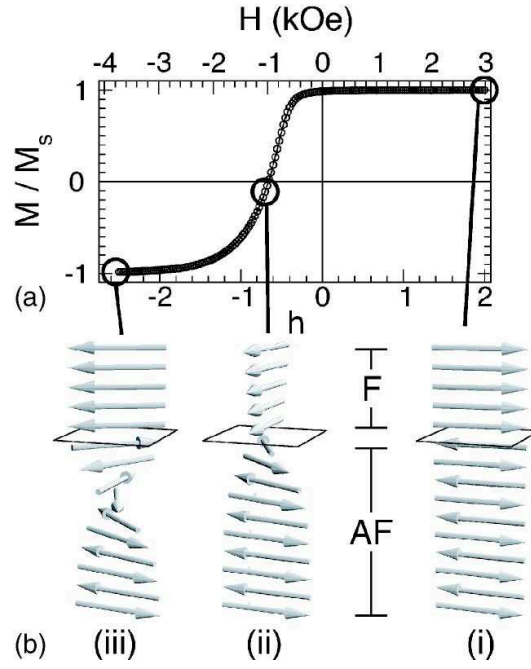


Figure 2.8: Magnetization curve (a) and spin configuration (b) at three different points of the magnetic field. A partial domain wall is created on the AFM in point (iii). Only the spins close to the FM/AFM interface are shown. [58]

than the breaking of the interlayer coupling. Despite that, the hysteresis loop is reversible, meaning that the coercivity is zero. To overcome this problem Kiwi and Stamps [52] introduced magnetic defects in the system, which lead to the pinning of the domain wall. They argued that the wall pinning and depinning transitions, give rise to asymmetric hysteresis loops with irreversible rotation.

2.1.7 Hoffmann model-Training effect

A model used specifically for the training effect of EB was created by Hoffmann [61], similar to that of Kiwi *et al.* The model, contrary to the planar domain wall model, considers two independent magnetic sublattices for the AFM using the Stoner-Wolfarth model. The model was modified for uniaxial and biaxial AFM anisotropy. So the energy per unit area, after the cooling process, for the Stoner-Wolfarth model using the new assumption, can be written as:

$$\begin{aligned} \mathcal{H} = & -\mu_o H M_{FM} t_{FM} \cos(\beta) - \mu_o H M_{AFM} t_{AFM} (\cos(\alpha_1) + \cos(\alpha_2)) \\ & - J_{INT} (\cos(\beta - \alpha_1) + \cos(\beta - \alpha_2)) \\ & - J_{AFM} M_{AFM} t_{AFM} \cos(\alpha_1 - \alpha_2) + E_{AN}(M_{AFM}), \end{aligned} \quad (2.14)$$

where

$$E_{AN}(M_{AFM}) = \begin{cases} K_{AFM} (\sin^2(\alpha_1) + \sin^2(\alpha_2)) & \text{uniaxial anis.} \\ K_{AFM} (\sin^2(2\alpha_1) + \sin^2(2\alpha_2)) & \text{biaxial anis.} \end{cases} \quad (2.15)$$

where $J_{AFM} < 0$ is the AFM coupling between the two AFM sublattices, α_1 and α_2 are the angles between the AFM easy axis and the first and second sublattice, respectively and M_{AFM} is the magnetization of the AFM. So the first two terms represent the Zeeman energy for the AFM and the FM, the third term the exchange coupling between the FM and the AFM and the fourth the exchange coupling of the two AFM sublattices. The FM couples to both AFM sublattices which corresponds to both compensated or uncompensated interface of the AFM. In this model no FM anisotropy is considered.

An analysis using the parameters of the above model plus an extra parameter describing the cooling field was made. The author connected specific orientations of the AFM sublattices with EB effect on consecutive hysteresis loops. They show that irreversible training effects (first loop EB) can occur as a result of inherent frustration of the AFM interface magnetic moments and symmetry of the AFM anisotropy.

2.1.8 Radu approach-The spin glass model

Radu [41] introduced the phenomenon of the frustration inside the Meiklejohn model, considering that the interface between FM and AFM layer is magnetically disordered behaving similar to a spin glass system. More specifically, it is considered that the AFM can contain, in a first approximation, two types of AFM state. One part has large anisotropy which freezes the AFM spins and another part with low anisotropy which allows the spins to rotate with the applied field. The latter kind of spins are frustrated (spin-glass state) and give rise to an increased coercivity.

A spin glass system is comprised of a collection of magnetic moments whose low-temperature state is a frozen disordered one, rather than e.g. a ferromagnetically ordered state. Two main requirements need to be fulfilled: 1) competition among different interactions between the moments, meaning that no single configuration of the spins is favored by the interactions (frustration) and 2) these interactions must be "random". In the specific case, the spin glass region can be formed due to the non-ideal interfaces e.g. interface roughness, non magnetic defects etc. So a new term is introduced to the energy expression. The energy per unit area, after the cooling process, for the Meiklejohn model using the new assumption, can be written as:

$$\begin{aligned} \mathcal{H} = & -\mu_o H M_{FM} t_{FM} \cos(\theta - \beta) + K_{FM} t_{FM} \sin^2(\beta) \\ & + K_{AFM} t_{AFM} \sin^2(\alpha) + K_{SG}^{eff} \sin(\beta - \gamma)^2 - J_{INT}^{eff} \cos(\beta - \alpha), \end{aligned} \quad (2.16)$$

where K_{SG}^{eff} is the effective spin glass anisotropy at the AFM interface, γ is the average orientation of the effective spin glass anisotropy and J_{INT}^{eff} is the effective interface coupling between FM and AFM.

With this model, the dependence of EB field and coercivity on angle between easy

axes and applied magnetic field and thickness of the AFM was investigated with excellent agreement with *CoFe/IrMn* bilayers.

2.2 Mesoscopic models and micromagnetics

Mesoscopic models usually consider different spin configuration in the x-y plane, meaning that now the x-y plane of the system is divided in smaller areas, each having different magnetization direction. The most important approaches are those considering a granular structure of the AFM and using finite element methods.

2.2.1 Non-interacting grained and thermal fluctuation aftereffect models

Kouvel *et al.* [62, 63] developed first a model considering a grain distribution. They modeled a system in which every magnetic unit was comprised of an ensemble of mutually-interacting FM and AFM domains. In this model magnetic viscosity effects were observed.

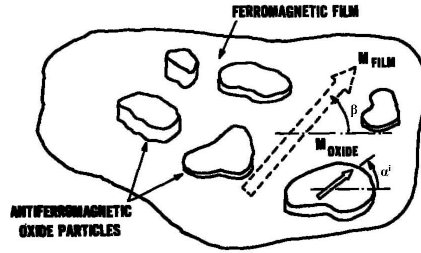


Figure 2.9: Diagram of the Fulcomer-Charap model [64], with the non-interactive AFM grains coupled with the underlying FM layer.

In 1972 a contribution was made by Fulcomer and Charap [64], who used a grain model for the description of an EB system. The model is based in the theory of the magnetic aftereffect of small particles. Specifically, they considered for the AFM small uniaxial particles which do not interact magnetically and which are exchange coupled to the FM. The particles follow a distribution for their size, shape and the angle between their magnetization and the FM easy axis, as shown in Fig. 2.9 . So the total energy of the system, after the cooling process, can be written as:

$$\begin{aligned} \mathcal{H} = & -\mu_o H M_{FM} V_{FM} (\cos(\beta) + \sin(\beta)) + K_{FM} V_{FM} \sin^2(\beta) \\ & + \sum_{i=1}^N [K_{AFM} A^i t_{AFM}^i \sin^2(\alpha^i) - J_{INT} A^i c^i \cos(\alpha^i - \beta)], \end{aligned} \quad (2.17)$$

where V_{FM} is the volume of the FM, A^i, t_{AFM}^i the area and the thickness of every AFM grain, α^i the angle between the magnetization of the AFM and each grain, and c^i

is the contact fraction of each grain. The sum goes over the total number of the AFM grains. The magnetic field is applied in the direction of the easy and hard anisotropy axis. The contact fraction reflects the idea of Néel [43] that the surface magnetic moment of different grains with the same area may not be the same.

For calculating an hysteresis loop beyond the energy term given above, an expression for the aftereffect is considered. Magnetic aftereffect (or viscosity) is relevant when the magnetization of a material does not change instantaneously, but lags behind the magnetic field changes. In an EB system the AFM can present magnetic aftereffect under the effective field of the FM. Whenever the FM moment is reversed, the exchange coupling term changes sign and switching the AFM grains is initiated by thermal fluctuations, the grains approach a new equilibrium distribution of angles α^i with a time constant t . Fulcomer and Charap reported that the smaller grains of every distribution due to thermal fluctuations show superparamagnetic behavior and also differently sized grains are coupled differently with the FM. A comparison between experimental findings for a *Co/CoO* system and Fulcomer-Charap model results, for the EB field and for the coercivity as function of temperature, showed very good agreement in most of results except for low temperature coercivity, as shown in Fig. 2.10.

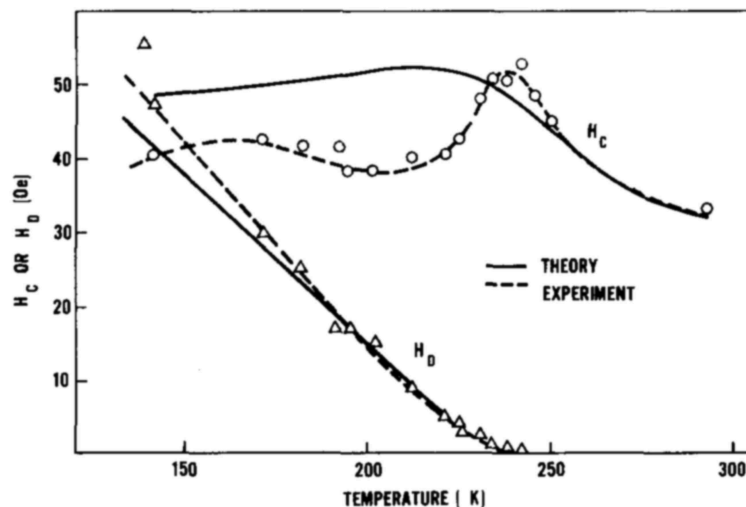


Figure 2.10: Comparison between experimental findings for a *Co – CoO* system and Fulcomer-Charap model results, for the EB field H_D and for the coercivity H_C as function of temperature. [64]

Many models involving grains were developed through the years using Fulcomer-Charap model as a initial idea. Fujiwara *et al.* [42] developed a similar model, including also the idea of Néel for planar domain walls. So the AFM layer has an surface anisotropy term as was presented on Mauri's model [44], with the exchange stiffness. Hou *et al.* [65] used a similar model with no interacting AFM grains to investigate the temperature dependence of the EB field. The additional characteristic of this model is the distribution of exchange coupling between FM and AFM, of anisotropy constant and of anisotropy kind. The

previous ideas were used by Brems *et al.* [66] to examine the training effect and asymmetry in exchange coupled polycrystalline bilayers. They showed that the training effect resulted from misalignment between the FM magnetization and the uncompensated magnetization of the granular AFM.

Stiles and McMichael[67, 68] proposed a grained EB model in which the AFM grains are uncoupled and the AFM interface is coupled directly via spin-flop with the FM interface. The spin-flop idea was first mentioned from Koon[69] and it will be described later as being a microscopic model. Despite this, they found that actually the spin-flop does not contribute to the EB phenomenon. Also, the grains are not changing easily their magnetization during the reversal of the magnetic field, causing the EB. The magnetization of each grain, after a critical angle, changes irreversibly and points toward the FM magnetization, contributing to the enhancement of the coercivity. This model considers a very good candidate model for the explanation of widespread results that appeared in different EB systems.

Tsunoda and Takahashi [70, 71] used a similar grained EB model with non-interacting AFM grains. They called this the single spin ensemble model, where the AFM magnetic anisotropy easy axes of every grain lay in the film plane with two-dimensional random distribution. The Meiklejohn model is applied between the FM layer and each AFM grain. They used this model to show that changes in the exchange coupling do not necessarily occur with changes of the microstructure or the intrinsic physical quantities of the system.

Saha and Victora [72] used a micromagnetic model with non-interacting AFM grains which interact with FM grains. Each AFM grain has random orientation of the easy axes and is considered rough interface. They investigated the reversal mechanisms of magnetization and the training effect. They compare the training effect of a biaxial AFM and of an uniaxial AFM. The case of biaxial AFM showed a steep reversal in the first hysteresis loop, which is found in many experimental investigations.

Choo *et al.* [73] used a similar model with non-interacting AFM grains which interact with strongly exchange coupled FM grains, considering also magnetostatic interactions. The microstructure of each layer is created using a Voronoi construction and each grain has different easy axis direction, assigned randomly from a log normal distribution. They used Monte-Carlo simulations, where thermally activated magnetization reversal is allowed with probability based on Arrhenius-Néel law ¹. Investigations of the effect of the thermal instability of the AFM as a function of temperature, layer thickness, grain size distribution and diameter were carried out. It is claimed, that the calculations give good qualitative

¹Arrhenius-Néel law considers that the magnetization of a grain flips with finite probability. The mean time between two flips is called the Néel relaxation time τ_N and is given by the following Néel-Arrhenius equation: $\tau_N = \tau_o \exp(KV/(K_b T))$ where τ_o is called the attempt time and is characteristic of the material, V is the volume of the grain.

agreement with experiment.

2.2.2 Interacting AFM grain model

In general, models that assume interacting AFM grains are controversial because the interaction term between two grains involves their magnetization, which for an AFM grain is close to zero. Thus, the interaction AFM grain term is always zero. Obviously, for grains which have a volume that gives an definite magnetization (have uncompensated spins) this term will be non-zero.

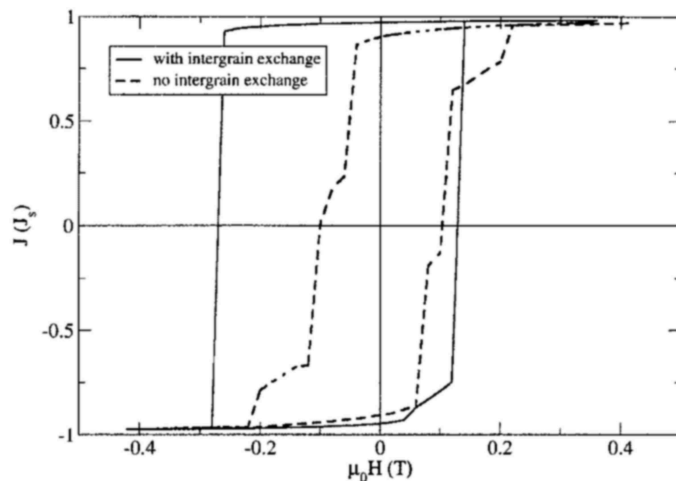


Figure 2.11: Hysteresis loop of an EB system with and without AFM intergrain exchange coupling. [74] In the case of intergrain exchange coupling an enhanced coercivity and a loop shift is produced.

Suess *et al.* [74, 75, 76] used a grained model for EB system where the AFM grains are exchange coupled and are perfectly compensated. The easy axis for every grain is set randomly. The model is simulating an $IrMn(\text{AFM})/\text{FM}$ system. They focus their investigation in the effect of intergrain coupling in the EB field and coercivity, using a finite element micromagnetic calculation. These new assumptions in addition to a spin-flop coupling at a perfectly compensated interface resulted a shifted hysteresis loop, as shown in Fig. 2.11. They observed partial domain walls along the interface as long as their width is larger than the grains. So, the energy, unlike previous partial domain wall models, is stored in lateral domain walls located between AFM grains. Also, they investigated the dependence of EB field on the thickness of the AFM as well as the training effect. They finally modeled a system, in which the easy axis follows a Gaussian distribution, investigating the effect of distribution width in the EB field. Kirchner *et al.* [77] using the same model, investigated the effect of uniaxial anisotropy constant and the thickness of the AFM layer in the EB field and in the structure of the domain state. They found that during reversal, 360° domain wall is created and annihilated in the FM, as shown in Fig. 2.12.

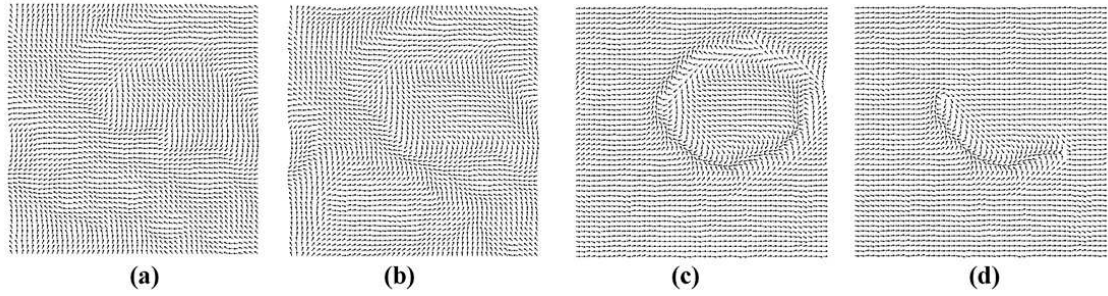


Figure 2.12: Formation and annihilation of a 360° domain wall (nucleation) in the FM. [77] The images give the calculated spin configuration of the FM at different applied fields. (a) Before reversal, (b) and (c) during reversal and (d) after the reversal.

Fujiwara *et al.* [78], expanding their model which came from Fulcomer-Charap's model, introduced direct exchange coupling between the AFM grains. In the AFM grain interaction term they used the sublattice magnetization of each grain. They investigated the unidirectional rotational hysteresis and the training effect dependence, where the latter is attributed on the lock and release mechanism of spins. Zhang *et al.* [79] using the same model also investigated the training effect. More specifically, they considered positive and negative exchange coupling between AFM grains. The conclusions gained for the training effect is the same with those of Fujiwara *et al.* [78].

2.2.3 Less-ideal models

A special category in models of all scales is the non-ideal models, which firstly occurred in mesoscopic models. By non-ideal models we mean models which do not use idealistic system structure, being more realistic. These models consider non-planar interface, as well as, non-magnetic impurities in the entire volume of the AFM. Imry and Ma [80] first argued that long-range magnetic order state such as AFM state can be unstable under a random field created by some non-magnetic impurities in the system or by AFM site impurities in a FM i.e. a non-smooth AFM-FM interface. This instability usually leads to the creation of domains in the AFM. Especially, as shown by Nowak *et al.* [81], an AFM inside high magnetic fields develops a domain state due to the inequality of two AFM sub-lattices sites caused from the impurities. Consequently the creation of a domain wall lowers the energy of the system as well as the passing of the domain wall from the non-magnetic impurities. We must note that both authors used microscopic model in their work.

The most known mesoscopic non-ideal model is that of Malozemoff [82, 83, 84] which uses the ideas of Imry and Ma [80] in an EB system with a non-sharp interface. In this model, he used domain walls that are perpendicular to the interface and more energetically favorable by the roughness of the interface between AFM and FM. In this case the interface roughness produces the random field which leads to the creation of domains walls in the AFM. Specifically, it is considered a rough interface on the atomic scale of a compensated

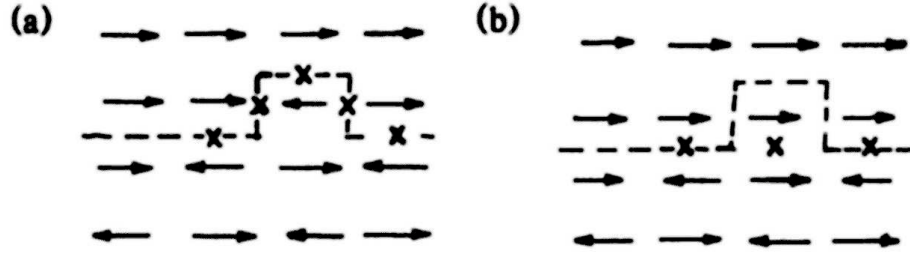


Figure 2.13: Possible spin configurations for a non-ideal interface in an EB system. The atomic step should be visualized on a two-dimensional interface. (a) Spin configuration before FM reversal, (b) after the FM reversal. The x signs denote frustrated bonds. [82]

AFM which can lead to uncompensated spins required for the hysteresis loop shift, as shown in Fig. 2.13. The random field, is created by atomic scale randomness of the interface, and considering that the FM is in a single-domain state, it is energetically favorable for the AFM to break up into domains to minimize the net random unidirectional interfacial anisotropy. Consequently, perpendicular domain walls are created in the interface and the bulk of the AFM, which are permanently present in the AFM layer, in contrast to the Mauri model where the parallel partial domain wall to the interface is created temporarily during the FM reversal.

The EB field according to this model is given by

$$H_{\text{eb}} = \frac{2z\sqrt{A_{\text{AFM}}K_{\text{AFM}}}}{\pi^2 M_{\text{FM}} t_{\text{FM}}} \quad (2.18)$$

where the symbols are the same as before and z is a number of order unity, which is dependent from the degree of roughness of the interface. The EB field formula is very close to the one of Mauri *et al.* [44]. This similarity is due to the fact that both models have characteristic domain wall energies at the interface. Despite that, the parameters used in this model are different and based on different picture of the phenomenon. In addition, this model explains the observed coercivity and remanent phenomena which appear during hysteresis cycling. A comparison of the EB field value with experimental data shows a very good agreement.

2.3 Microscopic models

In microscopic models, we use the exact spin configuration of each atom. So, from now on with spin we mean the total magnetic moment of the atom. This is happening for all the directions of the system i.e., x , y and z . Usually the model is derived using Monte Carlo simulations for minimisation of the energy or stochastic equation of motion i.e. Langevin equations for the numerical derivation of the arising Landau-Liftshitz equation. Although these models are being used to describe microscopic systems, they are not being described

from quantum mechanical laws but from classical ones.

2.3.1 Spin flop - Koon's model

A well-known contribution in the category of microscopic models is the one of Koon [69]. Koon considered a system with compensated spins at the interface and investigated the energy per area for multiple angles between the two outer monolayers (one of the AFM and one of the FM). It is found that the angle between the two outer layers (with the minimum energy) was 90° and the internal layers had frustrated spins. So he concluded that the spins at the interface between AFM and FM must be perpendicular in order to minimize the energy. This 90° coupling of the AFM and FM spins was called spin-flop state. This state is described by the biquadratic term: $J_{INT}(S_{AFM}S_F\cos(a-b))^2$, where S_{AFM} , S_F is the spins of AFM and FM at the interface, and a , b the angles of the AFM and FM spins, respectively. In addition, for reproducing an EB system he used the above conditions plus a restriction of the AFM spins to move in the plane of the interface during field reversal. At the end, it was concluded that domain walls parallel to the interface do appear, following an argument similar to that of Mauri *et al.* [44]. The produced magnetization curve was reversible i.e. no hysteresis loop, and was shifted by a quantity quite close to experimental EB field.

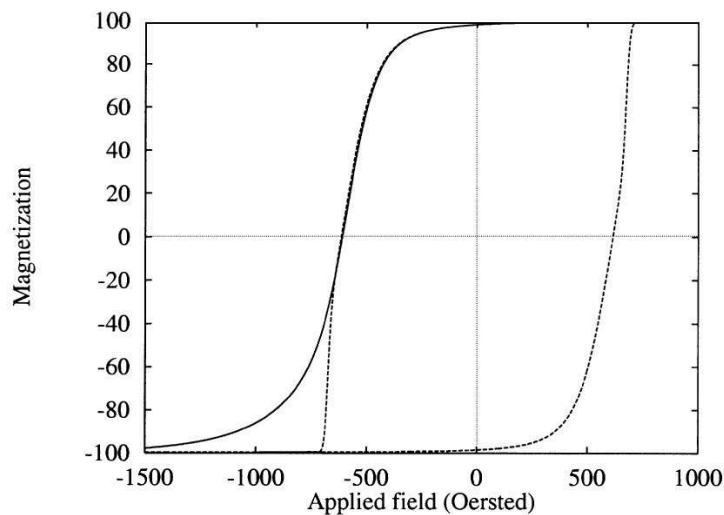


Figure 2.14: EB with reversible cycling is exhibited when the spin motion is restricted on the interfacial plane (solid line) but when the spins are free (dashed line) to move in any direction, the EB disappears showing a hysteresis cycling. [85]

At 1998, Schulthess and Butler[85], proved that Koon's model does not present EB. They used a microscopic Heisenberg model using the Landau-Lifshitz-Gilbert equation of motion, applying Koon's arguments about the spin-flop coupling. They did not consider restrictions to the movement of the interface spins as Koon did (movement only at the interface plane). The result was that EB disappears under this assumption and no domain

wall is created parallel to the AFM-FM interface. Particularly, when they used Koon's spin restriction, they found the same results as Koon, i.e. a shifted reversible magnetization loop, as shown in Fig. 2.14. When they used the unrestricted spins, they found a non shifted hysteresis loop showing that the energy of this configuration is smaller than the one for the creation of domain wall in the AFM parallel to the interface i.e. Koon argument. On the other hand, Schulthess and Butler showed that this model is very promising for the explanation of the enhancement of coercivity of EB systems as well as that the model transformed to have interface roughness gives EB field with the correct order of magnitude.

2.3.2 Various improved microscopic models

Interface roughness and dilution of AFM are very important parameters for the behavior of an EB system. Many publications investigated the effect of different configurations of this characteristic on the EB field and coercivity. Dantas *et al.* [86] considered an EB system where the AFM interface has small square "islands" penetrating inside the interface of the FM in order to represent the interface roughness. They used a Heisenberg model with every spin to represent the magnetic moment per unit cell. Their investigation of EB field and coercivity in function of the size of "islands" showed that the EB field is increasing and the coercivity is decreasing when the size of the islands is increasing from zero to the half of the size of the interface. Also they showed that for islands of half the size of the interface the magnetization curve consists of two minor loops, effect of the nucleation of domain walls at the islands edges.

Tsai *et al.*[87] used a Monte Carlo simulation of a Heisenberg model of the EB system to thermally investigate the magnetic order of the system using flat and rough interfaces and do a comparison between the two systems. The flat interfaces are fully uncompensated and the rough interfaces are compensated. On the latter, they found that the FM spins are oriented in a direction perpendicular to the AFM easy axis. Lederman *et al.* [88] using a similar model with different parameters for every sub-lattice of the AFM, investigate the result of different parameters on the system. More specifically, they came to the same result as previously about the orthogonal orientation of the FM spin for large values of interface exchange coupling. Contradictory results were obtained from single crystals and epitaxial films for low temperatures. The single crystals presented a perpendicular anisotropy in the FM with low EB, whereas epitaxial crystals presented longitudinal anisotropy with large EB.

Mitsumata *et al.*[89] considered a more complex Heisenberg model, using interaction up to the second nearest neighbor for every spin. The model also considers some special structure for the non-magnetic defects: collinear and noncollinear spin structure. For the numerical experiment, Monte-Carlo calculations are used for the cooling process and then

a numerical derivation of Landau-Lifshitz equation was used for the magnetization process. They showed that the noncollinear spin structure exhibits a hysteresis loop shift but the collinear spin structure exhibits only the enhancement of the coercivity of the EB system. In the system with the noncollinear spin structure, was related with the formation of domain wall in the AFM parallel to the interface. On the other hand, for the second system they needed to introduce the multidomain state at the EB structure to observe a hysteresis loop shift.

2.3.3 Domain state model

Miltenyi *et al.*[90] first showed experimentally that EB phenomenon is magnified by dilution of the AFM. Using a simple model and through Monte Carlo calculations, they proved the existence of domain states boosted from dilution of the AFM, which exhibits a phase diagram like the one which is shown in Fig. 2.15a). A phase transition in zero magnetic field from the paramagnetic state to the long-range AFM state is shown at the dilution dependent Néel temperature. For higher magnetic fields, at low temperatures the AFM develops a domain state. The formation of the AFM domains originates from the statistical imbalance of the non-magnetic defects of the two sublattices. Hence, the formation of a domain wall can be minimized when it passes through the non-magnetic defects.

In 2001 Nowak *et al.* [36] used an Ising model for the diluted AFM and a Heisenberg model for the simulation of a system similar to *Co/CoO*. The dependence of the EB field on the thickness and the dilution of the AFM were shown. Also, it was shown that formation of domains with a surplus magnetization, which causes the exchange bias, is boosted from the dilution of AFM. The creation of small domains for small thickness leads to large surplus magnetization, causing larger EB field and vice versa, as Imry and Ma[80] showed. The tendencies are in qualitative agreement with experimental findings [20]. The same writer[81] in a later publication showed that the creation of domains in the AFM is a result of the Imry-Ma argument, as mentioned before and shown in Fig. 2.15b). An extensive investigation of EB carried out using a Heisenberg model for both materials, with showing the dependence of EB on the dilution, the thickness of AFM, the temperature, where hysteresis loop is acquired, the cooling field as well as the number of consecutive hysteresis loop i.e. training effect. Also, they found that EB has a non-trivial dependence on the anisotropy of the AFM [91].

Energies were calculated using the appropriate Ising or Heisenberg Hamiltonians, considering only nearest neighbor exchange interactions and disregarding the magnetostatic

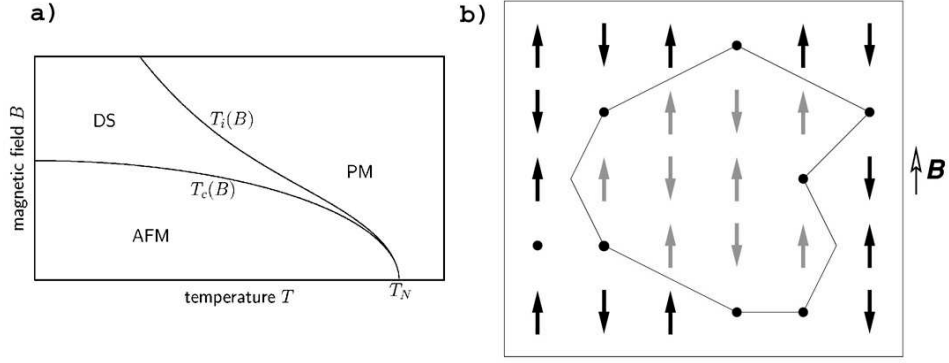


Figure 2.15: a) Schematic phase diagram of a three dimensional diluted AFM. DS is the domain state, PM is the paramagnetic state and AFM is AFM long-range state of an AFM. b) Schematic illustration of Imry-Ma argument. [81]

ones. So, the Hamiltonian of the system is given by :

$$\begin{aligned}
 \mathcal{H} = & -J_{FM} \sum_{\substack{\langle i,j \rangle \\ \in FM}} \mathbf{S}_i \cdot \mathbf{S}_j - \sum_{i \in FM} (d_x S_{ix}^2 + d_z S_{iz}^2) - \sum_{i \in FM} \mu \mathbf{B} \cdot \mathbf{S}_i \\
 & - J_{AFM} \sum_{\substack{\langle i,j \rangle \\ \in AFM}} \epsilon_i \epsilon_j \boldsymbol{\sigma}_i \cdot \boldsymbol{\sigma}_j - \sum_{i \in AFM} \mu \mathbf{B} \cdot \epsilon_i \boldsymbol{\sigma}_i \\
 & - J_{INT} \sum_{\substack{(i \in FM, \\ j \in AFM)}} \mathbf{S}_i \cdot \epsilon_j \boldsymbol{\sigma}_j
 \end{aligned} \tag{2.19}$$

where \mathbf{S}_i and $\boldsymbol{\sigma}_i$ are the classical spin vectors of the i th site of the FM and the AFM, respectively. Only FM anisotropy is considered with d_x the anisotropy constant of the easy axis and d_z is the anisotropy constant for the hard axis, used keeping the spins oriented in the plane of the FM and for simulating the shape anisotropy. Monte-Carlo simulations were performed in order to obtain the hysteresis loop of the system.

Misra et al.[92] using the domain state model, investigated the structure of interface domains as a function of the thickness and anisotropy of the AFM. They found that the size distribution of the domains of the interface follows a power law. Also, they showed that the interface magnetization after the cooling as well as its stability is crucial for the EB effect. The quantification of stability is introduced by the stability factor which is calculated from the average value of the stability of individual spin at the interface. The stability of spin is defined as the time average of z component of spin during the hysteresis loop divided by the initial value of the spin. Thus, using the above quantity they showed that the interface magnetization is due to an irreversible domain causing the upward shift of the hysteresis loop of the interface. Also, using a similar model [93] with a secondary dilution caused after the cooling process and taking the hysteresis loop, showed that this characteristic enhances further the EB field. This procedure simulates the experimental

method of enhancement of dilution of $FeNi/FeMn$ system using irradiation of the sample with He ions in presence of magnetic field [94, 95].

Beckmann *et al.*[96] used a Monte Carlo simulation for the explanation of asymmetric reversal modes, within the context of the domain state model for EB. The asymmetric reversal mode is the phenomenon in which different reversal modes on the descending and the ascending branches are observed, during the hysteresis loop. They investigated the effect of different angles between the easy axes of the AFM and the magnetic field. As they showed, for a range of angles the reversal was asymmetric, with a coherent rotation of the spin for the descending branch and a non-uniform reversal for the ascending branch. On the other hand, for the rest of the angles, spins rotated coherently both for the descending and ascending branch of the hysteresis loop.

Scholten *et al.*[97] using the same model, performed mean-field-type calculations. They focused their interest on the behavior of coercivity around Néel temperature of the AFM, where coercivity appeared significantly enhanced. This was attributed in the coupling of FM to the AFM interface magnetization. In addition, qualitative agreement was found with the previous investigations on the domain state model using Monte-Carlo simulations.

Spray *et al.*[27] investigated the influence of a rough interface on EB field and coercivity within the framework of the domain state model. More specifically, they quantified the interface roughness as the proportion of AFM interface layer spins which are replaced by FM spins. They found that the EB as well as coercivity are strongly dependent on the interface roughness. This dependence is affected by the dilution of the AFM. It is showed that the interface roughness leads to EB even without any dilution in the AFM, result which is in agreement with Malozemoff's model. Finally, the thickness dependence of the EB field is influenced significantly by the roughness of the interface.

2.4 Multiscale models

A special category of models is those that mix microscopic and mesoscopic ideas at the final simulation. More specifically, grain models is considered to have non-coherent magnetization e.g. spins. Papusoi *et al.* [98] used domain state model considering a granular AFM structure in which the grains are cuboid and non-interacting. Furthermore, the grains have the same easy axis direction. They investigated the role of the nonmagnetic defect concentration and of the temperature on the dependence of coercivity and EB field, showing that the latter presents a maximum as a function of this concentration. They also found that for increasing concentration the temperature dependence of the coercivity changes from a monotonic decrease to a nonmonotonic dependence, exhibiting a maximum near the blocking temperature.

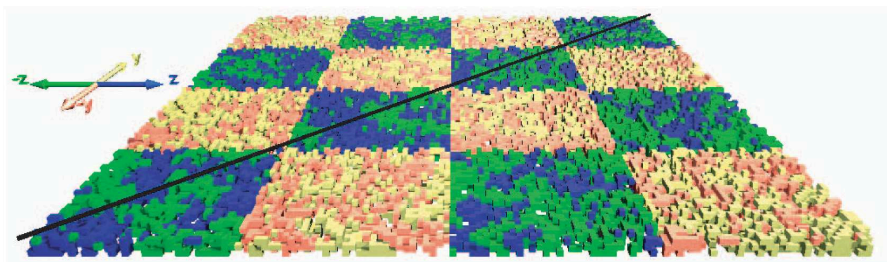


Figure 2.16: Spin configuration of an AFM. The lights colors indicate easy axis aligned along y axis and dark colors, along z axis. The black line indicates the direction of the easy axis of the FM. [99]

Beckmann *et al.* [99] extrapolated the domain state model introducing cuboid grains with perpendicular easy axes into the AFM, as shown in Fig. 2.16. Therefore, a checkerboardlike twin structure is created in the AFM. They investigated the effect of cooling field direction on the reversal modes of the system. Assymmetric reversal modes was found for the decreasing and increasing branch of the hysteresis loop.

Usov and Gudoshnikov [100] developed a model using a classical Heisenberg Hamiltonian for atomic magnetic moments with a dipolar interaction term and dividing the AFM layer to grains with random easy axis. Also, a perpendicular exchange coupling is considered in the FM/AFM interface. They used this model to compare the case of a uniform AFM with the case of a granular one, which was the only one that exhibited non-symmetrical hysteresis loop, with finite EB field.

Takano *et al.* [101, 102, 103] considered a model with a FM layer being in the single domain state and an AFM being granular with atomic spins and interfacial roughness. The interfacial plane of their model consists of a periodic pattern, as shown in Fig. 2.17a). To simulate roughness, they superimposed elliptical “islands” of monatomic thickness on the spin map, as shown in Fig. 2.17b), where the sampling region consists of a grain. The adding of one atomic layer, reverses the direction of the spin at each site covered by the island. Islands were superimposed sequentially, allowing overlap between them, as shown in Fig. 2.17c). They investigated the dependence of EB field on the grain size, where the correct magnitude (same as the experimental one) of the EB field is found.

2.5 Modelling nanoparticles and other structures

A special category of models is the one that describes nanoparticles. The main feature of this kind of models is that they are quite realistic due to the very small dimensions of the nanoparticles. Therefore the number of the simulated magnetic moments is very close to the one in real system. Zianni *et al.*[104] simulated a nanoparticle consisting from a FM core and from an AFM shell, as shown in Fig. 2.18a). They study the dependence of coercivity on the size and on the temperature of the nanoparticle, concluding that the

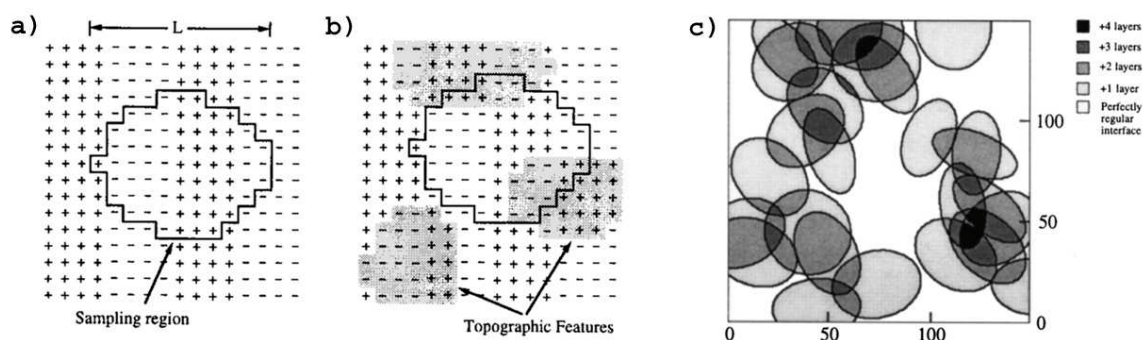


Figure 2.17: a) Topographical representation of a smooth interface plane with periodic pattern and with a sample region representing a model grain. b) Elliptical islands of a monoatomic layer were superimposed on the spin map to simulate roughness. Adding one atomic layer reverses the direction of the underlying spin. c) Topographical map containing overlapping islands. The legend correlates the different shades of gray with the height of interfacial elevation. The FM is on the top of this islands. [101]

step temperature dependence of coercivity can be attributed to the strong temperature dependence of the AFM anisotropy. Eftaxias *et al.* [105] using the same model found that coercivity depends mainly on interface size and EB field on the structure of the interface. A decrease of the core radius for a given particle size results in an increase of both EB and coercivity while an increase of the shell thickness reduces the coercivity. At low temperatures, an increase of the FM/AFM exchange coupling, increases the EB field and reduces the coercivity. In all cases the EB field has a stronger temperature dependence than the coercive field. Trohidou *et al.* [106] using the same model investigated the training and aging effects of an EB nanoparticle. They conclude that the training effect is an effect of contributions of both core and shell, and interface. Furthermore, it is demonstrated that with decreasing defect concentration the EB field increases and the coercivity decreases. Finally, Iglesias *et al.* [107, 108] used Monte Carlo simulations for the study of the microscopic origin of the EB phenomenon in a nanoparticle as the previous writers. It is found that different reversal mechanisms are ruling the two branches of the hysteresis loop, as Beckmann *et al.* [96] found for the FM/AFM system of film. They related their findings with the existence of net magnetization on the interface which dependence on the exchange coupling constant.

Givord *et al.* [109] simulated a ferromagnetic nanoparticle inside an AFM matrix using a macroscopic model similar to Meiklejohn's model, as shown in Fig. 2.18b),c). They showed that the energy barrier, which works against reversal is due to the AFM anisotropy. Furthermore, they showed that pre-existing canting of the AFM moments at the interface cause EB phenomenon. Another special EB system is the circular FM/AFM dots, in which a FM dot is in contact with a AFM substrate. Mejia-Lopez *et al.* [110] investigate this kind of system, considering a microscopic model including a dipolar energy term. They found that spin configuration form a vortex state. Vortex domains is very common in systems

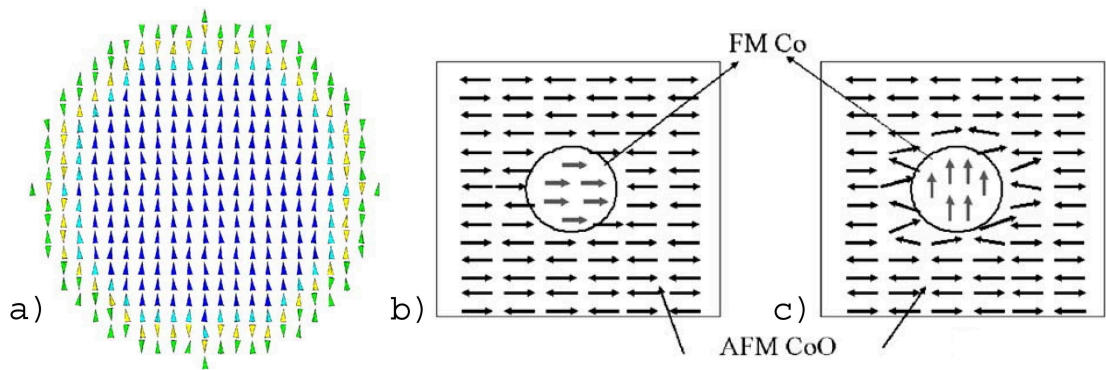


Figure 2.18: a) Spin configuration of an equatorial cut of a nanoparticle. FM core spins are colored in dark blue, AFM shell spins are colored in green while interface spins have been colored in light blue and yellow. [108] Spin configuration of Co nanoparticles embedded in CoO with b) uncompensated-parallel coupling and c) compensated-perpendicular coupling. [109]

with cylindrical shape. Moreover, they found non-uniform distribution of the magnetization in the FM, perpendicular to the interface, giving rise to different magnetization reversals in the two branches of the hysteresis cycle

Theory of magnetism in solids

3.1 Magnetism in solids

According to the behavior of materials under the influence of a magnetic field and the type of magnetic order, they can be separated into five categories: Diamagnetic, paramagnetic, the ferromagnetic (FM), antiferromagnetic (AFM) and the ferrimagnetic.

Magnetism in solids is closely connected with quantum mechanics, as a classical description of the atoms leads to no magnetic moments, even in a magnetic field. The main sources of the magnetic moment of an atom are: the spin of the electron, the orbital angular momentum of the electron around the nucleus and the deviation of this angular momentum induced by an applied magnetic field. Nuclear magnetic moments are around 10^{-3} times smaller than the moments of the electron and give rise to nuclear paramagnetism. In general, nuclear magnetization is ignored from the theoretical models.

Consider the orbital angular momentum number l of the electron which describes the total angular momentum which is given by $\hbar\sqrt{l(l+1)}$. This number takes values $l = 0, 1, \dots, (n-1)$ where n is the principal quantum number which describes the energy of a particular shell. We also consider the spin quantum number m_s which determines the component of the spin s along the direction of an applied field. This number takes values $m_s = \pm 1/2$ and thus the spin angular momentum s take values $\pm \hbar/2$. The l vectors add to form a resultant orbital angular momentum \mathbf{L} , and the s vectors, a resultant \mathbf{S} . For forming the atomic momentum, we need to combine the orbital and the spin momenta of the electrons of an atom. In magnetism, the Russel-Saunders coupling is used for the combination of the two electron momenta. Thus, the resultants \mathbf{L} and \mathbf{S} are combined to form the atomic momentum $\mathbf{J} = \mathbf{L} + \mathbf{S}$, with the quantum number $j = (l-s), (l-s+1), \dots, (l+s+1), (l+s)$ and total atomic magnetic quantum number $m_j = m_l + m_s$.

For a general atomic system the spin-orbit interaction energy is written as $\mathcal{H}_{s-o} = \xi(r)\mathbf{L}\cdot\mathbf{S}$, where $\xi(r)$ is a function of the distance of the electron from the nucleus. Knowing that $\mathbf{J}^2 = \mathbf{L}^2 + \mathbf{S}^2 + \mathbf{L}\cdot\mathbf{S}$, as \mathbf{L} and \mathbf{S} commute, we obtain $\mathbf{L}\cdot\mathbf{S} = (\mathbf{J}^2 - \mathbf{L}^2 - \mathbf{S}^2)/2$. Thus using the above Hamiltonian for spin-orbit interaction the total magnetic moment is $\boldsymbol{\mu}_{\text{total}} = \frac{\mu_o}{\hbar} g\mathbf{J}$, where μ_o is the Bohr magneton and g is the Landé factor which is given

by

$$g = 1 + \frac{j(j+1) + s(s+1) - l(l+1)}{2j(j+1)} \sim 2.04 \quad (3.1)$$

A similar discussion relates to the interaction of magnetic moment of the nucleus with the magnetic moment produced by the electrons, called the hyperfine interaction.¹ This interaction though too small to be important for the current investigation and many solid state applications, is of great importance in nuclear magnetic resonance studies.

The spin and the angular momentum of the electron give rise to the paramagnetic contributions of the magnetization and the change of this angular momentum induced by an applied magnetic field gives rise to the diamagnetic contribution. For example, the hydrogen atom has zero orbital moment, so the magnetic moment is comprised of the electron spin and a small induced diamagnetic moment. Helium, with both spin and orbital moment zero, there is only the induced diamagnetic moment. In general atoms with filled electron shells are diamagnetic due to the fact that they have zero spin and orbital moment. Finally, in this thesis we refer to the magnetization of the spin at the atomic lattice sites, which is just essentially this atomic magnetic moment. For many FM materials is a very accurate description, but the considerable contribution of the electron orbits should not be neglected. E.g. the magnetic moment coming only from spin contributions ($l = 0, j = 0, g = 2$) is twice as much as for the case of magnetic moment of a pure orbit ($s = 0, j = l, g = 1$).

The spin and angular momentum of the electron is responsible for paramagnetic behavior of the atom as well as for the atomic magnetic ordering e.g. ferromagnetism. The effect of the interaction of an external magnetic field on the electrons is responsible for the diamagnetic behavior. This can be understood qualitatively by considering Lenz's law for magnetism. According to this law, when the magnetic flux enclosed by a current loop is changed, a current whose magnetic field is opposite to the external field, is induced. Considering the electron's orbit as a current loop, it will be changed in a such sense that the magnetic moment will be induced in a direction opposite to that of the applied field. Thus, this diamagnetic moment will persist as long as the external field is applied.

¹Similarly to the electron magnetic moment, the nuclear magnetic moment is $\mu_{\text{spin-nucleus}} = \frac{\mu_N}{\hbar} g_I \mathbf{I}$, where g_I is the g-factor with constant value for a particular nucleus and \mathbf{I} is the angular momentum of the nucleus. μ_N is the nuclear magneton. Thus, the new total angular momentum \mathbf{F} is the sum of the nuclear and electronic angular momenta: $\mathbf{F} = \mathbf{I} + \mathbf{J}$, and the hyperfine interaction is $\mathcal{H}_{hf} = -\alpha \mathbf{I} \cdot \mathbf{J}$, where α is constant.

3.2 The exchange interaction

The magnetic order in magnetic materials is caused mainly by the exchange interaction. The direct exchange interaction is between spins of the ions at the lattice sites and it is caused by the overlap of the electronic wave functions.

Consider a system of N electrons which are bound to a grid of atoms. The eigenfunctions $\phi_i(\mathbf{r}_j)$ of an electron bound to atom j isolated from the rest of the system, where \mathbf{r}_j is the coordinates of the electron and its spin components. Since all the atoms are identical, the electron will have the same set of eigenfunctions, only at different coordinates. The function $\phi_i(\mathbf{r}_j)$ describes not only the function of the spatial coordinates but also the spin. Considering the orbital motion of the electron quenched, the electron eigenfunction may be written as $\phi_i(\mathbf{r}_j) = \varphi_i(\boldsymbol{\rho}_j)\chi_{i,j}$, where $\varphi_i(\boldsymbol{\rho}_j)$ is the solution of Schrödinger equation for an electron positioned at the $(\boldsymbol{\rho}_j)$ without spin and $\chi_{i,j}$ is a function of the spin coordinates only. Thus the antisymmetrical eigenfunction may have either of two forms:

$$\phi_i^I(\mathbf{r}_j) = \varphi_i^{\text{sym}}(\boldsymbol{\rho}_j)\chi_{i,j}^{\text{anti}} \quad \text{or} \quad \phi_i^{II}(\mathbf{r}_j) = \varphi_i^{\text{anti}}(\boldsymbol{\rho}_j)\chi_{i,j}^{\text{sym}} \quad (3.2)$$

where φ_i^{sym} and φ_i^{anti} are the symmetrical and antisymmetrical eigenfunctions that are dependent only on the spatial coordinates, respectively, whereas $\chi_{i,j}^{\text{anti}}$ and $\chi_{i,j}^{\text{sym}}$ are antisymmetrical and symmetrical spin functions, respectively.

Consider now the case of the spin function of a two electron system in which every electron has spin $\pm 1/2$. The tensor of the net spin is $s = s_1 + s_2$ with eigenstates basis the : $(s_1, s_2) = 1/2\{(1, 1), (-1, -1), (1, -1), (-1, 1)\}$. Using the eigenvalues basis of the net spin (s, s_z) , where $s = 0, 1$ the two possible values of the net spin of the system and s_z is the eigenvalue of the projection of the net spin on the z axis, where $-s \leq s_z \leq s$. Thus the basis is the: $(s, s_z) = \{(0, 0), (1, 1), (1, 0), (1, -1)\}$.

Next, suppose that there is an interaction between the two electron systems, given by a Hamiltonian H_{12} , which may be written

$$\mathcal{H}_{12} = \frac{Ze^2}{|\boldsymbol{\rho}_1 - \boldsymbol{\rho}_2|} + \frac{Ze^2}{|\mathbf{R}_1 - \mathbf{R}_2|} + \sum_{i=1,2} \left[\frac{p_i^2}{2m} - \frac{Ze^2}{|\boldsymbol{\rho}_i - \mathbf{R}_1|} - \frac{Ze^2}{|\boldsymbol{\rho}_i - \mathbf{R}_2|} \right] \quad (3.3)$$

where $\mathbf{R}_1, \mathbf{R}_2$ is the coordinates of the nucleus 1 and 2, respectively. Thus the first term is describing the electrostatic interaction between the two electron and the second term the interaction between the two nuclei. The summation over the two electrons, describes the momentum and the interaction of each electron with every nuclei. For finding the energy, we applied the equation: $\int \phi^* H_{12} \phi d\tau$. The energies for the states of Eq. 3.2 are, respectively $E_I = A^2(K_{12} + J_{12})$ and $E_{II} = B^2(K_{12} - J_{12})$, where

$$K_{12} = \int \varphi_+^*(\boldsymbol{\rho}_1)\varphi_-^*(\boldsymbol{\rho}_2)H_{12}\varphi_+(\boldsymbol{\rho}_1)\varphi_-(\boldsymbol{\rho}_2)d\tau_1d\tau_2 \quad (3.4)$$

and

$$J_{12} = \int \varphi_+^*(\rho_1)\varphi_-^*(\rho_2)H_{12}\varphi_-(\rho_1)\varphi_+(\rho_2)d\tau_1d\tau_2. \quad (3.5)$$

A and B are normalizing factors, $\varphi_+(\rho_1)$ is the eigenfunction of spatial coordinated of the electron 1 at the spin up state and similarly the others. Also, K_{12} is the average electrostatic energy, J_{12} is the so called exchange integral and is a direct result of the requirement that the electrons are indistinguishable.

Thus the energies E_I, E_{II} may be written in the operator form $E = K_{12} - 1/2J_{12} - 2J_{12}\mathbf{s}_1\mathbf{s}_2$. The last term it is called the direct exchange interaction between spins. For two atoms, i and j , that have one electron each the so called exchange Hamiltonian is

$$\mathcal{H} = -2J_{ij}\mathbf{s}_i\mathbf{s}_j \quad (3.6)$$

where J_{ij} is the exchange integral of the two electrons. For the case of atoms of an entire crystal with more than one electron with an unpaired spin and the exchange integral isotropic, equal to J_e , the Hamiltonian will be:

$$\mathcal{H} = -2J_e \sum_{i \neq j} \mathbf{S}_i \mathbf{S}_j \quad (3.7)$$

where $\mathbf{S}_i = \sum \mathbf{s}_i, \mathbf{S}_j = \sum \mathbf{s}_j$ are the total spins of atoms i and j , respectively. It was considered that the exchange energy between electrons of the same atom is constant, thus can be omitted. The summation is over the nearest neighbors of each atom i of the crystal. This coupling depends only on the relative orientation of the two spins, but not on their directions with respect to $\mathbf{R}_1 - \mathbf{R}_2$. This is due to the spin independence of the Hamiltonian Eq.3.3 which holds without any assumption about its spatial symmetry. In order to break the rotational symmetry in spin space, extra terms, e.g. dipolar interactions or spin-orbit coupling, must be included in the Hamiltonian Eq. 3.3. Thus, the produced spin Hamiltonian will describe anisotropic coupling, an important characteristic for the existence of easy or hard directions of magnetization and for the formation of domains (see section about anisotropy). Finally, when N atoms of total spin \mathbf{S} are widely separated (considering for simplicity that for each atom $\mathbf{J} = \mathbf{S}, \mathbf{L} = \mathbf{0}$), the ground state will be $(2S + 1)^N$ -fold degenerate. Thus the spin Hamiltonian describes the splitting of this vastly degenerate ground state when the atoms are close together.

A second order term can be also extracted of the form $\mathcal{H}_e = -J_b \sum_{i \neq j} (\mathbf{S}_i \mathbf{S}_j)^2$. If the z - axis is the axis of quantization then the Hamiltonian Eq.3.7 becomes $\mathcal{H} = -2J_e \sum_{i \neq j} S_{iz}S_{jz}$, which is called the Ising model.

The exchange integral J_e is crucial for the magnetic ordering of the materials. When J_e is positive, the Hamiltonian Eq. 3.7 favors parallel spins and FM order, whereas J_e is negative, it favors antiparallel spins and AFM order. The sign of the the exchange integral J_e depends on the eigenfunctions $\varphi(\rho)$ and especially on the terms of the Hamiltonian for

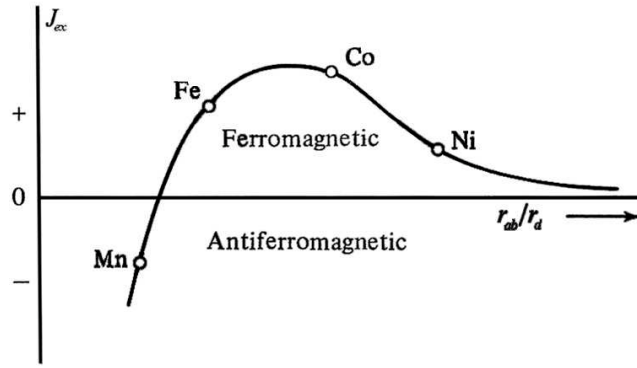


Figure 3.1: Schematic variation of the exchange integral as a function of the interatomic distance r_{ab} , usually referred as the Bethe-Slater curve. [111]

electrons ($Ze^2/|\rho_1 - \rho_2|$) and atoms ($Ze^2/|\mathbf{R}_1 - \mathbf{R}_2|$) electrostatic interaction. Bethe and Slater [112, 113, 114] measured the interatomic distances and the radius of the incompletely filled d subshell, to calculate the exchange integral. As shown in Fig. 3.1, the so called Bethe-Slater curve, they obtain the exchange integral as a function of the ratio of the interatomic distance divided by the radius of d orbitals. For large values of this ratio the exchange integral was positive and for small values it was negative, thus separating the FM $3d$ elements from the AFM $3d$ elements. Only $3d$ elements e.g. manganese, iron, cobalt and nickel were investigated. Finally, the classical atomistic model which we use in this thesis assumes no redistribution of energies and no interaction with the band structure - essentially the fermi energy for each atom is fixed. This gives a difference in the spin up and spin down (ideally) populations which is constant and consequently the exchange integral J_e will be constant.

3.3 The indirect exchange and the super-exchange

The direct exchange, as described in the previous section, arises from the direct electrostatic interaction among electrons from two different atoms. In addition to this exchange interaction, there are more complicated exchange interactions with the most important being the indirect exchange and superexchange. Superexchange interaction appears in materials when the two magnetic moments are separated by a nonmagnetic moment. Then, the magnetic interaction is mediated by the electrons in their common nonmagnetic neighbors. This mechanism was first introduced by Kramers[115] and Anderson[116] for AFM rocksalts, e.g. metallic alloys, oxides such as CoO , NiO , MnO . As shown in Fig. 3.2a), for the M^{2+} ions only, the nearest neighbors in each plane are parallel and antiparallel to the magnetic moments in the other planes. The planes are too far away for direct exchange coupling and an indirect coupling is mediated by the oxygen anions.

More specifically the nonmagnetic anions can be seen as two superimposed states with

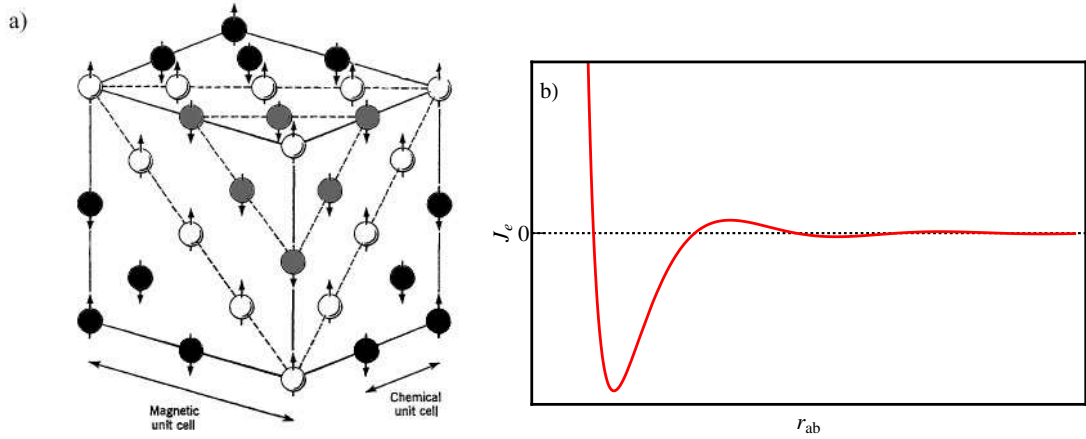


Figure 3.2: a) Schematic representation of the spin arrangement of the Mn^{2+} ions in MnO . The lattice for MnO is a rocksalt structure, though the O^{2-} ions are not shown in the figure. The different colors indicate the planes of closest neighbors with the same spin direction, interacting with direct coupling b) Dependence of indirect exchange integral on the separation between atoms.

one spin up electron and one with spin down, the net moment being zero. As shown in Fig. 3.3b) for a general case, when e.g. a Mn atom with spin up is brought close to the nonmagnetic anion O , its spin down state is attracted more closely to the Mn atom and the spin up is repelled away as being parallel to each other. Then a second Mn atom is brought close to the nonmagnetic anion O , being forced to have spin down. Hence, the MnO crystal has an AFM configuration.

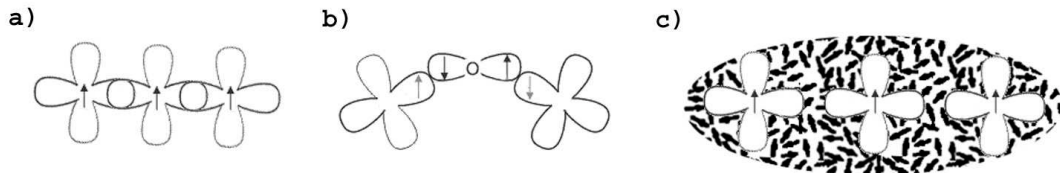


Figure 3.3: Schematic representation of a) direct exchange, in which the magnetic moments are coupled because of their spatial electron distribution overlap, b) superexchange, in which the magnetic moments are coupled because of both spatial electron distribution overlap with the same nonmagnetic atom and c) indirect exchange, in which the magnetic moments are coupled by interactions with the conduction electrons.

The indirect exchange is usually referred to RKKY interaction, named by Ruderman, Kittel [117], Kasuya[118] and Yosida[119], who first studied the exchange coupling in the rare earth metals. This interaction is based on the coupling of the magnetic moment of the partially filled f electrons of neighbouring atoms not directly but through the conduction electrons, as shown in Fig. 3.3c). It is considered the metallic analogue of superexchange in insulators and is stronger than the direct coupling, because f electrons overlap very little in general. This interaction can lead to both FM or AFM spin configurations. The exchange integral in this case has different dependence on the interatomic distance compared to direct coupling, as shown Fig. 3.2b), and can have positive or negative peaks giving rise

to FM or AFM coupling.

3.4 The anisotropy

As mentioned before, the exchange coupling is considered without any assumption about the spatial symmetry of the electron spin. This is not quite realistic, as magnetization tends to lie along certain crystallographic axes e.g. as shown in Fig. 3.4 for the magnetite, giving different values of saturation. Thus, an extra term must be introduced in the exchange Hamiltonian to describe this spatial anisotropy, an important characteristic for the existence of easy or hard directions of magnetization and for the formation of domains. This kind of anisotropy is the magnetocrystalline anisotropy. There are several kinds of anisotropy, like the shape anisotropy originating from magnetostatic properties, surface anisotropy or strain anisotropy.

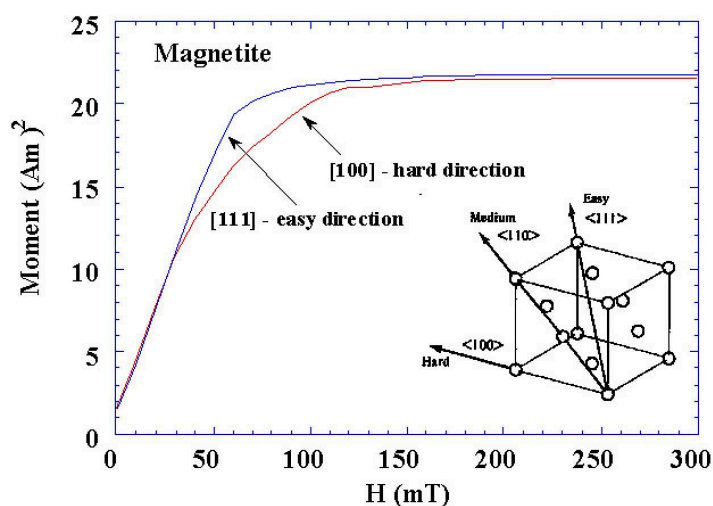


Figure 3.4: Magnetization curves of magnetite (Fe_3O_4) for different crystallographic orientation. [120]

3.4.1 Magnetocrystalline anisotropy

There are many ways to express the magnetocrystalline anisotropy such as power series of trigonometric functions of the angles the magnetization vector makes with the principal axes of the crystal. In the current thesis, a power series of the spin coordinates is used, thus the anisotropy term is direction-dependent. The magnitude of magnetization along the applied field is determined by the exchange interaction with contributions of the anisotropy being negligible for FM materials. In contrast, the direction of the magnetization is determined by the anisotropy, as the exchange is in general indifferent to the direction in space. Consequently, the direction of the quantization is the direction for which the anisotropy energy is minimal. This direction is usually referred to as the easy axis and for the

case where the anisotropy energy is maximum, is referred to as the hard axis. In this thesis we consider one, two (parallel to the plane) or three easy axis which are referred usually as uniaxial, biaxial or cubic anisotropy, respectively.

The most common anisotropy which is presented mainly in hexagonal crystals is the uniaxial or twofold anisotropy. It has one easy axis and is described by one parameter, the angle between the easy axis and the direction of magnetization. Usually the easy axis is parallel to a crystallographic axis, so in terms of spin, the uniaxial anisotropy is described

$$\mathcal{H}_{an} = -K_{1u}S_x^2 + K_{2u}S_x^4 + \dots, \quad (3.8)$$

where x is parallel to a crystallographic axis, S_x the x component of spin and K_{1u}, K_{2u} are the anisotropy constants. The values of the anisotropy constants for certain materials have been calculated using ab-initio calculations [121, 122]. The second term and the higher order terms are usually neglected. As shown in Fig. 3.5a) and b), the energy has minimum when the magnetization is along the x axis.

Similarly to uniaxial anisotropy, biaxial or fourfold anisotropy has two easy axes, perpendicular to each other. Both of the easy axes are parallel to a crystallographic axis, so in terms of spin, the biaxial anisotropy is described by

$$\mathcal{H}_{an} = -K_{1b}(S_x^4 + S_y^4) + \dots, \quad (3.9)$$

where x, y is parallel to a crystallographic axis, S_x, S_y the x, y component of spin respectively. The terms are quadrupole as the square term gives a easy plane (All the direction in the plane x - y are easy directions). As shown in Fig. 3.5c) and d), the energy has minimum when the magnetization is along the x and y axis.

Finally, cubic anisotropy has three easy axes, perpendicular to each other. The square terms $S_x^2 + S_y^2 + S_z^2$ are constant, thus, as in biaxial anisotropy, the quadrupole terms are used. All of the easy axes are parallel to a crystallographic axis, therefore in terms of spin, the biaxial anisotropy is described by

$$\mathcal{H}_{an} = -K_{1c}(S_x^4 + S_y^4 + S_z^4) + \dots. \quad (3.10)$$

As shown in Fig. 3.5e) and f), the energy has minimum when the magnetization is along the x, y or z axis, having 6 equivalent energy minima.

3.4.2 Shape anisotropy

The macroscopic shape of a structure can also be a source of anisotropy. For example, an elliptical particle magnetizes easily along the long axis as the demagnetizing field is stronger along the short axis. This is due to the formation of free poles at the boundary of the particle consisting of a single domain, as described by Néel. It originates in the

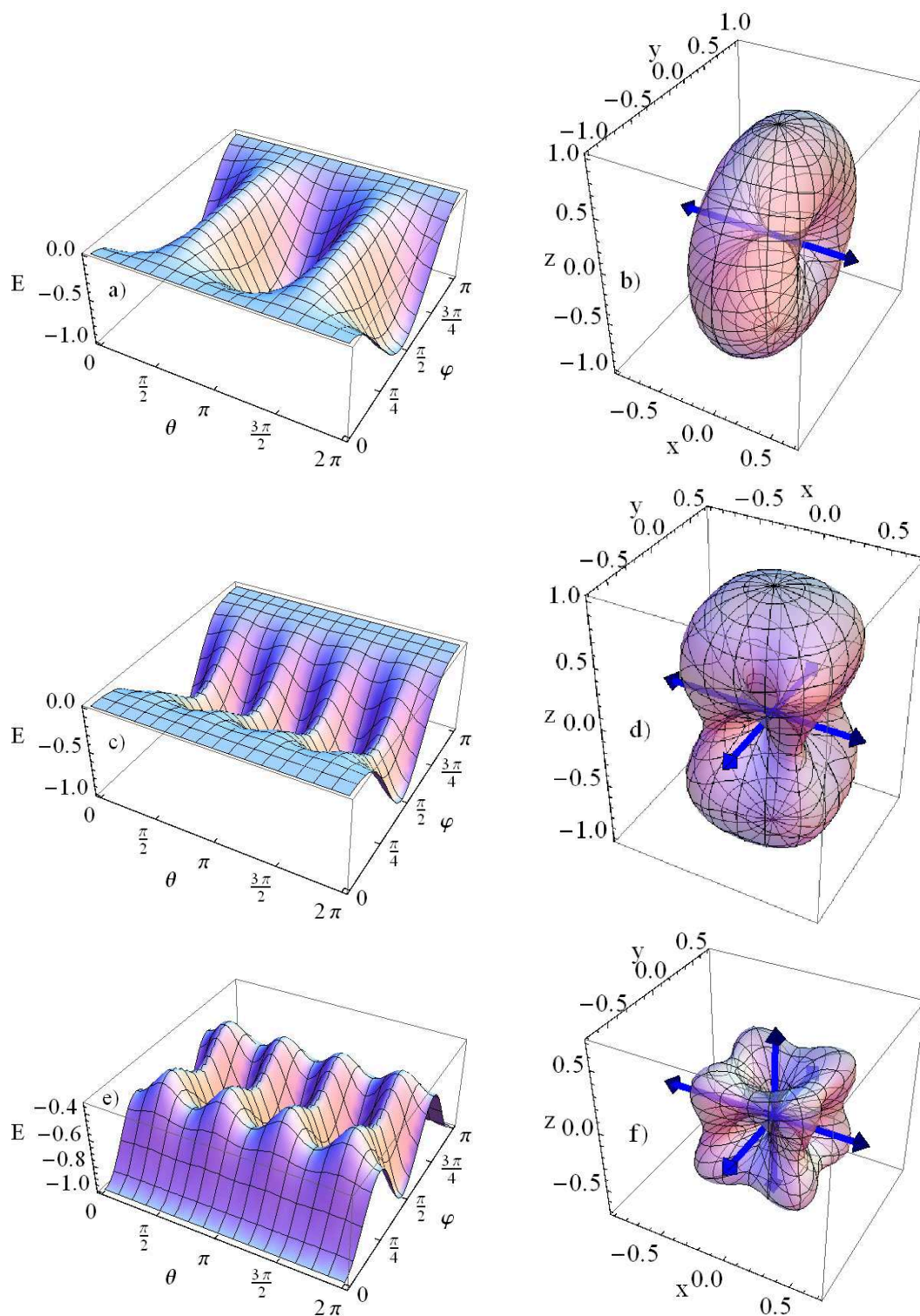


Figure 3.5: a), b) Uniaxial, c), d) biaxial and e), f) cubic magnetocrystalline anisotropy. The easy axes are represented with the blue vectors. The left 3D representations show the energy $E(\theta, \phi)$ as a function of the spherical coordinates of the spin \mathbf{S} , considering the $r (= \sqrt{S_x^2 + S_y^2 + S_z^2})$ coordinate equal to one and using the cartesian coordinate system. The right 3D parametric representations show the spherical radius $r = E(\theta, \phi)$ as a function of the spherical coordinates of the spin \mathbf{S} , using spherical coordinate system.

3.5. Magnetostatic dipole interaction

magnetostatic energy, which can be written $\mathcal{H}_{magn} = -1/2 \int_V dV \mathbf{M} \cdot \mathbf{H}$, where \mathbf{M} is the magnetization of the specimen and \mathbf{H} the applied magnetic field. For a uniformly magnetized specimen, using the proper boundary conditions at the surface, the energy becomes $\mathcal{H}_{magn} = -\frac{VM_s^2}{2} S_x \hat{D} S_x$, where M_s is the saturation magnetization of the material, \hat{D} is the demagnetization tensor. For a particle, the \hat{D} is comprised of a parallel (D_{\parallel}) and perpendicular (D_{\perp}) component to the symmetry axis. So the anisotropy energy can be rewritten as

$$\mathcal{H}_{shape} = -K_s S_x^2 \quad (3.11)$$

with $K_s = \frac{VM_s^2}{2}(D_{\perp} - D_{\parallel}) > 0$ having the role of an effective uniaxial anisotropy constant. Thus, the shape of the particle creates an easy axis along the most elongated direction of the particle. In the case of thin films, it is easier to consider a hard axis perpendicular to the film plane, e.g. z-axis, and the energy is taking the form

$$\mathcal{H}_{shape} = K_s S_z^2 \quad (3.12)$$

The FM layers have a finite saturation magnetization but the AFM layers have around zero saturation magnetization. Therefore it is considered that they do not have shape anisotropy.

3.5 Magnetostatic dipole interaction

The atom can be very easily considered as a microscopic magnetic dipole. As mentioned before, the magnetic moment of the atom is resulted by the orbital and spin angular momentum of the electrons. Magnetic moment can be considered ideally as a point-like source of strength M , comprised of a pair of magnetic poles of strength M , placed at zero distance apart, such that the magnetization is constant in this limit. Furthermore, the magnitude of this moment as we know is $g\mu_o S$. Using Maxwell's equation the magnetic field generated by the dipole is :

$$\mathbf{B}_{dip} = \frac{\mathbf{M}}{r^3} - \frac{3(\mathbf{M} \cdot \mathbf{r})\mathbf{r}}{r^5} \quad (3.13)$$

Thus, the energy of a system of N dipoles can be obtained by adding the energy that each dipole has due to the interaction with the dipolar fields created by the rest of dipoles:

$$\mathcal{H}_{dipol} = \sum_{i \neq j}^N \frac{\mathbf{M}_i \cdot \mathbf{M}_j}{r^3} - \frac{3(\mathbf{M}_i \cdot \mathbf{r}_j)(\mathbf{m}_j \cdot \mathbf{r}_i)}{r^5} \quad (3.14)$$

Dipole interaction is a long-ranged interaction which decreases slowly with the distance. The first term represents a long-range AFM coupling, with rotational dependence. The second one is an anisotropic term inducing an easy-plane anisotropy.

Now, if we consider a cubic lattice and assuming that the dipolar moments are aligned

along the x direction the Eq.3.13 becomes

$$\mathbf{B}_{\text{dip}} = M_x \left(\frac{1}{r^3} - \frac{3r_x^2}{r^5} \right) = M_x \frac{r^2 - 3r_x^2}{r^5}. \quad (3.15)$$

But in a cubic lattice all spatial directions are equivalent, we have $\frac{r_x^2}{r^5} = \frac{r_y^2}{r^5} = \frac{r_z^2}{r^5} = \frac{1}{3r^3}$, and therefore $\mathbf{B}_{\text{dip}} = 0$. Consequently, the energy $\mathcal{H}_{\text{dipol}}$ will be zero for cubic lattices with uniform magnetization. For non-cubic lattices, this is not zero but it will be a linear function of the magnetization depending on the crystalline symmetry.

3.6 Domains and Domain walls

Magnetic domains are regions where the magnetization has the same direction and magnitude. The boundary between these regions is called a domain wall and is the transition area from one direction to another direction of the magnetization, as shown in Fig. 3.6. The domain theory was introduced in 1907 by Weiss[123]. Domains are formed due to the minimisation of the magnetostatic energy. Actually, the competition between exchange interaction, which favors thicker domain wall, and anisotropy energy, which favors thinner domain wall reducing the number of spins pointing in non-easy directions, create domain walls of certain width and structure. The most common structures of domain walls are the Bloch walls and the Néel walls. Bloch walls appear in bulk specimens, where the rotation of the magnetization lies parallel to the plane of the specimen, as shown in Fig. 3.6a). Contrary to Bloch walls, in the Néel walls the rotation of the magnetization lies perpendicular to the plane of the specimen, as shown in Fig. 3.6b). Usually, Néel walls are favored when the thickness of the specimen is reduced and consequently the magnetostatic energy of the wall is increased due to the free poles at the top and bottom of the specimen.

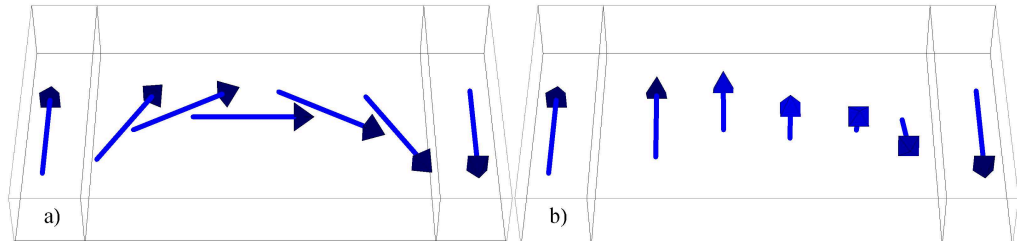


Figure 3.6: Domains with a) Néel and b) Bloch domain wall in a FM.

According to the behavior of domain wall depending the thickness of the specimen, the domain wall energy and width dependence on the film thickness for Bloch and Néel domain walls is drawn in Fig. 3.7 a) and b), respectively. It is obvious that for thin films, Néel walls are more stable, due to decrease of the domain wall energy and the width. On increase of specimen thickness there occurs a transition from Néel to Bloch walls leading to the formation of “cross-tie” walls. Finally, domain walls are present also in AFM materials,

3.6. Domains and Domain walls

not in continuum form but in each sublattice.

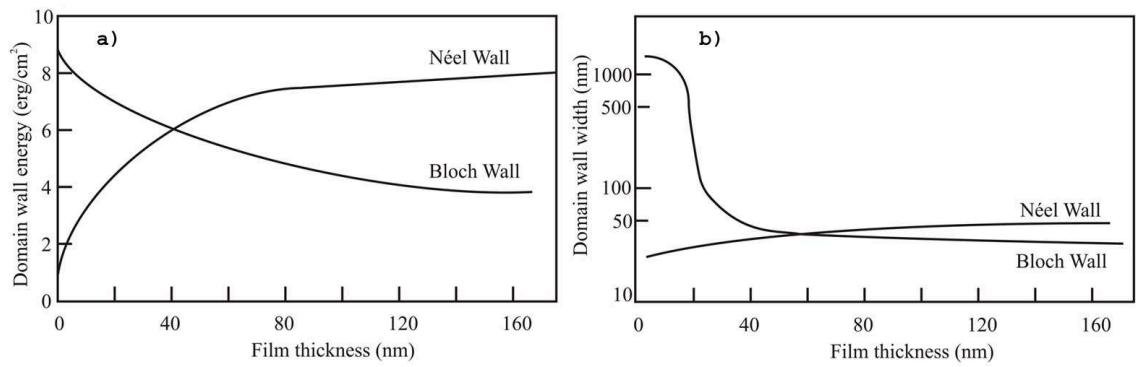


Figure 3.7: a) *Domain wall energy* and b) *width dependence on the film thickness for Bloch and Néel domain walls.* [124]

Atomistic Model-Methodology and initial results

In this chapter, we will do a first simulation using only the FM Hamiltonian or the AFM Hamiltonian. Then, will describe the domain state model presenting some initial results for the cooling field dependence. In general, to create a hysteresis loop we begin from a random state of the spins of the material and then slowly varying the magnetic field we minimize the energy of the system. After that we calculate the relevant quantities e.g. magnetization etc. For the minimisation of the energy of the system, this thesis uses the heat-bath Monte Carlo method which is described thoroughly in Appendix A.

4.1 Modelling a FM

As mentioned before, in a ferromagnetic material the strongly coupled magnetic moments tend to be aligned in parallel, resulting in a spontaneous magnetization, meaning that a magnetic moment exists even without an applied magnetic field. Above a critical temperature, called the Curie temperature, the spontaneous magnetization vanishes and the material has a paramagnetic behavior. Ferromagnetic behavior can be described energetically very easily by two terms plus the Zeeman energy. Thus we have a Hamiltonian of the form:

$$\mathcal{H} = -J_{FM} \sum_{i \neq j} \mathbf{S}_i \mathbf{S}_j - \mu_o \sum_i \mathbf{B} \cdot \mathbf{S}_i - \sum_i (k_x S_{ix}^2 + d_z S_{iz}^2), \quad (4.1)$$

for the case of a ferromagnetic film with uniaxial anisotropy and including dipolar interaction effects as a shape anisotropy. More specifically the first term is the exchange interaction where J_{FM} is the exchange integral, \mathbf{S}_i is the spin of each atom and the summation goes over all the atoms of the material for only first nearest-neighbors of a simple cubic lattice. The second term describes the Zeeman energy due to the interaction of the magnetic field \mathbf{B} with the magnetic moment \mathbf{S}_i of each atom, where μ_o is the Bohr magneton. The last term describes the uniaxial magnetocrystalline anisotropy energy of k_x with easy axis along x axis and the uniaxial shape anisotropy energy of d_z with hard axis along z axis. The sum goes over all the N atoms of the FM. An numerical investigation of the above model is

presented in the next sections, where its parameter of the simulation is investigated.

4.1.1 Investigation of trial step radius

For finding a proper trial step radius, we used a test system with $128 \times 128 \times 4$ spins and parameters to be $k_x = 0.1/J_{FM}$, $d_z = -0.1/J_{FM}$, $|\mathbf{B}| = 0.25/J_{FM}$ with angle of 20° from the x axis and close to zero temperature. The calculation begins with the magnetic moment pointing along the positive x axis and the magnetic field has a negative x component. Thus, the initial spin state is metastable and will reverse after some Monte-Carlo steps. The number of Monte-Carlo steps, in which the total magnetization of the thin film changes sign is considered the characteristic time.

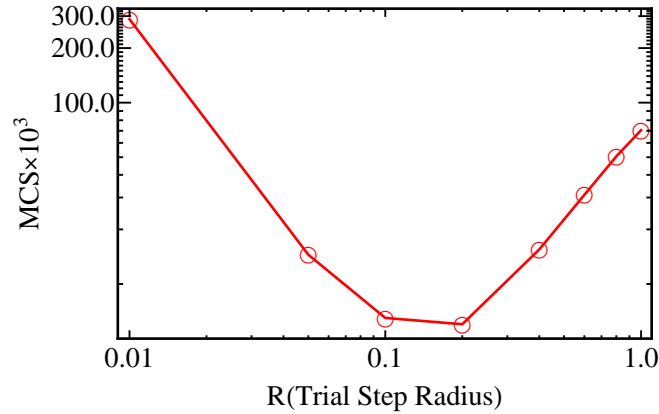


Figure 4.1: *Dependence of characteristic time in Monte-Carlo steps on trial step radius for a reversal of the magnetization of a ferromagnetic material.*

As shown in Fig.4.1, the R presents minimum characteristic time at values around 0.2. This is because large steps, due to exchange interaction, are not accepted. In general, the large steps are energetically unfavorable and the algorithm rejects them, causing inefficiency. In the current investigation, it is chosen $R = 0.4$ for the ferromagnet, so the system magnetization to not reverse abruptly during magnetic field reversal.

4.1.2 Calculation of Curie temperature and hysteretic dependence on temperature

The calculation of Curie temperature is important for the justification of the range of temperatures that the numerical investigation of exchange bias will take place. The system is the same as before but with no shape anisotropy ($d_z = 0$) and no magnetic field ($|\mathbf{B}| = 0$). The material, from the long-range ferromagnetic state on zero temperature, was heated up to $k_bT = 2.5/J_{FM}$, as shown in Fig. 4.2a). The temperature where the material ceases to have magnetization, a phase transition takes place from the ferromagnetic state to paramagnetic state and is close to $k_bT = 1.4/J_{FM}$.

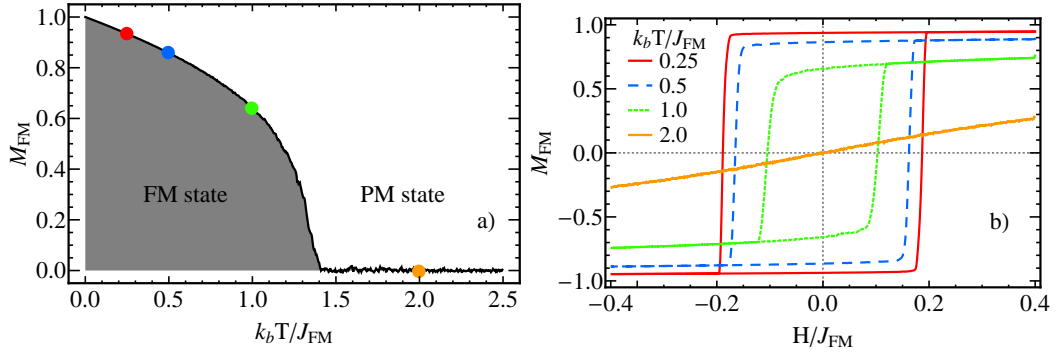


Figure 4.2: a) Phase transition of a ferromagnet. The colored points indicate the temperature in which hysteresis loops were created in b), respectively.

To see the effect of the temperature in a ferromagnetic material, we calculate the hysteresis loops at different temperatures, as shown in Fig. 4.2b). This system has shape anisotropy $d_z = -0.1J_{FM}$ and the applied magnetic field is $|\mathbf{B}| = 0.4J_{FM}$. Thus, when the temperature increases the coercivity as well as the remanent magnetization decreases. Obviously, this happens below the Curie temperature. Above T_C the ferromagnet behaves as a paramagnet without hysteretic behavior. The paramagnetic state of the ferromagnet is manifested in Fig. 4.2b) as a linear response on magnetic field changes. When the system is close to zero temperature, the coercivity approaches the value of coercivity of Stoner-Wolfarth model, the so called Stoner-Wolfarth limit.

4.1.3 Exchange integral and coordination number dependence

Now, keeping the temperature constant at $k_b T = 0.5J_{FM}$, we investigate the effect of exchange interaction in the system. The exchange interaction can be varied with two ways: changing the exchange integral and changing the number of nearest neighbors. The second can be achieved changing the crystal structure of the specimen. The dependence of the hysteresis loop on the exchange integral is shown in Fig. 4.3a) and on the crystal structure in Fig. 4.3b). The structures investigated are the simple cubic (sc), the hexagonal close packed (hcp), the body-centered cubic (bcc) and the face-centered cubic (fcc). In the last two ones, it is also used the $[111]$ crystallographic orientation. When the exchange integral increases the coercivity decreases. This occurs because increasing the exchange integral is like decreasing the anisotropy constant as it is usual to have the units of the Hamiltonian in units of J_{FM} . Thus, with decreasing anisotropy constant we have decreasing coercivity (this explained in more detail in the next section).

In the case of different crystal structures, the hysteresis loop dependence is not very clear. But introducing the number of the first nearest-neighbors, the so called coordination number, the dependence is more clear. In general, when the coordination number increases the coercivity and the remanent magnetization increases. This is due to the increase of

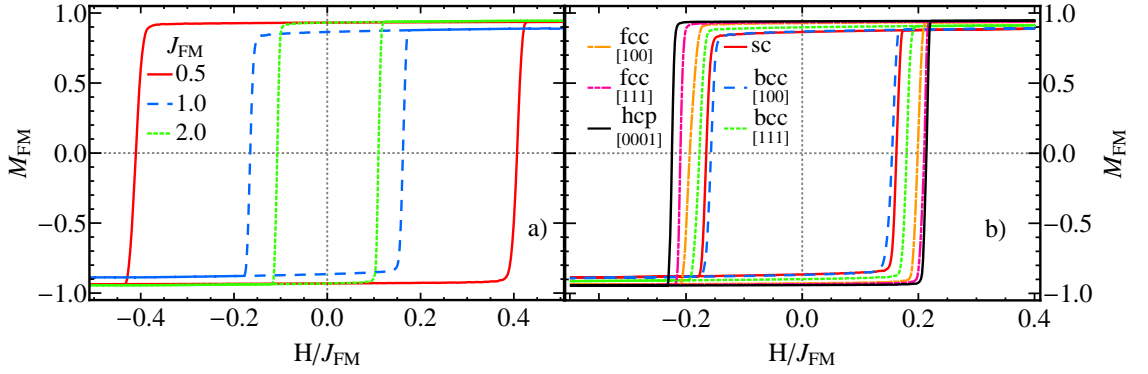


Figure 4.3: Hysteresis loop dependence on a) the exchange integral and b) the form of nearest neighbors.

Crystal. structure	Tot. Coord. Number	Coord. Number x-y
sc	6	4
bcc[100]	8	0
bcc[111]	8	4
fcc[100]	12	4
fcc[111]	12	6
hcp[0001]	12	6

Table 4.1: Coordination number of crystal structures.

the effective anisotropy per volume unit. That means that since the number of closest-neighbors increases per unit volume the anisotropy per volume (effectively) increases. Thus, is like the anisotropy constant increases and consequently the coercivity increases.

The total coordination number and the one along the same $x - y$ plane is shown in Table 4.1. Thus, when the total coordination number and the one along the same $x - y$ plane increases then the coercivity and remanent magnetization increases. E.g. for the case of bcc[100], although has larger total coordination number (8) than sc, the coercivity and remanent magnetization are smaller than sc ones because the coordination number along the same $x - y$ plane is much smaller (0). But for bcc[111] the coercivity and remanent magnetization are larger than sc ones. This occurs because in bcc[111] structure, the coordination number along $x - y$ plane is the same with the one in sc(4) and the total coordination number is larger (8) than the sc one (6). The coordination number along the $x - y$ plane is important because the system has periodic conditions only along this plane (not at the perpendicular direction). Thus, this trend is also a surface effect. Finally, there is a difference between the fcc[111] and the hcp[0001] structure, although they have the same coordination number, total and along $x - y$ plane. We assume that this is an effect of the different number of unit cells along z-axis between these structures. We mean that in our thin film consisting of four layers, hcp[0001] has two units cells (AB|AB) along z-axis but fcc[111] has one and one third unit cell (ABC|A).

4.1.4 Lateral size effect

The effect of lateral size of a FM system is investigated. As shown in Fig. 4.4, the lateral size does not effect the hysteresis loop. In all of our numerical investigations we used the 128×128 grid in order to minimize the finite size effects, but still create sufficiently large domain walls.

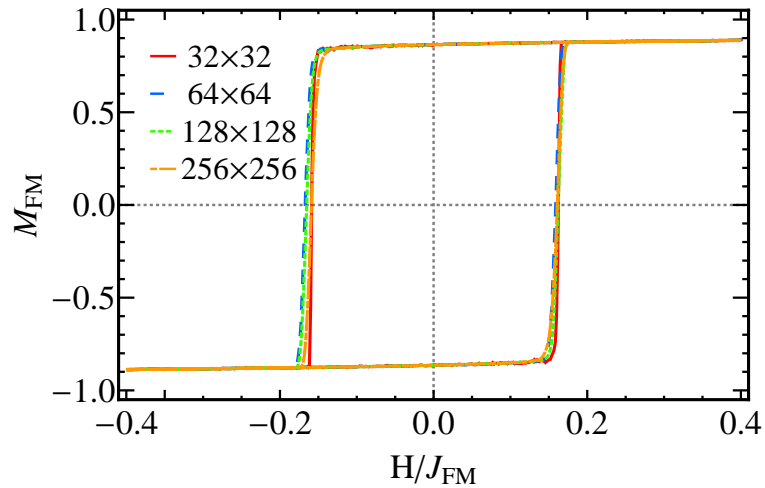


Figure 4.4: Hysteresis loop dependence on lateral size of the thin film.

4.1.5 Magnetocrystalline anisotropy dependence

The effect of magnetocrystalline anisotropy in the system is investigated for the same constant temperature as before and for a simple cubic structure with constant exchange integral. As shown in Fig. 4.5a), the hysteresis loop for uniaxial anisotropy has larger coercivity than in the case of biaxial and cubic anisotropy. This is due to the fact that the energy barrier between the spin states (spin up and spin down) of uniaxial anisotropy is larger than that of the biaxial and cubic anisotropy, as shown in the Section 3.4 in Fig. 3.5. Thus, the reversal is less energetically favorable in uniaxial anisotropy, consequently it needs larger reversal field producing larger coercivity on the hysteresis loop.

The dependence of the hysteresis loop on the anisotropy constant $k = d_x$ ($d_y = 0, d_z = 0.1$) for uniaxial anisotropy is shown in Fig. 4.5b). The coercivity of the hysteresis loop increases when the anisotropy constant increases because this constant controls the energy barrier between the two spin states. Also, it is shown how the anisotropy constant controls the Stoner-Wolfarth limit ($H_c = 2k$).

Finally, the dependence of the hysteresis loop on the angle between the easy axis of the uniaxial anisotropy and the applied magnetic field is shown in Fig. 4.5c). Along the easy axis ($\theta = 0$) the hysteresis loop is squared shape and when the applied field is perpendicular to the easy axis (parallel to the hard axis), the hysteresis loop has an

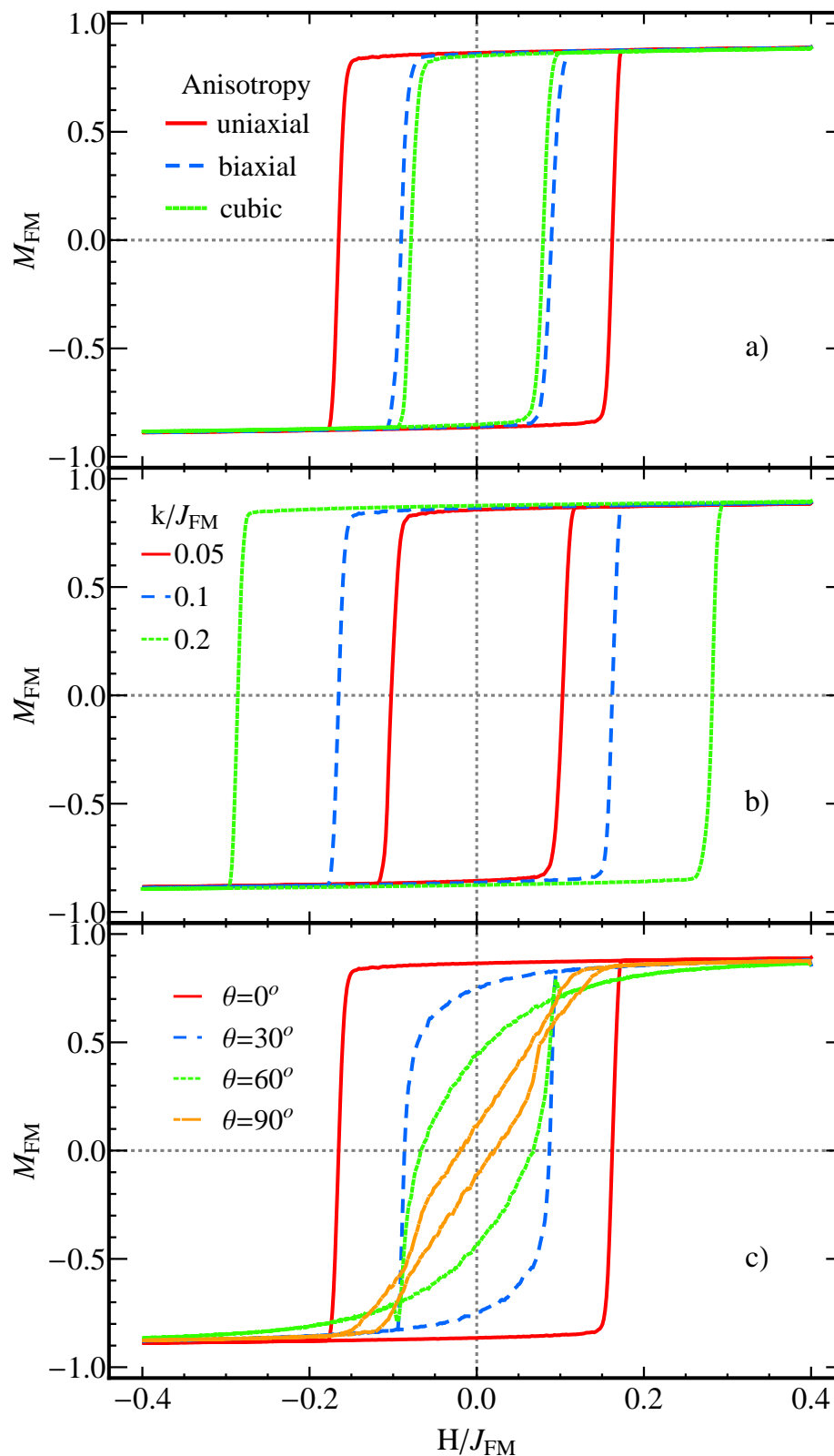


Figure 4.5: Ferromagnetic hysteresis loop dependence on the magnetocrystalline anisotropy characteristics. Hysteresis loops for different a) kinds of anisotropy, b) anisotropy constants (uniaxial) and c) angles between the easy axis and the applied magnetic field.

almost linear shape. This is the case where the magnetization curve loses its hysteretic characteristic and becomes fully reversible.

4.2 Modelling a diluted antiferromagnet

In an AFM material the strongly coupled magnetic moments tend to be aligned antiparallel, resulting in zero net magnetization. The lattice of an AFM can be split into two interpenetrating sublattices in which the magnetization is finite. This lattice is called bipartite and the state in which every spin is surrounded by nearest neighbor spins pointing in the opposite direction is called the Néel state. Above a critical temperature, called the Néel temperature, the AFM behavior vanishes and the material has paramagnetic behavior. The AFM behavior can be described energetically very easily by two terms plus the Zeeman energy. Thus we have

$$\mathcal{H}_{AFM} = -J_{AFM} \sum_{i \neq j} \epsilon_i \epsilon_j \boldsymbol{\sigma}_i \boldsymbol{\sigma}_j - \mu_o \sum_i \epsilon_i \mathbf{B} \cdot \boldsymbol{\sigma}_i - \sum_i k_x \epsilon_i \sigma_{ix}^2, \quad (4.2)$$

for the case of a AFM film with uniaxial anisotropy. There is no shape anisotropy due to lack of net magnetization, thus no magnetostatic energy. More specifically the first term is the exchange interaction where J_{AFM} is the exchange integral, $\boldsymbol{\sigma}_i$ is the spin of each atom and the summation goes over all the atoms of the material for only first nearest-neighbors of a simple cubic lattice. We do not consider higher order energy terms and more than first nearest-neighbors as they give negligible effects. Due to the dilution with non-magnetic impurities not all AFM lattice sites have an associated spin. This is introduced using the variable $\epsilon_i = 0, 1$, with individual values determined such that $p = N^{-1} \sum \epsilon_i$ is the packing fraction of the AFM spins, where N is the total number of atomic sites. The second term describes the Zeeman energy due to the interaction of the magnetic field \mathbf{B} in the magnetic moment $\boldsymbol{\sigma}_i$ of each atom. The last term describes the uniaxial magnetocrystalline anisotropy energy of k_x with easy axis along x axis.

As mentioned above, the net magnetization of an AFM is around zero and there is no hysteretic behavior during field reversal. We used a test system with $128 \times 128 \times 2$ spins and parameters $J_{AFM} = -0.5$, $k_x = 2|J_{AFM}|$ and dilution of 40%. Due to high anisotropy in AFM systems, the trial step is chosen with equal probability between a spin-flip, and a trial step with maximum radius $R = 0.9$. This trial step is quite efficient for an AFM because the spins tend to reverse quite abruptly, due to high anisotropy. An extensive numerical investigation of diluted AFMs can be found in Ref. [125, 126, 127, 128].

4.2.1 Calculating the Néel temperature of a diluted antiferromagnet

Using the Hamiltonian presented in the Section 4.2, we will calculate the Neel temperature of a diluted AFM. A phase diagram of a diluted AFM is shown before in Fig. 2.15a) in which the phase of an diluted AFM can be paramagnetic, domain state or long ranged AFM. The Néel temperature is a critical point for the behavior of the system. In order to calculate the Néel temperature of an AFM we have to calculate the maximum of $\frac{\partial M_{AFM}^+}{\partial T}$ during field heating for small magnetic field, where M_{AFM}^+ the magnetization of the sublattice that gives positive magnetization. This point marks the critical temperature in the crossover regime from random exchange to random field behavior as showed from Kleemann *et al.* [129]. Thus, as shown in Fig. 4.6, at the point where the second derivative of the M_{AFM}^+ is zero, the AFM starts to behave as a paramagnetic material and this gives the Néel temperature.

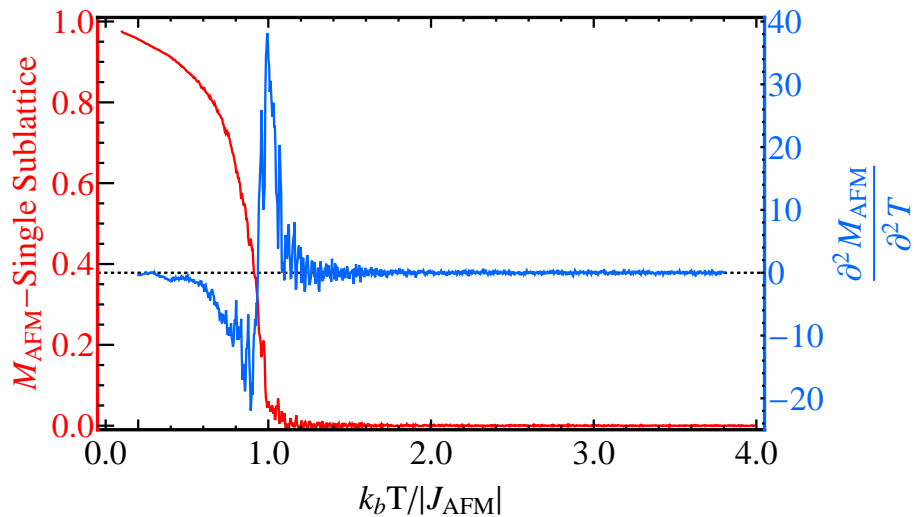


Figure 4.6: Phase transition of an AFM. The magnetization (red) and its second derivative (blue) of a single sublattice as function of temperature is showed.

4.3 The domain state model

Now we will describe the exchange bias model which is used in this investigation, gathering all the model characteristics that were discussed in the previous sections about the FM and the AFM. Thus, the model consists of a FM mono layer exchange coupled with a diluted AFM consisting of many layers. The overall system is a multi layered film of lateral size 128 sites per in-plane direction for all the cases of this study. In most investigations simple cubic crystal packing is used (except for the investigation examining the exchange bias dependence on the crystal packing) for the spins with periodic boundary conditions for the

4.3. The domain state model

in-plane boundaries and open for the out-of-plane boundary.

In particular, FM and AFM consist of classical Heisenberg spins coupled with nearest neighbor exchange constant J_{FM} and $J_{AFM} = -J_{FM}/2$ which determines its Néel temperature, respectively. Thus, the total Hamiltonian of our system will be

$$\mathcal{H}_{TOT} = \mathcal{H}_{FM} + \mathcal{H}_{AFM} + \mathcal{H}_{INT}, \quad (4.3)$$

where \mathcal{H}_{FM} is the FM classical Heisenberg Hamiltonian which is given by

$$\mathcal{H}_{FM} = -J_{FM} \sum_{\substack{\langle i,j \rangle \\ \in FM}} \mathbf{S}_i \cdot \mathbf{S}_j + \mathcal{H}_{FM}^{An.} - \sum_{i \in FM} \mu \mathbf{B} \cdot \mathbf{S}_i, \quad (4.4)$$

where $\mathcal{H}_{FM}^{An.}$ is the magnetocrystalline anisotropy of the FM which is given by either

$$\begin{aligned} \mathcal{H}_{FM}^{An.} = & - \sum_{i \in FM} (d_x S_{ix}^2 - d_z S_{iz}^2) \text{ or} \\ & - \sum_{i \in FM} (d_x S_{ix}^4 + d_y S_{iy}^4 - d_z S_{iz}^4) \text{ or} \\ & - \sum_{i \in FM} (d_x S_{ix}^4 + d_y S_{iy}^4 + d_z S_{iz}^4). \end{aligned} \quad (4.5)$$

This is for uniaxial, biaxial or cubic anisotropy, respectively. In the case of uniaxial and biaxial anisotropy, a hard axis is introduced which lies on the z axis with anisotropy constant $d_z = 0.1J_{FM}$, simulating the shape anisotropy, corresponding to a magnetization preference in the $x - y$ plane, as shown in Fig. 4.7. In addition, the hard axis approximates the dipolar interaction between the Heisenberg spins, although its value does not influence our results essentially because the FM magnetization lies in the plane. The easy axes lies on the x, y axes with anisotropy constant $d_x = d_y = 0.1J_{FM}$, which sets the zero-temperature limit coercive field for magnetization reversal by coherent rotation, i.e. the Stoner-Wohlfarth limit. In the case of cubic anisotropy $d_z = 0.1J_{FM}$.

The \mathcal{H}_{AFM} term is the AFM classical Heisenberg Hamiltonian which is given by

$$\mathcal{H}_{AFM} = -J_{AFM} \sum_{\substack{\langle i,j \rangle \\ \in AFM}} \epsilon_i \epsilon_j \boldsymbol{\sigma}_i \cdot \boldsymbol{\sigma}_j + \mathcal{H}_{AFM}^{An.} - \sum_{i \in AFM} \mu \mathbf{B} \cdot \epsilon_i \boldsymbol{\sigma}_i \quad (4.6)$$

where the term $\mathcal{H}_{AFM}^{An.}$ is the AFM magnetocrystalline anisotropy energy which is given by either

$$\begin{aligned} \mathcal{H}_{AFM}^{An.} = & - \sum_{i \in AFM} \epsilon_i k_x \sigma_{ix}^2 \text{ or} \\ & - \sum_{i \in AFM} \epsilon_i (k_x \sigma_{ix}^4 + k_y \sigma_{iy}^4) \text{ or} \\ & - \sum_{i \in AFM} \epsilon_i (k_x \sigma_{ix}^4 + k_y \sigma_{iy}^4 + k_z \sigma_{iz}^4) \end{aligned} \quad (4.7)$$

for the case of uniaxial, biaxial or cubic symmetry of the AFM anisotropy, respectively.

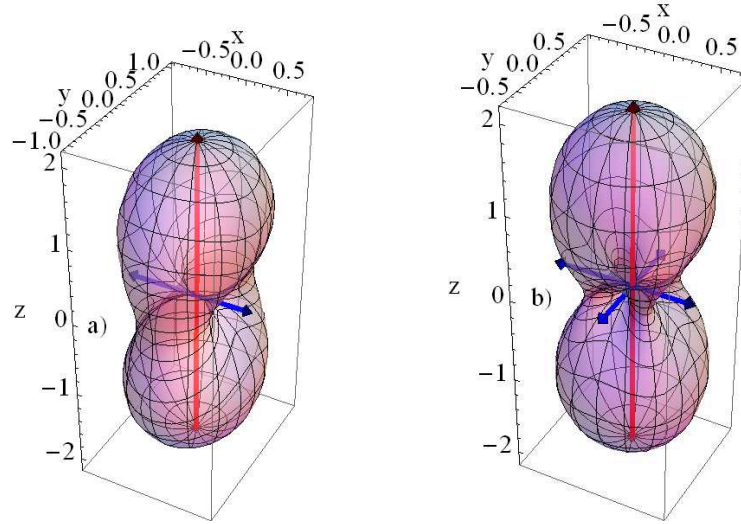


Figure 4.7: The energy surfaces of a) uniaxial and b) biaxial anisotropy with easy axes (blue vectors) and hard axis (red vector) due to shape anisotropy.

Equation 4.7 describes magnetocrystalline anisotropies with easy axes lying along the x , y or z axes. k_x , k_y , k_z are the anisotropy constants, with $k_x = k_y = k_z = J_{FM}$. In the case where the number of easy axes of an material are more or less than that of the other material, these easy axes are rotated by 45° (in one or two axes), hence to be bisected by the easy axes of the FM. This is due to our requirement not to be favored any particular direction because of the exchange interaction to the FM or AFM.

Finally, the \mathcal{H}_{INT} term is the interaction Hamiltonian between FM and AFM which is given by

$$\mathcal{H}_{INT} = -J_{INT} \sum_{\substack{i \in FM, \\ j \in AFM}} \mathbf{S}_i \cdot \epsilon_j \boldsymbol{\sigma}_j \quad (4.8)$$

where J_{INT} is assumed for simplicity to be equal to the absolute value of J_{AFM} . The quantities \mathbf{S}_i and $\boldsymbol{\sigma}_i$ are unit vectors which are accumulated with anisotropy and magnetic field terms. The effective magnetic field \mathbf{B} is applied at an angle of 20° from the x axis and in $x - y$ plane. This angle will be discussed further in the next chapter. The AFM dilution is simulated leaving a proportion of the lattice sites without a spin, using the variable $\epsilon_i = 0, 1$.

As before, Monte-Carlo simulation techniques are used to investigate the system implementing the heat-bath algorithm. The AFM spin trial step consists of a flip or of a random vector constrained in a sphere of radius 0.9, chosen with equal probability. The trial step for the FM spins consists of a random vector constrained in a sphere of radius 0.4.

The cooling process is performed using half a million Monte-Carlo steps from usually $k_B T = 3.4 J_{INT}$, to the desired temperature. A brief investigation of the cooling process is presented in the Appendix A. Each hysteresis loop is calculated using the same number of Monte-Carlo steps. For the investigation of the training effect, the consecutive hysteresis

loops were taken using as initial state the state of the previous loop. Every numerical calculation was performed 20 times with different initial conditions and dilution random number realizations. This allows mean value of every quantity to be taken, calculating the statistical error depicted in the error bars of the figures.

4.3.1 First simulation: Cooling process dependence

The cooling process of an exchange bias system is crucial for the stabilization of the AFM. More specifically, when the exchange coupling between the AFM and FM is positive and the sample is cooled with zero applied field the EB field is negative. When the cooling field increases, the absolute EB field increases until a maximum value and it slightly decreases, as shown in Fig. 4.8.

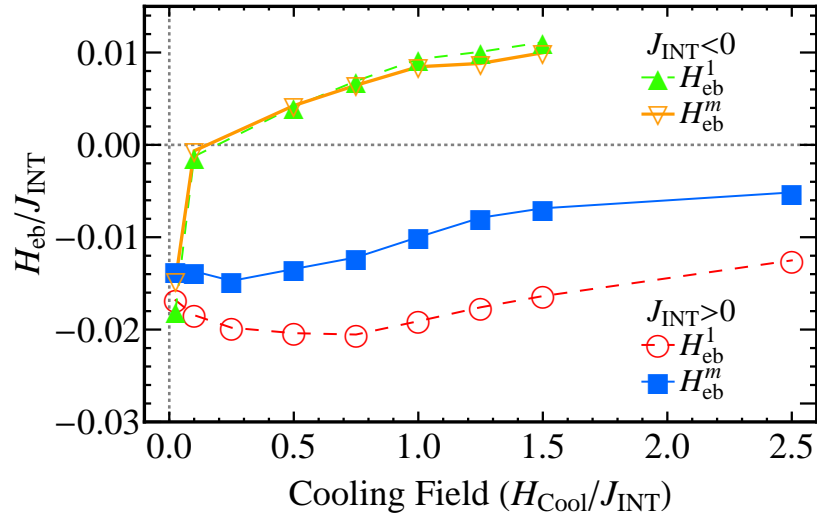


Figure 4.8: Cooling field effect on the EB field of the first and subsequent hysteresis loops for positive and negative value of the exchange interaction.

On the other hand, when the exchange coupling is negative and the cooling field increases the exchange bias field decreases and above a certain value of cooling field, the exchange bias field becomes positive. This value of cooling field, where there is no exchange bias field, it close to the exchange coupling constant, thus the two terms cancel each other and the FM is uncoupled for the AFM. Thus, positive exchange bias is exhibited in systems with negative exchange coupling, a result which agrees with experimental findings for Fe/FeF_2 and $Fe/MnFe_2$ bilayers[22]. This behavior is connected with the irreversible domain state magnetization in the AFM interface[81]. Finally, for systems with negative exchange coupling a strong training effect is exhibited while for positive coupling, there is no training effect.

Influence of the AFM and temperature on the training effect

In this chapter, we will search for the origins of the training effect developing an analysis of collective phenomena of spins and applied in a case study, based on the temperature dependence. The training effect is investigated in systems with uniaxial or biaxial AFM anisotropy and with two or five layers thickness. More specifically we will investigate the training effect in the FM discussing the fitting laws used for the cyclic variation of the EB field. Then a novel analysis is proposed for the AFM: the grouping of interfacial AFM spins in stable and unstable spins. The study of their behavior is directly connected with the training effect. Finally, the aforementioned analysis is applied to systems with different AFM dilution and thickness. Thus, a complete picture of the training effect dependence on the AFM characteristics is formed.

5.1 Training effect and fitting laws

5.1.1 Hysteresis loops

In an exchange bias system, we have the ability to measure the hysteretic magnetization of each layer. So, Fig. 5.1 shows the first and tenth hysteresis loop of the FM and the AFM interface. The parallel, the transverse and the in-plane magnetization component are drawn. Each of these pictures shows several characteristics of the system. From the parallel component of the FM magnetization, we can calculate the positive and negative coercive field and through them the exchange bias field and the coercivity. In the case of the AFM interface magnetization, from its parallel component, we can calculate the vertical shift of its hysteresis loop. This can happen using the coercive fields of the FM hysteresis loop as shown in Fig. 5.1 or taking the total time average of the AFM interface loop. These two quantities give the same effect with the difference that in case of non-standard shape of the loop, the total time average measures more precisely the vertical shift of the loop. In any case, this vertical shift of the AFM interface loop is called the domain state irreversible magnetization [81].

The transverse component shows the hysteretic magnetization along the perpendicular

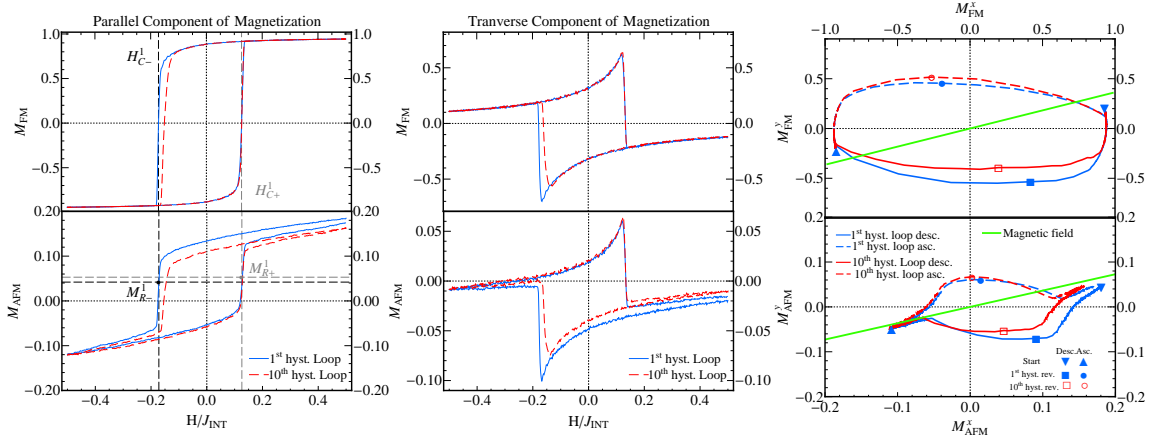


Figure 5.1: First and tenth hysteresis loop of the FM (top) and the AFM interface (bottom) of the parallel, transverse, in-plane component of magnetization. In the in-plane magnetization picture, the green line is the magnetic field axis.

axis. The in-plane component can show the symmetry of reversal during each consecutive hysteresis loop. The training effect in the parallel component appears as a movement of the left-hand branch of the hysteresis loop. The training effect in the perpendicular component is manifested as a decrease of the maximum of the left-hand magnetization during reversal.

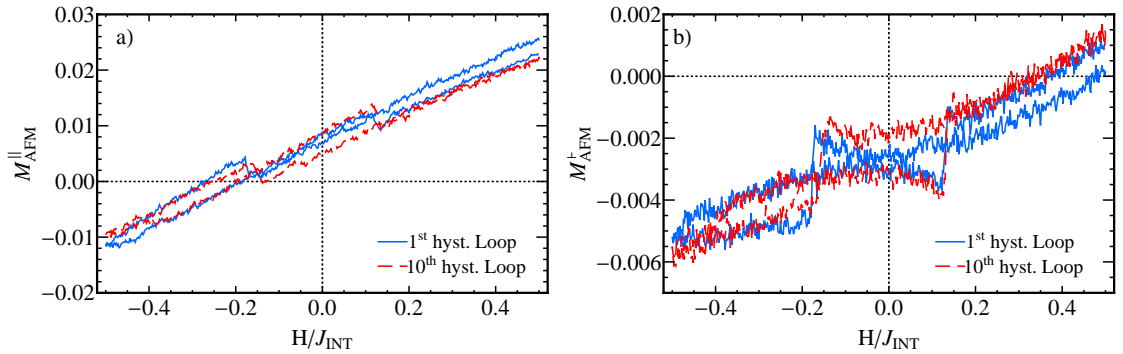


Figure 5.2: First and tenth hysteresis loop of the bulk AFM of the a) parallel and b) transverse component of magnetization.

These findings indicate a symmetrical first loop with predominantly coherent rotation as the reversal mode. This gradually changes to less symmetrical loops with (only) the left hand branch becoming less uniform. The symmetry of the hysteresis loop during reversal was investigated thoroughly by Beckmann *et al.* [96, 99] and was shown to depend on the angle between the easy axis of the AFM/FM and the magnetic field. As was shown, even the first loop can be asymmetric for certain angles. Therefore, the transition from a symmetric to an asymmetric mode is not a general effect, but it occurs for the specific angle we used in the current investigations (20°). For other angles, the asymmetry can exist from the first hysteresis loop onwards. The reason for this behavior can be found in

the change of the mean effective field acting in the FM during reversal[96]. This field has three different contributions, namely, from the exchange field of the AFM, the external magnetic field and the anisotropy FM field. The exchange field is the one which changes during training causing the mean effective field to change. For the angle we used in this chapter, during training the mean effective field becomes more aligned with the FM magnetization, leading to a smaller torque on the FM magnetization. This consequently favors less uniform reversal modes. An extensive study of the effect of the angle between magnetic field and FM easy axis on EB systems is presented in the next chapter.

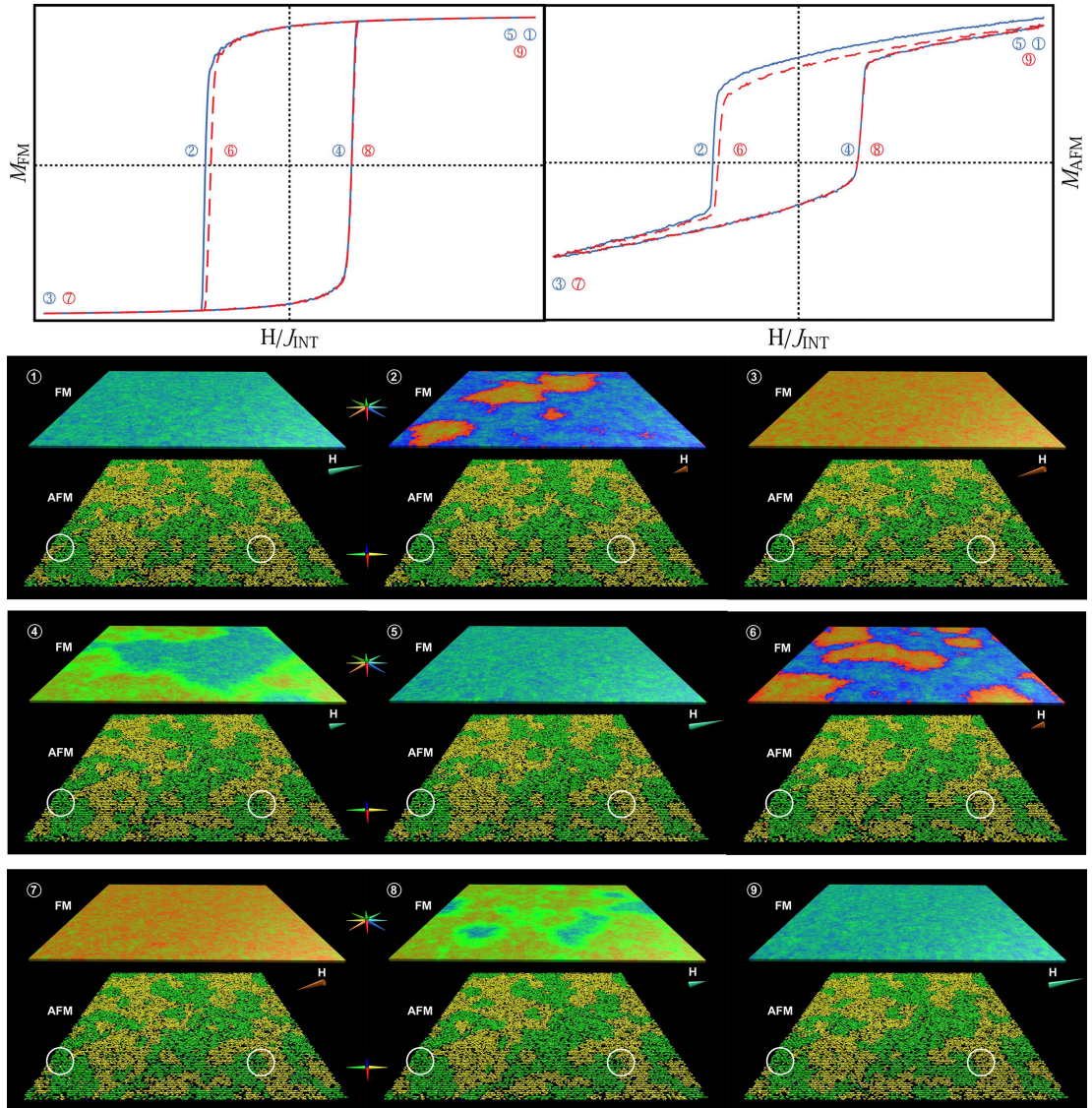


Figure 5.3: Snapshots of an EB system during the first two hysteresis loops. The number on the left of every snapshot is indicating the respective point in the hysteresis loop. The color scheme of the spins is indicated for the FM by the star (top) and for the AFM by the cross (bottom). The left circle shows a region of spins which become stable after the first reversal and the right circle shows a region of spins that are unstable during all reversals.

The hysteresis loops of the bulk AFM are drawn in Fig. 5.2. The magnetization of these layers is quite low as can be seen from the range of the hysteresis loops, although

these magnetization cycles are hardly considered hysteretic. This is because they do not interact directly with the FM but only with the interface, thus they behave like a standalone AFM.

Finally, some snapshots of the EB system during the first two hysteresis loops are drawn in Fig. 5.3. We can see that the FM is reversed through nucleation. Thus a temporary domain wall is created which is parallel to the y-axis. The smaller domain which is created inside the domain wall has magnetization parallel to the final one. The AFM is in more stable condition, where nothing seems to change during consecutive reversals. But if we focus on the right circle we will see that some spins are reversed with the magnetic field in all reversals. In the left circle we will see spins which reverse during the first reversal but remain stable during the subsequent reversals. We will discuss thoroughly these two kinds of spins in the next sections. In the analysis of the results we keep in mind that the behaviour during the first loop is qualitatively different from that of succeeding loops. Thus we consider two fitting techniques, one of which allows to quantify this difference.

5.1.2 Analysis of the training effect

The training effect as aforementioned, is a phenomenon that involves an evolution of magnetic properties during consecutive hysteresis loops. For a single set of parameters, we have a series of exchange bias field values from the consecutive hysteresis loops. As shown in Fig. 5.4, for several temperatures we have many curves of the exchange bias field or the coercivity as function of the number of hysteresis cycles. It is very difficult from this view to extract conclusions for the behavior of the training effect. Thus, for a better understanding of the training effect and for further analysis of the results, two fitting laws were applied to the data.

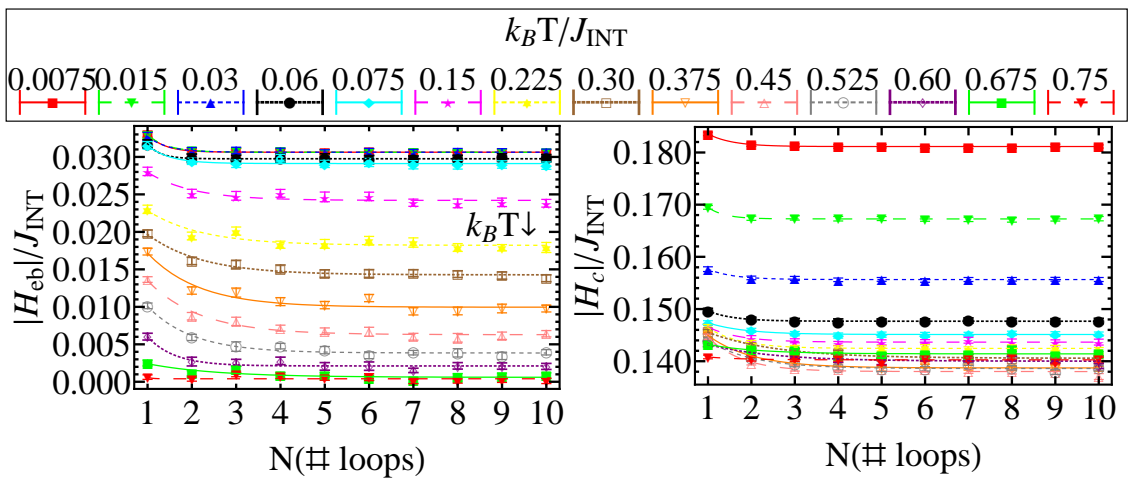


Figure 5.4: Training effect of exchange bias field (left) and coercive field (right) for several temperatures.

Firstly, the common empirical power law connecting H_{eb} and the number of consecutive loops N is given by

$$H_{\text{eb}}(N) = H_{\text{eb}}^e + k/\sqrt{N}, \quad (5.1)$$

where k is constant and H_{eb}^e is the equilibrium exchange bias, i. e. the remaining H_{eb} after an infinite number of loops. Introduced first by Paccard *et al.*[8], this law holds only for ($N > 1$) and, consequently, cannot describe necessarily the steep training effect between the first and the second loop.

A new law was deduced by Binek[130], using a relaxation model. This model came from a discretized Landau-Khalatnikov equation used for the relaxation of an AFM toward equilibrium. The resulting law is a recursive sequence which relates the $(N + 1)$ th loop with the N th one and has the form

$$H_{\text{eb}}(N + 1) = -\gamma(H_{\text{eb}}(N) - H_{\text{eb}}^{e-rs})^3 + H_{\text{eb}}(N), \quad (5.2)$$

where γ is a constant and H_{eb}^{e-rs} is the equilibrium exchange bias. With a proper rearrangement of the previous equation, it is obvious that large values of γ refer to small absolute training effects meaning that the $H_{\text{eb}}(N) - H_{\text{eb}}^{e-rs}$ is small, consequently meaning small deviations from the equilibrium EB field. Small values of γ correspond to large absolute training effect. For γ close to zero means that the system remains in a frozen state with $H_{\text{eb}}(N + 1) = H_{\text{eb}}(N)$, unable to reach the equilibrium value of EB field in finite N , due to lack of thermal excitations.

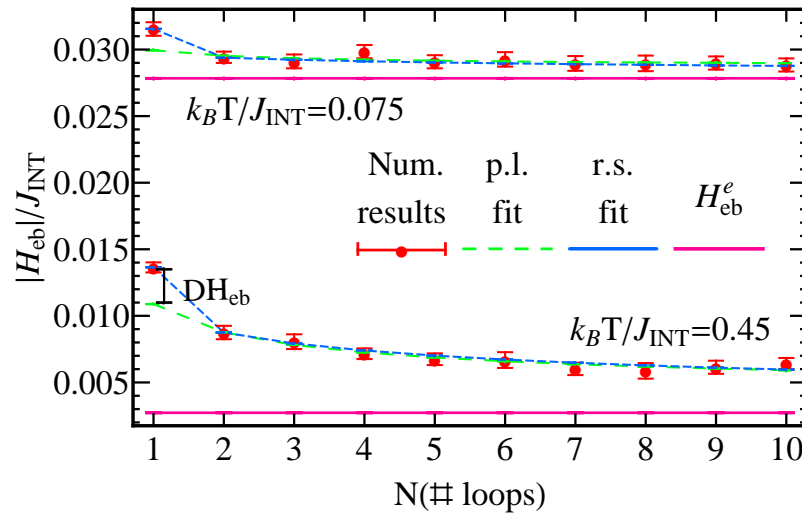


Figure 5.5: Two examples of the fitting laws for two different temperatures with depiction of equilibrium exchange bias field (purple line). The recursive sequence (r.s.) (blue line) fits the numerical results (red symbols) of the EB field of first hysteresis loop in addition to the subsequent EB fields which is only fitted using the power law (p.l.), fit (green line).

The difference between k and γ is that k corresponds to the behavior after the first loop

and γ includes it. So e.g. for two values of temperature, as shown in Fig. 5.5, we applied the two fitting laws and we draw also the equilibrium EB field. Firstly, if we use the power law for the first loop in addition to the subsequent loops, although the fitting is working very well for $N > 1$, for $N = 1$ the fitting fails. On the other hand, the recursive sequence fitting works very well for all loops. As we can see for the lowest temperature the training effect is small, and the EB field seems to remain stable after a number of consecutive hysteresis loops, meaning that is in a metastable state. In the highest temperature the training effect is large, with the EB field moving toward the equilibrium state.

Although, the recursive sequence describes quite well the training effect, it does not separate the behavior of the first loop. Therefore we additionally analyze the difference DH_{eb} of the power law as extrapolated to the first hysteresis loop and the actual simulation result for exchange bias field of the first loop, as illustrated in Fig. 5.5,

$$DH_{\text{eb}} = H_{\text{eb}}^1 - (H_{\text{eb}}^e + k). \quad (5.3)$$

In general, the power law fitting and the difference dH_{eb} will be used for the analysis of the exchange bias field during consecutive hysteresis loops. For clarity, we used the normalized quantities $\kappa = \frac{k \times 10^{-3}}{J_{\text{INT}}}$ and $\Delta H_{\text{eb}} = \frac{DH_{\text{eb}} \times 10^{-3}}{J_{\text{INT}}}$.

5.2 Athermal and thermal training effect

As shown by Hoffmann's [61] model and supported by many experimental results, the training effect can be divided into thermal and athermal effects. This distinction was introduced firstly by Fernandez-Outon *et al.* [131] and is based in the behavior of the first loop EB field. The athermal training is considered to be the large shift of the descending branch of the first loop, which persists even at very low temperatures where the thermal training, driven by thermally activated magnetization processes, ceases to exist.

The initial cooling procedure produces an AFM spin structure which may be in a metastable state; the training effect can then be considered to be the macroscopic signature of configurational rearrangement of the spin structure toward equilibrium. Despite that, because of the variety of results, coming from different EB systems and experimental techniques [4, 3], the uniqueness of the mechanism has to be questioned. These reconfigurations could be a reorientation of the AFM domains at the AFM/FM interface during field reversal or domain wall movements. Certainly, the AFM domain state of 3-D systems is metastable, giving rise to non-equilibrium phenomena, and consequently to training effects.

Some characteristic results are illustrated for three values of temperature in Fig. 5.6. Here we show the original data (not normalized) along with the power law fits and the resulting equilibrium EB field. Firstly, even if we use the power law from the first loop

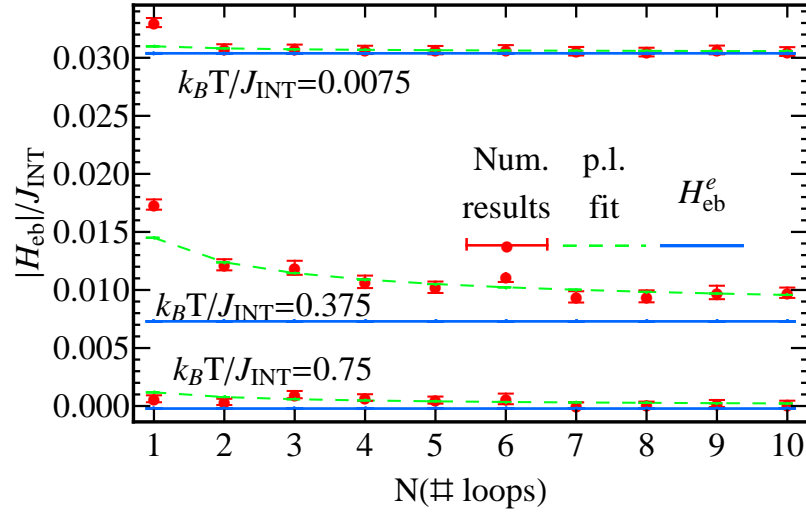


Figure 5.6: Numerical results (symbols) and power law fits (dashed lines) for three different temperatures along with the equilibrium exchange bias fields (horizontal lines).

onwards the fits only work well for $N > 1$, for $N = 1$ the fitting fails. As we can see for the lowest temperature the training effect is small, and the EB field seems to remain stable after only a small number of consecutive hysteresis loops. The first hysteresis loop deviates from the power law, a characteristic of athermal training. For higher temperatures the training effect is large, with the EB field decaying toward a much lower equilibrium value, but again with a bigger difference between first loop and the power law fit. Thus, this characteristic of the athermal training, remains also in the thermal training regime. Finally, for temperatures close to the blocking temperature the training effect is small with the difference between first loop and power law also small, a characteristic of low or zero training effect.

5.3 Temperature dependence: Behaviour of the ferromagnet

The atomistic model presented earlier has been applied to calculations of systems with uniaxial and biaxial anisotropy for the AFM as well as different AFM thicknesses. For the case of biaxial anisotropy, the easy axes are rotated by 45° , hence are bisected by the easy axis of the FM, as shown in Fig. 5.7. This is due to our requirement not to favor any particular direction because of the interface exchange interaction with the FM. The Néel temperatures were calculated for each individual system separately, using a heating process from almost zero temperature of the long-range ordered AFM state[128]. The inflection point of the staggered magnetization was then calculated as a function of temperature, estimating the Néel temperature for the uniaxial system to be $k_B T_N = 0.93 J_{INT}$ and $1.14 J_{INT}$, and for the biaxial system $k_B T_N = 0.60 J_{INT}$ and $0.81 J_{INT}$ for 2 and 5 layers

AFM thickness, respectively. Each hysteresis loop is calculated using the same number of Monte-Carlo steps. For the investigation of the training effect, consecutive hysteresis loops were calculated using each time the state of the previous loop as initial state. Also, we calculated statistical averages of the EB field and other quantities over 20 different realizations of random number sequences. The main effect of this for the simulations is the different realizations of defect distributions in the AFM.

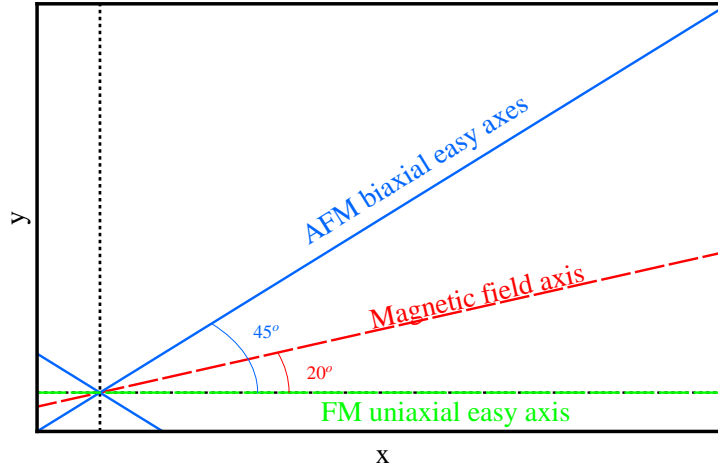


Figure 5.7: Easy axes of an exchange bias system with biaxial AFM anisotropy.

5.3.1 Hysteresis loop of parallel and transverse component

A typical hysteresis loop calculated solely from the FM part of the system is shown in Fig. 5.1. The exchange bias field (H_{eb}) and the coercivity (H_c) were calculated for different temperatures for every configuration. We investigated four different system configurations, two with uniaxial AFM anisotropy and two with a biaxial anisotropy, both with two and five AFM layers. The dependence of H_{eb} , H_c on the number of consecutive hysteresis loop cycles are presented in Fig. 5.8 for different temperatures and AFM thicknesses for the case of uniaxial AFM anisotropy. The error bars indicate the statistical error due to averaging over a set of 20 different realizations of the defect distribution in the AFM.

It is clear, that for all kind of parameters the largest decrease of EB field takes place between the first and second hysteresis loops. The training effect becomes weaker for the subsequent hysteresis loops. The coercivity shows a qualitatively similar training effect as observed for the EB field. For temperatures as low as only 1% of the Néel temperature ($0.0075J_{\text{int}}$) H_{eb} is reduced by about 10-15% and H_c by about 1-2% after ten loops when compared with its initial value. This is in good agreement with experimental findings for epitaxial *NiFe/FeMn* EB bilayers [34] where for a temperature of 5K a corresponding decrease of H_{eb} of about 30-35% was found and 2-4% for H_c . This suggests that there is a domain state in the bilayer which may arise from the interface roughness or non-magnetic defects in the epitaxial film.

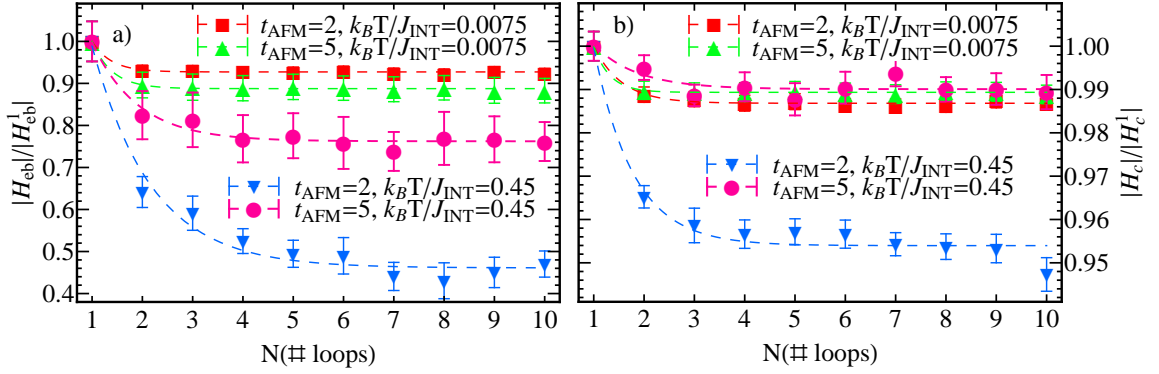


Figure 5.8: Training effect of a) the exchange bias field and b) the coercivity for different temperatures and AFM thicknesses. AFM with uniaxial anisotropy. The values are normalized to the value of the first hysteresis loop.

5.3.2 Exchange bias field

Our results for the temperature dependence of the training effect for the four aforementioned systems are shown in Fig. 5.9. The results for the first and second loop are shown as well as the equilibrium value obtained via the power law fit. The fitting parameters κ and the difference ΔH_{eb} are drawn in the upper graphs. The range of temperatures used is according to the system blocking temperature, which is defined as the temperature where the exchange bias field becomes zero. Due to the rescaling of the temperature range with respect to the Néel temperature of each system, the real temperature range is different for each of the systems.

For the case of AFM uniaxial anisotropy with low AFM thickness (Fig. 5.9a), the strength of the training effect has a maximum for intermediate temperatures ($T/T_N \approx 0.4$). This is because at very low temperatures, the system is easily frozen in metastable states leading to a higher equilibrium EB field due to lack of thermal excitation. By intermediate temperatures we mean temperatures in the center between zero and the blocking temperature of the system, i. e. the temperature where the EB field becomes zero. On the other hand for the highest temperatures the EB fields are rather small and drop quickly to the equilibrium value which is equal to zero. In between is the temperature range with the highest training effect. This behavior is also apparent from the graph of the fitting parameter κ which shows a maximum at $T/T_N = 0.4$ while the difference ΔH_{eb} remains constant for not too high temperatures. Only for the highest temperatures close to the blocking temperature, ΔH_{eb} decreases steeply. For the thicker AFM (Fig. 5.9b), the strength of the training effect follows the same trend but with the maximum of the training effect shifted towards higher temperatures. The main difference is that the additional AFM layers offer more stability to the system as well as to the created domains so that the training effect is smaller.

The EB systems with biaxial anisotropy of the AFM (Fig. 5.9c) and d) show some

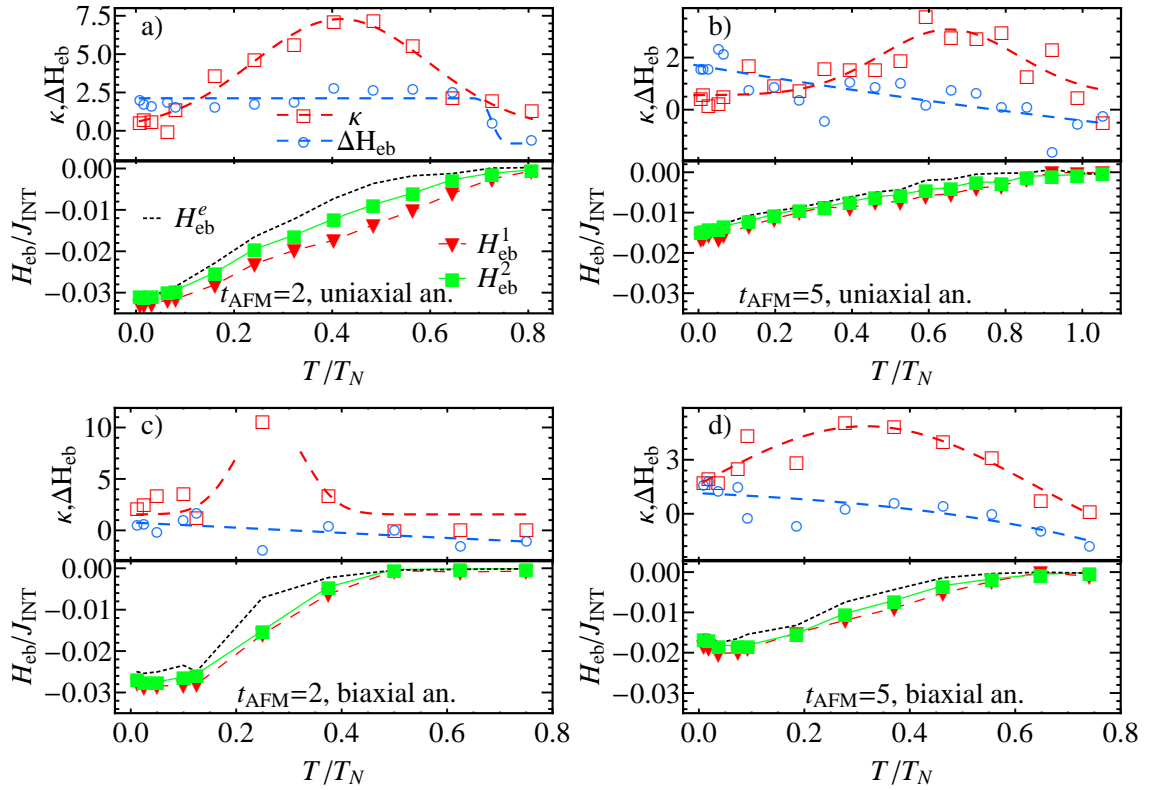


Figure 5.9: Temperature dependence of the training effect for systems with a) uniaxial AFM anisotropy and $t_{\text{AFM}} = 2$, b) uniaxial AFM anisotropy and $t_{\text{AFM}} = 5$, c) biaxial AFM anisotropy and $t_{\text{AFM}} = 2$ and d) biaxial AFM anisotropy and $t_{\text{AFM}} = 5$. The temperature axis is scaled to the Néel temperature of every system. H_{eb}^1 and H_{eb}^2 : EB field of the first and the second hysteresis loop, respectively. H_{eb}^e : Equilibrium EB field following the power law fit. Upper graphs: Temperature dependence of the normalized fitting law parameter κ and ΔH_{eb} obtained as explained in the text.

significant differences in comparison to the uniaxial systems. Firstly, the EB effect appears only for lower temperatures. The resulting lower blocking temperature results from a lower energy barrier for reversal of AFM domains. As in the uniaxial case, the blocking temperature is also affected by the thickness of the AFM. For higher AFM thickness the blocking temperature increases, once again a result of the enhanced stability of the system due to the increased AFM thickness. Secondly, for the case of biaxial AFM anisotropy, the training effect shows a different dependence on temperature. This can be clearly seen from the graphs of the fitting parameters. The power law parameter κ shows a maximum at $T/T_N = 0.3$ meaning that the training effect after the second loop is high. The difference ΔH_{eb} has a monotonic decrease. In total, the difference between these two curves is in the low temperature range, where we see large training effect for the first to the second loop but much smaller for the subsequent loops. Similar effects exist for both of the thicknesses of the AFM, but as previously, the EB persists at higher temperatures for the thicker AFM.

The behavior of the training effect can be compared with the experimental trend mea-

sured by Khapikov [32] for a granular $NiO/Ni_{81}Fe_{19}$ bilayer. If we consider that the blocking temperature of that system is around $250K^o$, then the lower limit of temperature range that is used is around $T/T_N = 0.16$ in terms of our temperatures units for the system with the uniaxial anisotropy and thickness equal to 2 layers. Thus, for this range, the temperature dependence is the same and the relative decrease of the EB field due to training is in very good agreement (both 30% for $T/T_N = 0.16$).

In general, the behavior of EB field (where training exist), independently of the AFM thickness and anisotropy, can be separated in two regions according to the temperature:

1. Athermal training. This is the region with low κ and high ΔH_{eb} , usually in the low temperature regime. As shown in Fig. 5.9 for $k_B T/J_{INT} = 0.0075$, the EB field of the first loop is significantly higher than the EB field of the subsequent loops. After the second loop the EB field remains constant.
2. Thermal training. This is the region with high κ and high ΔH_{eb} , usually in the higher temperatures regime, but not very close to blocking temperature. As shown in Fig. 5.6 for $k_B T/J_{INT} = 0.375$, the EB field of the first loop is still much higher than those of the subsequent loops. But here, after the second loop the EB field is continuously decreasing with high parameter κ .

These two kinds of training effect are connected with the behavior of the AFM. Particularly, with the increase of the stability of the AFM interface and the decrease of its magnetization. Our preliminary analysis suggests that the effect depends on the stability of the FM/AFM interface structure. More specifically, the interfacial spins of the AFM showed different behavior during cycling. The largest portion was frozen towards the easy axes of the AFM anisotropy creating domains and a smaller portion, which is in the domain walls, rotates with the external field causing domain wall motion. The training effect is connected with the behavior of these spins which become frozen in a specific direction and consequently increasing the surface of the domains. This analysis is discussed thoroughly in the next sections.

A similar analysis was made by Radu *et al.* [132], where they showed that the training effect is connected with both interfacial and bulk spins which move towards equilibrium with different rate. Also, Roy *et al.*[133] and Fitzsimmons *et al.*[134] analyzed the pinned and unpinned spins not only on the interface but also in the bulk, characterising them as compensated and uncompensated. They proposed a model using the results of their analysis which is consistent with our model and results. Finally, Morales *et al.* [135] using a trilayer to eliminate the AFM/FM interlayer exchange coupling, showed that EB is not a purely interfacial effect and the bulk AFM spins are important for the pinning of the interfacial spins.

5.3.3 Coercive fields

Because of the possible asymmetry of the hysteresis loops we also investigated the coercive fields of every cycle. The positive and the negative coercive field ¹ of the first and second hysteresis loop are shown in Fig. 5.10 for each of the aforementioned systems. For simplicity the absolute value of the negative coercive field is used. When the curves of the positive and negative field coincide, the EB field vanishes.

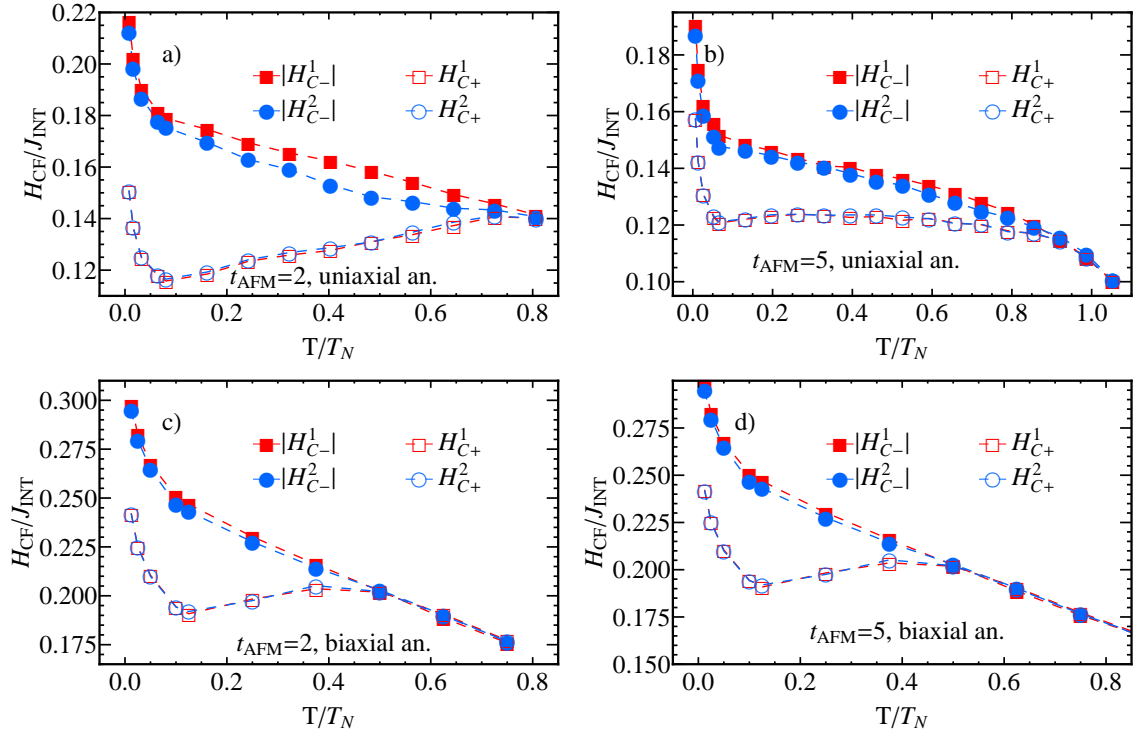


Figure 5.10: Temperature dependence of the training effect of the coercive fields for systems with a) uniaxial AFM anisotropy and $t_{\text{AFM}} = 2$, b) uniaxial AFM anisotropy and $t_{\text{AFM}} = 5$, c) biaxial AFM anisotropy and $t_{\text{AFM}} = 2$ and d) biaxial AFM anisotropy and $t_{\text{AFM}} = 5$. H_{C+}^1 and H_{C+}^2 : Positive coercive field of the first and the second hysteresis loop, respectively. Similarly for the absolute value of the negative coercive field. The temperature axis is scaled to the Néel temperature of every system and as previously, the temperature range was adjusted according to the system blocking temperature (similar to Fig. 5.9).

Firstly, for all cases we can conclude that the training effect occurs predominantly in the negative coercive fields since there is hardly any difference in the subsequent curves for the positive coercive fields. This means also that one finds a decrease of coercivity during cycling over several loops. This is caused because during the initial cooling procedure an

¹Negative coercive field is that occurs during the descending branch of the loop and the positive coercive field is that occurs during the ascending branch of the loop. Although, they usually occur in the negative and positive side of x-axis, respectively, many times occur in one only side. That's why many times are referred as first and second coercive field, respectively

AFM domain state is formed with a spin structure optimized for the positive field and FM magnetization direction. Obviously, this domain structure is less stable when field and FM are reversed. Hence, more changes in the domain structure may occur on the opposite side of the loop as compared to the initial side where this structure is stable. Also, although non-monotonically, the negative coercive field always decreases with increasing temperature. On the other hand, the positive coercive field has regional extrema. For the case of uniaxial AFM anisotropy, the positive coercive field has a minimum at rather low temperatures, $T/T_N = 0.08$.

The asymmetry in the hysteresis loop is suggested to be an effect of increasing population of the stable AFM spins. More specifically, the irreversible magnetization of the AFM interface decreases. This is caused by the increase of the stable spin population which results in a decrease of their net magnetization, during consecutive field cycling. Thus the unstable spin population in the AFM, which is responsible for the coercivity, reduces; causing the aforementioned behavior of coercivity. For lower temperatures, the behavior of the coercive field changes rapidly. Experimentally [136] it was shown that the origin of the striking difference between the first magnetization reversal and all subsequent reversals is an effect of a metastable single domain state destroyed during the first reversal and transformed into a stable multidomain state.

5.4 Temperature dependence: Behavior of the antiferromagnet

Now using the same model we examine the behavior of the AFM. The AFM magnetization is usually zero macroscopically due to the balance of the magnetic moments in all spin sublattices. It is generally accepted that when the AFM spins on the interface are compensated, then a break of this symmetry is required to explain EB. As described by Scholl *et al.* [37], the breaking of this symmetry can be associated with interface roughness[27], magnetic domain[82], defect[90], grain structure[101] or combinations of these four. Thus, a clear view of the FM/AFM interface is needed for a clear microscopic description of the EB. Recent experimental methods [137, 138] using x-ray resonant magnetic scattering, have made possible direct observations of the AFM/FM interface allowing study of the behavior of the interface spins, in particular their stability against reversal. Studies of the training effect showed that it is related to the direction of the frozen AFM spins [139] although neutron reflectivity experiments[136, 13] in the FM showed transition from a single-domain state, for the first cycle, to a multi-domain state, for the subsequent cycles.

The spin structure of the AFM/FM interface after the initial cooling procedure is known to differ from its equilibrium state. The training effect is considered to be the macroscopic

signature of configurational rearrangement of the spin structure toward equilibrium. These reconfigurations could be a reorientation of the AFM domains at the AFM/FM interface during field reversal or domain wall movements. Thus, in this section we analyze the population of the pinned spins of the AFM interface as well as their magnetization, concluding that these reconfigurations are domain wall movements.

5.4.1 Irreversible magnetization of AFM interface

As shown in Fig. 5.1, the magnetization of the AFM interface shows hysteresis, following the coupling to the FM and its vertical shift acts as an additional effective field on the FM, resulting in the EB. Another important characteristic of this loop is the change of magnetization before reversal. E.g. for the descending branch of the loop, the magnetization from the initial state up to the point before the reversal sets in. This is in contrast to the hysteresis loop of the FM in which the magnetization remains almost constant. This is due to the frustrated spins of the AFM interface. This is studied further in the next section for lower temperatures.

This vertical shift of the magnetization of the AFM interface as aforementioned is called the irreversible domain state magnetization M_{irr} [81]. In this study we will use the total time average of the hysteresis loop for the calculation of this shift.

Our results for the temperature dependence of the training effect for the four aforementioned systems are shown in Fig. 5.11. For the detailed qualitative comparison of this quantity, the simulation results for the first and second loop are shown for the EB field and AFM irreversible magnetization. The range of temperatures used is limited by the maximum blocking temperature of each system, which is defined as the temperature where the exchange bias field becomes zero. Due to the rescaling of the temperature range with respect to the Néel temperature of each system, the real temperature range is different for each of the systems.

When the AFM has uniaxial anisotropy, the irreversible domain state magnetization of the AFM has the same qualitative trend as the EB field. The quantities are different by a multiplying factor of around 0.6, which is the concentration of the spins in the AFM. This can be explained by the usual estimate[81] of EB field $l\mu H_{eb} = J_{INT}(0.6 \cdot M_{irr})$ where l is the thickness of the FM, giving $H_{EB}/J_{INT} = 0.6 \cdot M_{irr}$. Although, this formula establishes a good connection between the two quantities (H_{eb}, M_{irr}), we see that there is a significant difference in the values for some of the temperatures. This discrepancy can be corrected if we consider the improved formula, established by Scolten *et al.* [97]. Thus the aforementioned estimate becomes :

$$H_{eb}/J_{INT} = \frac{0.6 \cdot M_{irr}}{1 + J_{INT}\chi_{AFM}^{(2)}} < 0.6 \cdot M_{irr}, \quad (5.4)$$

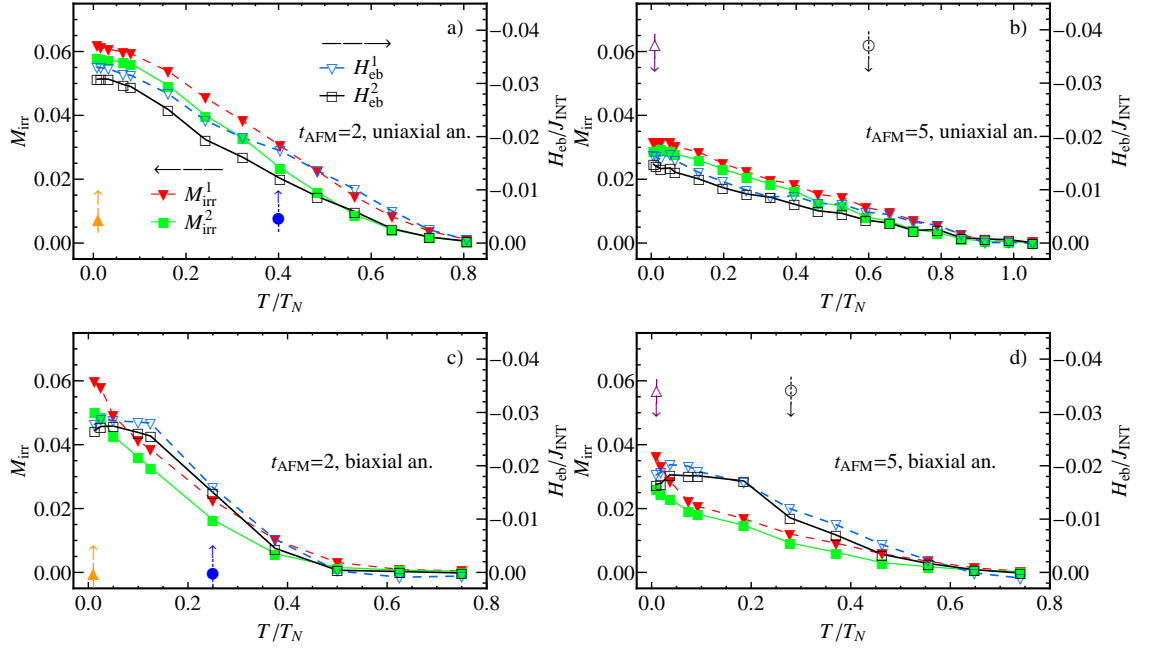


Figure 5.11: Temperature dependence of the training effect for systems with a) uniaxial AFM anisotropy and $t_{\text{AFM}} = 2$, b) uniaxial AFM anisotropy and $t_{\text{AFM}} = 5$, c) biaxial AFM anisotropy and $t_{\text{AFM}} = 2$ and d) biaxial AFM anisotropy and $t_{\text{AFM}} = 5$. The temperature axis is scaled to the Néel temperature of every system. H_{eb}^1 and H_{eb}^2 : EB field of the first and the second hysteresis loop, respectively. M_{irr}^1 and M_{irr}^2 : Irreversible domain state magnetization of the AFM interface of the first and the second hysteresis loop, respectively. The colored arrows and markers show the temperatures that are going to be used in the Fig.5.14, in which the athermal (lower temperature) and the thermal (higher temperature) training effect are exhibited in each system.

where $\chi_{\text{AFM}}^{(2)}$ is the second approximation for AFM susceptibility considering dilution into the AFM. This value will be always positive and temperature dependent. Thus, the denominator of Eq. 5.4 is larger than one ($J_{\text{INT}} = 0.5J_{\text{FM}}$) and consequently the resulting values for the EB field will be smaller than given by the previous formula.

The training effect of the EB field, in low and high temperatures is small, but high at intermediate temperatures. The same trend is followed by the irreversible domain state magnetization. For low AFM thickness, there is small difference between the EB field and irreversible domain state magnetization of the second hysteresis loop in intermediate temperatures which is due to thermal fluctuations.

Although the trend is the same for the case of biaxial AFM anisotropy, the EB field and the irreversible domain state magnetization have small difference in the first half of the temperature range. This difference is because the aforementioned formula is derived for systems with uniaxial AFM anisotropy. The derivation of a similar formula for systems with biaxial AFM anisotropy is very difficult due to the larger complexity of the energy terms compared to the uniaxial case.

5.4.2 Spin and Domain types

A domain state is formed in the AFM during the cooling process. This domain state consists of domains and domain walls that penetrate the AFM layer. Some typical AFM interface spin configurations before and after the first and second reversal are shown in Fig. 5.12 for the case of uniaxial (top) and biaxial (bottom) AFM anisotropy. For the uniaxial AFM anisotropy, we see domains with staggered magnetization parallel or antiparallel to the easy direction (x -axis). For the biaxial AFM anisotropy, we see domains oriented in orthogonal directions: each domain lying along one of the easy axes of the biaxial anisotropy. Each domain can have its staggered magnetization parallel or antiparallel to the easy direction.

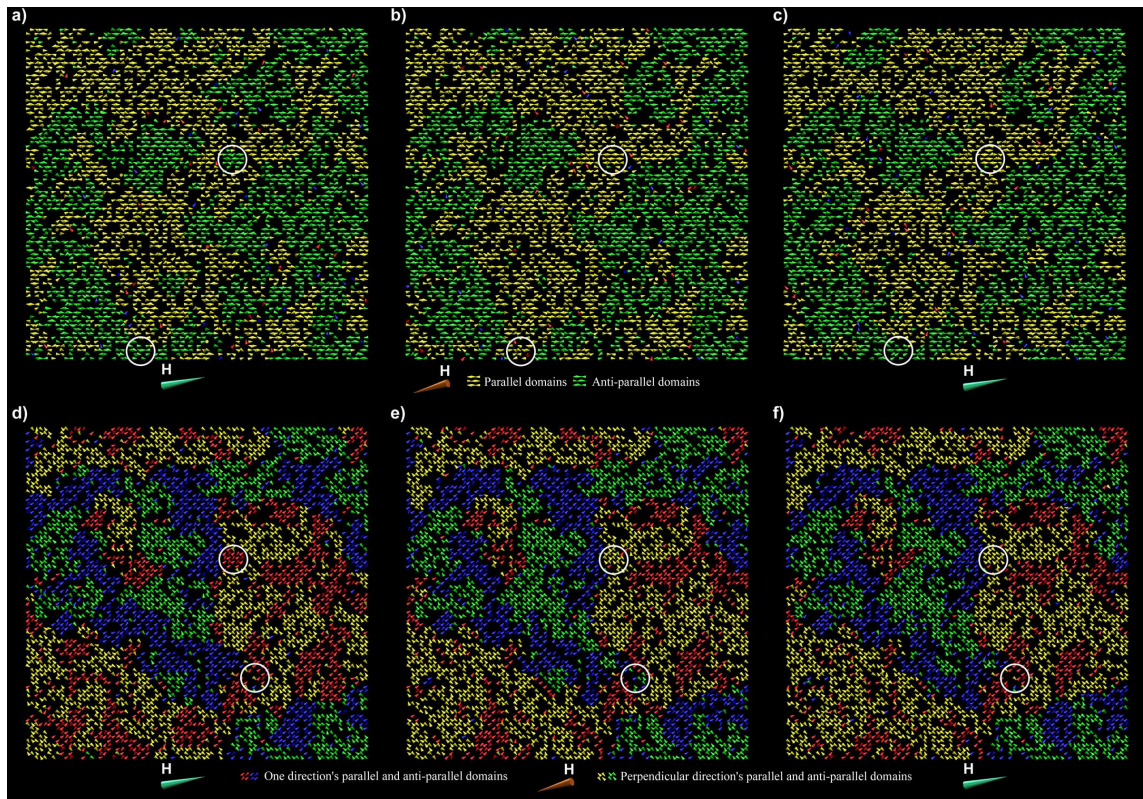


Figure 5.12: AFM interfacial spin configuration snapshots of an uniaxial (top) and a biaxial (bottom) AFM in an EB system. The snapshots are before the first reversal (a,d)), after the first reversal (b,e)) and after the second reversal (c, f)). The colors are for separating the different AFM domains. For the uniaxial AFM (top), the green and the yellow separates domains pointing in the x direction. For the biaxial FM (bottom) the green and the yellow separates domains pointing in the direction of first and third quadrant while blue and red separates domains pointing in the direction of second and fourth quadrant. The top circles show spins that become stable and the bottom circles show spins that are unstable i.e. they change direction after each reversal.

As shown in Fig. 5.12 in the bottom circles, there are unstable spins, which are those which change their state during the hysteresis cycle. These spins can be divided into two categories. In the first category are spins which reverse only when the FM reverses, i.e. they are strongly coupled to the FM and respond to the changes in the exchange field from

the FM. In the second category we place spins which are able to follow the external field. These spins are predominantly responsible for the magnetization decrease in the AFM layer between positive saturation and reversal of the FM. These are spins which have zero or small exchange coupling to neighboring spins, which arises due to geometric frustration. Thus, we refer to these spins as frustrated. We note that this is a different definition to that used in [132], but it will be used here consistently. Furthermore, the unstable spins are mostly located at the edge of the domains, e.g. at the domain walls. Thus, their reversal moves the domain walls making it likely that these spins are responsible for the training effect.

Finally, there are spins in the case of the biaxial AFM anisotropy that do not reverse completely, but change from one easy direction to the perpendicular easy direction during a field reversal. These spins will be also considered as “unstable” ones for the following analysis.

5.4.3 Analysis of stable spins

There are many ways of measuring the stability of a single spin. Misra *et al.* [92] suggested to look at the time average of the x-component during a complete reversal. This average will be close to the initial value for stable spins and close to zero for spins rotating with the magnetic field. The problem with this quantification of the stability is its generalization to more than one dimensions. Thus, in the current investigation, we examine the state of each spin before and after each magnetization reversal and calculate the angle between them. Next is to invent a criterion based in a cut-off angle which will separate the stable from the unstable spins.

In Fig. 5.13 is shown the distribution of reversal angles of the first reversal for several temperature and systems. The criterion which we will use is based on using as a cut-off angle, the angle that separates the two main peaks of the distribution of the reversal angles. This, of course, will work better when the peaks are quite high. As shown in Fig. 5.13, this happen at 90° for the case of the uniaxial anisotropy and at 45° for the case of the biaxial anisotropy. Thus, in general the cut-off angle is close to the initial angle, energy barrier. As we can see, this criterion is working well for temperatures in the range of athermal (i.e. uniaxial $T/T_N = 0.008$) and thermal (i.e. uniaxial $T/T_N = 0.403$) training but for high temperatures (i.e. biaxial $T/T_N = 0.625$) the two peaks in the distribution are very low and are comparable to the midrange reversal angles. Thus in high temperatures the criterion is not working very well but at these temperatures there is no EB and consequently this range is of no interest.

Focusing now on temperatures of athermal and thermal training (the two lowest values of temperature in Fig. 5.13) there is a significant difference between EB systems with

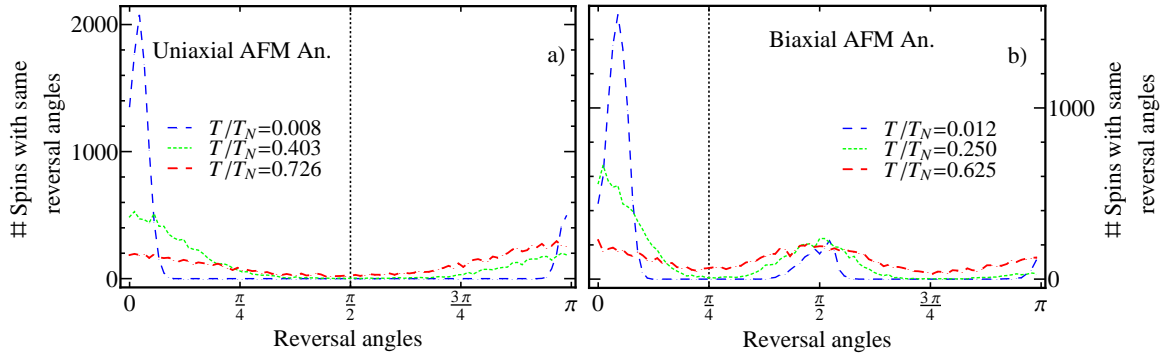


Figure 5.13: Distributions of reversal angles of the first reversal for systems with a) uniaxial AFM anisotropy and b) biaxial AFM anisotropy for several temperatures and 2 AFM layers. The lines show the cut-off angle between the stable and unstable spins.

uniaxial and biaxial AFM anisotropy. In systems with uniaxial AFM anisotropy, there are spins that fully reverse (180°) during field cycling and are considered unstable (unfrozen) spins while spins that are not reversed (0°) are considered stable (frozen) spins. Now, in systems with biaxial AFM anisotropy, we observe three peaks in the distribution of reversal angles, with two of them being quite high. These two main peaks represent the reversal angles of the majority of the spins. Thus, again at 0° are the stable spins and at 90° and 180° are the unstable spin. Comparing the number of the spins reversed by 90° to the number reversed by 180° (almost zero) it can be concluded that in systems with biaxial AFM anisotropy, the AFM interface hysteresis loop is created not by full reversals but by 90° reversal i.e. by aligning with the closest perpendicular easy axes.

We calculate then the percentage of the stable spins in the bulk and in the interface of the AFM, as shown in Fig. 5.14a) and b), using one temperature for athermal and one for thermal training, as shown in Fig. 5.11. We consider bulk AFM, all the layers of the AFM except the interfacial one. In the bulk of the AFM all the spins were found to be stable and to remain stable during the hysteresis cycling, for low temperatures. For higher temperatures, there are more unstable spins in the bulk which population does not change during hysteresis cycling. In both of the cases, the magnetization of the stable spins was definite and constant during the consecutive hysteresis loops, as can be seen in Fig. 5.15a) and b). This behavior is consistent with the description of the bulk AFM which is given in many publications [133, 134, 132].

A special focus is given to the spin behavior in the interface of the AFM. As we see from Fig. 5.14c) for the uniaxial case, in general the system with thicker AFM has more stable spins compared to the thinner AFM at the same temperature. This is because the additional layer in the AFM, it is known to offer more stability to the interface and the system. So more interfacial spins are pinned. Both systems, with different AFM thickness, follow the same trend in the concentration of the stable interfacial spin as a function of

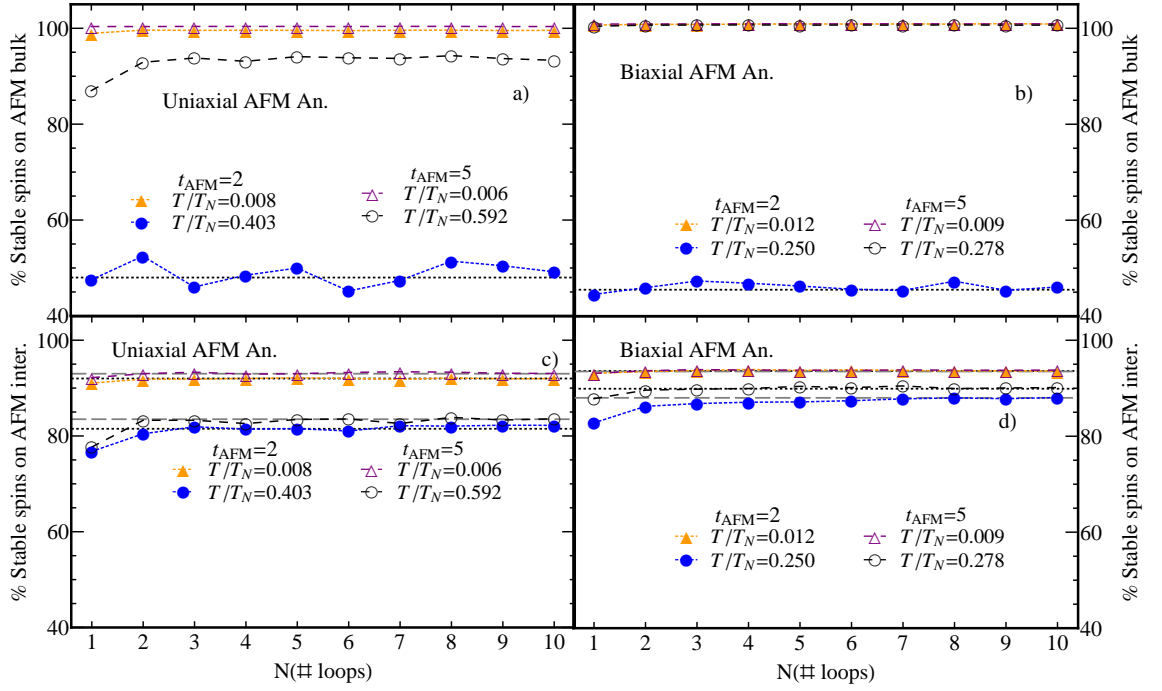


Figure 5.14: Training effect of the concentration of the stable spins in the AFM bulk (top) and interface (bottom) for a),c) uniaxial anisotropy and b),d) biaxial anisotropy for several temperatures and AFM thicknesses.

temperature and number of consecutive loops. The concentration of the stable interfacial spins increases with decreasing temperature, due to lack of thermal excitations. This is causing the increase of EB field with decreasing temperature. Similar effects are observed for the biaxial AFM anisotropy, as shown Fig. 5.14d).

The concentration of the stable interfacial spins increases steeply from the first to the second hysteresis cycle. This is a result of the cooling process, after which many spins achieve a metastable state. During the first loop these spins make irreversible transitions into new, more stable states, exhibiting at most very small changes over subsequent cycles. After the second hysteresis loop the concentration of the stable AFM interfacial spins remains constant.

Thus, the concentration of the stable interfacial spins increases with increasing consecutive hysteresis loops. This trend is in contrast to the variation with temperature. Specifically, the increase of the stability at low temperatures increases the EB field. However, the increase in the number of stable spins with hysteresis cycle leads to a decrease in the EB field. This apparent contradiction arises from fact that it is possible that the more stable state is more compensated, thus leading to smaller EB field. As a result we cannot characterize the EB field with the concentration of stable spins alone. Thus, we need to investigate the magnetization of these spins.

Fig. 5.15c) and d) shows the magnetization ($M_{S.I.S.}$) of the stable AFM interfacial

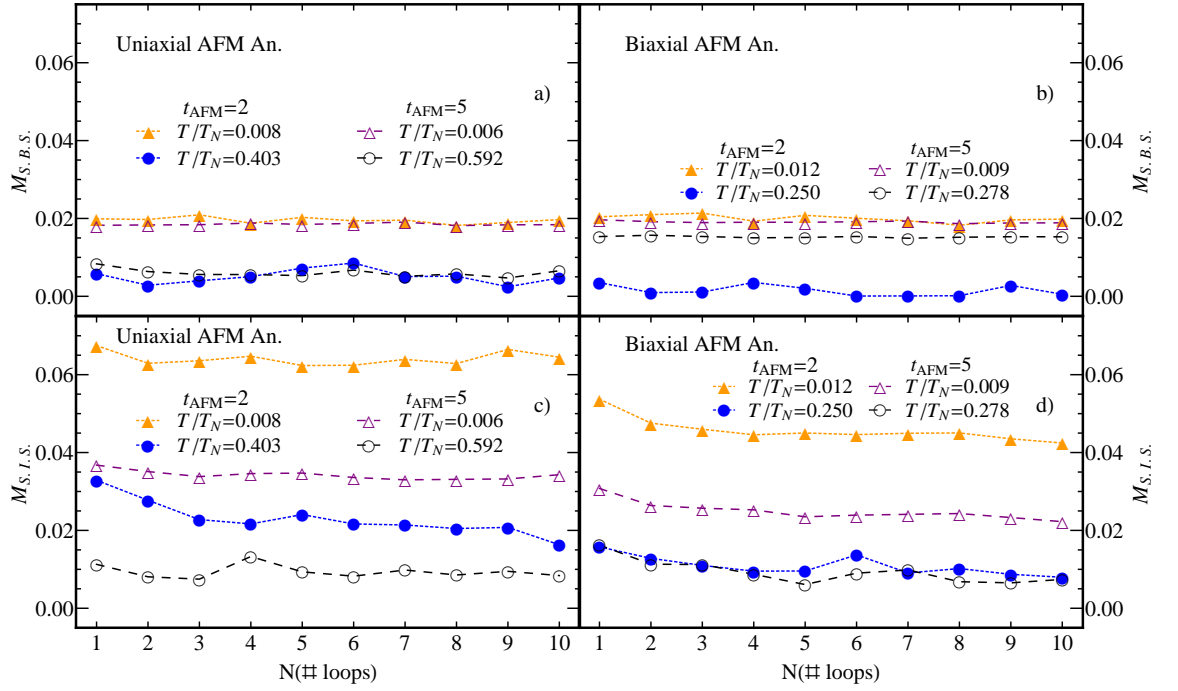


Figure 5.15: Training effect of the magnetization of the stable spins in the AFM bulk ($M_{S,B.S.}$) (top) and interface ($M_{S,I.S.}$) (bottom) for a), c) uniaxial anisotropy and b), d) biaxial anisotropy for several temperatures and AFM thicknesses.

spins as a function of the number of consecutive loops for the aforementioned systems and temperatures. In all of the cases, the magnetization decreases with increasing number of consecutive hysteresis loops. This decrease explains the decrease of the irreversible domain state magnetization of the AFM interface and consequently the decrease of the EB field, e.g. the training effect. Also, the dependence of the magnetization of the stable AFM interfacial spins on the temperature is consistent with the temperature trend of EB field. Systems with thicker AFM exhibit smaller magnetization of the stable AFM interfacial spins due to different domain structures favored by the additional thickness.

For the athermal training, in all cases, the $M_{S,I.S.}$ magnetization decreases steeply from the first to the second consecutive hysteresis loop, and after that it remains roughly constant. This behavior explains the decrease of the irreversible domain state magnetization of the AFM interface and consequently the decrease of the EB field, e.g. the athermal training effect. Also, it shows that the spins that become stabilized after the first reversal, were pointing to the positive magnetization axis and also to the cooling field direction. Thus, during the first reversal, they flip and stabilize to the negative magnetization axis causing a decrease in the total magnetization $M_{S,I.S.}$. Furthermore, systems with thicker AFM exhibit a smaller magnetization due to different domain structures favored by the additional thickness. Furthermore, we can see that the bulk has a constant magnetization during training with almost the same value for different AFM thicknesses, while the $M_{S,I.S.}$

has much bigger values which change during training and for different AFM thicknesses.

For the thermal training, the $M_{S.I.S.}$ magnetization decreases steeply from the first to the second consecutive hysteresis loop, but after that it continues to decrease less steeply. The first decrease of the $M_{S.I.S.}$ magnetization is explained as in the previous case. But now after the second hysteresis cycle, we have a continuous decrease of the $M_{S.I.S.}$ magnetization although the number of the stable spins remains constant. This is due to the fact that the stabilized spins are not fully aligned in their corresponding easy direction. It means that due to the thermal fluctuations the spins are rotated by a small angle from the easy direction but not far to be considered unstable spins. This small angle reduces during the consecutive hysteresis loop, aligning further these spins to the negative magnetization axis, causing the reduction of the $M_{S.I.S.}$ magnetization. Furthermore, we can see that the bulk has a zero magnetization during training while the $M_{S.I.S.}$ has much bigger values which change during training and for different AFM thicknesses.

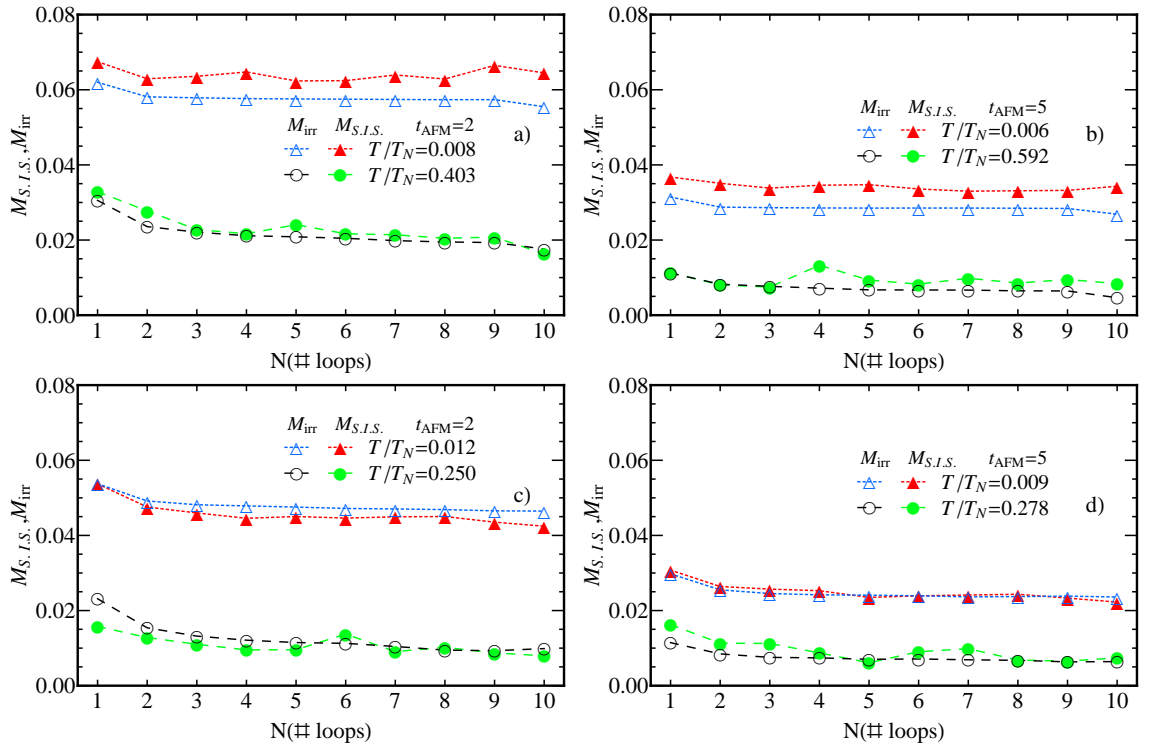


Figure 5.16: Comparison of the magnetization of the stable interfacial spins ($M_{S.I.S.}$) and of irreversible domain state magnetization (M_{irr}) for systems with a) uniaxial AFM anisotropy and $t_{AFM} = 2$, b) uniaxial AFM anisotropy and $t_{AFM} = 5$, c) biaxial AFM anisotropy and $t_{AFM} = 2$ and d) biaxial AFM anisotropy and $t_{AFM} = 5$.

Finally, we show the irreversible domain state magnetization M_{irr} as a function of the stable interfacial spins magnetization $M_{S.I.S.}$ for comparison in Fig. 5.16. It is clear that these two magnetizations are connected because, in addition to the fact that they follow the same trend, the values of $M_{S.I.S.}$ magnetization are quite close or inside the error range of the values of M_{irr} magnetization. Thus, this is a clear proof that the M_{irr} magnetization

and consequently the EB shift is a result of the magnetization of the stable spins.

In summary, the training effect of EB field is caused by the increase of stability of the AFM interface which leads to the decrease of the magnetization of stable interfacial spins. On the other hand, the EB field increase due to temperature decrease caused by the same phenomenon when it leads to the increase of the magnetization of stable interfacial spins.

5.4.4 Low temperature effects

Diluted AFMs can present magnetic frustration due to the vacancies which can create a triangular lattice symmetry. This situation is known as geometrical frustration and the AFM interaction is incompatible to that. This lattice symmetry in the AFM interface can be significant when there is only one, three or five nearest AFM neighbors. There will always be one FM nearest neighbor which will be canceled by one AFM neighbor. As shown in Fig. 5.1, the AFM interface has not constant magnetization before each reversal. That means there are some spins that follow the external magnetic field. These spins are behaving paramagnetically, which means that they are not strongly exchange coupled due to geometric frustration; as a result we refer to these as frustrated spins. This effect is more pronounced at low temperatures, as shown in Fig. 5.17, for uniaxial and biaxial AFM anisotropy.

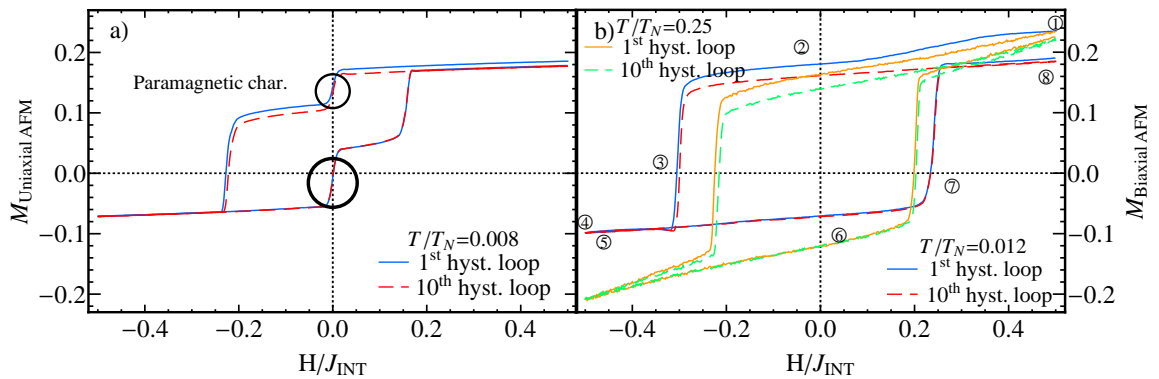


Figure 5.17: Magnetization of the AFM interface of systems with a) uniaxial and b) biaxial AFM anisotropy of the first and of a subsequent hysteresis loop. a) shows results at low temperature with the paramagnetic characteristic and b) shows results at high and low temperature for comparison. The cycle numbers in b) are for future reference.

For uniaxial AFM anisotropy, (as can be seen in Fig. 5.17a) there are two additional reversals at close to zero magnetic field. This shows a paramagnetic characteristic in the behavior of the AFM interface. The frustrated spins with zero net exchange coupling behave paramagnetically and follow the applied field. This phenomenon is present in the consecutive hysteresis loops.

In the case of biaxial AFM anisotropy (Fig. 5.17b)), there is a big step before the

reversal of the external magnetic field which is not repeated in consecutive loops. The frustration in this system is shown by the significant reversible magnetization component before reversal, as in high temperatures. This reflects the paramagnetic behavior of the frustrated spins. The large step only at the first hysteresis loop seem to be an effect of the cooling process.

The above effect can be shown in Fig. 5.18, where the in-plane component of magnetization of the AFM interface for high and low temperature is depicted. For high temperature, when the magnetic field is decreasing, the magnetization vector first contracts, then rotates and finally expands. When the field is increased from negative saturation, a symmetric magnetization response is observed and this is repeated for the subsequent hysteresis loops. But this is not happening for the case of low temperature. As can be seen, after the initial contraction of the magnetization vector, it only rotates during the subsequent reversal. That means that the spins responsible for the contraction and the expansion of the magnetization vector, after the cooling process, they are trapped by a local minimum created by the biaxial easy axes.

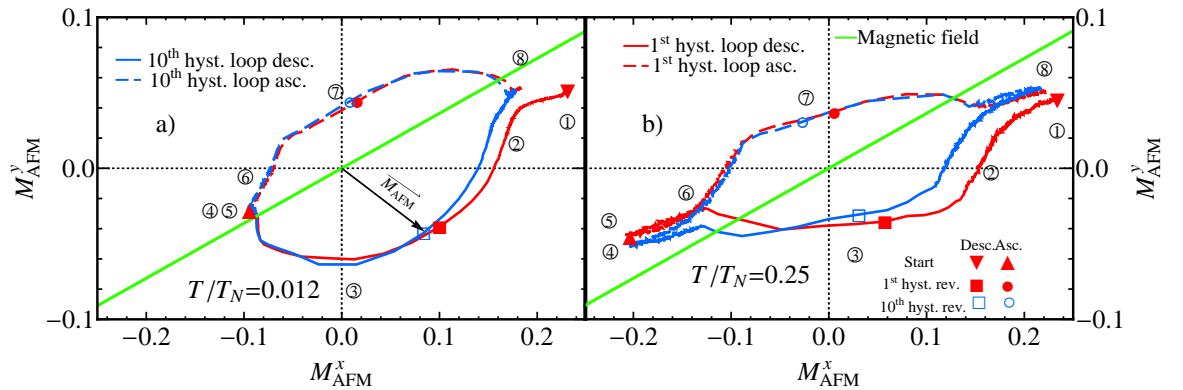


Figure 5.18: First and tenth hysteresis loop of the AFM interface of the in-plane component of magnetization for a) $T/T_N = 0.012$ and b) $T/T_N = 0.25$ for biaxial AFM anisotropy. The green line is the magnetic field axis and points indicate the start and the coercive fields of the hysteresis loop. The numbers indicate the points of the hysteresis loop, as shown in Fig. 5.17.

The trapping of the spins to a local minimum can be shown with a plot of the energy surface of the EB system. This can be done by considering a two spin model, one for the FM and one for the AFM. The model has only terms for anisotropy and exchange coupling between the AFM and the FM layers. Fig. 5.19a) shows the energy contour plot as function of the FM and AFM spin angle, which presents four minima and four maxima. Two of the maxima are bigger than the other maxima due to their collocation with the FM maxima. Thus, an AFM spin “sees” an energy landscape of the form of Fig.5.19b). While at high temperature the spins can pass the energy barrier in 90° and 270° (point ③ and ⑦) angle, at low temperature this has low probability. Thus, they stay oriented towards that direction and can not contribute to the increase of the magnetization vector (point

④ and ⑧ in Fig.5.19).

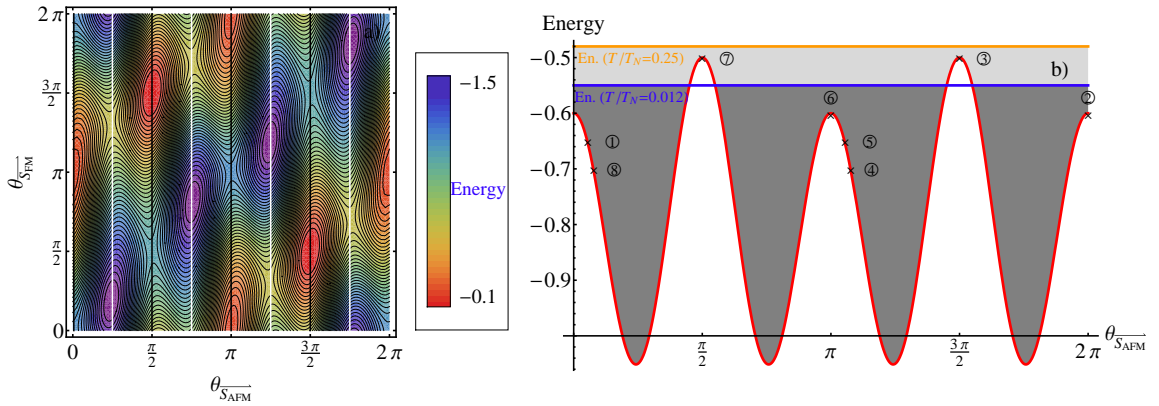


Figure 5.19: a) Energy contour plot of a EB system with biaxial AFM anisotropy as function of angle of the FM and AFM spin angle. The white lines show the energy minima and the black lines the energy maxima according to AFM spin angle. b) One-dimensional representation of effective energy for AFM spins as function of the AFM spin angle. The yellow line is for the energy of AFM spins in high temperature and the blue line shows the energy in low temperature. The number indicate the points of the hysteresis loop, as shown in Fig. 5.17.

Fig. 5.20 shows the distribution of the nearest neighbors for AFM interfacial spins at high and low temperatures for systems with uniaxial and biaxial AFM anisotropy. The spins with zero AFM neighbors interact with the FM only, so they behave like FM spins and rotate with the FM. Thus, all of them are unstable. The spins with one AFM neighbor are frustrated, so they rotate with the external magnetic field. As can be seen, for low temperatures, there is a small percentage of the AFM interfacial spins that are unstable, having two or more nearest AFM neighbors. Also, systems with biaxial AFM anisotropy have more unstable spins compared to systems with uniaxial AFM anisotropy, as can be seen for unstable spins with two π or more nearest AFM neighbors. As explained before, this is due to the lower energy barriers in the biaxial AFM anisotropy.

In order to examine which spins are rotated during the reversals, we construct a distribution of the nearest neighbors of the interfacial AFM spins. This shows the distribution of the nearest neighbors of the spins that change during the two reversals in the ascending branch and the descending branch of the hysteresis loop. Fig. 5.21a) shows the case of uniaxial anisotropy. As can be seen, firstly the spins that have no neighbors and consequently are interacting only with the FM, reverse with the FM. The frustrated spins are the ones shown in striped columns with one and three nearest neighbors. They reverse when the magnetic field reverses, thus being totally paramagnetic. The number of frustrated spins on the descending branch are fewer than on the ascending branch. This explains the smaller paramagnetic reversal of the descending loop, in comparison to the ascending branch.

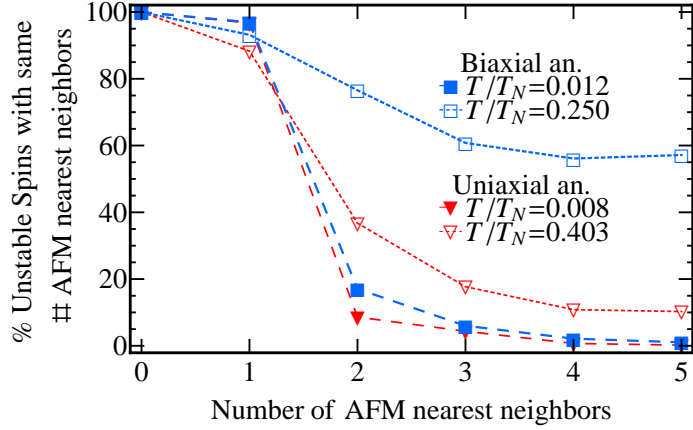


Figure 5.20: Distribution of the nearest neighbors for AFM interfacial spins for high and low temperatures for systems with uniaxial and biaxial AFM anisotropy. The percentage of the total AFM interfacial spins which are unstable during the 1st hysteresis loop. The FM neighbor is excluded.

Fig. 5.21b) shows the distribution of the nearest neighbors for AFM interfacial spins for biaxial FM anisotropy. The large decrease in the first AFM hysteresis loop is not an effect of the frustrated spins, but of the spins with two AFM nearest neighbors. These spins after the cooling process were pointing to one of the easy axes. But after the beginning of hysteresis loop they change direction and they remain trapped in the other easy axes of the AFM, which act as local minima.

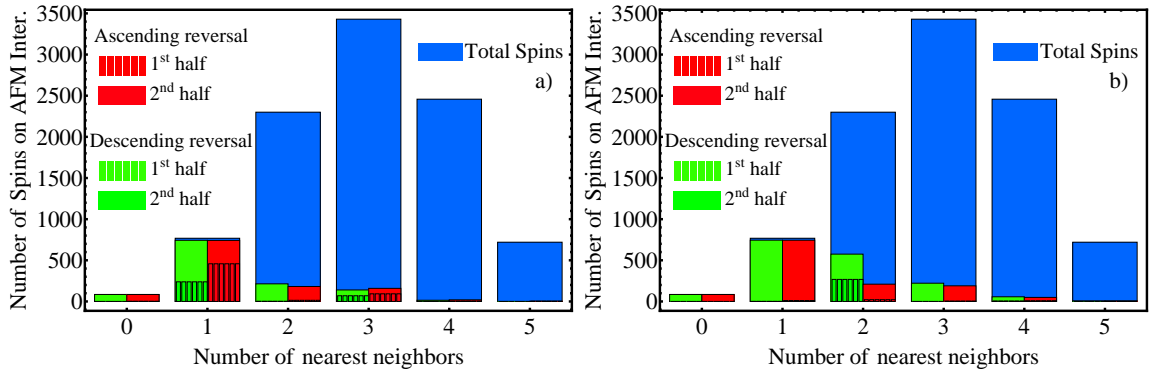


Figure 5.21: Distribution of the nearest neighbors for AFM interfacial spins for a) uniaxial and b) biaxial AFM anisotropy. Blue color shows the total distribution. The other colors show how many spins reversed until e.g. the 1st half of descending loop and so on.

5.5 Influence of the AFM thickness

Using the same model, we will investigate the effect of different AFM thicknesses on the EB field, coercivity and the training effect using constant temperature ($k_b T = 0.15 J_{INT}$) and dilution (40%). It is necessary to investigate the Néel temperature of the AFM as it is changing with different AFM thicknesses. In the following sections an investigation of the

Néel temperature and of the training effect as a function of AFM will be presented. Also, a discussion about the Type I and Type II training effect of coercive fields will follow.

5.5.1 Néel temperature

The Néel temperatures were calculated for each individual system separately, using a heating process from almost zero temperature from the long-range ordered AFM state[128]. The inflection point of the staggered magnetization was then calculated as a function of temperature, estimating the Néel temperature for every AFM thickness, as shown in Fig. 5.22. Néel temperature increases with increase of AFM thickness, due to the increase of stability offered for the extra layers. This trend seems to increase asymptotically to a stable value for Néel temperature which is expected for a finite size analysis.

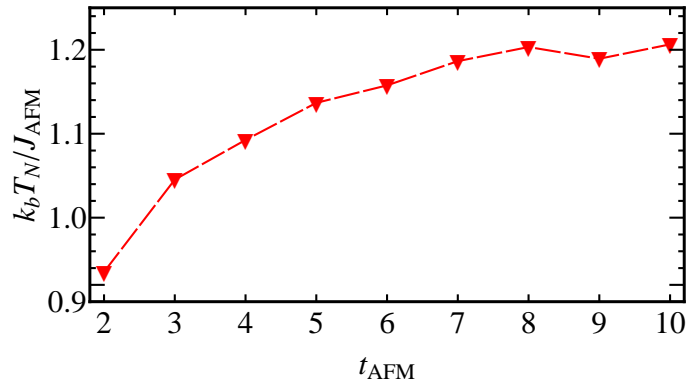


Figure 5.22: Néel temperature dependence on the AFM thickness.

5.5.2 Exchange bias training effect

The dependence of H_{eb} , H_c on the number of consecutive hysteresis loop cycles is presented in Fig. 5.23 for different AFM thicknesses for a system with uniaxial AFM anisotropy at constant temperature. The error bars indicate the statistical error due to averaging over a set of 20 different realizations of the defect distribution in the AFM.

For thickness up to 10 layers, H_{eb} is reduced by about 10-20% and H_c by about 1-2% after ten loops when compared with its initial value. Also, for high thicknesses, the error bars are bigger and the EB field and coercivity fluctuated rapidly. This is due to low EB field at high thicknesses, which cause the large decrease in the relative EB field and in its error.

Our results for the thickness dependence of the training effect are shown in Fig. 5.24. The results for the first and second loop are shown as well as the equilibrium value obtained via the power law fit. The fitting parameters κ and the difference ΔH_{eb} are drawn in the upper graphs.

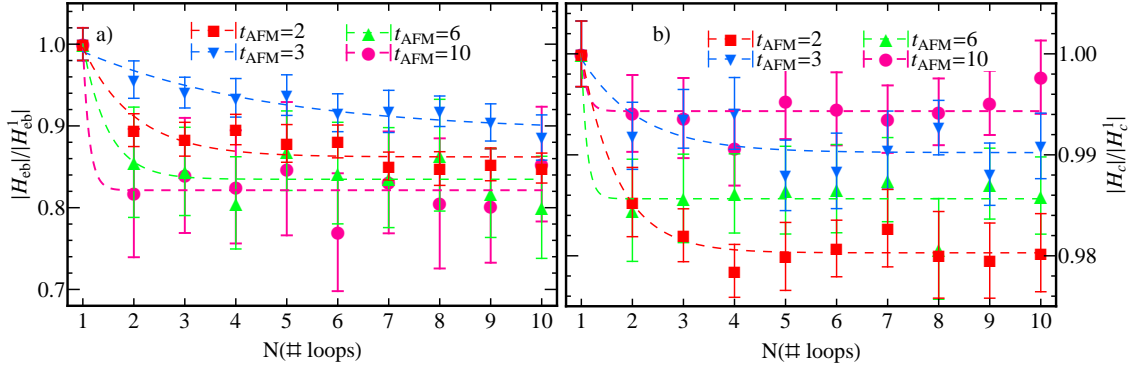


Figure 5.23: Training effect of a) the exchange bias field and b) the coercivity for different AFM thicknesses at constant temperature.

The EB field of the first loop as well as the second loop decreases with increasing AFM thickness. The strength of the training effect has a maximum value for the smaller thickness ($t_{\text{AFM}} = 2$). This is due to the fact that additional AFM layers offer more stability to the system as well as to the created domains so that the training effect is smaller. In addition, the EB field for large values of thickness tends asymptotically to constant non-zero value.

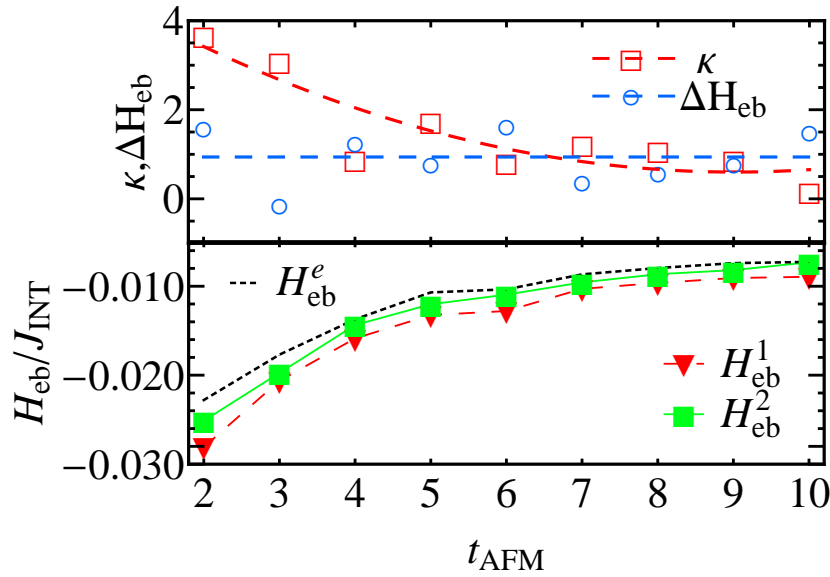


Figure 5.24: AFM thickness dependence of the training effect. H_{eb}^1 and H_{eb}^2 : EB field of the first and the second hysteresis loop, respectively. H_{eb}^e : Equilibrium EB field following the power law fit. Upper graph: AFM thickness dependence of the fitting law parameter κ and ΔH_{eb} obtained as explained in the text.

From the graph of the fitting parameter κ , where κ decreases with increasing AFM thickness, it is apparent that for low AFM thicknesses the EB field is continuously decreasing after the second loop, while for the thickest AFM, κ is close to zero meaning that EB field remains constant. The difference ΔH_{eb} remains constant and finite showing that the first loop EB always deviates from the fitting law. So, there is thermal to athermal

training transition when the AFM thickness increases. This is because the maximum of the training effect as function of temperature is shifted towards higher temperatures for higher AFM thicknesses, as shown in the section 5.3 . As the temperature remains constant with increasing thickness and this maximum shifts towards higher temperature, the training effect strength, measured by κ , decreases coinciding to zero value.

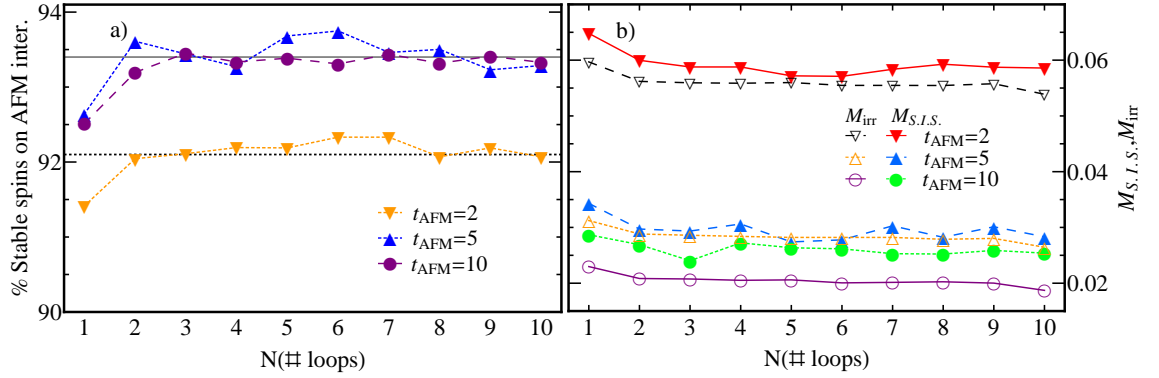


Figure 5.25: Training effect of a) the concentration of stable spins in the AFM interface and b) their net magnetization $M_{S,I.S.}$ for different AFM thicknesses. Also, the irreversible domain state magnetization of the AFM interface is drawn for comparison.

Fig. 5.25a) shows the concentration of stable AFM interfacial spins and in b) the dependence of $M_{S,I.S.}$ and M_{irr} on the number of consecutive loops for systems with different AFM thicknesses. The concentration of the stable AFM interfacial spins decreases with decreasing AFM thickness but increases with increasing number of hysteresis cycles. But the dependence of the magnetization of the stable AFM interfacial spins on the AFM thickness, is consistent that of EB field. Specifically the $M_{S,I.S.}$ and M_{irr} have roughly the same trend and values. We note that this is consistent with the trends with temperature. Systems with thicker AFM exhibit smaller magnetization of the stable AFM interfacial spins due to different domain structure favored by the additional thickness. Thermal training exhibited in low AFM thickness with decreasing $M_{S,I.S.}$ and stable concentration of AFM interfacial spins after the second loop. Athermal training is exhibited in high AFM thickness with stable $M_{S,I.S.}$ after the second loop, but with smaller values of EB field.

5.5.3 Coercive fields: The Type I and Type II training effect

Finally, Fig. 5.26 shows the training effect of the positive and negative coercive field. For simplicity the absolute value of the negative coercive field is used. It can be concluded that the training effect occurs predominantly in the negative coercive fields since there is hardly any difference in the subsequent curves for the positive coercive fields. This means also that one finds a decrease of coercivity during cycling over several loops and with increasing AFM thickness. But the negative coercive field tends to a constant value, which means that coercivity remains constant as function of AFM thickness for a thick AFM.

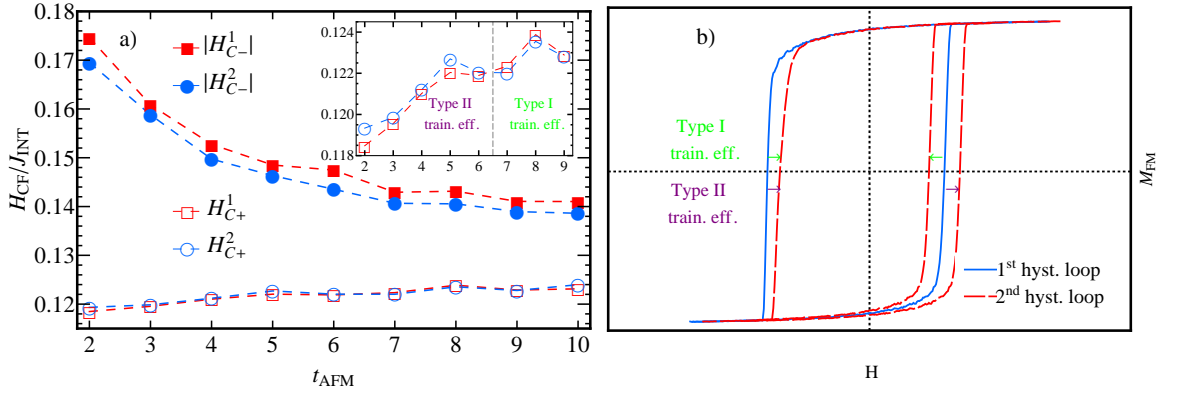


Figure 5.26: a) AFM thickness dependence of the training effect of the coercive fields. H_{C+}^1 and H_{C+}^2 : Positive coercive field of the first and the second hysteresis loop, respectively. Similarly for the absolute value of the negative coercive field. Inset shows magnification of the negative coercive field where the Type I and Type II training effect can be distinguished. b) Schematic representation of Type I and Type II training effect.

As is shown in the inset of Fig. 5.26a), for AFM thickness larger than six layers ($t_{AFM} = 6$), the training effect of the positive coercive field changes behavior. For AFM thickness values smaller than six, the positive coercive field of the first hysteresis loop (red points) is smaller than that of the second hysteresis loop (blue points) while for larger values of AFM thickness, is larger. More specific, according to Zhang *et al.*[33], when the positive branch of the loop shifts toward the positive field direction during hysteresis cycling, we have Type II training effect ($t_{AFM} < 6$). When it moves toward the negative field direction, it is Type I training effect ($t_{AFM} > 6$). A schematic representation of Type I and Type II training effect is shown in Fig. 5.26 b). Thus, we see a transition from Type II to Type I training effect at AFM thickness of six layers. This occurs because for higher thicknesses, the stable spins increase but their total magnetization decreases significantly. Thus, the magnetization of the unstable spins become more significant in the hysteresis loop. Subsequently, during consecutive hysteresis cycling, the decreasing of the enhanced coercivity (unstable spins effect) is more apparent giving rising to Type I training effect.

5.6 Influence of the AFM dilution on training effect

Now, we will investigate the effect of different AFM dilutions on the EB field, coercivity and the training effect using constant temperature ($k_b T = 0.15 J_{INT}$) and thickness (two layers). The dilution in the AFM is implemented using non-magnetic defects (zero-spin lattice sites) in a percentage p of the total AFM spins. As previously, it is necessary to investigate the Néel temperature of the AFM as it is changing with different AFM dilutions. In the following sections an investigation of the Néel temperature and of the training effect as a function of AFM will be presented. Also, a more thorough discussion about the

training effect in the AFM will follow.

5.6.1 Néel temperature

As before, the Néel temperatures were calculated for each individual system separately, using a heating process from almost zero temperature from the long-range ordered AFM state [128]. The inflection point of the staggered magnetization was then calculated as a function of temperature, estimating the Néel temperature for every AFM dilution, as shown in Fig. 5.27. For increasing AFM dilution, the Néel temperature decreases linearly since the long-range ordered AFM state is less favored due to the lack of nearest-neighbors.

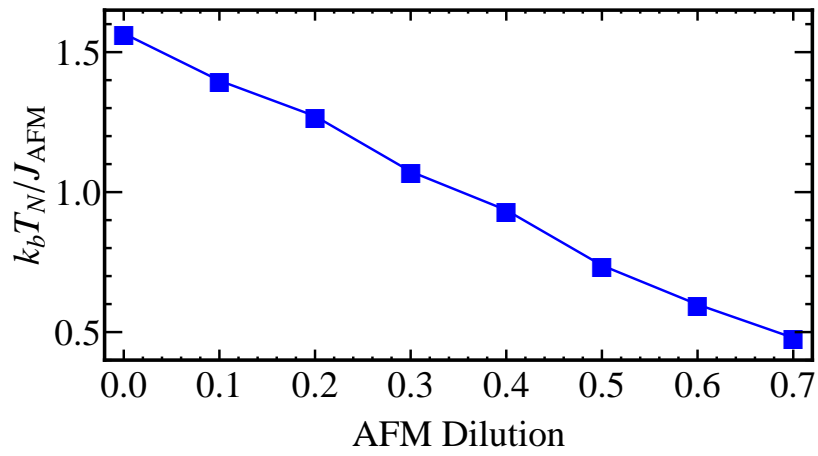


Figure 5.27: Néel temperature dependence on the AFM dilution.

5.6.2 Exchange bias and coercive field training effect

The dependence of H_{eb} , H_c on the number of consecutive hysteresis loop cycles is presented in Fig. 5.28 for different AFM dilutions for a system with uniaxial AFM anisotropy at constant temperature. The error bars indicate the statistical error due to averaging over a set of 20 different realizations of the defect distribution in the AFM.

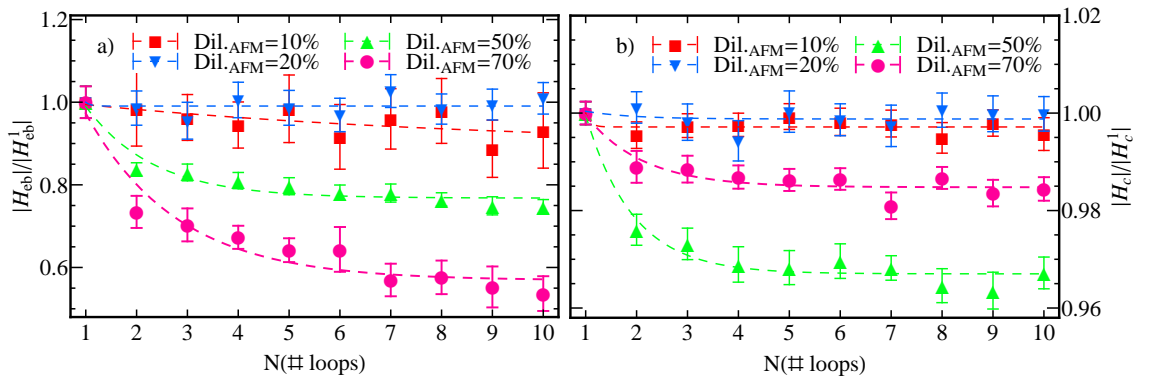


Figure 5.28: Training effect of a) the exchange bias field and b) the coercivity for different AFM dilutions at constant temperature.

For AFM dilution up to 70%, H_{eb} is reduced by about 0–40% and H_c by about 0–4% after ten loops when compared with its initial value. Thus, for higher dilutions the training effect of the EB field is more intense and seems to happen monotonically in contrast to the trend of the training effect of coercivity where the more intense training effect is in the midrange dilution values ($\sim 50\%$).

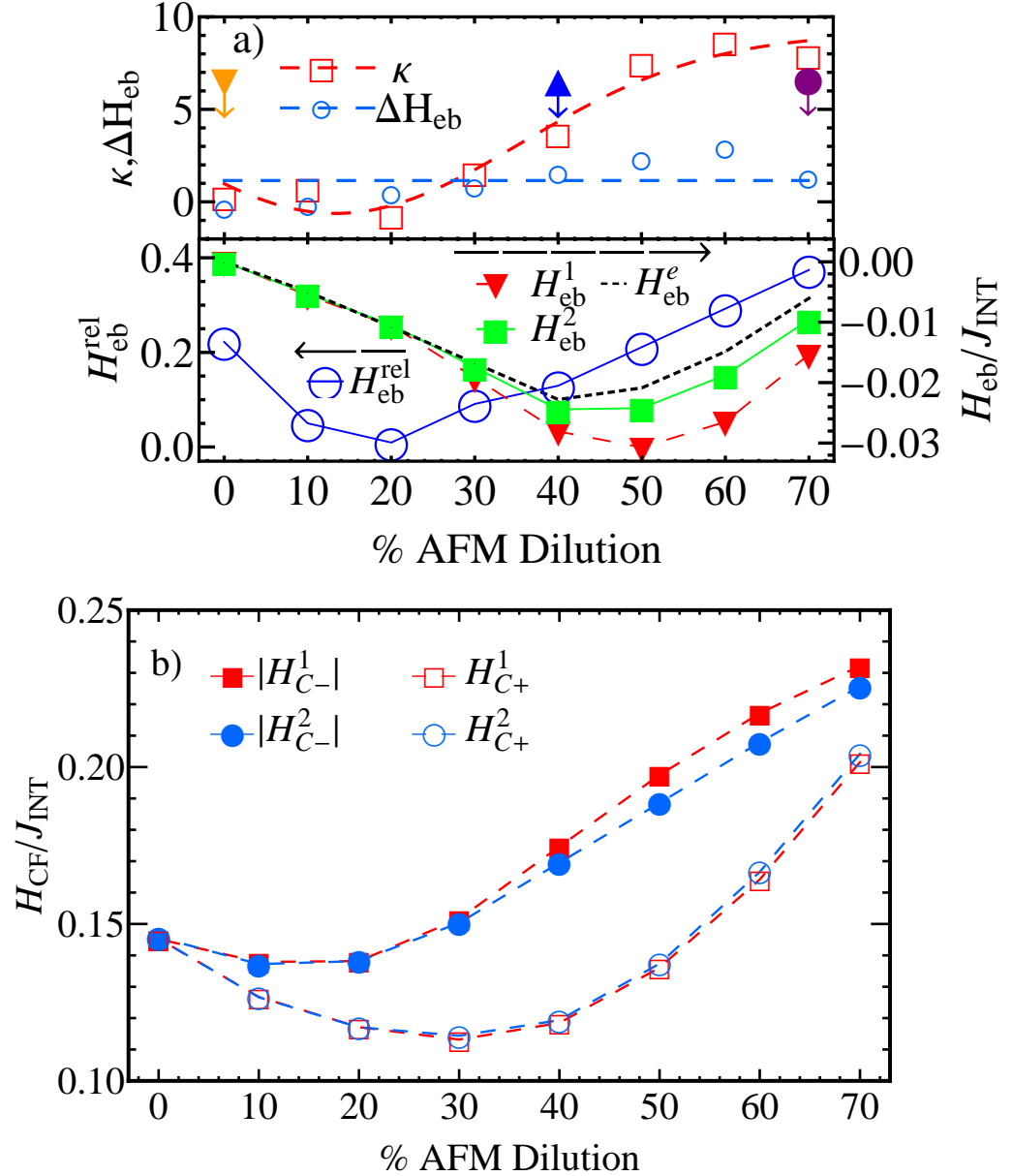


Figure 5.29: AFM dilution dependence of the training effect. a) H_{eb}^1 and H_{eb}^2 : EB field of the first and the second hysteresis loop, respectively. H_{eb}^e : Equilibrium EB field following the power law fit. $H_{\text{eb}}^{\text{rel}}$: Relative training effect. Upper graph: Dilution dependence of the fitting law parameter κ and ΔH_{eb} obtained as explained in the text. The colored arrows and markers show the dilution values that are going to be used in the Fig. 5.30. b) $H_{\text{C}+}^1$ and $H_{\text{C}+}^2$: Positive coercive field of the first and the second hysteresis loop, respectively. Similarly for the absolute value of the negative coercive field.

Our results for the dilution dependence of the training effect are shown in Fig. 5.29.

The results for the first and second loop are shown as well as the equilibrium value obtained via the power law fit. Also, the relative training effect $H_{\text{eb}}^{\text{rel.}} = \frac{|H_{\text{eb}}^1 - H_{\text{eb}}^{10}|}{H_{\text{eb}}^1}$ is calculated, for a comparison with the experimental findings presented by Keller *et al.* [20].

The EB fields of the first loop as well as the second loop increase with increasing AFM dilution until reaching an optimum dilution ($\sim 50\%$). Afterward, the EB fields decrease. The training effect becomes more apparent for dilution higher than 30%. The training effect seems to be maximum when the EB field is maximum in its optimum value. The relative training effect curve shows that the minimum training effect is around 20% and increases for higher values. We compare our result with the experimental findings of Keller *et al.* [20] and a similar trend for the EB field was found. Their optimum EB field occurs in lower dilution than predicted here. This could be because the authors of Ref. [20] state that their values of dilution are underestimated from the fact in a real thin film they are other structural defects and vacancies beyond dilution that are unmeasurable.

As can be seen from the curve of fitting parameter κ , the training effect increases with increasing dilution. Thus, for high dilutions, after the first loop the EB field continues to reduce rapidly. Also, there is a small increase of the ΔH_{eb} difference with increasing dilution. In total, these characteristics show thermal training effect. This is due to the reduction of the size and connectivity of the AFM spin lattice. Subsequently, the domain-wall motion becomes easier upon FM magnetization reversal leading to an increase of the training effect.

Fig. 5.29b) shows the dependence of training effect of the positive and negative coercive field on the AFM dilution. As before, for simplicity the absolute value of the negative coercive field is used. As in previous coercive fields trends, it can be concluded that the training effect occurs predominant in the negative coercive fields since there is hardly any difference in the subsequent curves for the positive coercive fields. This happens for dilutions larger than 0.3. Both coercive fields, above 0.3 dilution, are increasing showing a total increase of the coercivity of the FM.

5.6.3 Behavior of the AFM

Fig. 5.30a) shows, for systems with 0%, 40% and 70% AFM dilution, the dependence of concentration of AFM interfacial stable spins on the number of hysteresis cycles. In general systems with lower AFM dilution have more stable spins compared to higher AFM dilution at the same temperature and AFM thickness. More specifically, for zero dilution the AFM interface is totally stable even after several hysteresis cycles. So all the interfacial spins are pinned. With higher AFM dilution, the concentration of the stable interfacial spins increases with hysteresis loop cycles. This increase of the concentration is more intense for 70% dilution, which is the highest dilution. As for the thickness dependence, the increase

of the stability increases the EB field. However, the increase in the number of stable spins with hysteresis cycle leads to a decrease in the EB field. This apparent contradiction arises from fact that it is possible that the more stable state is more compensated, thus leading to smaller EB field. As a result we cannot characterize the EB field with the concentration of stable spins alone. Thus, we need to investigate the magnetization of these spins.

In Fig. 5.30b), the dependence of the magnetization of the stable AFM interfacial spins $M_{S.I.S.}$ on the number of consecutive loops along with the M_{irr} for comparison is shown. For zero dilution, the magnetization of the stable AFM interfacial spins is zero and all the spin are stable. This shows a fully compensated AFM interface, as all the spins are stable independently of the number of the consecutive hysteresis loop, resulting in zero EB field and no training effect. For 40% and 70% dilution, the concentration of the stable AFM interfacial spins remains stable after the second loop. Despite that, the $M_{S.I.S.}$ for 70% dilution decreases (thermal training) and for 40% dilution remain stable (athermal training) after the second loop. As previously, the $M_{S.I.S.}$ and the M_{irr} are in very good quantitative agreement.

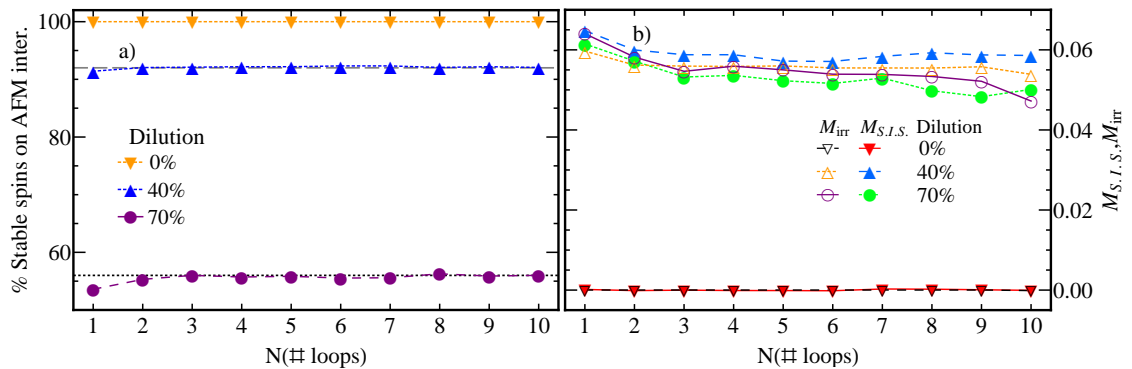


Figure 5.30: Training effect of a) the concentration of stable spins in the AFM interface and b) their net magnetization $M_{S.I.S.}$ for different AFM dilutions. Also, the irreversible domain state magnetization M_{irr} of the AFM interface is drawn for comparison.

Also, the remanent magnetization of the AFM interface is calculated i.e. the reversible domain state magnetization M_{rev} , in Fig. 5.31a). This is the height of the AFM hysteresis loop and is calculated from the magnetization values when the magnetic field is zero (ideally). The reversible domain state magnetization for zero dilution is zero, meaning that there is not a hysteresis loop and the interface is fully compensated, as shown in Fig. 5.31b). For higher values of dilution, the interface becomes uncompensated with quite high reversible domain state magnetization. With increasing dilution, up to 30%, the reversible and irreversible domain state magnetization have the same value, meaning that the hysteresis is shifted fully towards the positive AFM interfacial magnetization axis. Thus, always after the first reversal of the magnetic field, the magnetization has almost zero value.

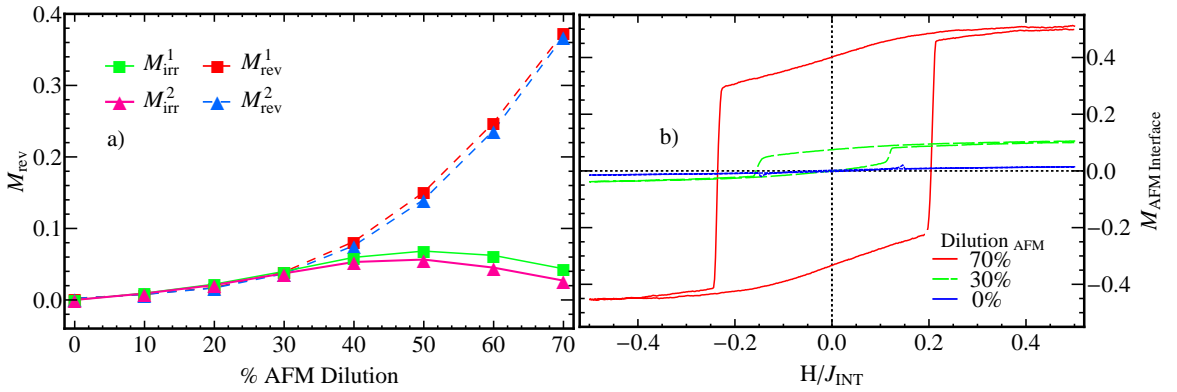


Figure 5.31: a) Training effect of the reversible and irreversible domain state magnetization of the AFM interface as function of AFM dilution. M_{rev}^1 and M_{rev}^2 : Reversible domain state magnetization of the AFM interface of the first and the second hysteresis loop, respectively. b) Effect of different AFM dilutions on AFM interfacial hysteresis loop.

Finally, Fig. 5.32 shows an AFM interface spin configuration snapshot for a system with 40% and 20% AFM dilution. The system with 40% AFM dilution presents many small AFM domains as the energetically favorable state due to the dilution. This means that their domain walls are passing through the magnetic defects. In the case of 20% AFM dilution, we see that we have only two large domains with their spins fully compensated. Also, their domain walls reside mostly between spins, with very little use of the non-magnetic defects. In total, the dilution leads to a more uncompensated interface which is less stable with smaller domains.

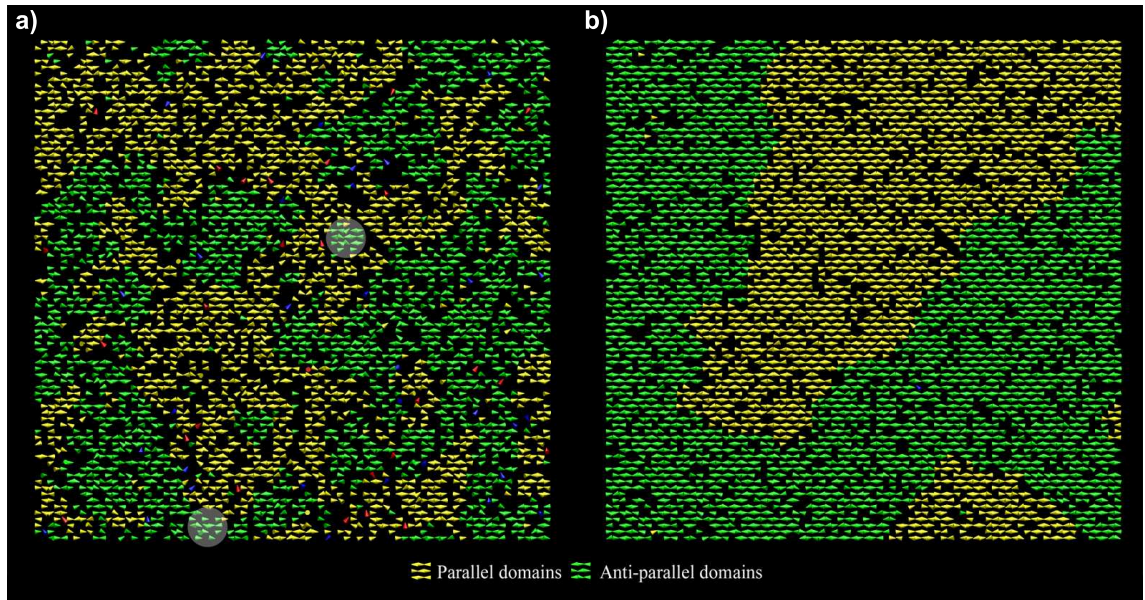


Figure 5.32: AFM interface spin configuration snapshots for a system with a) 40% and b) 20% AFM dilution. The colors are for separating the different AFM domains. The white circles in a) show two AFM domains which their domain walls consist of magnetic defects (gaps).

5.7 Summary

In this chapter an extensive investigation of the dependence of the training effect on temperature was presented. The EB field for consecutive hysteresis cycles was fitted by a power law curve and the parameters of this curve were calculated. According to the parameters of the fitting law for different temperatures, the training effect was separated into two categories: the athermal training effect, where after the second hysteresis cycle the EB field remains constant, and the thermal training effect, where the EB field decreases. Always, we have a steep decrease of EB field between the first and the second hysteresis loop. This steep decrease is an effect of meta-stable AFM spins, which were initially aligned during the cooling process into energy minima. These energy minima have insufficiently large barriers to retain these spins stable against change of sign of the exchange field during reversal of the FM layer.

A novel analysis of the AFM interfacial spins showed that the steep decrease between the first and second loop is an effect of the decrease of the population of the stable spins. After the second loop, this population always stays constant. For the athermal training, the magnetization of these stable spins stays constant except for a slow decrease caused by thermal activation (the thermal training effect). That means that the stable spins are not absolutely oriented to the easy direction but rather they relax gradually to an easy direction. The magnetization of the stable spins, has the same values and trends the irreversible domain state magnetization which is equal to the EB field. Thus, this is a direct proof that the behavior of the stable spins is causing the EB field and the training effect.

For low temperatures, the hysteresis loop of the AFM interface shows some interesting effects. For EB systems with AFM uniaxial anisotropy, the frustrated spins are shown predominantly in the hysteresis loop, as a paramagnetic part around zero magnetic field. Furthermore, for EB systems with AFM biaxial anisotropy, a reduction of the magnetization is seen before the first reversal. This is due to the lack of thermal excitation which leads to trapping of AFM spins in an easy direction due to a large energy barrier.

Although, the two kinds of training effects are connected with the temperature trend, there is also strong dependence in AFM thickness and dilution. Thus, e.g. for high temperatures with low AFM thickness, we have a thermal training effect but with extra AFM layers or lower AFM dilution, we have predominantly athermal training. Furthermore, with increasing AFM thickness, there is a transition from Type II to Type I training effect for the positive coercive fields.

Magnetocrystalline anisotropy dependence of the training effect

In this chapter, we will investigate a large range of EB systems varying the characteristics of the anisotropy in both AFM and FM. The change of the anisotropy characteristics, changes the position, the number as well as the value of the energy minima and barriers. These changes affect the behavior of the EB, the training effect and the reversal modes. We will then focus on the most interesting systems and we will categorize them according to their behavior during consecutive hysteresis loop. More specifically, their reversal modes will be analyzed and their dependence on the angle of the magnetic field from the FM easy axis will be investigated. The training effect of the reversal modes is investigated where mainly three types can be recognized.

6.1 Training effect dependence on anisotropy types and parameters

The atomistic model presented earlier has been applied on systematic calculations of systems with different types and parameters of anisotropy of each material, using constant temperature ($k_bT = 0.15J_{INT}$), AFM thickness (2 layers) and dilution (40%). More specifically, nine combinations of anisotropy types were combined with nine combinations of anisotropy parameters, thus in total 81 different systems. Three magnetocrystalline anisotropies were applied in each material: uniaxial, biaxial and cubic anisotropy and all the combinations with the anisotropy constants are presented in Tab. 6.1.

For each case, we applied different orientations on the easy axes of anisotropy, so not to favor any particular direction in cases of different numbers of easy axes in the AFM and FM. So when we have the same kind of anisotropy in both of the materials, the angle between them is zero. When we have biaxial in one material and uniaxial in the other, the biaxial easy axes are rotated around the z-axis by 45° , e.g. as shown in Fig. 5.7. When one of the materials has cubic and the other uniaxial or biaxial anisotropy, the cubic easy axes are rotated twice: around the z-axis and around the y-axis by 45° , as shown in Fig. 6.1.

6.1. Training effect dependence on anisotropy types and parameters

Anis. Comb.	FM anis.	FM anis. constants	AFM anis.	AFM anis. constants
1	uniaxial	$(k_{FM}, 0.0, d_z)$	uniaxial	$(k_{AFM}, 0.0, 0.0)$
2	uniaxial	$(k_{FM}, 0.0, d_z)$	biaxial	$(k_{AFM}, 0.0, 0.0)$
3	uniaxial	$(k_{FM}, 0.0, d_z)$	cubic	$(k_{AFM}, 0.0, 0.0)$
4	biaxial	(k_{FM}, k_{FM}, d_z)	biaxial	$(k_{AFM}, k_{AFM}, 0.0)$
5	biaxial	(k_{FM}, k_{FM}, d_z)	uniaxial	$(k_{AFM}, k_{AFM}, 0.0)$
6	biaxial	(k_{FM}, k_{FM}, d_z)	cubic	$(k_{AFM}, k_{AFM}, 0.0)$
7	cubic	(k_{FM}, k_{FM}, k_{FM})	cubic	$(k_{AFM}, k_{AFM}, k_{AFM})$
8	cubic	(k_{FM}, k_{FM}, k_{FM})	uniaxial	$(k_{AFM}, k_{AFM}, k_{AFM})$
9	cubic	(k_{FM}, k_{FM}, k_{FM})	biaxial	$(k_{AFM}, k_{AFM}, k_{AFM})$

Table 6.1: Anisotropy combinations

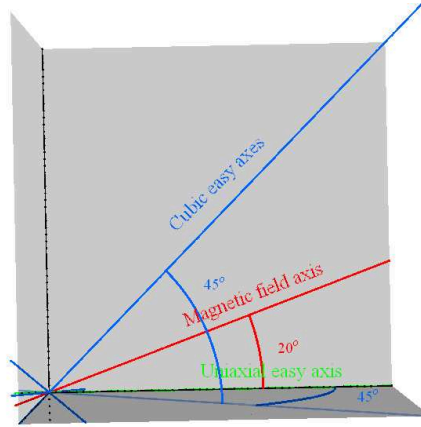


Figure 6.1: Easy axes of an EB system with cubic and uniaxial anisotropy.

The anisotropy constants were varied to study the effects of different strengths of anisotropy. Specifically, the values of anisotropy constant $k_{FM}, k_{AFM} = 0.02J_{FM}, 0.1J_{FM}$ and $1.0J_{FM}$ represent weak, intermediate and strong anisotropy, respectively. For a FM, the anisotropy is described in Chap. 4, by Eq. 4.5, where the anisotropy constants are shown in Tab. 6.1 for each case and $d_z = 0.1J_{FM}$ is for describing the hard axis. Similarly, for an AFM the anisotropy is described by Eq. 4.7. Thus, we take nine combinations of the above three values of the anisotropy constants.

The EB field and the coercivity as function of anisotropy combination and constants is shown in the Fig. 6.2 for strong AFM anisotropy, in the Fig. 6.3 for intermediate AFM anisotropy and in the Fig. 6.4 for weak AFM anisotropy. The error, due to averaging over 20 different realizations, is also depicted. For strong AFM anisotropy, the cases where the anisotropy constants of the FM k_{FM} is $0.1J_{FM}$ and $0.02J_{FM}$ (Fig. 6.2) are the more interesting ones, as they exhibit the largest EB field and training effect. In the other cases, the EB field is zero or quite small with large error bar. This is due to the large domain size created at the AFM interface, as was discussed in Ref. [91] for different values of the AFM anisotropy constants. The large error bar shows that there is a big fluctuation in the EB field, and consequently there is not a reliable conclusion for the EB field for that

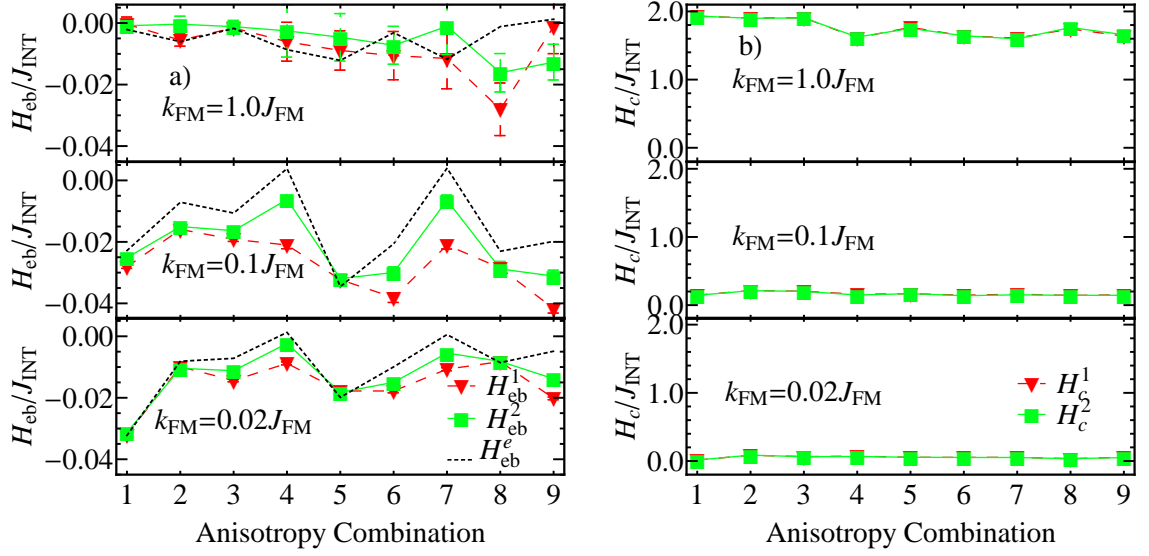


Figure 6.2: Training effect of a) EB field and b) coercivity for strong AFM anisotropy ($k_{AFM} = 1.0J_{FM}$) for several FM anisotropy constants and combinations. Anisotropy combinations are explained in the text.

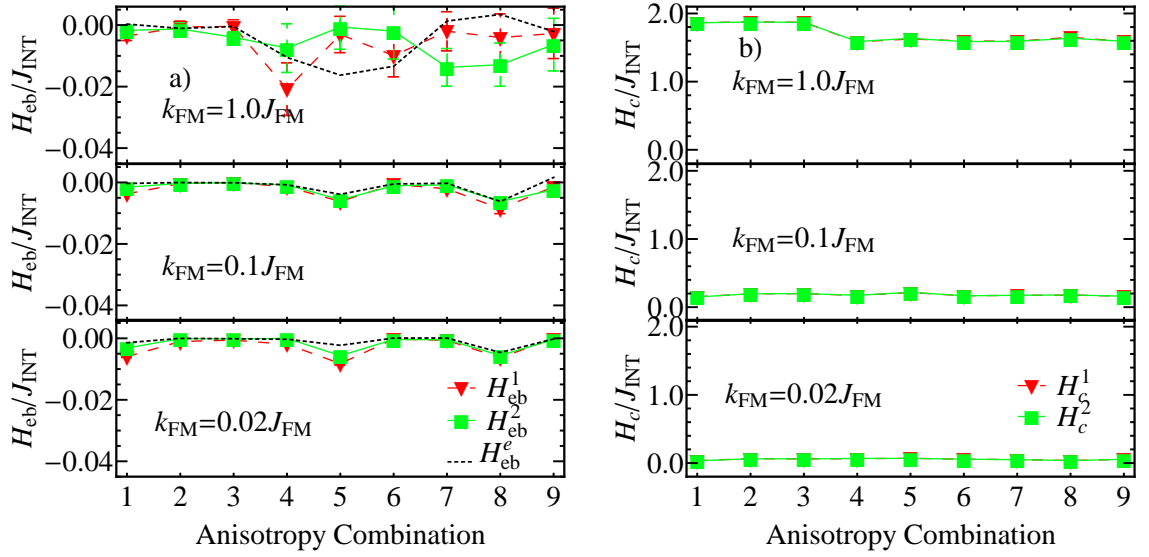


Figure 6.3: Training effect of a) EB field and b) coercivity for intermediate AFM anisotropy ($k_{AFM} = 0.1J_{FM}$) for several FM anisotropy constants and combinations. Anisotropy combinations are explained in the text.

system. Most of the systems feature a very weak change in coercivity across the different anisotropy combinations. The coercivity follows the Stoner-Wolfarth limit according to the FM anisotropy constant and there is a small decrease in the non-uniaxial anisotropies due to the smaller energy barrier between the spin states as explained in the Sec. 4.1.5.

From these results, we examined more thoroughly only the systems with the largest EB field and the most intense training effect, which as mentioned previously, are the ones with intermediate and low FM anisotropy. Fig. 6.5 shows the consecutive hysteresis loops for these systems for intermediate FM anisotropy ($k_{FM} = 0.1J_{FM}$) and weak FM anisotropy

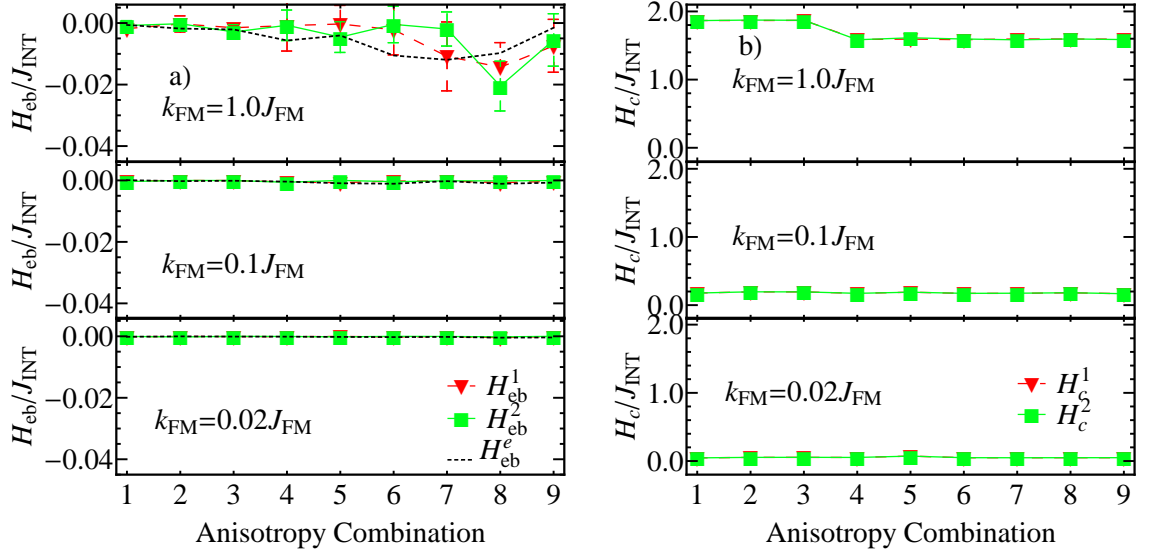


Figure 6.4: Training effect of a) EB field and b) coercivity for weak AFM anisotropy ($k_{AFM} = 0.02J_{FM}$) for several FM anisotropy constants and combinations. Anisotropy combinations are explained in the text.

($k_{FM} = 0.02J_{FM}$). For a clearer view of the reversal mechanism of the FM, the in-plane component of magnetization of the FM for $k_{FM} = 0.1J_{FM}$ is shown in Fig. 6.6 and for $k_{FM} = 0.02J_{FM}$ in Fig. 6.7.

Firstly, for the case of the intermediate FM anisotropy (meaning $k_{FM} = 0.1J_{FM}$ from now on), it can be seen from the hysteresis loops, that when the FM has more than one easy axes (biaxial or cubic anisotropy) the reversal is more steep (second and third line in Fig. 6.5). In the graph of the in-plane component of FM magnetization, we can see in the uniaxial FM anisotropy (first line in Fig. 6.6) that the negative y-component of the magnetization increases before the reversal with a decrease of the x-component. On the contrary, in the biaxial FM anisotropy (second line in Fig. 6.6), the y-component of the magnetization does not increase much, with the x-component staying stable before reversal. That is why during reversal the x and y-components change rapidly, i.e. steep reversal. This is due to the size of the energy barriers, which are larger in the case of uniaxial anisotropy. For the case of the weak FM anisotropy (meaning $k_{FM} = 0.02J_{FM}$ from now on), when the FM has more than one easy axes (biaxial or cubic anisotropy) the reversal is similar to the one easy axis. This is due to the fact that the energy barriers are lower and the reversal to the next local minimum happens less rapidly.

Now, we will focus on the reversal modes of each combination of anisotropy for the intermediate FM anisotropy. We will separate the reversal modes into four different groups. When the FM has uniaxial anisotropy (three top graphs in Fig. 6.6, group (I) and group (II), the magnetization reversal is symmetrical and coherent in both sides of the hysteresis loop. As mentioned before, on the descending branch of the hysteresis loop, the y-component

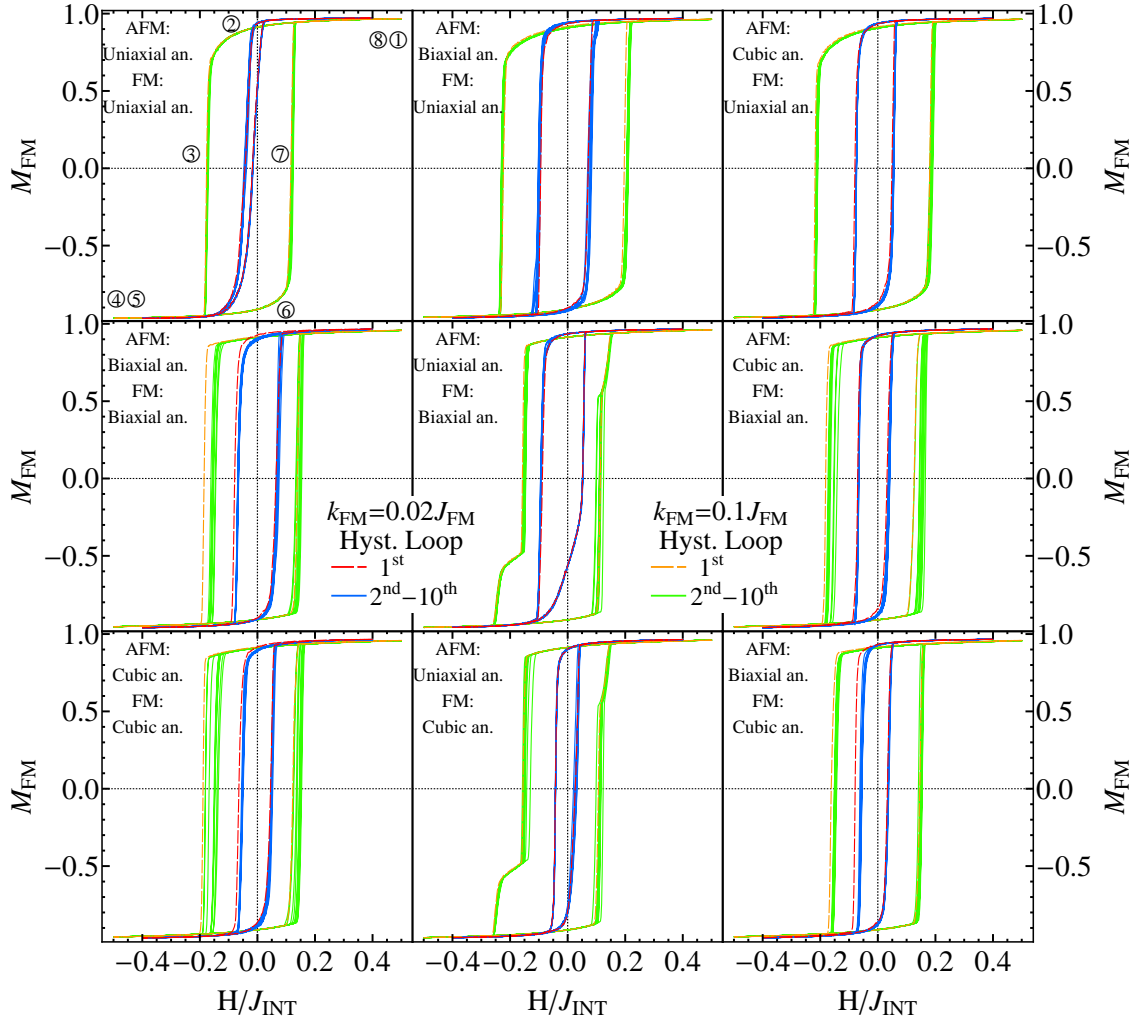


Figure 6.5: FM consecutive hysteresis loops for $k_{FM} = 0.1J_{FM}$ (large coercivity) and $k_{FM} = 0.02J_{FM}$ (small coercivity) for 1st cycle dashed lines and 2th – 10th cycle (solid lines). The number are for future reference. ①, ⑤: Start of the first and second reversal, respectively. ④, ⑧: End of the first and second reversal, respectively. ②, ⑥: Zero magnetic field. ③, ⑦: Zero magnetization.

of magnetization increases (absolute value) before the reversal, remains almost constant during the reversal and decreases after the reversal. In the case of biaxial anisotropy in both materials, the magnetization reversal is similarly symmetrical and coherent. But now the y-component of magnetization remains almost constant before reversal, and increases or decreases during reversal.

For the other cases, we see that an extra angle is presented on the trajectory of the magnetization vector, meaning a large increase of the y-component, due to the extra easy axis. More specific for the anisotropy combinations 6, 7, 9 and less intense in 4 (group III) we observe a decrease of this y-component after nine hysteresis cycles. This is connected with the large training effect that is apparent in these cases, as shown in Fig. 6.5.

Finally, for the case of uniaxial AFM anisotropy and cubic or biaxial FM anisotropy

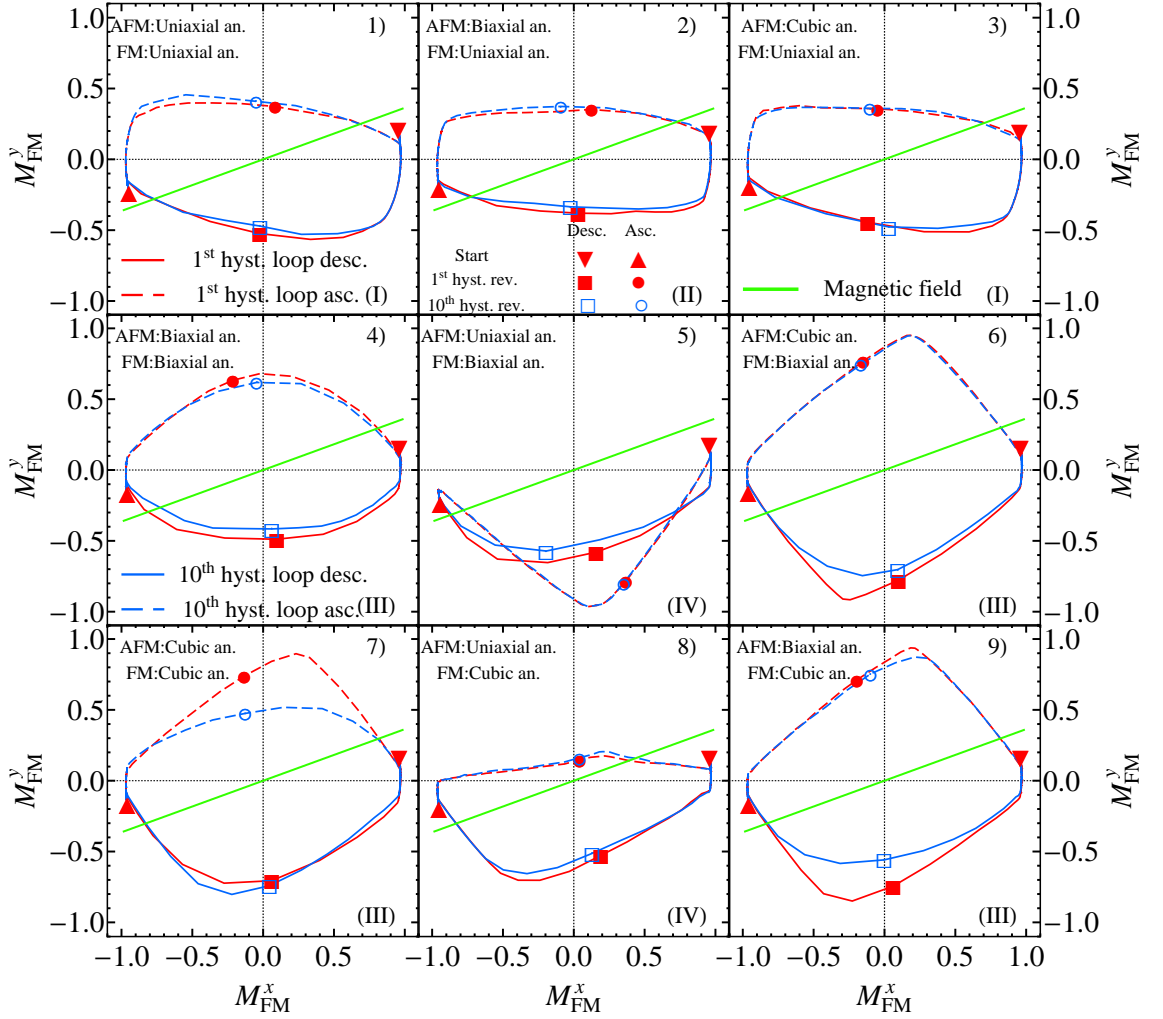


Figure 6.6: *In-plane component of magnetization of the first and tenth hysteresis loop of the FM for $k_{FM} = 0.1J_{FM}$ for several combinations of kind of anisotropy. The green line is the magnetic field axis. The Roman numerals indicate the group number of each system.*

(combination 5, 8), one of the reversals has smaller y-component of magnetization compare to the other (group (IV)). Thus, we have a nonuniform reversal mode with vanishing total magnetization in the anisotropy combination 8 and with rotation occurs via the same side for both branches of the hysteresis loop (in 5 and partially in 8).

We will focus, now, on the reversal modes of each combination of anisotropy for the weak FM anisotropy, as shown Fig. 6.7. In the case of the uniaxial FM and AFM anisotropy (anisotropy combination 1), the reversal is coherent on both sides of the hysteresis loop. Similar cases are given when the AFM has cubic anisotropy with uniaxial (2) or biaxial (3) FM anisotropy (group (I)). The difference between the aforementioned cases is in the rotation of magnetization which occurs symmetrically on both sides or on one side. Obviously, here the x and y-component of magnetization are having the same maximum value and subsequently the total magnetization remains almost constant during the reversal.

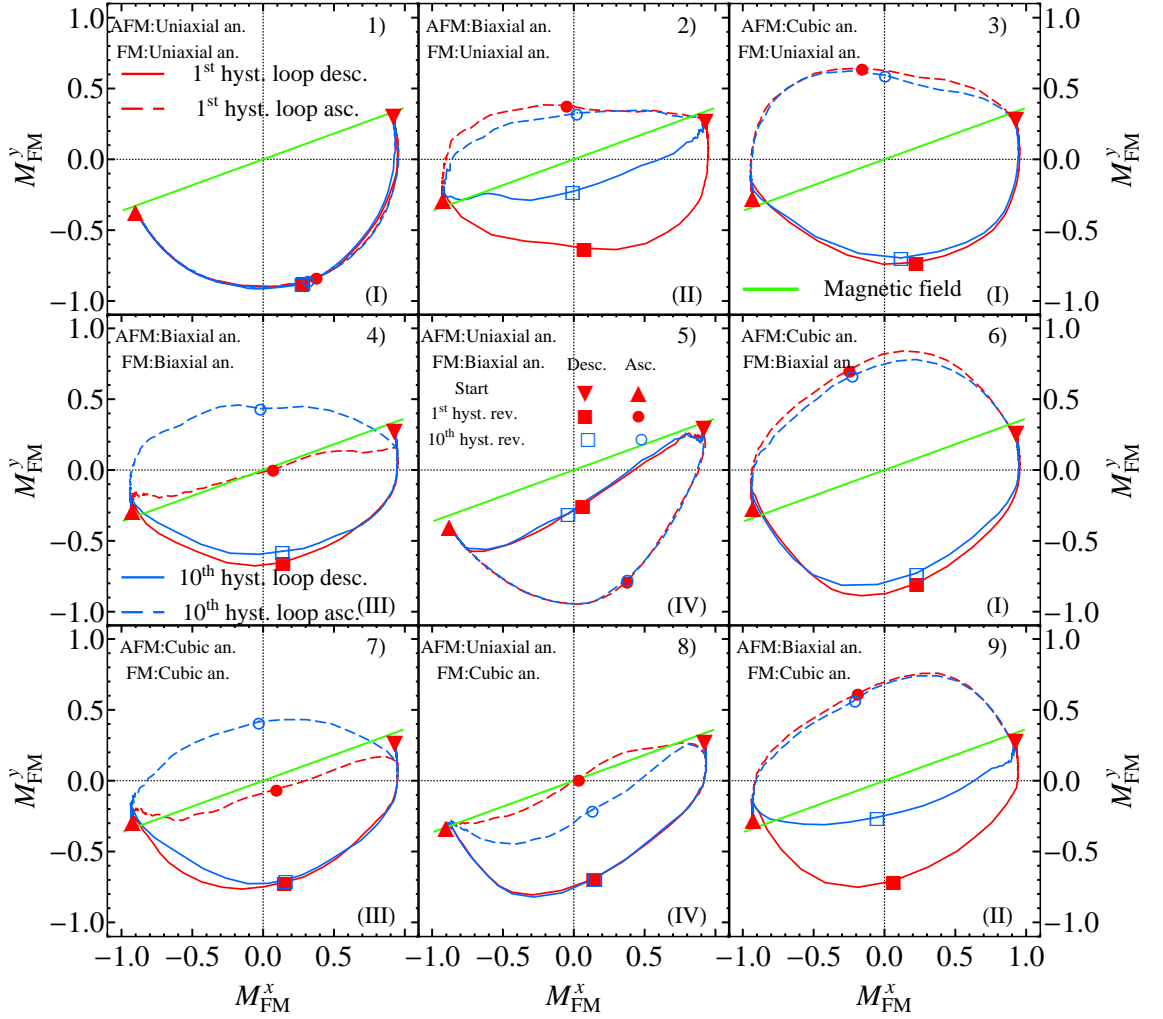


Figure 6.7: *In-plane component of magnetization of the first and tenth hysteresis loop of the FM for $k_{FM} = 0.02J_{FM}$ for several combinations of kind of anisotropy. The green line is the magnetic field axis. The Roman numerals indicate the group number of each system.*

The other cases which all of them are non symmetric can be divided into three more categories. To the first category (group (III)) belong the systems with the ascending branch of the hysteresis loop having zero y-component on the first cycle but to be increased on the next cycles up to the tenth one. This is the case of anisotropy combination 4 and 7, where both materials have biaxial or cubic anisotropy. To the second category (group (II)), in contrast to before, belong the systems with the descending branch of the hysteresis loop having finite y-component on the first cycle to be decreased close to zero on the next cycles up to the tenth one. This is the case of anisotropy combination 2 and 9, where the system has AFM biaxial anisotropy with uniaxial or cubic FM anisotropy. Finally, to the third category (group (IV)), belong the systems with one of the branches of the hysteresis loop having close to zero magnetization in every cycle and always on the same side with the other branch. This is the case of anisotropy combination 5 and 8, where the system

has FM uniaxial anisotropy with biaxial or cubic AFM anisotropy.

From the previous discussion, it is now more easy to focus in more specific cases. These are the systems with uniaxial or biaxial FM anisotropy and uniaxial or biaxial AFM anisotropy (anisotropy combinations 1,2,4,5). So, for intermediate FM anisotropy, we do not investigate further the systems with anisotropy combination 3 because are similar to combination 1 ones (group (I), in terms of reversal modes. Also, systems with anisotropy combinations 6,7,9 are similar to combination 4 ones (group (III), and combination 8 ones is similar to combination 5 ones (group (IV). For weak FM anisotropy, we do not investigate further systems with anisotropy combinations 3,6 because are similar to combination 1 ones (group (I). Also, systems with anisotropy combination 9 is similar to combination 2 ones (group (II), and systems with combination 7 are similar to combination 4 ones (group (III). Finally, systems with anisotropy combination 8 are similar to combination 5 ones (group (IV).

6.2 Influence of angle between easy axis and magnetic field

We will investigate the influence of angle between easy axis and magnetic field on the reversal modes and the training effect of EB systems with uniaxial or biaxial FM anisotropy and uniaxial or biaxial AFM anisotropy (one case from each group). Each time only one anisotropy combination will be investigated for intermediate and weak FM anisotropy, i.e. for the prementioned values of FM anisotropy constants.

6.2.1 Uniaxial FM anisotropy - Uniaxial AFM anisotropy (Group (I))

FM reversal modes

We will focus, now, on the reversal modes of the FM for the case of uniaxial anisotropy in both materials when we have intermediate ($k_{FM} = 0.1J_{FM}$) or weak ($k_{FM} = 0.02J_{FM}$) FM anisotropy for different angles between the magnetic field and the FM easy axis. In Fig. 6.8 the consecutive hysteresis loops are shown together with the in-plane magnetization components for several angles between magnetic field and FM easy axis for the two aforementioned systems. As we can see the hysteresis loop for intermediate FM anisotropy has steep reversal which with increasing angle θ becomes less steep and the hysteretic behavior also decreases i.e. the coercivity decreases. This trend is consistent with the Stoner-Wolfarth model. On the other hand, for weak FM anisotropy the hysteresis loop

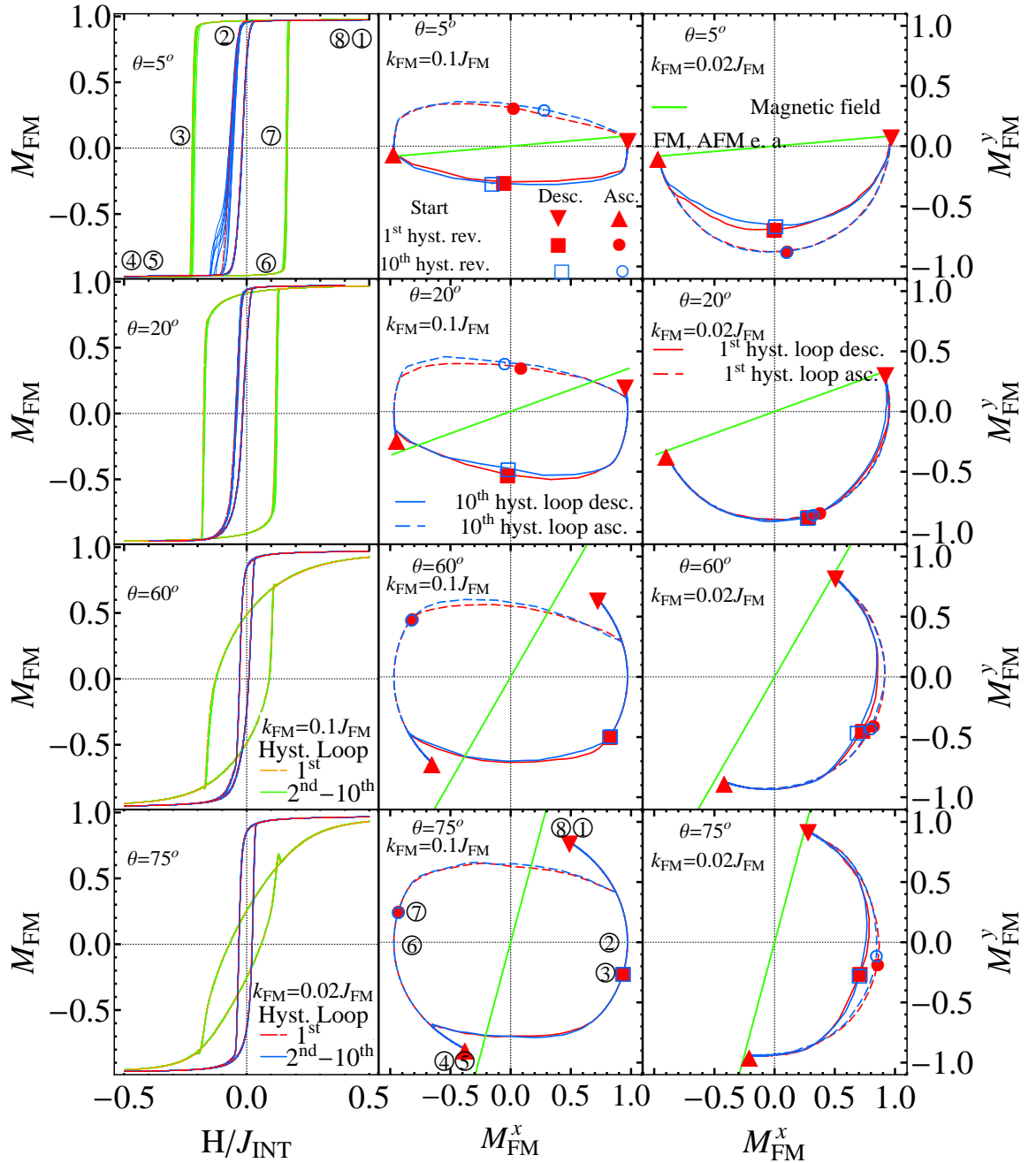


Figure 6.8: Different components of magnetization for several angles between magnetic field and FM easy axis. Left: Hysteresis loop of the first and subsequent cycles of the FM for systems with $(k_{FM}) = 0.1J_{FM}$ and $(k_{FM}) = 0.02J_{FM}$. Middle: In-plane component of magnetization of the first and second cycle of the FM for systems with $(k_{FM}) = 0.1J_{FM}$. Right: In-plane component of magnetization of the first and second cycle of the FM for systems with $(k_{FM}) = 0.02J_{FM}$. The green line in the middle and left figures is the magnetic field axis. The numbers correlate the pathway of the hysteresis loop (left) with the in-plane magnetization component (right).

seems independent of θ , with quite low coercivity. This is due to low energy barriers which allow spins to reverse freely.

Comparing now the in-plane magnetization for intermediate and weak FM anisotropy, we see that the reversal modes are different. For intermediate FM anisotropy, when the angle θ increases, the magnetization vector after and before reversal is pointing in a direction which is midway between the FM easy axis (x-axis) and the magnetic field direction. More specifically, it is pointing closer to the magnetic field direction since the magnetic field is stronger than the field created by the FM uniaxial anisotropy. The reversal shows a feature indicated by the path between the points (③, ④, ⑤), in the case of $\theta = 75^\circ$. This is observed in Stoner-Wolfarth type behavior for large angles and follows the complex switching path indicated by these points. When the magnetic field is smaller than the anisotropy field, the magnetization vector rotates up to the 45° angle where at that point the two fields are equal (point ④). Then, the magnetic field is bigger than the anisotropy field and consequently “pulls” the magnetization vector closer to its direction and increases the angle from the easy axis (point ⑤).

For weak FM anisotropy, the magnetization vector before and after reversal is parallel to the magnetic field. This is due to the small anisotropy field which does not effect the magnetization reversal. Furthermore, the magnetization rotation occurs via the same path (the lower half plane defined by the field direction) for both branches of the loop, as there is not a sufficient field to transverse the magnetization to the other side. For small angles, there is a smaller net contribution of the perpendicular magnetization on the descending branch. Finally, the reversal occurs in both cases with coherent rotation.

Snapshots of the spin configuration of the FM are shown in Fig. 6.9 for the aforementioned systems. Although, before the reversal, the systems behave the same (point ① and ②) during and after reversal there are significant differences. We see that for the system with intermediate FM anisotropy, during the reversal (point ③), the spins reverse steeply 90° from their last orientation before reversal. Thus, in the point ④, they are all oriented along the 225° axis and then in point ⑤ reoriented close to the magnetic field axis (255°). For systems with low FM anisotropy, the reversal is more gradual with spins directed to the magnetic field axis (255°). Subsequently, they are rotated by a smaller angle from their last orientation than those of intermediate FM anisotropy.

FM EB training effect

Our results for the angle θ dependence of the training effect for the aforementioned systems are shown in Fig. 6.10. The results for the first and the second loop are shown as well as the equilibrium value obtained via the power law fit for the EB field (Fig. 6.10a) and the coercivity (Fig. 6.10b). The fitting parameters κ and the difference ΔH_{eb} are

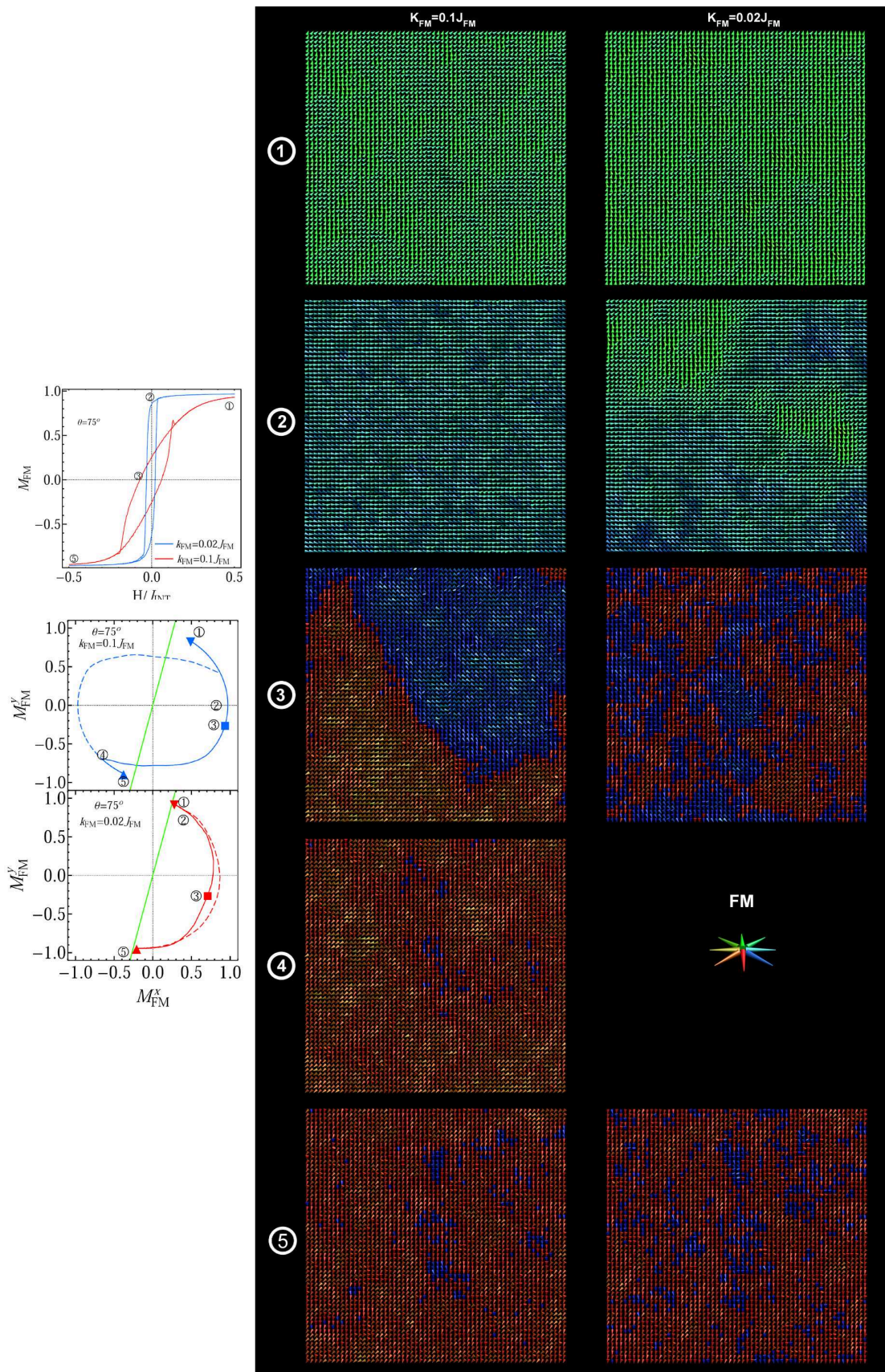


Figure 6.9: *FM spin configuration snapshots for systems with $k_{FM} = 0.1J_{FM}$ (center) and $k_{FM} = 0.02J_{FM}$ (right). The number on every line of snapshots is indicating the respective point in the hysteresis loop (left). See text for explanation.*

drawn in the bottom graphs. The EB field for systems with weak and intermediate FM anisotropy decreases with increasing angle θ . For low values of angle θ systems with weak FM anisotropy have larger EB field than intermediate ones but this behavior reverses for larger angles ($\theta > 45^\circ$). Coercivity decreases with increasing angle θ , as is predicted from the Stoner-Wolfarth model for systems with intermediate FM anisotropy. For weak FM anisotropy, the coercivity remains almost stable and with quite small value compare to the systems with intermediate FM anisotropy.

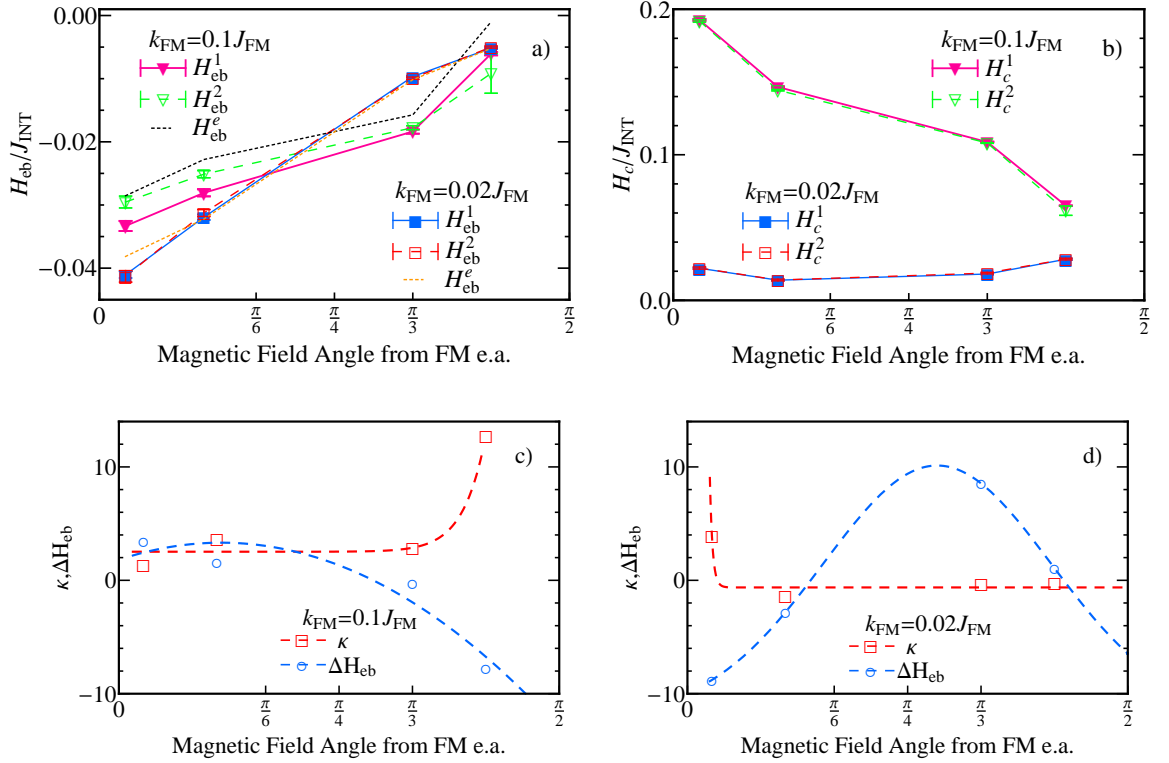


Figure 6.10: Dependence of the training effect on magnetic field angle for a) EB field and of b) coercivity for systems with $k_{FM} = 0.1J_{FM}$ and $k_{FM} = 0.02J_{FM}$. Magnetic field's angle dependence of the normalized fitting law parameter κ and ΔH_{eb} for systems with c) $k_{FM} = 0.1J_{FM}$ and d) $k_{FM} = 0.02J_{FM}$.

Now, as we can see from the Fig. 6.10, the training effect is larger for systems with intermediate FM anisotropy. This can be seen from the trend of κ where it increases with increasing angle θ while for weak FM anisotropy κ is zero for almost all the values of the angle (except $\theta = 5^\circ$). This shows a more stable AFM state and athermal training effect in systems with low FM anisotropy. For intermediate FM anisotropy, in low angles θ the training effect is still thermal as κ is not zero, i.e. the AFM is still unstable after the second hysteresis loop. ΔH_{eb} for this case has small values except for high angle θ where it has large negative value but this is due to the large error at that point as shown in Fig. 6.10a). For weak FM anisotropy, it has a maximum at around 45° and negative large values at the edges. This is not obvious in the Fig. 6.10a) because after the second hysteresis loop the training effect is very small and thus even small difference of EB field between the first and

the second cycle is appearing as large ΔH_{eb} difference.

AFM interface reversal modes

We will focus, now, on the reversal modes of the AFM for the case of intermediate ($k_{FM} = 0.1J_{FM}$) FM anisotropy for different angles between the magnetic field and the FM easy axis. In Fig. 6.11 the in-plane magnetization component of the AFM for several angles between magnetic field and FM easy axis is shown. As we can see the magnetization

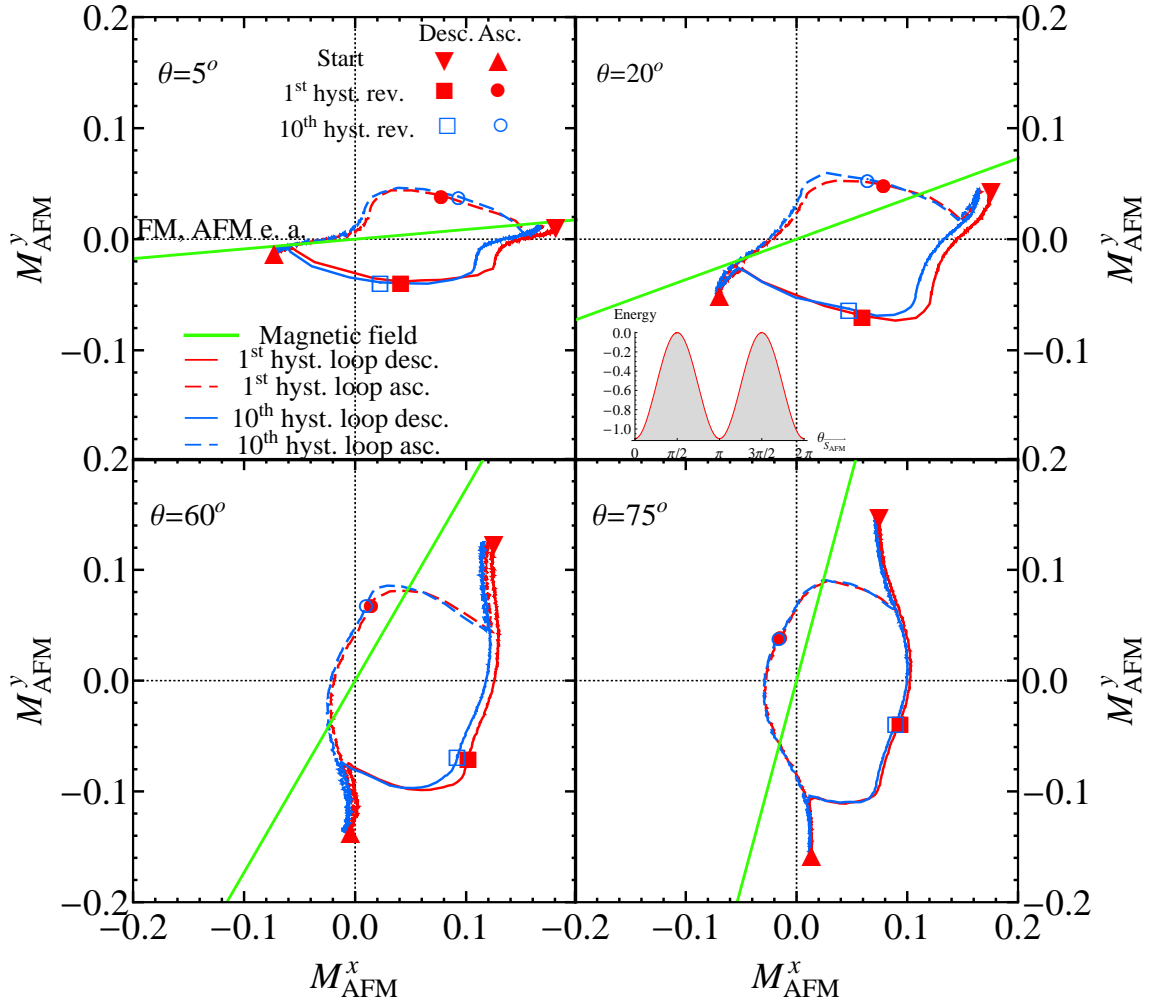


Figure 6.11: In-plane component of magnetization of the first and tenth hysteresis loop of the AFM for $k_{FM} = 0.1J_{FM}$ for several angles between magnetic field and FM easy axis. Inset shows the effective energy of an AFM spin as function of AFM spin angle.

vector of the AFM interface first contracts and then rotates on each reversal for low angles θ . Reversals occurs in both sides. This mechanism changes for higher angles θ . On the descending branch of the hysteresis loop, we have first rotation and then expansion. On the ascending branch of the loop, we have first contraction and then rotation. This happen in an asymmetric way, with the ascending branch having much smaller AFM magnetization vector than the descending branch. Actually, it seems as if the hysteresis cycle of the

magnetization vector is shifted along the x-axis. This is because the AFM interface spins can not pass the energy barrier (h. a.) of the negative y-axis. This is due to the small projection of the spin in the negative easy axis which reduces the exchange field. Finally, the training effect is related to the reduced x-component of the AFM interface magnetization on the descending branch of 10th hysteresis loop. This effect is reduced with increasing angle θ , e.g. for $\theta = 75^\circ$ the x-component of the AFM magnetization vector on the descending branch of the 10th loop is the same as in the 1st loop.

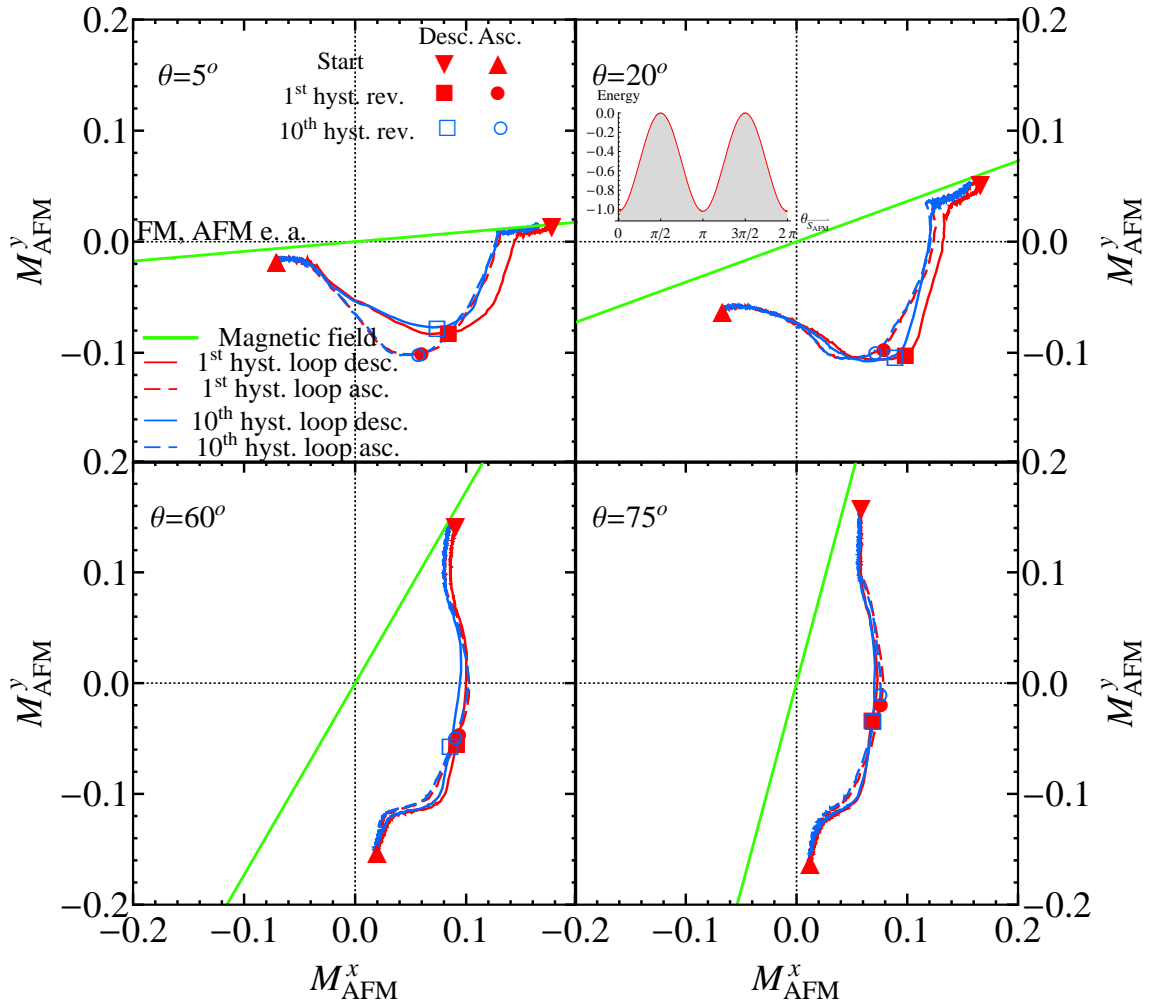


Figure 6.12: In-plane component of magnetization of the first and tenth hysteresis loop of the AFM for $k_{FM} = 0.02J_{FM}$ for several angles between magnetic field and FM easy axis. Inset shows the effective energy of an AFM spin as function of AFM spin angle.

In Fig. 6.12 the in-plane magnetization component of the AFM for several angles between magnetic field and FM easy axis for systems with weak ($k_{FM} = 0.02J_{FM}$) FM anisotropy is shown. As we can see the magnetization vector of the AFM interface is effected a lot from the behavior of the FM with superposition of the AFM anisotropy field. For low angles, the fields created from the FM interaction and the AFM easy axis, help the AFM interface magnetization vector to rotates and pass form the negative y-axis which is a hard axis. The rotation occurs always in the same path for both branches of the loop

for the following reason. For high angles θ , the magnetization vector can pass the energy well on the positive x-axis but can not pass the energy barrier on the negative y-axis. This is because the FM magnetization vector exerts smaller magnetic torque to the AFM magnetization vector, as it is directed up to the magnetic field direction which is quite close to the y-axis.

AFM EB training effect

The dependence of the concentration of stable AFM interfacial spins on the angle θ for the aforementioned systems are shown in Fig. 6.13 for a) intermediate and b) weak FM anisotropy. As we can see, there is always a steep increase of concentration from the first to the second hysteresis cycle, due to fact that many spins were in metastable state after the cooling process. Also in both systems, when the angle θ increases, the stable spins increase. This is because at large angles, the x-component of the magnetic field decreases

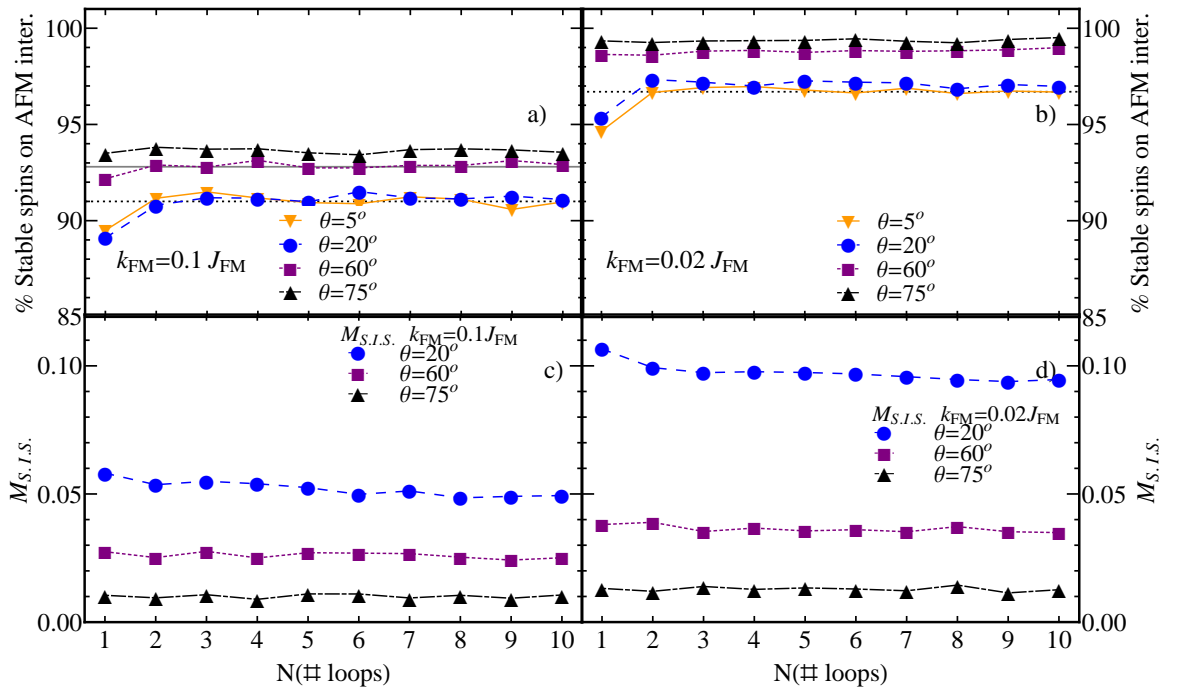


Figure 6.13: Angular dependence of the training effect of the (top) concentration and of the (bottom) magnetization ($M_{S.I.S.}$) of the stable spins in the AFM interface for a system with a), c) $k_{FM} = 0.1 J_{FM}$ and b), d) $k_{FM} = 0.02 J_{FM}$.

and subsequently the applied torque is smaller causing fewer spins to rotate. The increasing stable spins favors smaller $M_{S.I.S.}$, as shown in Fig. 6.13 for c) intermediate and d) weak FM anisotropy, meaning that the stable spins, which point to the negative direction, increase. This is again an effect of the cooling process during which the magnetic field is oriented close to the hard axis. Thus more AFM spins are oriented towards the negative direction than if the magnetic field is oriented close to the positive easy direction.

Furthermore, systems with weak FM anisotropy have more stable spins because the torque created from the FM exchange field is smaller (especially for large angles). This is due to the reversal only from the negative component of the FM magnetization (measured parallel to the orientation of the magnetic field each time). E.g. for $\theta = 75^\circ$ the FM magnetization reverses almost only from the positive M_{FM}^x , thus there is no torque with component in opposite direction for the AFM spins resulting in many stable spins.

6.2.2 Uniaxial FM anisotropy - Biaxial AFM anisotropy (Group II)

FM reversal modes

Now, we will focus our interest on systems in which have uniaxial AFM anisotropy, rather than biaxial. Fig. 6.14 shows consecutive hysteresis loops and the in-plane magnetization components for several angles θ for intermediate and weak FM anisotropy. As we can see the hysteresis loop and the in-plane magnetization for intermediate FM anisotropy has the same behavior as in the previous system (uniaxial anisotropy in both materials, see Fig. 6.8) with the only difference in the value of the coercivity. Thus, the reversal modes remain the same but coercivity is increased which, as we explained in the previous chapter, is an effect of lower energy barriers of the biaxial AFM anisotropy. This leads to reversal of the AFM layer following the reversal of the FM.

For weak FM anisotropy, the reversal modes of the FM are quite different. Firstly, note that the hysteresis loop is larger than for the previous system and now follows the Stoner-Wolfarth model, where the hysteresis loop is becoming less steep with increasing angle θ . The in-plane magnetization is quite different from the previous system and changes rapidly with increasing angle. For large angles, the reversal is coherent with reversal occurring on both sides. For small angles, we have a nonuniform reversal mode with vanishing total magnetization ($\theta = 5^\circ$). Especially for the ascending branches of the loop, the first reversal of the FM spins is coherent and then gradually is converted to incoherent reversal with vanishing total magnetization. This can be seen in Fig. 6.15 in which during the reversal, there are created domains with opposite magnetization leading to zero net magnetization. The reason for this behavior must be found in the reversal modes of the AFM (Sec. 6.2.2) because only the type of the AFM anisotropy is changing in comparison to the systems with uniaxial anisotropy in both materials.

FM EB training effect

Our results for the angle θ dependence of the training effect for the aforementioned systems and quantities are shown in Fig. 6.16. The EB field for systems with weak and

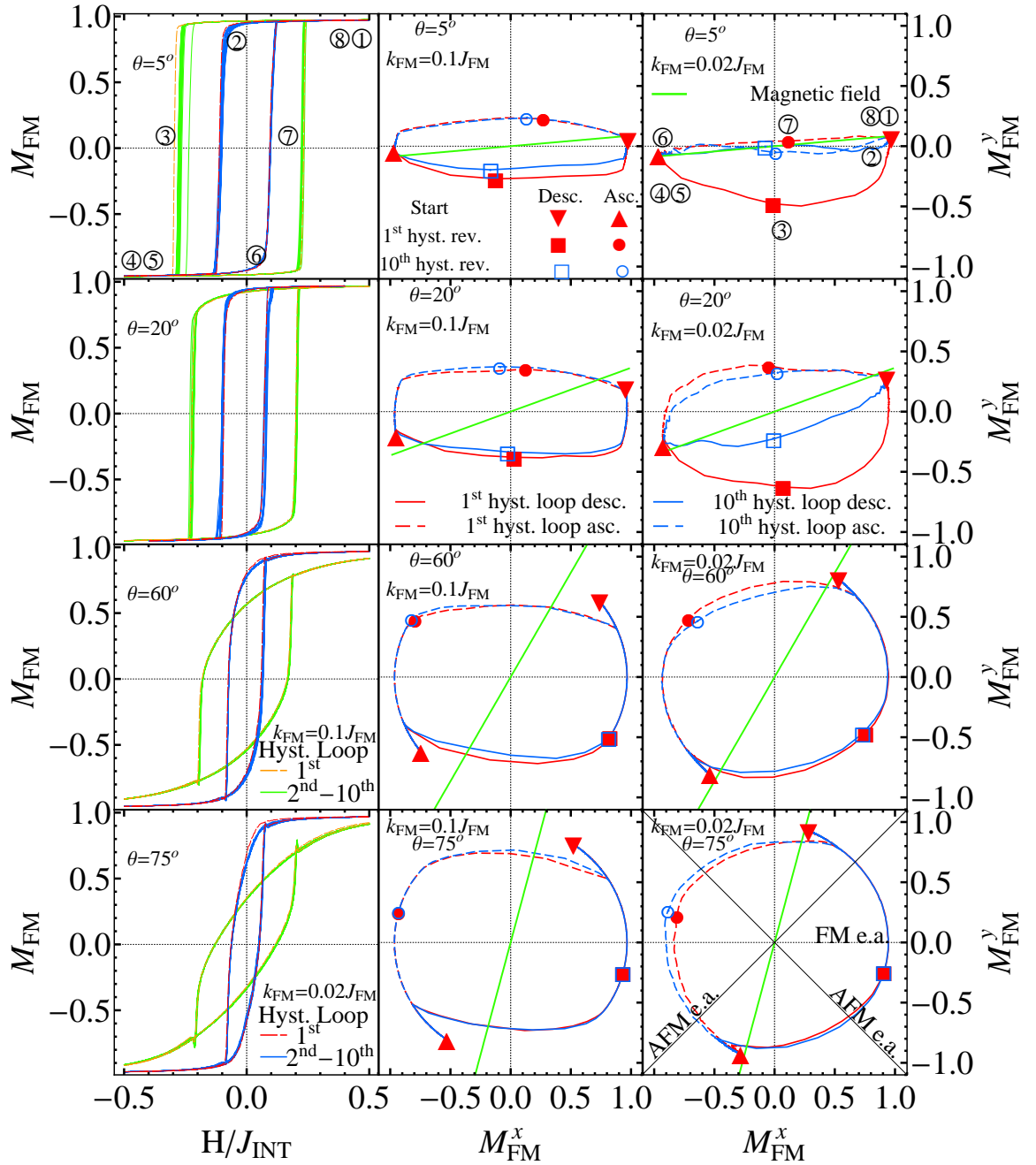


Figure 6.14: Different components of magnetization for several angles between magnetic field and FM easy axis. Left: Hysteresis loop of the first and subsequent cycles of the FM for systems with $k_{FM} = 0.1J_{FM}$ and $k_{FM} = 0.02J_{FM}$. Middle: In-plane component of magnetization of the first and second cycle of the FM for systems with $k_{FM} = 0.1J_{FM}$. Right: In-plane component of magnetization of the first and second cycle of the FM for systems with $k_{FM} = 0.02J_{FM}$. The green line in middle and left figures is the magnetic field axis. The numbers correlate the pathway of the hysteresis loop (left) with the in-plane magnetization component (right).

6.2. Influence of angle between easy axis and magnetic field

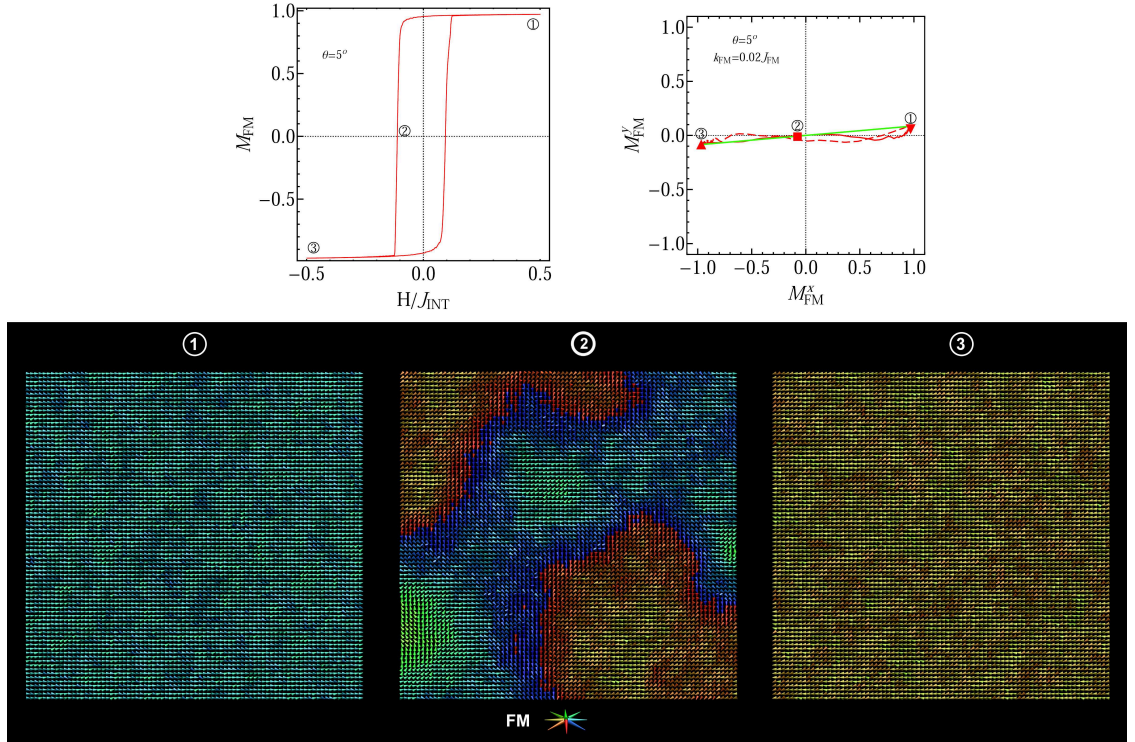


Figure 6.15: FM spin configuration snapshots for a system with $k_{FM} = 0.02J_{FM}$ for $\theta = 5^\circ$ and biaxial AFM anisotropy, where incoherent reversal with vanishing total magnetization is seen (②). The number on the top of every snapshot is indicating the respective point in the hysteresis loop (top).

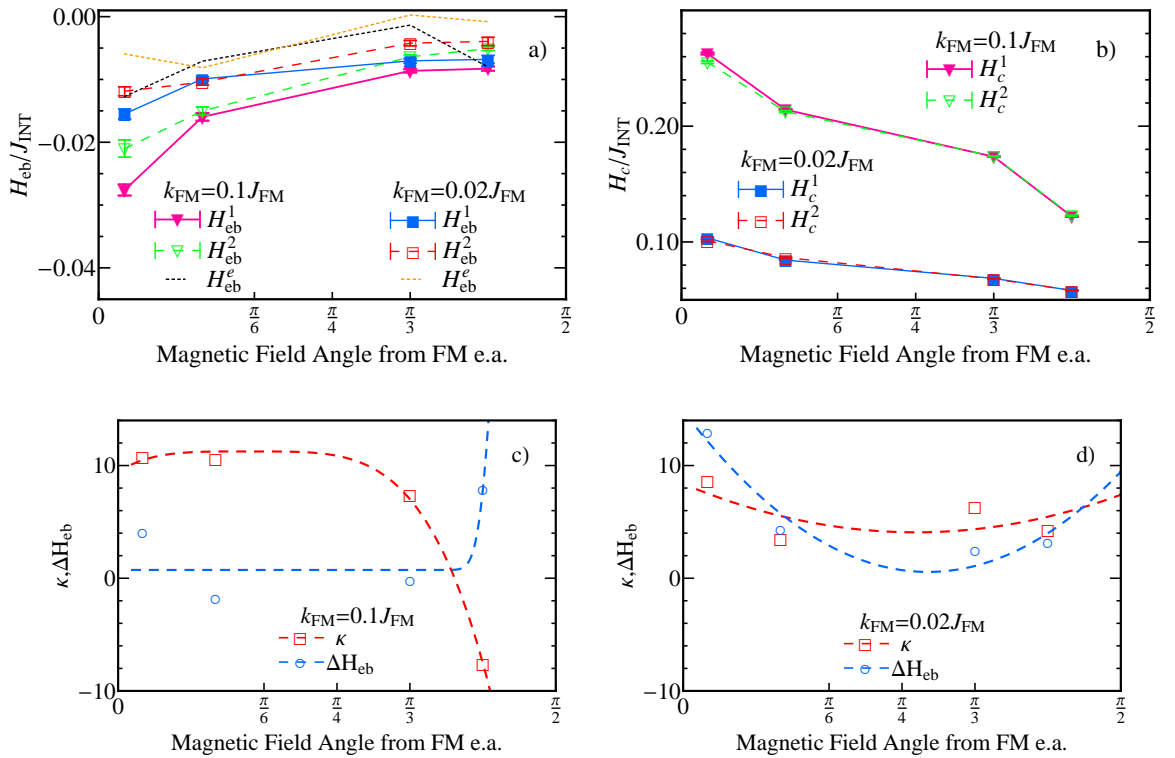


Figure 6.16: Dependence of the training effect on magnetic field angle for a) EB field and of b) coercivity for systems with $k_{FM} = 0.1J_{FM}$ and $k_{FM} = 0.02J_{FM}$. Magnetic field's angle dependence of the normalized fitting law parameter κ and ΔH_{eb} for systems with c) $k_{FM} = 0.1J_{FM}$ and d) $k_{FM} = 0.02J_{FM}$.

intermediate FM anisotropy decreases with increasing angle θ , as previously. For low values of angle θ , systems with weak FM anisotropy have larger EB field but this behavior reverses for larger angles ($\theta > 45^\circ$). Coercivity decreases with increasing angle θ , as is predicted from the Stoner-Wolfarth model and weak FM anisotropy systems are always have smaller coercivity values in comparison to the systems with intermediate FM anisotropy.

As we can see from the Fig. 6.16, the training effect is always quite large in both systems. This can be seen from the trend of κ where, in both cases, it remains almost constant with large value (thermal training) independently of the angle θ . For the case of intermediate FM anisotropy with $\theta = 75^\circ$, κ is negative showing that the hysteresis loop is moving more to the left with consecutive cycles. ΔH_{cb} for this case have large value but in general for intermediate anisotropy its value remains low. For weak FM anisotropy, it has a minimum at around 45° and large values at the edges.

AFM interface reversal modes

In Fig. 6.17 the in-plane magnetization component of the AFM for several angles be-

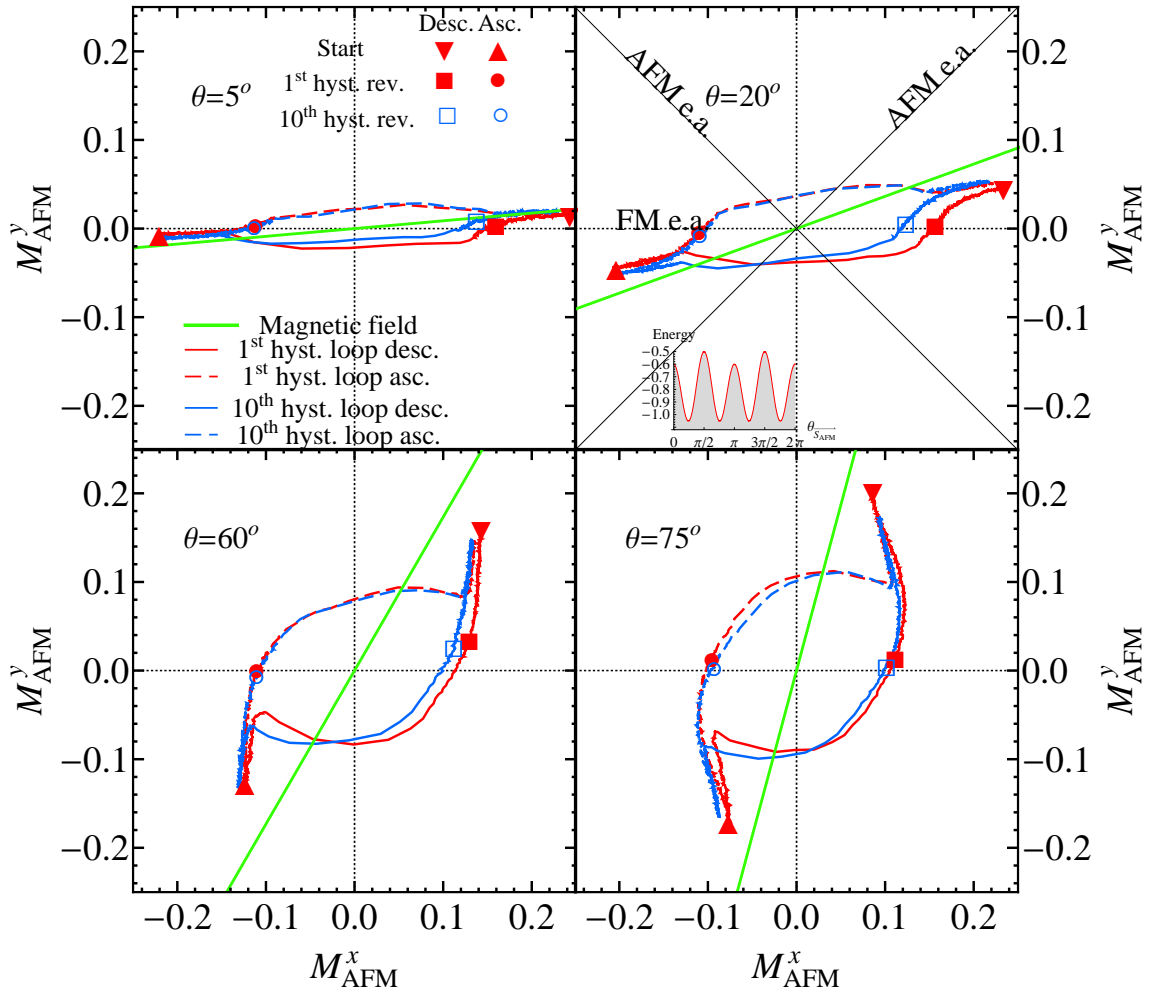


Figure 6.17: In-plane component of magnetization of the first and tenth hysteresis loop of the AFM for $k_{FM} = 0.1J_{FM}$ for several angles between magnetic field and FM easy axis. Inset shows the effective energy of an AFM spin as function of AFM spin angle.

tween magnetic field and FM easy axis for the case of intermediate ($k_{FM} = 0.1J_{FM}$) FM anisotropy is shown. As we can see the magnetization vector of the AFM interface for small angles reverses with almost vanishing magnetization, but with increasing angle θ the reversal occurs more coherently with the vector of AFM magnetization having increasing transverse (in respect to the magnetic field axis) component. This is due to the large torque exerted by the FM as the FM easy axis is along the x-axis.

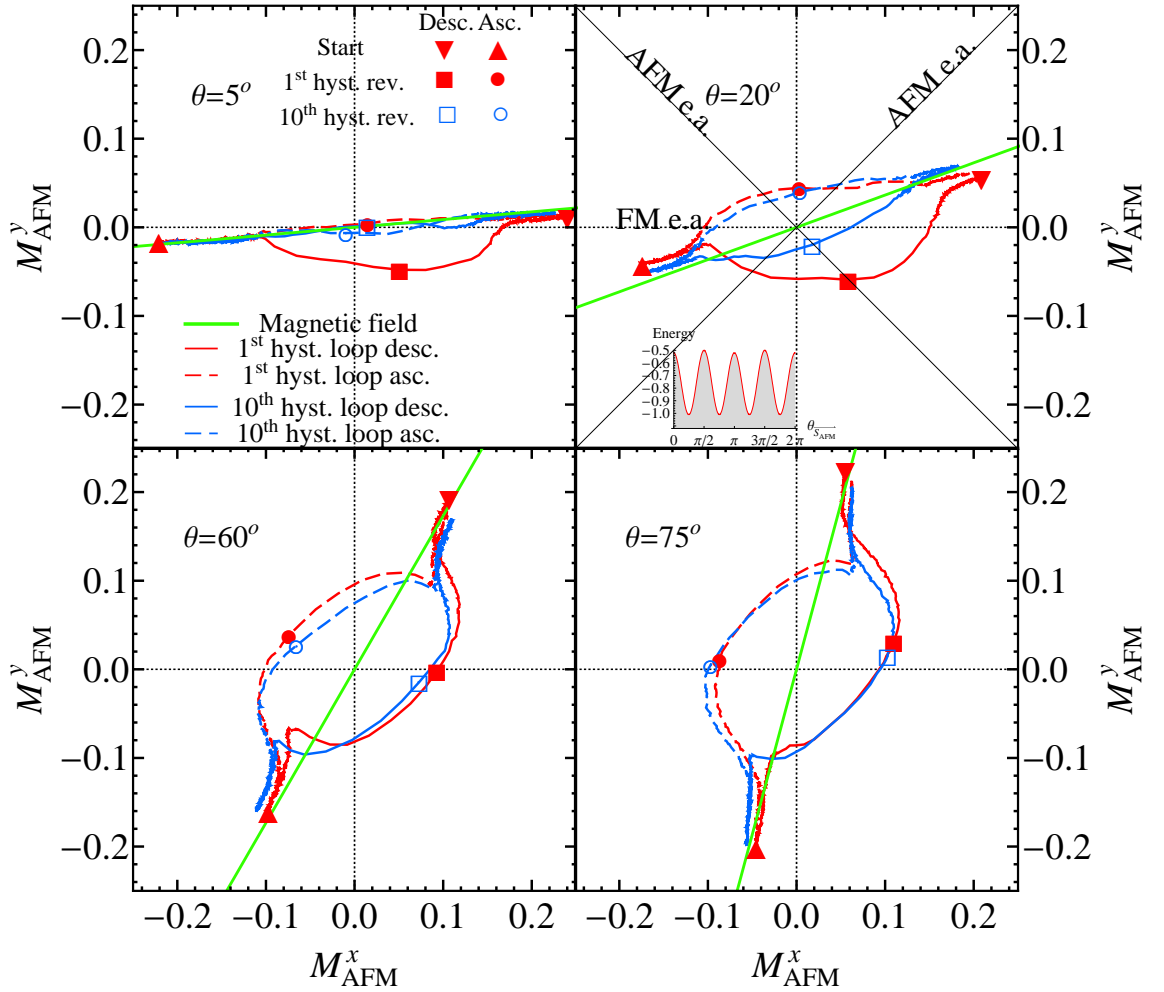


Figure 6.18: In-plane component of magnetization of the first and tenth hysteresis loop of the AFM for $k_{FM} = 0.02J_{FM}$ for several angles between magnetic field and FM easy axis. Inset shows the effective energy of an AFM spin as function of AFM spin angle.

Fig. 6.18 shows the in-plane magnetization component of the AFM for several angles between magnetic field and FM easy axis for systems with weak ($k_{FM} = 0.02J_{FM}$) FM anisotropy. For low angles the vector of the AFM interface magnetization during the first reversal has a negative value but after that has zero value (vanishing magnetization). This is because during the cooling process many spins are align along the 45° AFM easy axis which is the closer one. Then during the first cycle, they rotate and stabilize in the next easy axes they found (-45° and -135°). This is happening because along that easy axis the torque created by the negative magnetic field is too small to rotate them due

to large angle between negative magnetic field and the easy axis. For large θ angles, the aforementioned angle is smaller and subsequently the torque is much bigger. Thus the spins are not stabilized in these easy axes and thus coherent behavior is exhibited.

AFM EB training effect

The dependence of the concentration of stable AFM interfacial spins on the angle θ for the aforementioned systems is shown in Fig. 6.19 for a) intermediate and b) weak FM anisotropy. There is always a much larger step increase of concentration from the first to the second hysteresis cycle in comparison to the systems with uniaxial AFM anisotropy. Again this is an effect of the cooling process in addition to the fact that now the spins have two more stable axes. During the cooling process most spins orient along the one of the easy axes, however the energy barriers are too small to provide long-term stability since many spins are switched irreversibly during the first cycle.

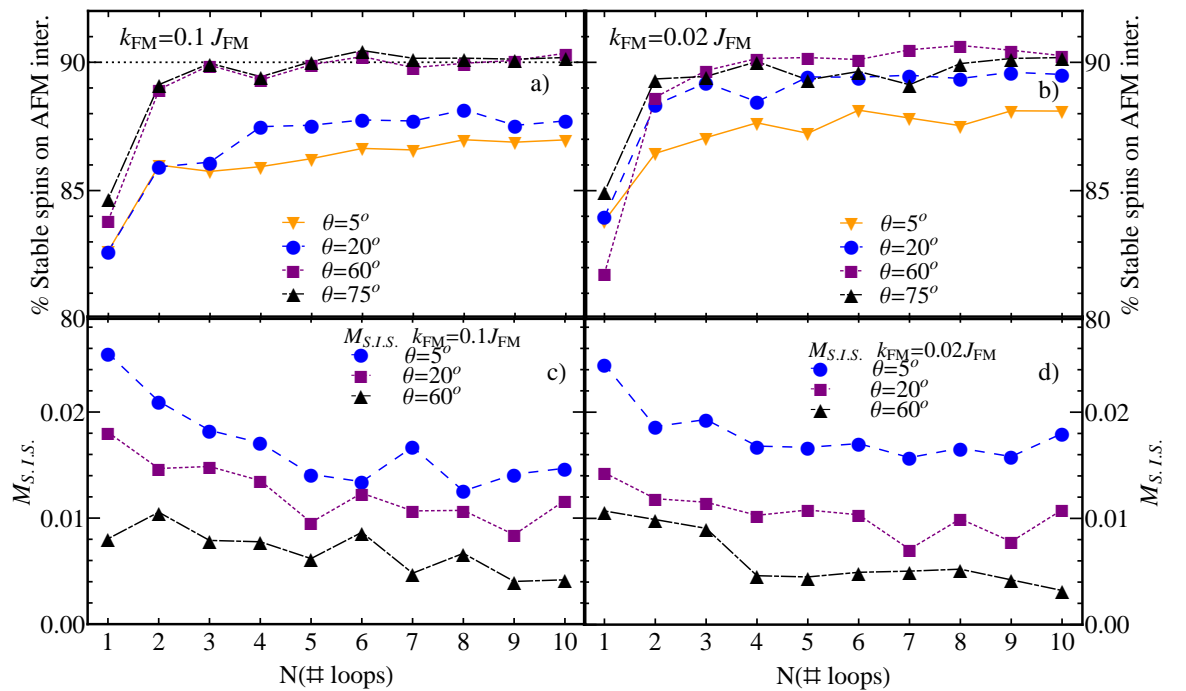


Figure 6.19: Angular dependence of the training effect of the (top) concentration and of the (bottom) magnetization ($M_{S,I.S.}$) of the stable spins in the AFM interface for a system with a), c) $k_{FM} = 0.1 J_{FM}$ and b), d) $k_{FM} = 0.02 J_{FM}$.

6.2.3 Biaxial FM anisotropy - Biaxial AFM anisotropy (Group III)

FM reversal modes

Now, will focus our interest in systems with biaxial anisotropy in both of the materials. Fig. 6.20 shows consecutive hysteresis loops and the in-plane magnetization components

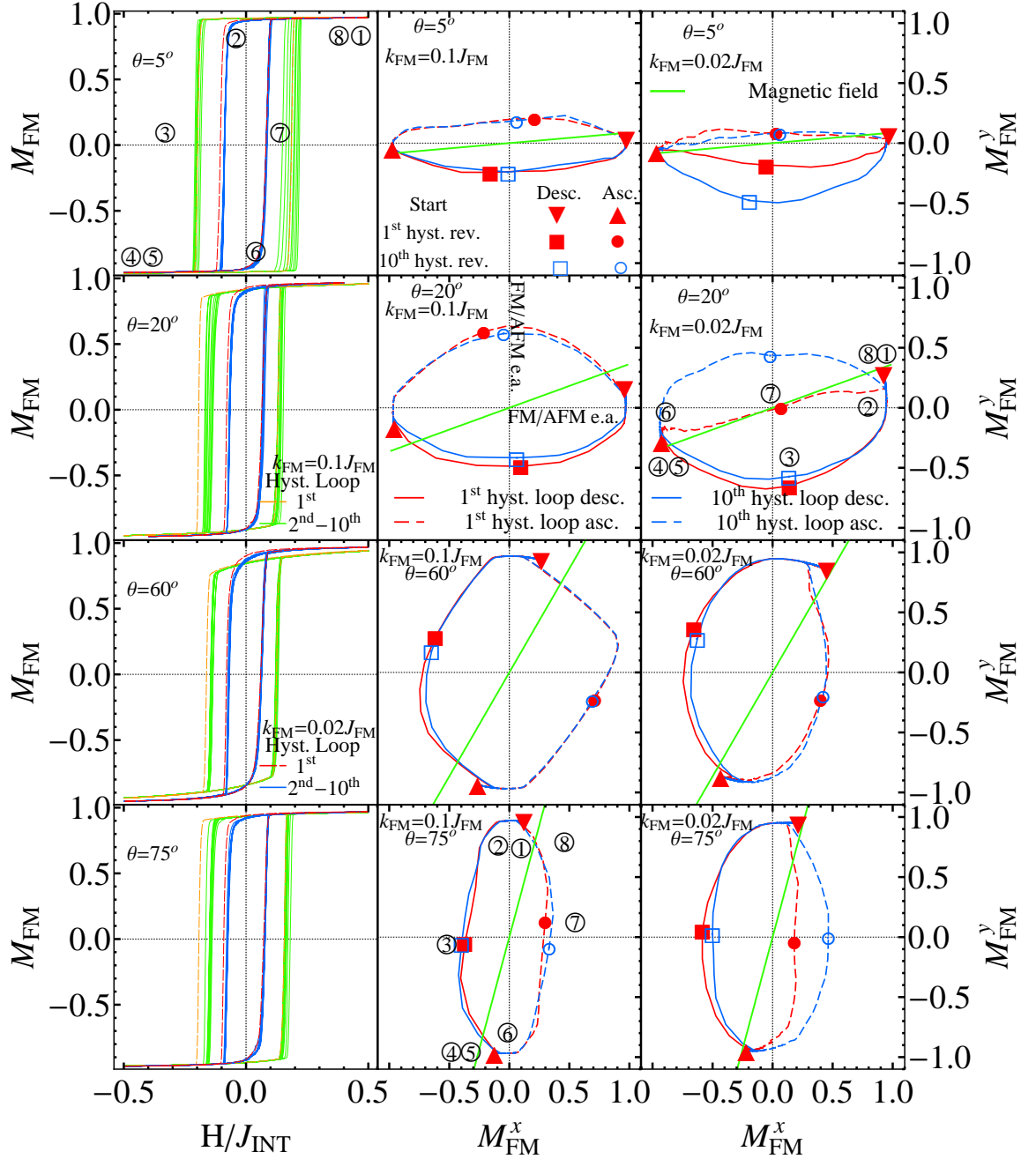


Figure 6.20: Different components of magnetization for several angles between magnetic field and FM easy axis. Left: Hysteresis loop of the first and subsequent cycles of the FM for systems with $k_{FM} = 0.1J_{FM}$ and $k_{FM} = 0.02J_{FM}$. Middle: In-plane component of magnetization of the first and second cycle of the FM for systems with $k_{FM} = 0.1J_{FM}$. Right: In-plane component of magnetization of the first and second cycle of the FM for systems with $k_{FM} = 0.02J_{FM}$. The green line in middle and left figures is the magnetic field axis. The numbers correlate the pathway of the hysteresis loop (left) with the in-plane magnetization component (right).

for several angles θ for intermediate and weak FM anisotropy. As we can see, the hysteresis loop becomes less steep with increasing angle θ up to 45° (hard axis). For larger angles, the hysteresis loop becomes steep again.

For both weak and intermediate FM anisotropies, the reversal modes of the FM change rapidly with the angle θ . When angle θ is smaller than 45° , the FM magnetization rotates coherently, beginning and ending each reversal from the x-axis and always having definite y-component (during the reversal). When angle θ is bigger than 45° , the aforementioned procedure is rotated by 90° . This is due to the second easy axis along the y-direction. Thus the reversal procedure is symmetrical along the 45° axis.

For weak FM anisotropy, another interesting effect occurs for magnetic fields oriented close to the easy axes. The first or the second reversal is nonuniform with vanishing total magnetization but then the reversal becomes gradually more coherent, with definite transverse component. This is more apparent for angles away from 45° , e.g. for 20° for the descending branch of the loop, the reversal is always coherent but for the ascending branch, it is nonuniform with vanishing magnetization in the first loop. However, there is a gradual transition to coherent rotation, as shown by the tenth cycle loop in Fig. 6.20. The reason for this behavior must again be found in the reversal modes of the AFM (Sec. 6.2.2) as is considered a result of the training effect.

FM EB training effect

Our results for the angle θ dependence of the training effect for the aforementioned systems and quantities are shown in Fig. 6.21. The EB field for systems with weak and intermediate FM anisotropy, it seems, to have a minimum as a function of angle θ . Systems with weak FM anisotropy have always smaller EB field as well as training effect. Coercivity also seems to have a minimum as a function of angle θ along the hard axis, as is predicted from the Stoner-Wolfarth model. Furthermore, weak FM anisotropy systems always have smaller coercivity values in comparison to the systems with intermediate FM anisotropy. The above results for the EB field and the coercivity have the same trend with the results presented on Ref.[140], although their system had the hard axis in y direction and they found positive EB for angles larger than the hard axis direction. Thus, similarly the data satisfy the condition $H_{eb}(\theta + \pi/4) = H_{eb}(\theta)$ and $H_c(\theta + \pi/4) = H_c(\theta)$.

As we can see from the Fig. 6.21, the training effect is always quite large in both systems and leads to zero EB field. This can be seen from the trend of κ , where both cases have large value (thermal training) independently of the angle θ . For the case of intermediate FM anisotropy, κ has a maximum in 45° angle but a minimum for the case of weak FM anisotropy. ΔH_{eb} for both cases have large value and minimum in 45° angle.

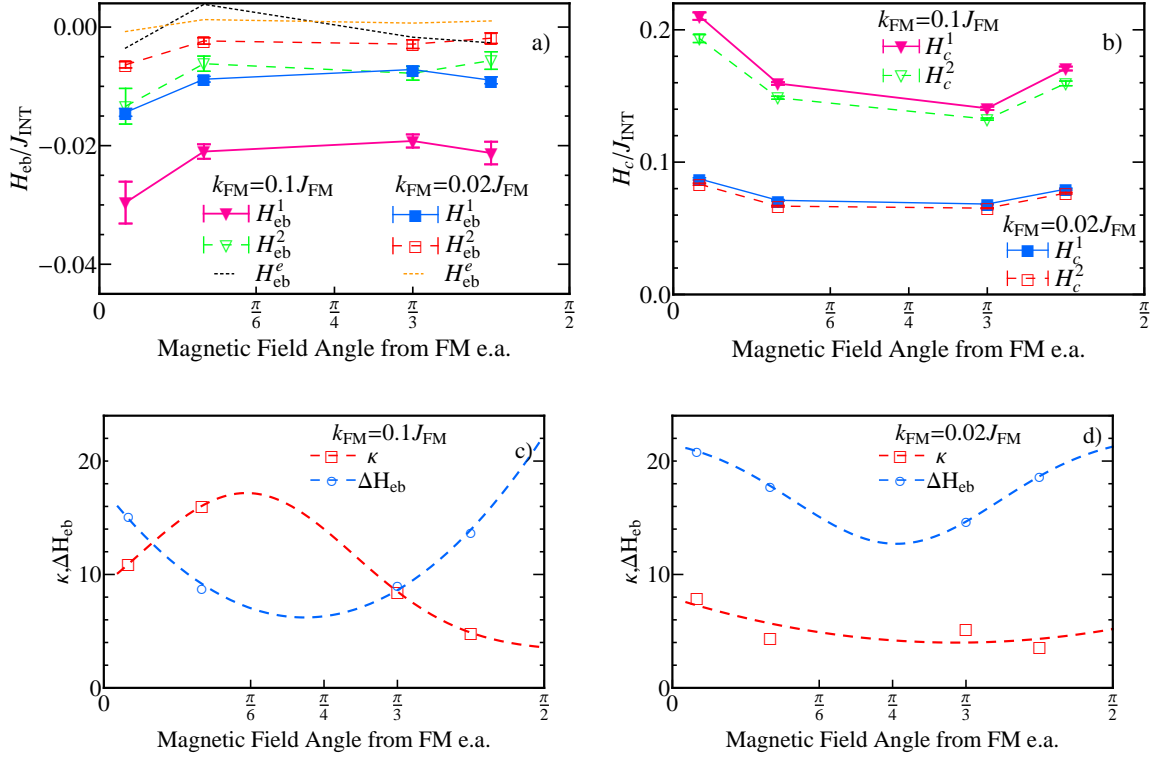


Figure 6.21: Dependence of the training effect on magnetic field angle for a) EB field and of b) coercivity for systems with $k_{FM} = 0.1J_{FM}$ and $k_{FM} = 0.02J_{FM}$. Magnetic field's angle dependence of the normalized fitting law parameter κ and ΔH_{eb} for systems with c) $k_{FM} = 0.1J_{FM}$ and d) $k_{FM} = 0.02J_{FM}$.

AFM interface reversal modes

In Fig. 6.22 the in-plane magnetization component of the AFM for several angles between magnetic field and FM easy axis for the case of intermediate ($k_{FM} = 0.1J_{FM}$) FM anisotropy is shown. As we can see the magnetization vector of the AFM interface has the same behavior as for systems with uniaxial FM and biaxial AFM anisotropy (Sec. 6.2.2) rotated in order to make the easy axes to coincide. Fig. 6.23 shows the in-plane magnetization component of the AFM for several angles between magnetic field and FM easy axis for systems with weak ($k_{FM} = 0.02J_{FM}$) FM anisotropy. The results for large angles ($\theta = 60^\circ, 75^\circ$) are the same as for intermediate FM anisotropy.

For low angles, the behavior of the AFM magnetization vector is more complicated. While during the first reversal the magnetization rotates coherently with definite y component, the second reversal is noncoherent with vanishing magnetization. This reversal is gradually converted to coherent rotation with definite y component. For understanding this procedure we will describe what happens in cooling process and in the first reversals for $\theta = 20^\circ$ as follows:

1. Cooling process: Most of the AFM spins are aligned along positive x-axis as being the closest energy minimum. This orientation is quite energetically favorable as being

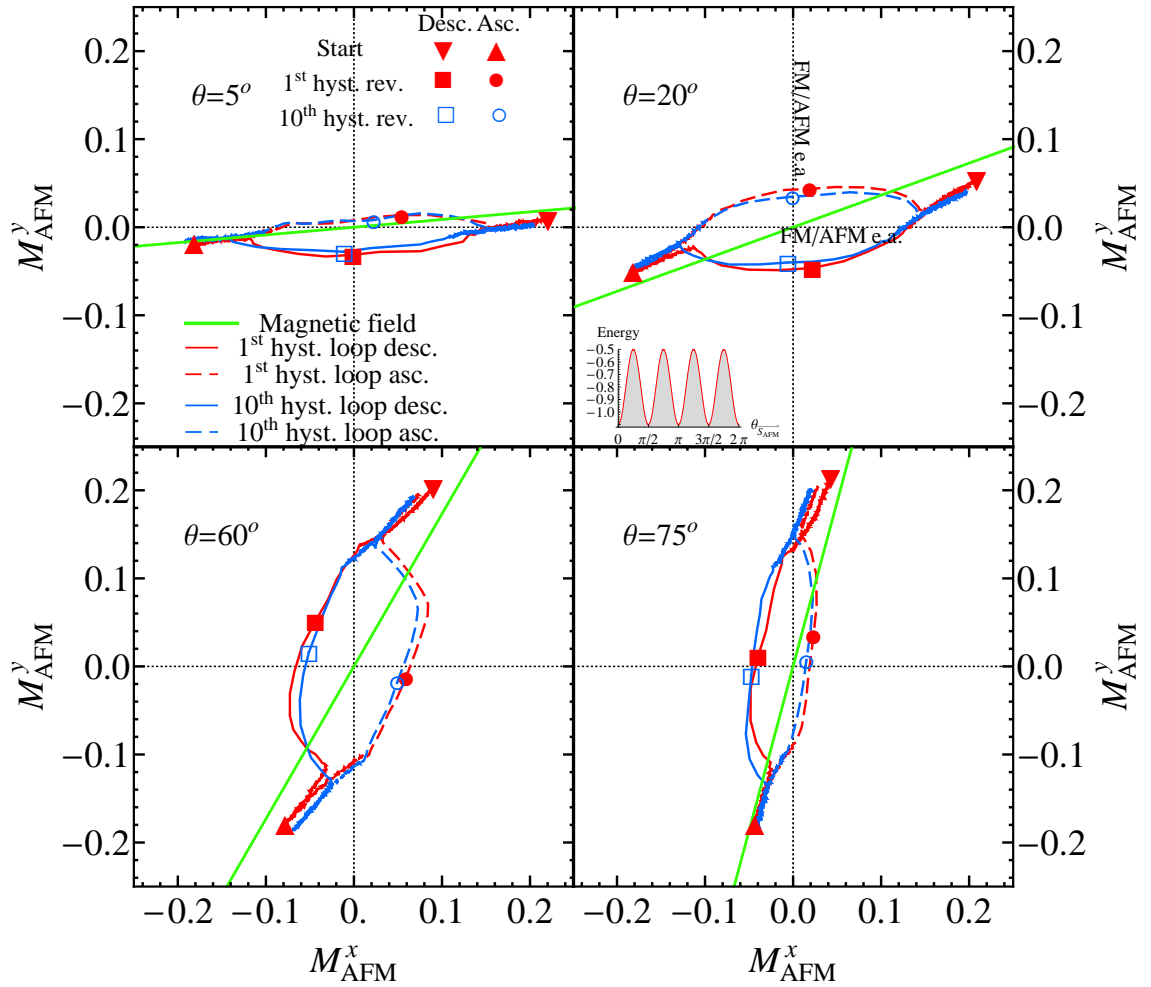


Figure 6.22: In-plane component of magnetization of the first and tenth hysteresis loop of the AFM for $k_{FM} = 0.1J_{FM}$ for several angles between magnetic field and FM easy axis. Inset shows the effective energy of an AFM spin as function of AFM spin angle.

an easy axis for both AFM and FM.

2. 1st reversal: Many spins are aligned with the negative y-axis after a coherent rotation. The increasing negative torque (negative magnetic field) which is exerted to the initially positive x-axis oriented spins is not big enough to flip them to the negative x-axis.
3. 2nd reversal: The increasing positive torque (positive magnetic field) which is exerted to the negative y-axis oriented spins can not rotate them. Thus, there is a reversal with vanishing magnetization.
4. 3rd reversal: Similar to first reversal but now the most of the spins are stabilized pointing in positive x-axis and negative y-axis. The increasing negative torque which is exerted to the negative y-axis spins rotate many of them to the negative x-axis.
5. 4th reversal (Yellow points in Fig. 6.23): Spins reverse through the negative x-axis where one of the easy axes is.

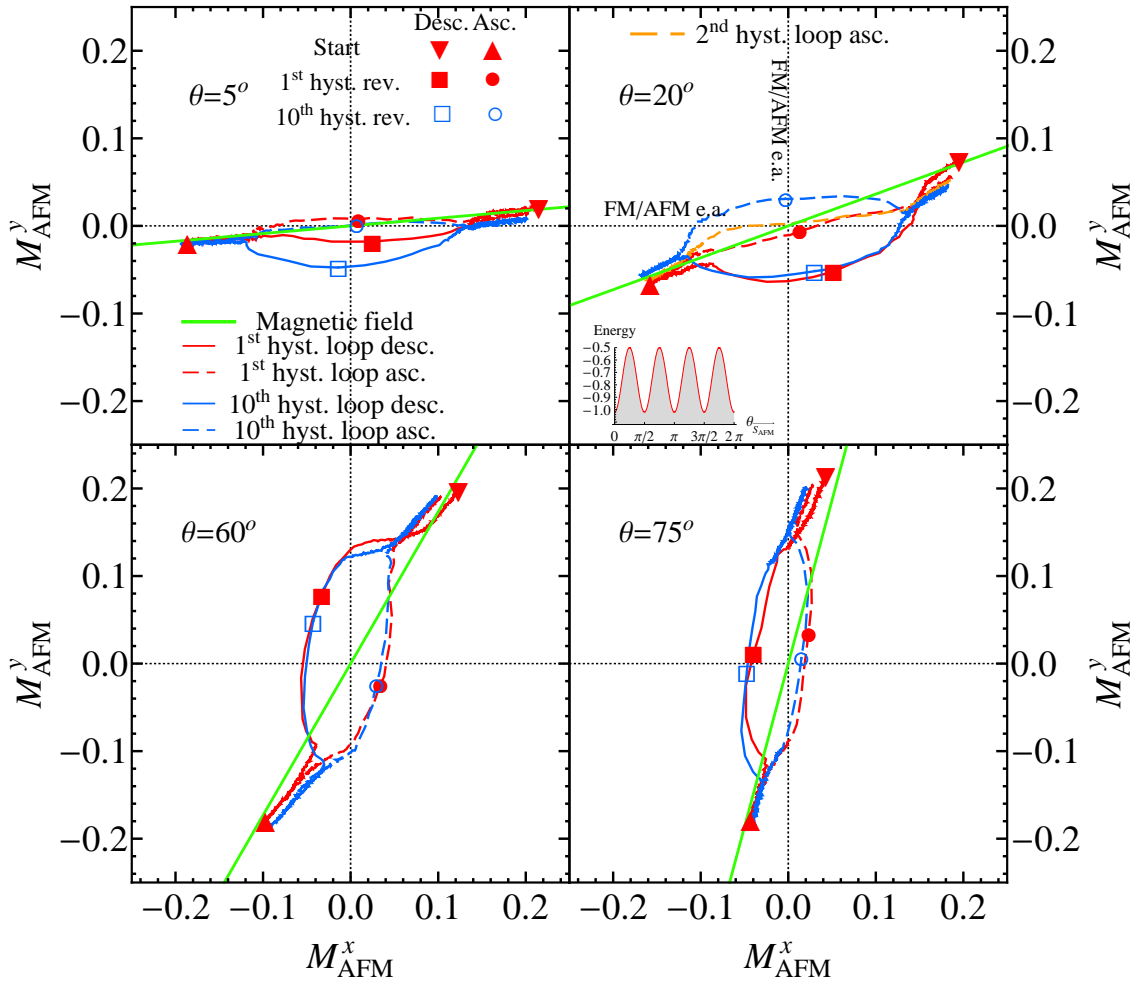


Figure 6.23: In-plane component of magnetization of the first and tenth hysteresis loop of the AFM for $k_{FM} = 0.02J_{FM}$ for several angles between magnetic field and FM easy axis. Inset shows the effective energy of an AFM spin as function of AFM spin angle.

The increasing positive torque which is exerted to the negative x-axis oriented spins, during the ascending branch after the first cycle (4^{th} , 6^{th} , ... reversal), rotates even more spins through the negative x-axis and the positive y-axis. After that, many spins are stabilized along these axes. Thus, the reversal becomes coherent with definite y component. The results for the stability of the AFM spins are similar with the previous case of biaxial AFM anisotropy, thus are not presented.

6.2.4 Biaxial FM anisotropy - Uniaxial AFM anisotropy (Group V)

FM reversal modes

An EB system with biaxial FM and uniaxial AFM anisotropy is the last combination of anisotropies that we will investigate. The reversal modes of the FM for this system when

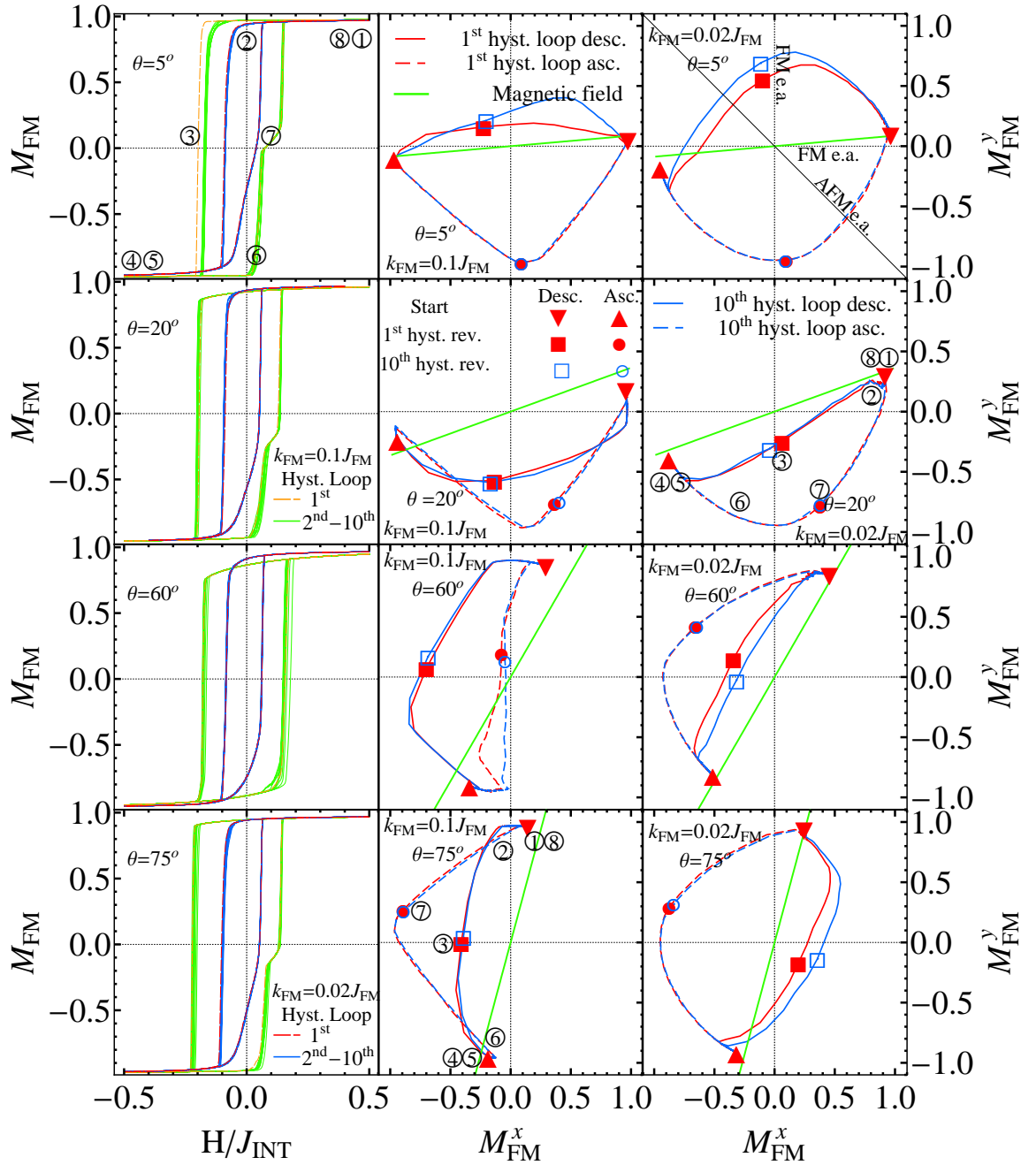


Figure 6.24: Different components of magnetization for several angles between magnetic field and FM easy axis. Left: Hysteresis loop of the first and subsequent cycles of the FM for systems with $k_{FM} = 0.1 J_{FM}$ and $k_{FM} = 0.02 J_{FM}$. Middle: In-plane component of magnetization of the first and second cycle of the FM for systems with $k_{FM} = 0.1 J_{FM}$. Right: In-plane component of magnetization of the first and second cycle of the FM for systems with $k_{FM} = 0.02 J_{FM}$. The green line in middle and left figures is the magnetic field axis. The numbers correlate the pathway of the hysteresis loop (left) with the in-plane magnetization component (right).

we have intermediate ($k_{FM} = 0.1J_{FM}$) or weak ($k_{FM} = 0.02J_{FM}$) FM anisotropy are shown in Fig. 6.24. The easy axis of the AFM are at 45° from the FM easy axes. Similar to the previous system, the reversal procedure is symmetrical along the 45° axis due to the second easy axis long the y-direction. Also, the reversals, almost in all cases (all angles, intermediate and weak FM anisotropy) occur on the same path as that of the first reversal (descending branch of the loop). This is an effect caused from the AFM interface magnetization and will be discussed in the next section.

As we can see in the hysteresis loop for intermediate FM anisotropy, there is a steep increase (a step close to zero magnetization) in the positive coercive field in the ascending branch of the hysteresis loop. This can be considered a two stage reversal, one before and one after zero magnetization. Similarly, for the hysteresis loop for weak FM anisotropy, there is a more gradual increase in the coercive field. This effect can be seen in the magnetization (in-plane) vector diagrams, as the angle in the trajectory of the magnetization vector (after point © in Fig. 6.24). That means that during reversal the magnetization is oriented along the transverse negative FM easy axis (y-axis) and finally along the positive FM easy axis (x-axis). Again, this is an effect of the AFM interface magnetization and the AFM easy axis.

FM EB training effect

Our results for the angle θ dependence of the training effect for the aforementioned systems and quantities are shown in Fig. 6.25. The EB field for systems with weak and intermediate FM anisotropy seems to have a minimum as a function of angle θ . Systems with weak FM anisotropy have always smaller EB field as well as training effect. There is no clear trend for coercivity as its calculation, is affected by the aforementioned step increase on the ascending loop branch. The training effect in systems with the aforementioned anisotropies, is quite small for large angles. For small angles ($\theta = 5^\circ$), the training effect is quite intense (thermal training), as can be seen from Fig. 6.25a), b).

AFM interface reversal modes

Fig. 6.26 shows the in-plane magnetization component of the AFM for several angles between magnetic field and FM easy axis for the case of intermediate ($k_{FM} = 0.1J_{FM}$) FM anisotropy. As we can see the magnetization vector of the AFM interface has similar behavior to systems with uniaxial FM and AFM anisotropy (Sec. 6.2.1). The AFM reverses from the same side as the FM during the descending branch of the loop but during the ascending can not reverse through the opposite side as the magnetization vector can not cross the energy barrier created by the AFM hard axis. Now, because of that, the AFM, through the interface interaction, does not let the FM reverse from the other side. Further-

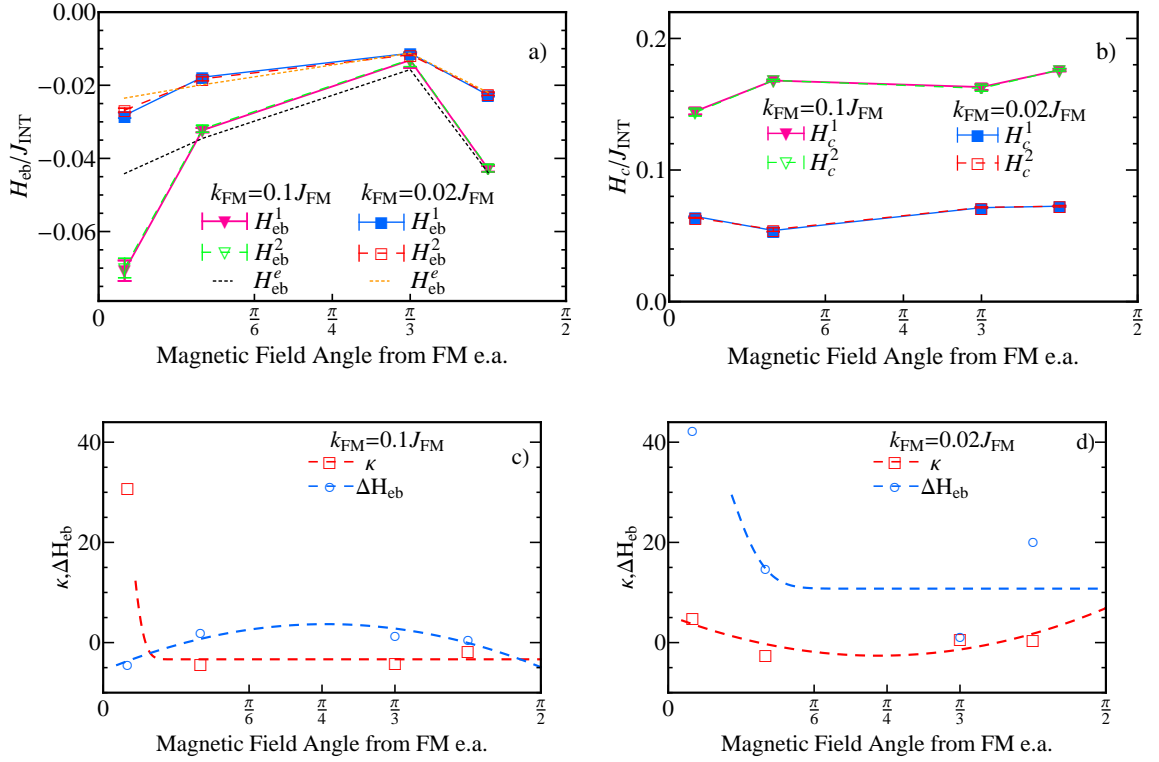


Figure 6.25: Dependence of the training effect on magnetic field angle for a) EB field and of b) coercivity for systems with $k_{FM} = 0.1J_{FM}$ and $k_{FM} = 0.02J_{FM}$. Magnetic field's angle dependence of the normalized fitting law parameter κ and ΔH_{eb} for systems with c) $k_{FM} = 0.1J_{FM}$ and d) $k_{FM} = 0.02J_{FM}$.

more, the AFM magnetization, during the tenth ascending reversal and when the magnetic field becomes positive, reverses very “early”. This is because many AFM spins are oriented along the AFM hard axis which is an unstable state. Thus, they need very small torque to start rotating and subsequently rotate “earlier”. Through the FM/AFM interaction, they subsequently affect the behavior of the FM. Similarly, for weak FM anisotropy, this occurs more gradually, as is shown in Fig. 6.27. The results for the stability of the AFM spins are similar with the previous case of uniaxial AFM anisotropy, thus are not presented.

6.3 Summary

We examined the training effect in a large set of anisotropies in EB systems. Uniaxial, biaxial and cubic type of anisotropies were used in all the possible combinations in the AFM and the FM. Furthermore, the anisotropy constants were varied to create strong, intermediate and weak anisotropy in the materials. Comparing the results, we focus on systems with strong EB field and training effect. These are for strong AFM anisotropy and weak as well as intermediate FM anisotropy. Then according to the reversal modes during consecutive hysteresis cycles, we focus only on systems with uniaxial and biaxial anisotropies.

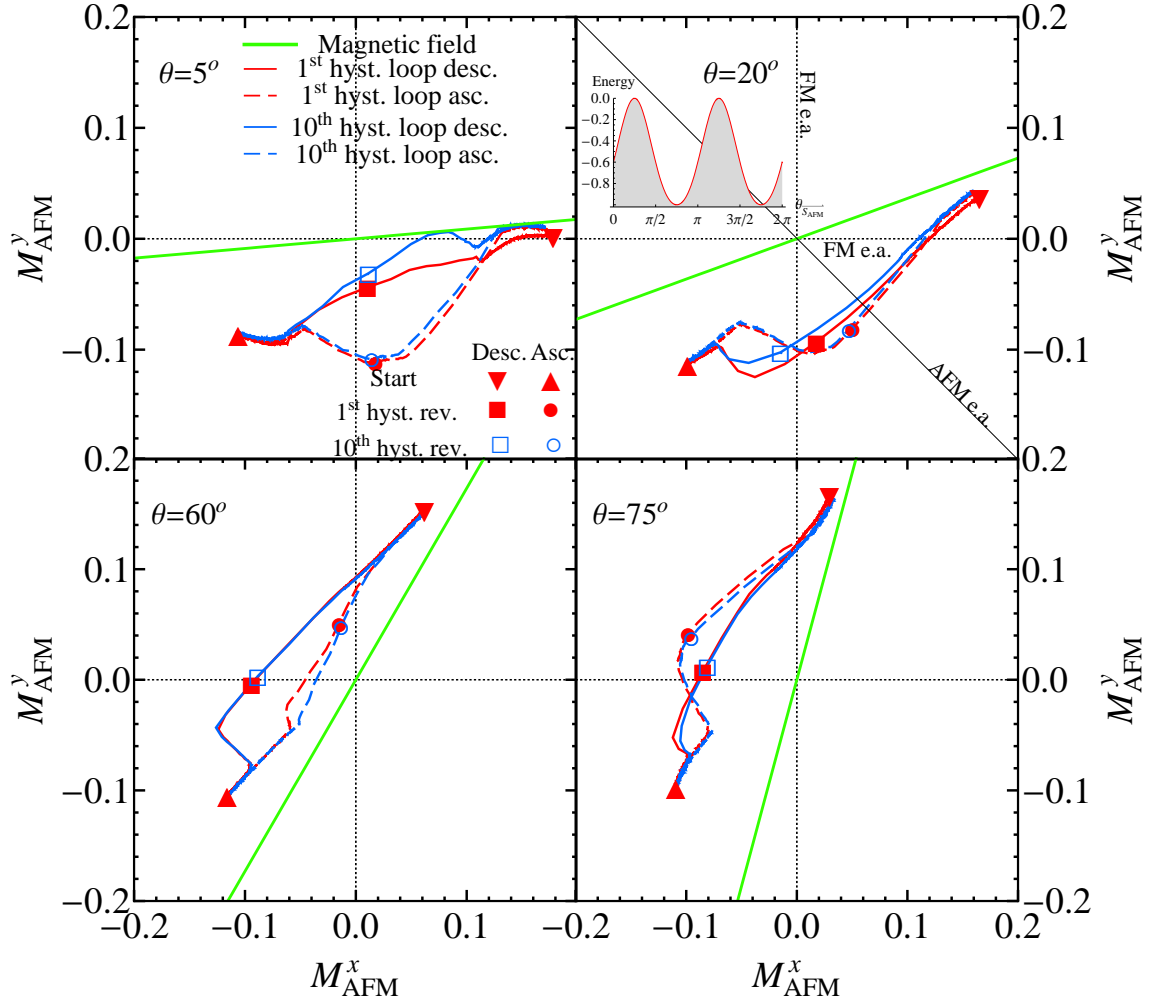


Figure 6.26: In-plane component of magnetization of the first and tenth hysteresis loop of the AFM for $k_{FM} = 0.1J_{FM}$ for several angles between magnetic field and FM easy axis. Inset shows the effective energy of an AFM spin as function of AFM spin angle.

Each possible combination of uniaxial and biaxial anisotropies is investigated solely for different magnetic field angles. According to the behavior of the reversal modes during consecutive hysteresis loops, they can be categorized in three types:

1. The reversal mode remains the same during consecutive hysteresis loops and usually occurs with coherent or non-coherent rotation.
2. The reversal mode is with vanishing magnetization during the first hysteresis loop but evolves gradually to a coherent rotation with increasing cycles.
3. The reversal mode is via coherent rotation during the first hysteresis loop but it is converted to a non-coherent rotation with vanishing magnetization.

The above effects can occur under specific anisotropy conditions, which actually is hidden in the topological characteristics (position, values) of the energy barriers and minima. Specifically, the last two reversal modes are presented in systems with biaxial AFM

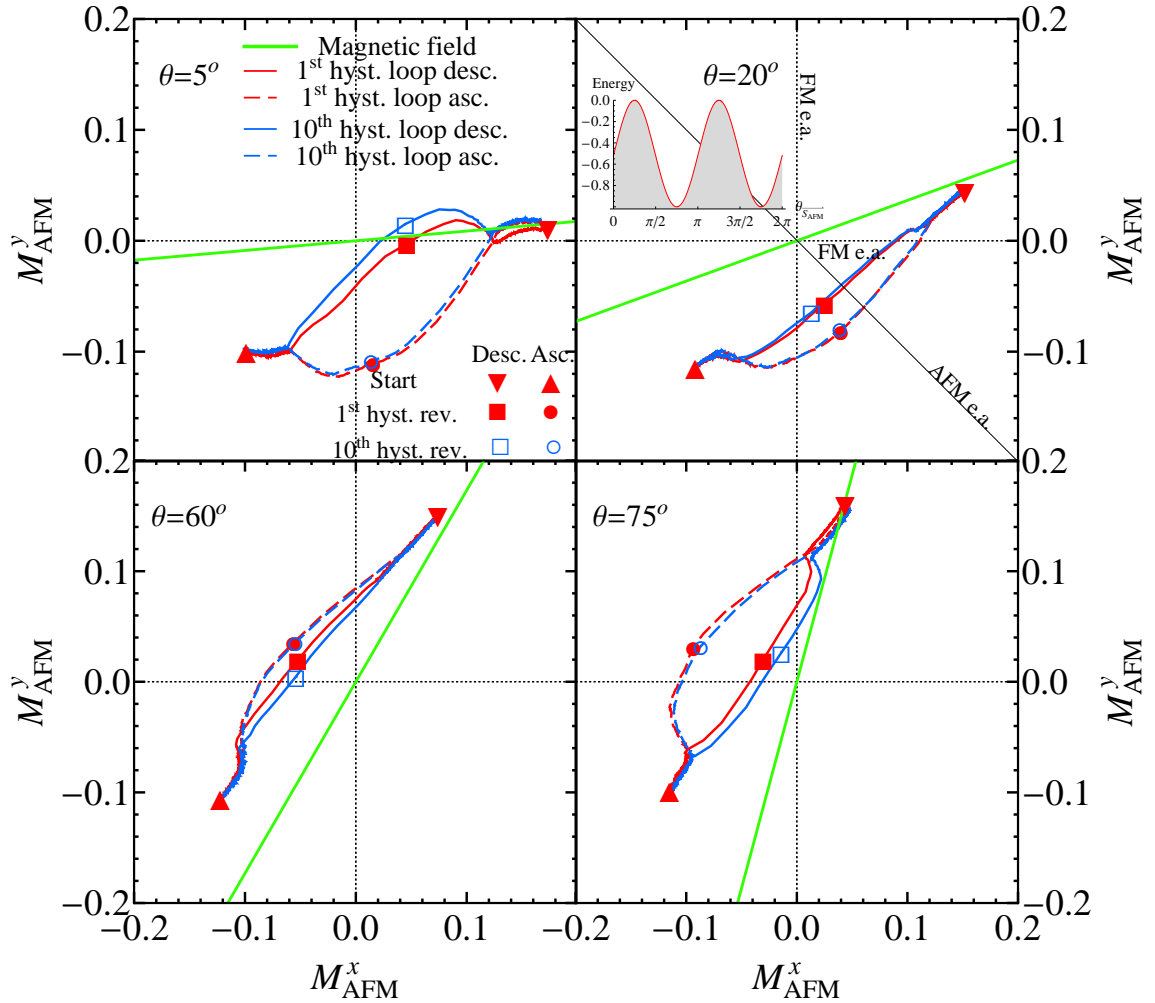


Figure 6.27: In-plane component of magnetization of the first and tenth hysteresis loop of the AFM for $k_{FM} = 0.02J_{FM}$ for several angles between magnetic field and FM easy axis. Inset shows the effective energy of an AFM spin as function of AFM spin angle.

anisotropy and with low FM anisotropy. These reversal modes favor large EB fields and training effect. Also, the cooling field orientation is crucial to that behavior and plays an important role in the AFM stable and unstable spin behavior. The combinations that favor the highest EB field and coercivity are the ones having biaxial FM anisotropy. For all the cases, high EB field and coercivity are favored when the magnetic field direction is closer to the one of the FM easy axis. The training effect, in general is large for systems with biaxial AFM anisotropy independently on the angle of the magnetic field direction. For systems with uniaxial AFM anisotropy, the training effect is small when the magnetic field direction is close to the AFM easy axis but it becomes quite large when the magnetic field direction is close to AFM hard axis. Similar conclusions are found for the concentration of stable AFM spins and their magnetization.

Influence of the FM/AFM coordination number on the training effect

In this chapter, we introduce some new characteristics in our model, to enhance the realism of it. We will investigate the effect of the FM/AFM coordination number in the EB quantities and in the training effect. More specifically the FM/AFM coordination number is the maximum number of neighbors of one material in the interface that a spin of the other material can have. This can not be controlled very easily but here we introduce two ways to achieve that. First using interface roughness, which in the atomistic scale is the mixing of the two materials in one or more layers. A second way is to use different crystallographic structures e.g. fcc or hcp. We will consider, for simplicity, that the crystallographic structure is always the same for both materials, although for epitaxial EB systems the crystallographic structure can be varied for different material and layer. First, we will discuss the effect of interfacial roughness in a simple cubic system with and without AFM dilution. Then, in the next section, we will examine the effect of interfacial roughness on other cubic structured EB systems. Also, we will focus on a bcc structured EB system which has a fully uncompensated interface. Finally, in the last section, we will discuss the effect of interfacial roughness in hexagonal structured systems.

7.1 Interface roughness dependence of the training effect

As a new aspect in our model, we now introduce the interface roughness, which is the intermixing of the FM and AFM sites at the interface, as shown in Fig. 7.1. This intermixing represents the roughness of the AFM/FM interface which always exists in a real system, although it is a vast simplification of a real interface, which usually will have larger roughness with more than one layer involved. Furthermore, this roughness enhances the maximum interface coordination number from one, which is for systems with sharp interface, to five, for systems with rough interface (for simple cubic systems).

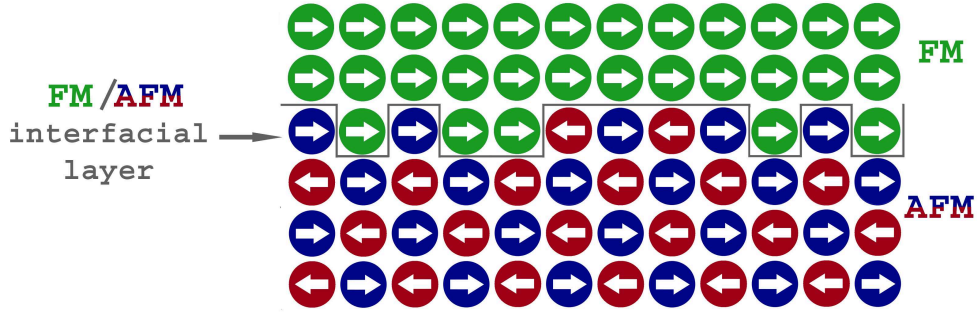


Figure 7.1: A sketch of an EB system with rough interface. The interface layer consists of FM and AFM spins.

For the quantitative description of the interface mixing we will use the method described in Ref.[27]. The aforementioned intermixing will be described by the mixing coefficient R . This coefficient is considered to be the proportion of the spins which are FM and not AFM or magnetic defects, in the interface AFM layer. Thus, is the concentration of the FM spins in this interfacial mixed layer, excluding the non-magnetic defects. The dilution p still acts in this layer. Thus, this layer consists of a total proportion of $(1 - p)$ magnetic sites, with $(1 - p)R$ FM sites and $(1 - p)(1 - R)$ of AFM sites. This method essentially produces an interface layer which is entirely AFM for zero R and takes on the character of a system of dilute (isolated) FM impurities in an AFM structure at low R . With increasing R the FM impurities cluster and at large R the layer has the characteristic of AFM impurities in a FM system.

We examine two different systems, one with dilution 40% and one without dilution. The training effect of the EB field as well as the fitting parameters κ and ΔH_{eb} are shown in Fig. 7.2 for a system a) with 40% dilution b) without dilution. The trend of the EB field is similar to the results obtained using an Ising model for the AFM by Spray and Nowak [27], i.e. non-monotonic behavior exhibiting a peak at some value of R . The peak becomes less pronounced at 40% dilution, which is consistent with the aforementioned model. The maximal EB field is achieved for $R = 0.3$ i.e. for systems with small amount of FM spins in the interface layer.

In case of no AFM dilution system, for low values of R , the EB field maximum may be associated with “lone FM spins”. More specifically, starting from small R , a small number of lone spins FM spins embedded in the AFM interface layer. This lone FM spins have five AFM neighbor spins and one FM neighbor spins, thus are pinned by the AFM ($5J_{\text{INT}} > J_{\text{FM}}$) and consequently enhance the EB field. The lone FM spins increase with increasing R , giving an increase in EB field. But at large R , there is more chance of FM atoms forming small clusters. That means that the embedded FM spins follow the hysteresis loop due to strong coupling with the FM, which leads to decrease in EB field.

As shown in Fig. 7.2b), systems with no dilution exhibit very strong EB field and

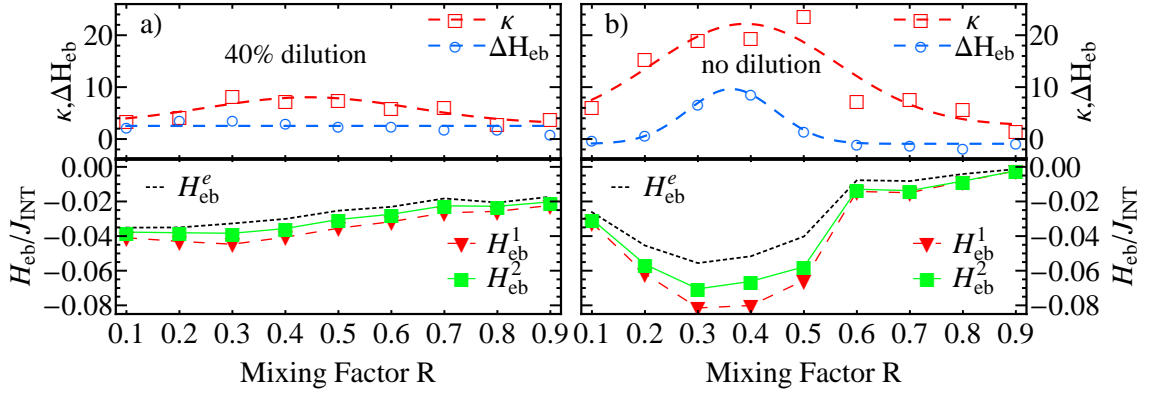


Figure 7.2: Interface roughness dependence of the training effect for systems with a) 40% dilution and b) no dilution. H_{eb}^1 and H_{eb}^2 : EB field of the first and the second hysteresis loop, respectively. H_{eb}^e : Equilibrium EB field following the power law fit. Upper graphs: Interface roughness dependence of the normalized fitting law parameter κ and ΔH_{eb} .

strong response in EB to the introduction of roughness. This is because the FM spins in the interface enhance more the interface coupling than the defects. Consequently, the FM spins act as domain wall pinning spins in the AFM enhancing the domain state. The EB existence with no dilution and some interface roughness coincides with the model of Malozemoff [83, 82, 84]. For higher dilutions, the interface mixing has a small effect as now the number of AFM neighbors for a lone FM spin is fewer due to dilution. Thus, these lone spins are not so tied with the AFM. Also, this is because the domain state of the AFM is well formed due to dilution and consequently roughness can not improve it further.

The training effect, in both cases of dilution, exhibits a maximum at the point where the EB field is maximum ($R \approx 0.35$) but remains non zero for all R , meaning that is always thermal training present. This is again an effect of the lone FM spins which are in the interface AFM layer. Although the lone FM spins have a domain wall pinning action, they also are in a metastable state, gained during the cooling process, as are the remaining AFM interface spins. Thus, for low R , due to larger population of metastable spins (AFM and lone FM interface spins) the training effect is more intense. As before this effect decreases with higher dilution and higher R due to clustering of the FM spins.

In Fig. 7.3, the trend of the coercive fields as function of the intermixing factor R is shown for the two cases of AFM dilution. The coercive fields are enhanced by the interface roughness. For low interface roughness, there are lone FM spins inside the AFM-dominated interface layer, which are pinned in both directions of the AFM easy axis. These spins which are directed opposite to the remaining FM spins, act as nucleation sites, leading to reversal at smaller coercive fields, as shown in Fig. 7.4. As mentioned previously, for high interface roughness, there are lone AFM spins inside the FM-dominated interface layer, which reverse with the FM as the coupling with the AFM is quite small. Thus, due to their large anisotropy, these lone AFM spins act like a highly anisotropic FM spins.

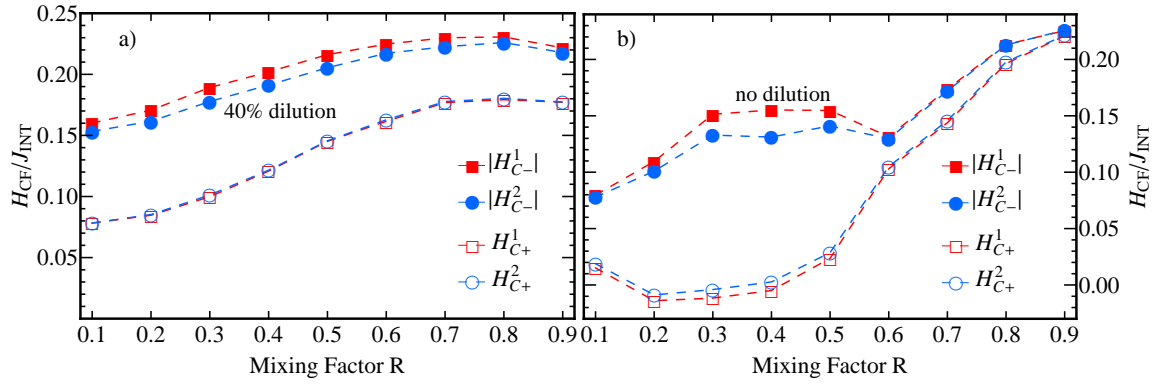


Figure 7.3: Interface roughness dependence of the training effect of the coercive fields for systems with a) 40% dilution and b) no dilution. H_{C+}^1 and H_{C+}^2 : Positive coercive field of the first and the second hysteresis loop, respectively. Similarly for the absolute value of the negative coercive field.

Consequently, this effect induces a higher effective uniaxial anisotropy in the FM, thereby increasing the coercive fields.

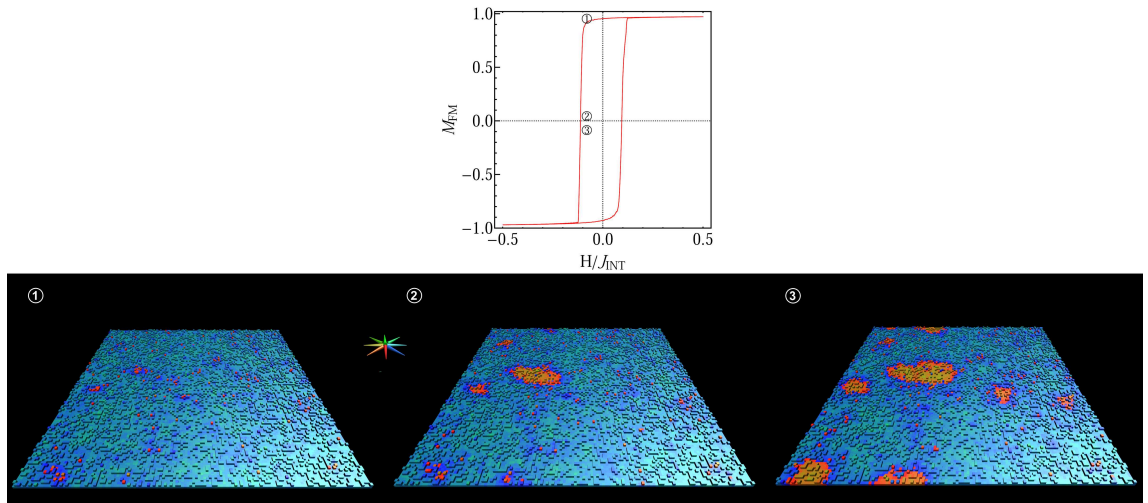


Figure 7.4: Snapshots of the FM before (①) and during (②, ③) reversal showing only the FM spins of the mixed layer. Snapshot ① shows the FM spins which act as nucleation sites.

7.2 EB systems with sc, fcc and bbc structure

In this section we will discuss the effect of interface roughness in EB systems with sc, bcc and fcc structure. The modeling of these systems can be done by translating the index comprised of the closest neighbors to a cubic lattice. Using a cubic matrix for the description of the system spins, we create for every atom a list of neighbors, appropriately placed in this matrix. The neighbors are placed periodically in the appropriate places and the construction of the matrix is completed using periodic conditions at the edges of the

layers. Thus, a full layer consists of two mixed smaller layers which interact not directly but via their boundaries.

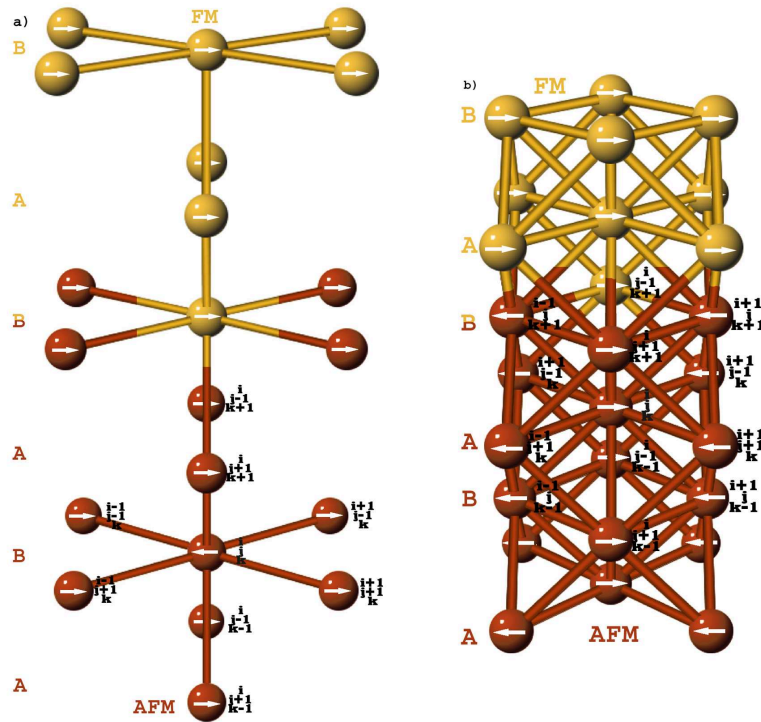


Figure 7.5: Schematic representations of the EB systems that we used with a) bcc structure with the $[110]$ crystallographic orientation along the interface and b) fcc structure with the $[100]$ crystallographic orientation along the interface. The layers of the structures (ABAB...) and the index coordinates of the neighbors of a central atom (ijk) are shown.

The EB system now consists of two layers of FM, three layers of AFM and one mixed. The investigation carried out using constant temperature at $k_b T = 0.15 J_{INT}$ and 40% AFM dilution. The systems that we investigate in this section have compensated interfaces and are presented in the Fig. 7.5. The bcc structured system has crystallographic orientation $[110]$, as this is the one with compensated interfacial spins. A bcc structured system with $[100]$ crystallographic orientation having fully uncompensated interfacial spins is investigated in the next section, as a special case. The sc structured system for $R = 0.0$ or 1.0 has FM/AFM coordination number one, the bcc structured system has two and the fcc structured system has four. With interface roughness the maximum FM/AFM coordination number is five, six and eight, respectively.

The training effect of the EB field as well as the fitting parameters κ and ΔH_{eb} are shown in Fig. 7.6 for a) sc, b) bcc and c) fcc structured system. The sc structured system has the same trend as the one we saw in the previous section with the only difference in the values of the quantities, as here we have more layers of FM and AFM. Thus, the EB field values are smaller but the trend remains the same. The same trend is also observed for the bcc structured system with larger EB field values. This is because now the AFM/FM coordination number is increased by one, meaning that a spin in the interface layer will

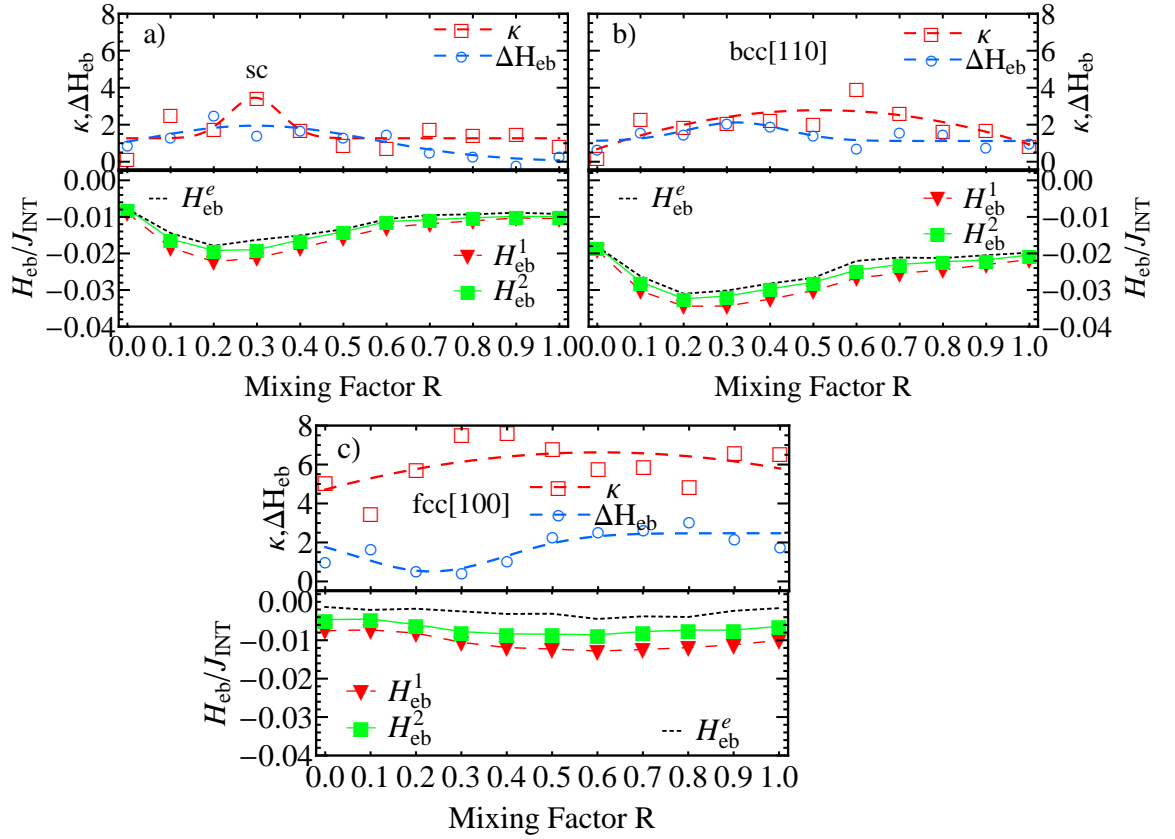


Figure 7.6: Interface roughness dependence of the training effect for systems with a) sc structure, b) bcc[110] structure and c) fcc structure. H_{eb}^1 and H_{eb}^2 : EB field of the first and the second hysteresis loop, respectively. H_{eb}^e : Equilibrium EB field following the power law fit. Upper graphs: Interface roughness dependence of the normalized fitting law parameter κ and ΔH_{eb} .

always (for any value of interface layer) have one more closest neighbor than for the sc case. For example, when $R = 0.0$ an FM spin at the interface is coupled with two AFM spins. This means the FM is more strongly coupled to AFM leading to a larger EB.

For a fcc structured system, one can expect that the EB effect will be stronger, with the same trend as before, because the FM/AFM coordination number increases and also the FM and AFM are more strongly coupled. But, as is shown in Fig. 7.6c), this does not occur; in fact the EB is almost independent of the interface mixing. This is due to the arrangement of the spins in the interface creating an AFM atomic compensation at the interface for the FM spins. For example, for $R = 0.0$ an FM spin has four AFM spins as closest neighbors which are fully compensated. Thus, the EB effect is due to the dilution which is enhanced to a small extent by the interface roughness. For low values of the interface roughness, where we have lone FM spins, the EB field is slightly increased as it has four AFM (uncompensated) neighbors. Thus, the same mechanism as that described in the first section of this chapter for the sc systems, occurs here.

The trend of the training effect remains the same as previously for the case of the sc and bcc structured systems. For fcc structured systems κ increases slightly with R but

always having a non-zero value, thus there is always thermal training. The training effect is quite large in comparison to the previous systems. This may be because much more AFM spins are metastable because each AFM spin is coupled with four FM spins. Thus, during the cooling many AFM spins are oriented to the positive easy direction parallel to the cooling field, because then are more strongly coupled to the FM. The small increase in the training effect is due to the decrease of the AFM thickness, as is shown in the previous chapters.

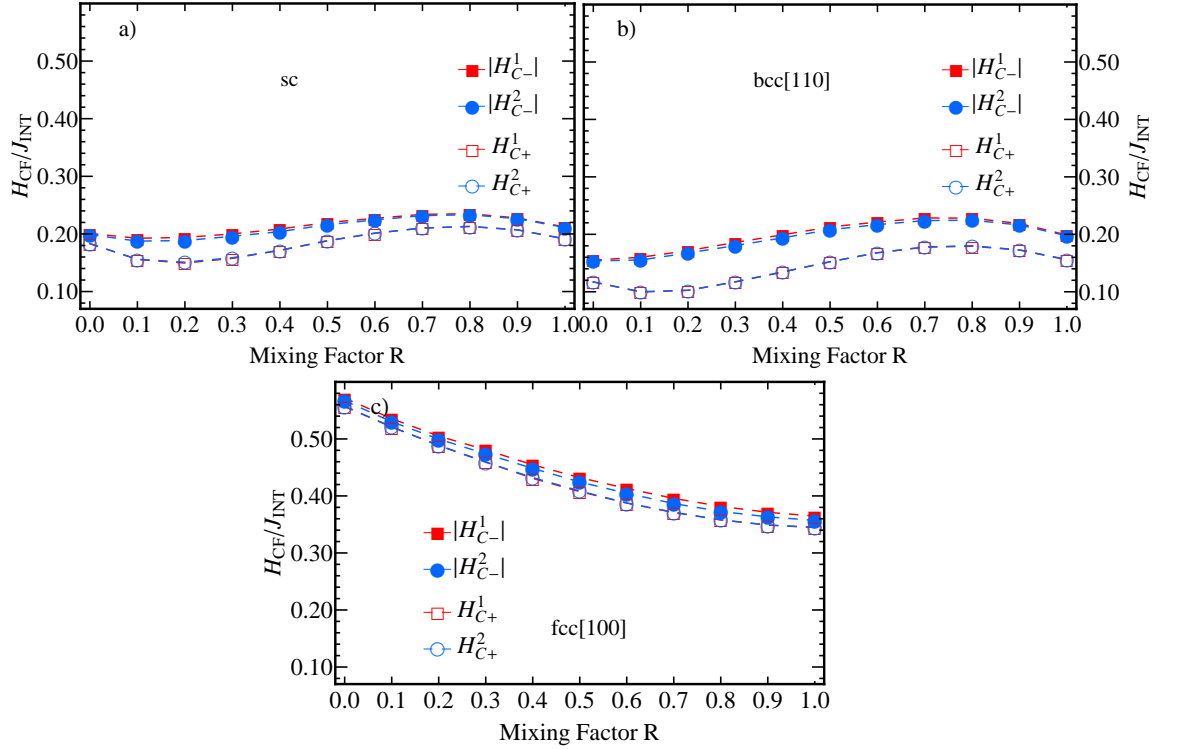


Figure 7.7: Interface roughness dependence of the training effect of the coercive fields for systems with a) sc structure, b) bcc[110] structure and c) fcc structure. H_{eb}^1 and $H_{\text{C}+}^1$ and $H_{\text{C}+}^2$: Positive coercive field of the first and the second hysteresis loop, respectively. Similarly for the absolute value of the negative coercive field.

The training effect of the coercive fields is shown in Fig. 7.7 for a) sc, b) bcc and c) fcc structured systems. The sc and the bcc structured systems have the same trend as that shown previously. The bcc structured system has larger coercivity because, as was explained in the previous chapter, the FM anisotropy per volume increases. Similarly, the coercivity of the fcc structured system is larger although coercive fields decrease with increasing interface mixing. This is not fully understood, but suggests a larger population of AFM spins of the type which are reversed by the FM on each branch of the loop, due to smaller AFM thickness with increasing R .

7.3 A special case: A fully uncompensated interface

A special case of cubic structured EB systems is the bcc structure with $[100]$ crystallographic orientation which has a fully uncompensated interface, as shown in Fig. 7.8. Because of the dilution, domains will be created perpendicular to the interface and consequently domain walls will be parallel to the interface. This is similar to the Mauri's model[23] described in the previous chapters.

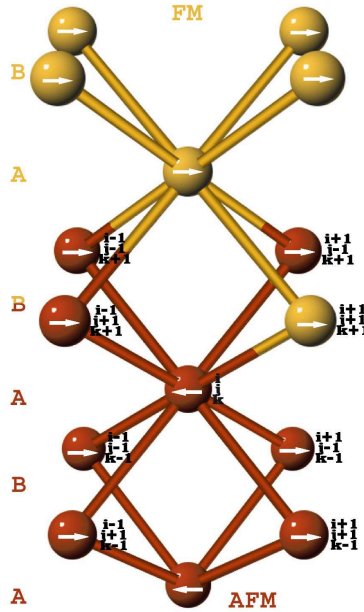


Figure 7.8: Schematic representations of the EB systems that we used with $bcc[100]$ structure. The layers of the structures (ABAB...) and the index coordinates of the neighbors of a central atom (ijk) are shown.

The training effect of the EB field as well as the fitting parameters κ and ΔH_{eb} are shown in Fig. 7.9a) for this system. In general, the EB field is quite large in comparison to the previous systems, a result of the uncompensated interface. The first maximum in the EB field as function of interface roughness is due to lone FM spins in a AFM environment, similar the behavior of sc EB systems. The difference here is that the coupling is with AFM spins not lying in the same x-y plane as the lone FM spin but in the next one. But the lone FM spins are pinned by the domains perpendicular to the interface which are biased in a certain direction during the cooling process, enhancing the coupling between the FM and the AFM. Thus the EB field increases. Then, with increasing interface roughness a balance between positive and negative FM/AFM interactions occurs. This means that the number of FM spins coupled with only positive and only negative AFM spins is the same, and consequently the FM is coupled to a fully compensated AFM causing zero EB field (this corresponds to the value $R = 0.4$).

The second maximum in EB field for $R \approx 0.7$ occurs because now the interface layer consists mainly of FM spins. That leads the next layer, which is AFM, to magnetize in the

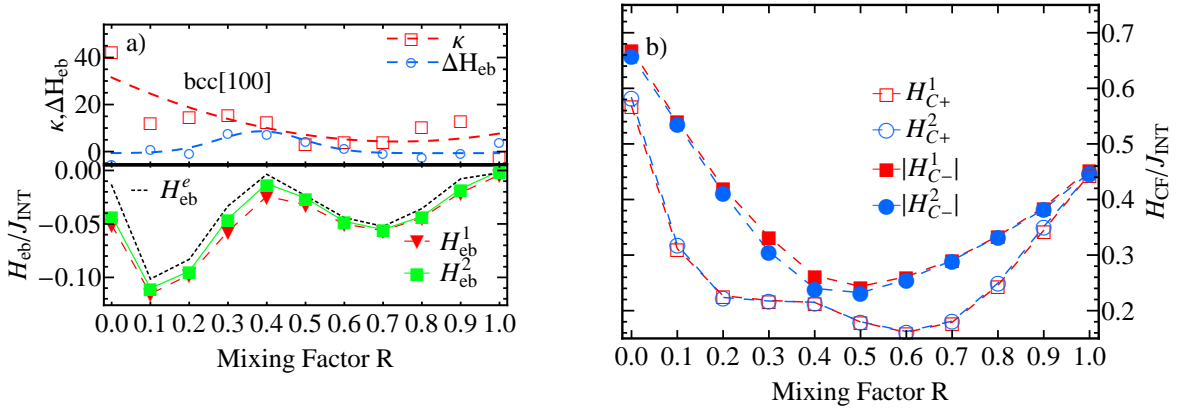


Figure 7.9: Interface roughness dependence of the training effect a) of the EB field and of b) of the coercive fields for systems with bcc structure. H_{eb}^1 and H_{eb}^2 : EB field of the first and the second hysteresis loop, respectively. H_{eb}^e : Equilibrium EB field following the power law fit. Upper graphs: Interface roughness dependence of the normalized fitting law parameter κ and ΔH_{eb} . H_{C+}^1 and H_{C+}^2 : Positive coercive field of the first and the second hysteresis loop, respectively. Similarly for the absolute value of the negative coercive field.

opposite direction during the cooling process. This AFM magnetization direction enhances the EB field. Then for very high values of R (≈ 1.0) the EB field decreases to zero as now we have an extra layer of FM and as it is known the EB field decreases with increasing FM layer thickness. Also, this extra layer of FM has non-magnetic defects which reduce the coupling with the AFM.

The training effect decreases with increasing interface roughness as shown in Fig. 7.9a), according to the behavior of the fitting parameter κ . For $R = 0.0$, the interfacial AFM spins are quite unstable as during the cooling process all of them point to one direction (fully uncompensated interface). Thus during the reversal of the magnetic field (which corresponds to reversal of the FM layer), many of the interfacial AFM spins can reverse as the non-magnetic defects make them less coupled with the AFM. Consequently, with increasing hysteresis cycles the interface becomes less uncompensated. Then for higher values the compensation in the interfacial spins is more common during the cooling process. Thus, the AFM spins are more stable and the training effect is becoming smaller with increasing roughness.

Finally, in Fig. 7.9b), the training effect of the coercive fields as function of interface roughness is shown. The coercive fields have a minimum at the interface roughness value ($R = 0.4$) where the EB field is zero. In that point there is the balance between positive and negative FM/AFM interactions occurs and consequently positive and negative coercive fields are the same. As before the FM spins act as nucleation points during both of the reversals, causing reversals at lower coercive field and consequently lower coercivity.

7.4 Hexagonal structured EB systems

In this section we will discuss EB systems with hexagonal crystallographic structure. The most common hexagonal systems are the hcp and fcc structures with interface along the $[110]$ crystallographic orientation, as shown in Fig. 7.10. The difference between the two structures is that in hcp structures the atoms are positioned (on the angles and on the center of a hexagon of the same layer) creating ABAB... layers, while in fcc structure are positioned creating ABCABC.. layers.

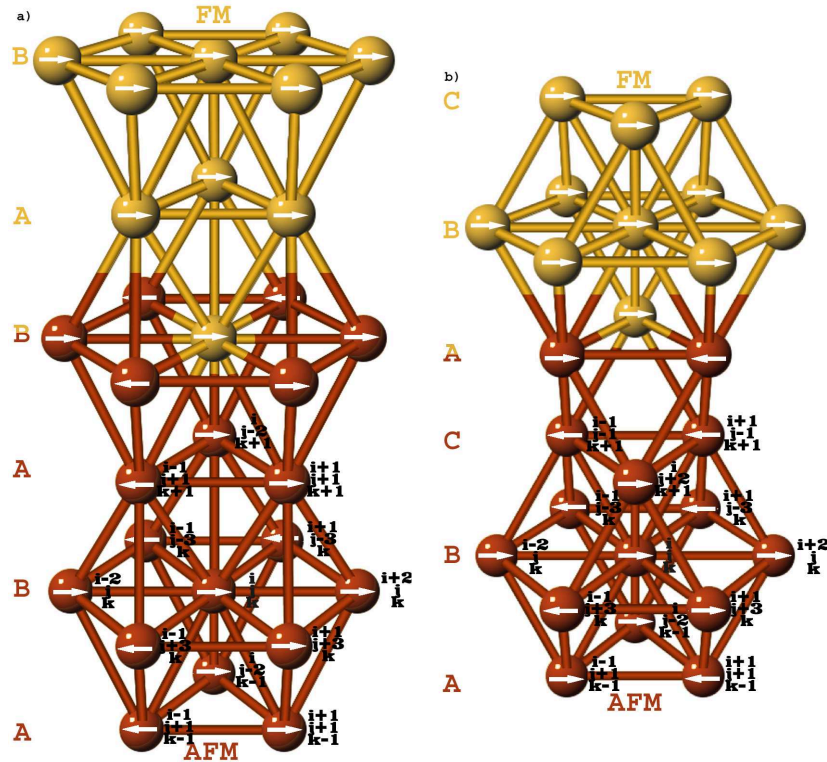


Figure 7.10: Schematic representations of the EB systems that we used with a) hcp structure and b) fcc structure with interface along the $[110]$ crystallographic orientation. The layers of the structures (ABCABC...) and the index coordinates of the neighbors of a central atom (ijk) are shown.

The training effect of the EB field as well as the fitting parameters κ and ΔH_{eb} are shown in Fig. 7.6 for a) the hcp system and b) the fcc system. For the hcp structured system, there is a smaller EB field compared to bcc systems for no interface roughness. This is because the hcp system, although having larger FM/AFM coordination number (three) than the bcc (two), two of the three AFM neighbors spins of an FM spin are self-canceled (compensated interface). Thus an FM spin is effectively coupled with one AFM spin.

The EB field of the hcp structured system decreases with increasing interface roughness. For understanding the mechanism behind this trend, we will consider again the case of low interface roughness with lone FM spins. The lone FM spins have nine AFM neighbors

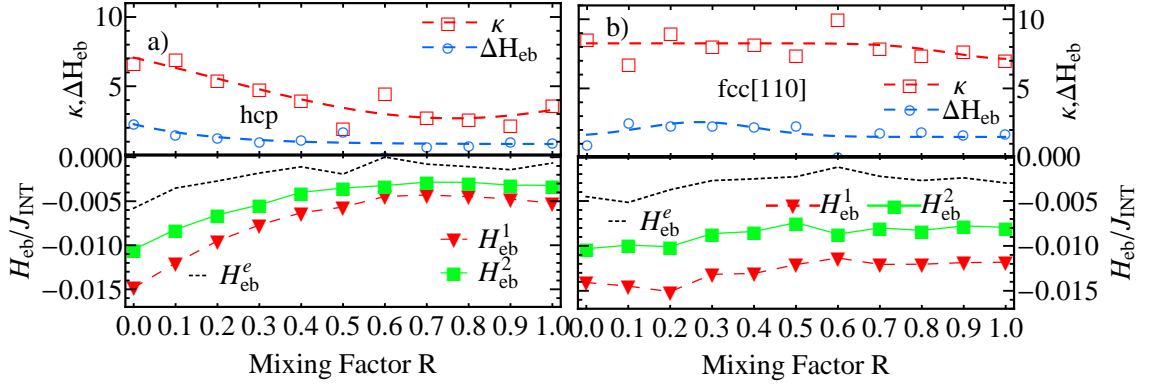


Figure 7.11: Interface roughness dependence of the training effect for systems with a) hcp structure and b) fcc[110] structure. H_{eb}^1 and H_{eb}^2 : EB field of the first and the second hysteresis loop, respectively. H_{eb}^e : Equilibrium EB field following the power law fit. Upper graphs: Interface roughness dependence of the normalized fitting law parameter κ and ΔH_{eb} .

which due to compensation, self-cancel leaving only one AFM spin effectively coupled to the lone FM spin. This lone FM spin has three FM neighbors in the FM layer which each of these have three neighbors in the interface layer, the lone FM spin and two AFM spins which are self-canceled. Thus in total, without interface roughness these three FM spins will effectively coupled with an AFM spin each but with interface roughness only the lone spin below them is effectively coupled with an AFM spin. Thus, in the first case we have three effective bonds between AFM and FM for three atoms but in the latter we have only one bond for four atoms. This means that interface roughness lead to weaker coupling between FM and AFM producing smaller EB field.

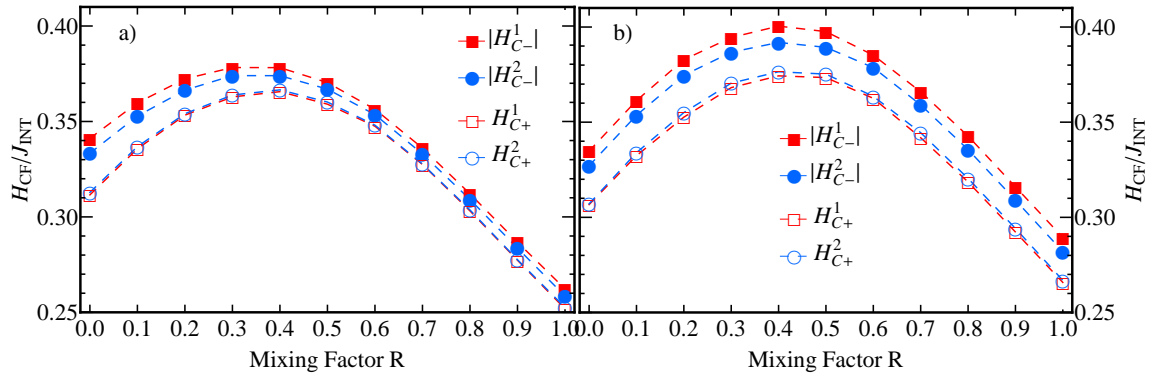


Figure 7.12: Interface roughness dependence of the training effect of the coercive fields for systems with a) hcp structure and b) fcc[110] structure. H_{C+}^1 and H_{C+}^2 : Positive coercive field of the first and the second hysteresis loop, respectively. Similarly for the absolute value of the negative coercive field.

As can be seen from the fitting parameter κ , the training effect decreases with increasing interface roughness. The training effect, similar to previous systems, is stronger for interface roughness which causes stronger coupling between FM and AFM. Although, the fcc system

differs very little from the hcp structure and there is a small decrease of the EB field with increasing interface roughness, the training effect is quite high. The response of EB and the training effect on changes of interface roughness seems quite small.

Finally, in Fig. 7.12, the training effect of the coercive fields as function of interface roughness for the a) hcp and b) fcc EB system is shown. The coercive fields have a maximum value when the interface roughness is equal to 0.5. That means that an AFM spin will have on average six AFM and six FM neighbors (in the case of no dilution). The coupling to the FM is stronger and thus, as previously, the AFM will behave as a highly anisotropic FM spin increasing the coercive fields.

7.5 Summary

The FM/AFM coordination number in an EB system was varied using two new characteristics in our model: the interface roughness and the various crystallographic structures. The crystallographic structures which we used are the sc[100], bcc[100], bcc[110], fcc[100], fcc[110] and hcp[0001] where the crystallographic orientations indicate those along the interface. The different orientation of the structure as well as the interface roughness had different result on the trends of the EB field, the training effect and the coercive fields.

The interface roughness was quantified as the percentage of FM spins in the interface layer. The results showed a strong dependence on the interface roughness for systems with 40% dilution and no dilution. For the case of no AFM dilution the model exhibited strong EB with finite training effect. Furthermore, due to lone FM spins which behave like AFM spins, the EB field has a maximum for low interface roughness.

Coercivity exhibits a minimum and maximum value for low and high interface roughness, respectively. This result is an effect of lone spins of the AFM and the FM. For low interface roughness, there are lone FM spins in an AFM environment which act as nucleation sites leading to reversal at smaller coercive fields. For high interface roughness, there are lone AFM spins in a FM environment which act as highly anisotropic FM spins leading to increase of coercive fields.

For systems with simple cubic structure and smooth interface, the EB field increases with the FM/AFM coordination number as the exchange coupling between the FM and AFM increases e.g. for systems with bcc and fcc structure. But this increase of the FM/AFM coordination number does not, in all cases, result in an increase of the exchange coupling. For example, although fcc systems have the higher FM/AFM coordination number (four), the AFM spins, to which a FM spin is exchange coupled, are compensated giving zero effective exchange coupling and consequently quite small EB field.

Furthermore, bcc systems with [100] orientation in the interface have a fully uncom-

compensated interface and the EB field has very high values. The domains, which are created in the bcc system, are perpendicular to the interface. The EB field dependence on the interface roughness is then more complicated, with two maxima and a minimum values. The first maximum, as before, is due to lone FM spins. The minimum in mid-range value of interface roughness is due to a balance between positive and negative FM/AFM interactions. The second maximum, at large values of interface roughness, occurs because the interface layer consists mainly of FM spins, which during the cooling process magnetize the next layer (AFM) in the opposite direction, enhancing the EB field.

Hcp and fcc systems, with [110] orientation in the interface, were investigated. Although the FM/AFM coordination number is quite large for these systems (12), the EB field is small due to atomistic compensation. In these systems, the interface roughness does not enhance at all the EB field. Without interface roughness three FM spins are effectively coupled with an AFM spin each but with interface roughness only the lone spin below them is effectively coupled with an AFM spin. Thus, in the first case we have three effective bonds between AFM and FM for three atoms but in the latter we have only one bond for four atoms.

Conclusions and further work

The current research focused on the dependence of the training effect on various EB system parameters. A novel analysis was developed for the study of the AFM during consecutive hysteresis loops. New characteristics were added to the domain state model increasing the realism of this model. In the following we will summarize the results of the previous chapters and refer to the central conclusions.

8.1 Model and analysis

Our atomistic calculations are based on the domain state model, using Monte-Carlo techniques for the minimization of the energy. We calculated statistical averages of the quantities over 20 different realizations of random number sequences. The training effect was studied considering ten consecutive hysteresis loops after the initial cooling process.

The FM was studied using the EB field and coercivity. To study the training effect, the values in each hysteresis loop cycle for every set of variables were calculated. For every parameter set a sequence of values of the main parameters, for example the EB field, were produced making this study quite difficult. To analyze the results, a fitting process was applied, calculating the parameters of the resulting fitted curve for hysteresis loops from the second hysteresis cycle onwards. These parameters show the strength of the training effect and the equilibrium EB field. Furthermore, we studied the difference of the fitting law as extrapolated to the first hysteresis loop and the actual simulation results for the EB field of the first loop.

The AFM was studied using the irreversible magnetization of the interface AFM layer, i.e. the vertical shift of the hysteresis loop. To study the training effect in the AFM, we categorized the AFM spins according to their behavior. The spins were categorized in four categories:

1. **Stable Spins.** The spins are always pointing towards the same direction with small thermal fluctuations and are considered pinned to that direction.
2. **Meta-Stable Spins.** The spins are in a meta-stable state created during the cooling process. During the first reversal, they reverse only once and they are pinned to a new easy direction.

3. **Unstable Spins.** The spins reverse with the FM creating the AFM hysteresis loop.
4. **Frustrated Spins.** The spins reverse with the magnetic field. This behavior is a result of geometric frustration created at the interface because of the dilution.

8.2 Temperature effects

The temperature dependence of the EB was investigated in four systems, with different AFM anisotropy and thickness. These systems exhibit similar trends for increasing temperature. The training effect, according to the temperature behavior, was categorized in two kinds:

1. **Athermal training effect.** The EB field remains almost constant after the second hysteresis loop. It is termed “athermal”, because it is exhibited at low temperatures and the AFM spins always remain oriented to the easy axis due to lack of thermal excitations.
2. **Thermal training effect.** The EB field decreases with increasing hysteresis cycling. It is exhibited at mid-range temperatures and the AFM spins are not totally aligned to the easy direction due to thermal fluctuations, but they precess-relax towards this direction causing reduction of the total AFM magnetization.

In general, in both cases, the EB field decreases steeply from the first to the second hysteresis loop, an effect of meta-stable spins. At low temperatures, the AFM exhibits some extra characteristics. The frustrated spins are more apparent in the hysteresis loop, where around zero field a paramagnetic behavior is exhibited. Furthermore, for biaxial systems many spins, due to lack of thermal excitations, are trapped in specific orientations by energy barriers that can not overcome.

8.3 AFM characteristics effects

The effect of the AFM characteristics in the EB field as well as the training effect were investigated thoroughly. The effect of AFM dilution and thickness were examined for constant temperature for EB systems with AFM uniaxial anisotropy. The Néel temperature increases asymptotically to a stable value with increasing AFM thickness whereas it decreases with increasing dilution. The EB field also increases asymptotically to a stable value with increasing AFM thickness. The training effect of the EB field decreases with increasing AFM thickness. The training effect of the coercive fields changes behavior with increasing AFM thickness and this behavior can be categorized to two types:

1. **Type I training effect.** The positive coercive field decreases with increasing hysteresis cycles, causing decrease of the coercivity of the loop from both branches. This type of training effect is exhibited for high AFM thicknesses (> 6 AFM layers).
2. **Type II training effect.** The positive coercive field increases with increasing hysteresis cycles. This type of training effect is exhibited for low AFM thicknesses (< 6 AFM layers).

The negative coercive field always decreases with increasing hysteresis cycles. The AFM dilution enhances the EB field up to a maximum value. The training effect is very low for small values of AFM dilution but it increases with increasing dilution.

8.4 Anisotropy effects

The energy “landscape” created by the easy and the hard axes of the materials affects the behavior of the EB system and especially its variation during consecutive hysteresis loops. We varied the type (uniaxial, biaxial, etc.) of the anisotropy in the FM and AFM as well as its magnitude, studying the effect on the reversal modes of the FM. Also, we varied the angle of the magnetic field because, as is known from the literature, this parameter affects the reversal modes of the FM. The training effect of the reversal modes of the FM is categorized in three categories:

1. **Unchanged symmetric reversal modes.** The reversal modes during increasing hysteresis remain unchangeable and symmetric with coherent or incoherent rotation.
2. **Symmetric-asymmetric transitional reversal modes.** The reversal modes are symmetric with coherent rotation on the first loop and gradually are converted to asymmetric rotation with vanishing magnetization.
3. **Asymmetric-symmetric transitional reversal modes.** The reversal modes are asymmetric with vanishing magnetization on the first loop and gradually are converted to symmetric with coherent rotation.

The last two reversal modes are presented in systems with biaxial AFM anisotropy and with low FM anisotropy. These reversal modes favor large EB fields and training effect. In general:

1. High EB field and coercivity are favored when the magnetic field direction is close to the one of the FM easy axis.
2. The training effect is large for systems with biaxial AFM anisotropy independently on the angle of the magnetic field direction.

3. For systems with uniaxial AFM anisotropy, the training effect is small when the magnetic field direction is close to the AFM easy axis but it becomes quite large when the magnetic field direction is close to AFM hard axis.

8.5 Rough interface effects

A new characteristic introduced in our model is the interface roughness, which is more realistic, as in real EB systems the interface will never be ideally smooth. Thus, we introduce a layer that consists of both FM and AFM spins. We quantify the interface roughness the percentage of FM spins in this layer. The results showed a strong dependence on the interface roughness for systems with 40% dilution and no dilution. For the case of no AFM dilution the model exhibited strong EB with finite training effect. Furthermore, due to lone FM spins which behave like AFM spins, the EB field has a maximum for low interface roughness.

Coercivity exhibits a minimum and maximum value for low and high interface roughness, respectively. This result is an effect of lone spins of the AFM and the FM. For low interface roughness, there are lone FM spins in an AFM environment which act as nucleation sites leading to reversal at smaller coercive fields. For high interface roughness, there are lone AFM spins in a FM environment which act as highly anisotropic FM spins leading to increase of coercive fields.

8.6 Crystallographic structure effects

More complicated crystallographic structures were used to enhance the coupling between the FM and AFM. In the interface of systems having sc, bcc and fcc structure, the number of neighbors per atom is one, two and four, respectively (for smooth interfaces with no dilution). Although, the coupling between the AFM and the FM increases, the EB does not always increase. When we have systems with sc and bcc structure, a FM spin in the interface is coupled to one and two AFM spins, respectively, oriented in the same direction. These systems exhibit similar trends when the interface roughness is varied, with the bcc structured system showing stronger EB fields. For the case of fcc structured systems, a FM spin is coupled with four AFM spins in the interface, which are self-canceled. Thus, the system exhibits an “atomistic compensation” effect. Thus, the AFM interacts very weakly with the FM and the EB field is low.

A special case of bcc structure is the one in which the interface is fully uncompensated. The EB field in this system is quite large and domains are created perpendicular to the interface. The EB field dependence on the interface roughness is more complicated, with

two maxima and a minimum value. The first maximum, as before, is due to lone FM spins. The minimum at an intermediate value of interface roughness is due to balance between positive and negative FM/AFM interactions. The second maximum, at high value of interface roughness, occurs because the interface layer consists mainly of FM spins, which during the cooling process magnetize the next layer (AFM) in the opposite direction, enhancing the EB field.

Finally, hexagonal systems were investigated using the hcp and the fcc crystallographic structures oriented to the interface as appropriate. Although the FM/AFM coordination number is quite large for these systems (12), the EB field is small due to atomistic compensation. In these systems, the interface roughness does not enhance at all the EB field. Without interface roughness three FM spins are effectively coupled with an AFM spin each but with interface roughness only the lone spin below them is effectively coupled with an AFM spin. Thus, in the first case we have three effective bonds between AFM and FM for three atoms but in the latter we have only one bond for four atoms.

8.7 Outlook and future prospects

The main purpose of the present research is the theoretical investigation of aging effects in magnetic bilayers that are used in industry for commercial applications. Atomistic simulations were used to gain a theoretical understanding of the physics of these systems. The domain state model for EB systems is a well-established model which was used for the explanation of the EB phenomenology. In this thesis, the domain state model is used for the explanation and investigation of the training effect studying the effects of many parameters of the system. Special attention was given to the AFM interface layer and especially in the behavior of its spins. A direct connection of the behavior of these spins with the training effect of the EB quantities was successfully established. The model was further extrapolated using new characteristics, making it more realistic. The use of different kinds of anisotropies beyond uniaxial, the introduction of interface roughness and the use of different crystallographic structures beyond sc are some of them.

The current model can further developed and more characteristics, that are found in realistic systems, should be included. The latest extrapolation of the model is the use of “ab-initio” techniques for the calculation of the exchange integrals of the EB system. The calculated exchange integrals can then be used in the domain state model. Different EB structures should be also investigated such as core-shell nanoparticles and thin film granular systems. Granular systems are quite numerous and many models were developed using intergranular coupling. It is important to develop multiscale models for granular systems, using atomistic calculations for the interior of the grain but also including some

8.7. Outlook and future prospects

intergranular exchange. Also, different shapes of the grains were used considering some randomness on that, like squares with dilution, elliptical with different quadrant radius, Voronoi shapes etc. The use of these characteristics in calculations of the training effect will further enhance our knowledge about the stability and aging effects of EB systems.

Heat-Bath Monte Carlo

For the minimisation of the energy of the system, this thesis uses the heat-bath Monte Carlo method. In general, Monte-Carlo methods are well established in the context of equilibrium thermodynamics [141]. Contrary to the Langevin dynamics approach, where the evolution of the system can easily correlated with the real time, Monte-Carlo methods are not correlated with the real time, but represent states of the system at thermodynamic equilibrium. Thus, in a Monte-Carlo simulation no precession of magnetic moments is observed, but the random-walk like motion of the moments which is due to the coupling to the heat bath.

The Monte-Carlo algorithm begins with selecting randomly a single spin from the lattice randomly and a trial step is made in this spin. Then, the energy difference of the system is calculated according to the Hamiltonian of the system. Thus, this trial step is accepted with probability:

$$P_{\mathbf{S} \rightarrow \mathbf{S}'} = \frac{1}{1 + \exp\left(\frac{E(\mathbf{S}') - E(\mathbf{S})}{k_B T}\right)} \quad (\text{A.1})$$

where \mathbf{S} and \mathbf{S}' is the spin before and after the trial step, respectively, E the calculated energy and T the temperature of the system. When a series of random trial steps is attempted once per spin, scanning the whole lattice, then a Monte-Carlo step is completed. The Monte-Carlo step defines the quasi-time scale of the simulation.

The trial step is very important for the efficiency of the algorithm as well as for the physical interpretation of the dynamic behavior of the algorithm. E.g. in an Ising model the trial step is a spin-flip, but in a Heisenberg model there are an infinite number of degrees of freedom for the trial step. In the current investigation we use as a trial step to be chosen from an uniform distribution in a sphere radius R from the initial position [142], as shown in Fig. A.1. The selection of this step must fulfill two conditions: firstly the time averages must yield identical results as ensemble averages, according to ergodicity. Secondly, the trial step must be symmetrical to its reverse process. Here, for the selection random vectors on a sphere with constant probability distribution, Marsaglia algorithm [143] was used. Firstly a random vector is chosen with constant probability distribution inside a sphere of radius R by use of the rejection method of Marsaglia algorithm. Then, this random vector is added to the initial spin. Finally, the resulting spin is normalized.

The R for FM and AFM materials can be significantly differ, so a test before choosing it, is needed.

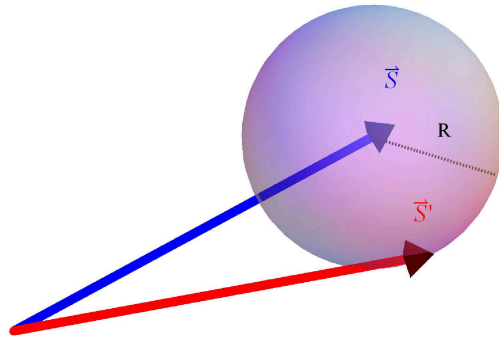


Figure A.1: Schematic representation of the selection of the new spin for the trial step in a Monte-Carlo step. The spin S attempts to move inside a sphere of radius R around its initial position, resulting the new spin S' .

Nomenclature

$\theta_{\vec{S}_{FM}}, \theta_{\vec{S}_{AFM}}$	Angle of the FM and AFM spin
H_{CF}	Coercive field of hysteresis loop
H_{Cool}	Cooling magnetic field
M_{irr}, M_{rev}	Irreversible and reversible antiferromagnetic magnetization on the interface
$M_{S.B.S.}$	Magnetization of stable spins in the bulk
$M_{S.I.S.}$	Magnetization of stable interfacial spins
$\alpha, \alpha_1, \alpha_2, \alpha_i$	Angle of the total, two sublattices and ith grain AFM magnetization from the AFM easy axis
β, β_i	Angle of the total and ith layer FM magnetization from the FM easy axis
B	Magnetic field vector
F	Total angular momentum of atom
I	Angular momentum of nucleus
J	Atomic angular momentum
L	Orbital angular momentum of electron
M_{AFM}, M_{AFM}^+	Total and positive sublattice antiferromagnetic magnetization
M_S	Saturation magnetization
S_i	Spin vector of the ith site of the ferromagnet
$\chi_{AFM}^{(2)}$	Second approximation for AFM susceptibility
ϵ_i	Dilution index for ith site

γ	Chapter 2: Angle between FM and AFM easy axis, Chapter 5: Recursive sequence fit parameter
\hbar	Planck constant
λ	Interface exchange ratio
μ	Anisotropy ratio
μ_o	Bohr magneton
θ	Angle between magnetic field and the FM easy axis
ξ	Distance between AFM and FM
A^i	Area of <i>i</i> th grain
A_{12}	Antiferromagnetic exchange stiffness at the interface
A_{AFM}	Antiferromagnetic exchange stiffness in the bulk
c^i	Contact fraction of <i>i</i> th grain
$DH_{eb}, \Delta H_{eb}$	Difference between power law and 1st hysteresis loop EB field, normalized
d_x, K_{FM}, K_a	Ferromagnetic (uniaxial) anisotropy constant for easy axis
d_z	Ferromagnetic anisotropy constant for hard axis
g	Landé factor
H_{C+}	Positive coercive field
H_{C-}	Negative coercive field
H_c	Coercivity
H_{eb}	Exchange bias field
H_{eb}^1, H_{eb}^m	Exchange bias field of the first hysteresis loop and mean value of the nine subsequent loops.
H_{eb}^e, H_{eb}^{e-rs}	Equilibrium exchange bias field of power law and recursive sequence fit
j	Quantum number of atom

J_{AFM}	Antiferromagnetic exchange interaction integral
J_{FM}	Ferromagnetic exchange interaction integral
J_{INT}, J_{INT}^{eff}	Interface exchange interaction (effective) integral between AFM and FM
k, κ	Power law fit parameter, normalized
k_B, k_b	Boltzmann constant
K_d	Unidirectional anisotropy constant for easy axis
k_x, K_{AFM}	Antiferromagnetic anisotropy constant for easy axis
K_{1b}	Biaxial anisotropy constant for easy axes
K_{1c}	Cubic anisotropy constant for easy axes
K_{1u}, K_{2u}	First and second order uniaxial anisotropy constant for easy axis
K_{SG}^{eff}	Effective spin glass anisotropy in the AFM interface
K_S	Shape anisotropy constant
l	Quantum number of orbital angular momentum of electron
m_j	Atomic magnetic momentum
m_s	Spin quantum number of electron
M_{FM}, M_i	Total and ith layer FM magnetization
N	Number of atomic sites, number of hysteresis loop
n	Principal quantum number of electron
p	AFM dilution with non-magnetic defects
R	Chapter 3: Trial step radius, Chapter 7: AFM/FM mixing factor
s	Spin angular momentum of electron
T_B	Blocking temperature of an exchange bias system
T_C	Curie temperature of a ferromagnet
T_I	Initial temperature of the cooling process

T_N	Néel temperature of an antiferromagnet
t_{AFM}	Antiferromagnetic sample thickness
t_{FM}	Ferromagnetic sample thickness
V_{FM}	FM Volume
z	Degree of interface roughness
\mathbf{H}, H	Magnetic field strength vector and amplitude
\mathbf{M}, M	Magnetization vector and amplitude inside a material
AFM	Antiferromagnet/Antiferromagnetic
AMR	Anisotropic Magnetoresistance
bcc	Body-centered cubic
EB	Exchange bias
fcc	Face-centered cubic
FM	Ferromagnet/Ferromagnetic
GMR	Giant Magnetoresistance
hcp	Hexagonal close packed
MRAM	Magnetic random access memory
RKKY	Indirect exchange or Ruderman, Kittel, Kasuya, Yosida interaction
SQUID	Semiconductor quantum interference device
TMR	Tunnel Magnetoresistance
σ_i	Spin vector of the i th site of the ferromagnet

Bibliography

- [1] U.S. Department of Energy, Office of Basic Energy Sciences, Office of Science. *The Scale of Things* (2006). http://www.er.doe.gov/bes/scale_of_things.html.
- [2] Wikipedia, the free encyclopedia. *Hysteresis* (2009). <http://en.wikipedia.org/wiki/Hysteresis>.
- [3] J. Nogués, J. Sort, V. Lanlais, V. Skumryev, S. Surinach, J. S. Munoz, and M. D. Baró. *Exchange bias in nanostructures*. Phys. Repts. **422**, 65 (2005).
- [4] J. Nogués and I. K. Schuller. *Exchange Bias*. J. Magn. Magn. Mat. **192**, 203 (1999).
- [5] W. H. Meiklejohn and C. P. Bean. *New Magnetic Anisotropy*. Phys. Rev. **102**, 1413 (1956).
- [6] W. H. Meiklejohn and C. P. Bean. *New Magnetic Anisotropy*. Phys. Rev. **105**, 904 (1957).
- [7] W. H. Meiklejohn. *Exchange Anisotropy- A Review*. J. Appl. Phys. **33**, 1328 (1962).
- [8] D. Paccard, C. Schlenker, O. Massenet, R. Montmory, and A. Yelon. *A New Property of Ferromagnetic-Antiferromagnetic Coupling*. Phys. stat. sol. **16**, 301 (1966).
- [9] Roger Wood, Hitachi Global Storage Technologies. *IEEE Magnetics Society Summer School: Magnetic Recording* (2008). University of Colorado at Colorado Springs, Colorado Springs, CO, Aug. 3-8, 2008.
- [10] M. Baibich, J. Broto, A. Fert, F. Vandau, F. Petroff, P. Eitenne, G. Creuzet, A. Friederich, and J. Chazelas. *Giant Magnetoresistance of (001)Fe/(001)Cr Magnetic Superlattices*. Phys. Rev. Lett. **61**, 2472 (1988).
- [11] J. Zhu. *Thermal and current driven noise in magnetoresistive sensors*. APDSC presentation (2006).
- [12] V. Skumryev, S. Stoyanov, Y. Zhang, G. Hadjipanayis, D. Givord, and J. Nogués. *Beating the superparamagnetic limit with exchange bias*. Nature **423**, 850 (2003).
- [13] F. Radu, M. Etzkorn, R. Siebrecht, T. Scmitte, K. Westerholt, and H. Zabel. *Interfacial domain formation during magnetization reversal in exchange-biased CoO/Co bilayers*. Phys. Rev. B **67**, 134409 (2003).

- [14] M. R. Fitzsimmons, P. Yashar, C. Leighton, I. K. Sculler, J. Nogués, C. F. Majkrzak, and J. A. Dura. *Asymmetric magnetization reversal in exchange-biased hysteresis loops*. Phys. Rev. Lett. **84**, 03986 (2000).
- [15] C. Leighton, M. R. Fitzsimmons, A. Hoffmann, J. Dura, C. F. Majkrzak, M. S. Lund, and I. K. Schuller. *Thickness-dependent coercive mechanisms in exchange-biased bilayers*. Phys. Rev. B **65**, 064403 (2002).
- [16] N. J. Gokemeijer, J. W. Cai, and C. L. Chien. *Memory effects of exchange coupling in ferromagnet/antiferromagnet bilayers*. Phys. Rev. B **60**, 3033 (1999).
- [17] N. J. Gokemeijer and C. L. Chien. *Memory effects of exchange coupling in CoO/Ni₈₁Fe₁₉ bilayers*. J. Appl. Phys. **85**, 5516 (1999).
- [18] L. E. Fernandez-Outon, K. O'Grady, and M. J. Carey. *Thermal phenomena in IrMn exchange biased systems*. J. Appl. Phys. **95**, 6852 (2004).
- [19] F. Garcia, F. Fettar, S. Auffret, B. Rodmacq, and B. Dieny. *Exchange-biased spin valves with perpendicular magnetic anisotropy based on (Co/Pt) multilayers*. J. Appl. Phys. **93**, 8397–8399 (2003).
- [20] J. Keller, P. Miltényi, B. Beschoten, G. Güntherodt, U. Nowak, and K. D. Usadel. *The domain state model for exchange bias II: Experiment*. Phys. Rev. B **66**, 14431 (2002).
- [21] T. J. Moran and I. K. Schuller. *Effects of cooling field strength on exchange anisotropy at permalloy/CoO interfaces*. J. Appl. Phys. **79**, 5109–5111 (1996).
- [22] J. Nogués, D. Lederman, T. Moran, and I. Schuller. *Positive exchange bias in FeF₂ – Fe bilayers*. Phys. Rev. Lett. **76**, 4624–4627 (1996).
- [23] D. Mauri, E. Kay, D. Scholl, and J. K. Howard. *Novel method for determining the anisotropy constant of MnFe in a NiFe/MnFe sandwich*. J. Appl. Phys. **62**, 2929–2932 (1987).
- [24] R. Jungblut, R. Coehoorn, M. T. Johnson, J. Aan de Stegge, and A. Reinders. *Orientational dependence of the exchange biasing in molecular-beam-epitaxy-grown Ni₈₀Fe₂₀/Fe₅₀Mn₅₀ bilayers (invited)*. J. Appl. Phys. **75**, 6659–6664 (1994).
- [25] A. Paul, C. M. Schneider, and J. Stahn. *Reversal mechanism and suppression of training in an exchange-coupled system*. Phys. Rev. B **76**, 184424 (2007).
- [26] J. Nogués, T. Moran, D. Lederman, I. Schuller, and K. Rao. *Role of interfacial structure on exchange-biased FeF₂ – Fe*. Phys. Rev. B **59**, 6984 (1999).

- [27] J. Spray and U. Nowak. *Exchange bias in ferromagnetic/antiferromagnetic bilayers with imperfect interfaces*. J. Phys. D: Applied Physics **39**, 4536–4539 (2006).
- [28] T. Blachowicz, A. Tillmanns, M. Fraune, R. Ghadimi, B. Beschoten, and G. Güntherodt. *Exchange bias in epitaxial CoO/Co bilayers with different crystallographic symmetries*. Phys. Rev. B **75**, 054425 (2007).
- [29] G. Wang, T. Yeh, C.-L. Lin, J. M. Sivertsen, and J. H. Judy. *Structure and properties of sputtered FeMn/NiFe bilayer thin films*. IEEE Trans. Magn. **32**, 4660–4662 (1996).
- [30] M. J. Carey and A. E. Berkowitz. *Exchange anisotropy in coupled films of Ni₈₁Fe₁₉ with NiO and Co_xNi_{1-x}O*. Appl. Phys. Lett. **60**, 3060–3062 (1992).
- [31] C.-H. Lai, H. Matsuyama, R. L. White, T. C. Anthony, and G. G. Bush. *Exploration of magnetization reversal and coercivity of epitaxial NiO{111}/NiFe films*. J. Appl. Phys. **79**, 6389–6391 (1996).
- [32] A. F. Khapikov, J. W. Harrel, H. Fujiwara, and C. Hou. *Temperature dependence of exchange field and coercivity in polycrystalline NiO/NiFe film with thin antiferromagnetic layer: Role of antiferromagnet grain size distribution*. J. Appl. Phys. **87**, 4954 (2000).
- [33] K. Zhang, T. Zhao, and H. Fujiwara. *Training effect in ferro(F)/antiferromagnetic(AF) exchange coupled systems: Dependence on AF thickness*. J. Appl. Phys. **91**, 6902 (2002).
- [34] M. Fecioru-Morariu, J. Wrona, C. Papusoi, and G. Güntherodt. *Training and temperature effects of epitaxial and polycrystalline exchange biased bilayers*. Phys. Rev. B **77**, 054441 (2008).
- [35] S. Manzoor, M. Vopsaroiu, G. Vallejo-Fernandez, and K. O'Grady. *Grain-size effects in exchange-biased FeMn/NiFe bilayers*. J. Appl. Phys. **97**, 10K118 (2005).
- [36] U. Nowak, A. Misra, and K. D. Usadel. *Domain state model for exchange bias*. J. Appl. Phys. **89**, 7269 (2001).
- [37] A. Scholl, F. Nolting, J. Seo, H. Ohldag, J. Stöhr, S. Raoux, J.-P. Locquet, and J. Fompeyrine. *Domain-size-dependent exchange bias in Co/LaFeO₃*. Appl. Phys. Lett. **85**, 4085 (2004).
- [38] E. C. Stoner and E. P. Wohlfarth. *A mechanism of magnetic hysteresis in heterogeneous alloys*. Phil. Trans. Roy. Soc **A240**, 599 (1948).

- [39] M. Kiwi. *Exchange bias theory*. J. Magn. Magn. Mat. **234**, 584 (2001).
- [40] A. M. Goodman, K. O'Grady, H. Laidler, N. W. Owen, X. Portier, A. K. Petford-Long, and F. Cebollada. *Magnetization Reversal Processes in Exchange-Biased Spin-Valve Structures*. IEEE Trans. Magn. **37**, 565 (2001).
- [41] M. Radu. *Fundamental Aspects of exchange bias*. Dissertation, Fakultät für Physik und Astronomie an der Ruhr-Universität Bochum (2005).
- [42] H. Fujiwara, C. Hou, M. Sun, H. S. Cho, and K. Nishioka. *Effect of exchange coupling of polycrystalline antiferromagnetic layers on the magnetization behavior of soft magnetic layers*. IEEE Trans. Magn. **35**, 3082 (1999).
- [43] L. Néel. *Etude Theorique-du Couplage Ferro-Antiferromagnetique Dans les Couches Minces*. Annales de Physique **2**, 61 (1967).
- [44] D. Mauri, H. C. Siegmann, P. S. Bagus, and E. Kay. *Simple model for thin ferromagnetic films exchange coupled to an antiferromagnetic substrate*. J. Appl. Phys. **62**, 3047 (1987).
- [45] J. Geshev. *Analytical solutions for exchange bias and coercivity in ferromagnetic/antiferromagnetic bilayers*. Phys. Rev. B **62**, 5627 (2000).
- [46] H. Xi and R. M. White. *Antiferromagnetic thickness dependence of exchange biasing*. Phys. Rev. B **61**, 80 (2000).
- [47] H. Xi, R. M. White, and S. M. Rezende. *Irreversible and reversible measurements of exchange anisotropy*. Phys. Rev. B **60**, 14837 (1999).
- [48] A. I. Morosov and A. S. Sigov. *Interface roughness and unidirectional anisotropy of thin ferromagnetic film on uncompensated surface of antiferromagnet*. J. Magn. Magn. Mat. **242**, 1012–1014 (2002).
- [49] A. I. Morosov and A. S. Sigov. *Unidirectional anisotropy in a ferromagnet-antiferromagnet system*. Physics of the Solid State **44**, 2098–2103 (2002).
- [50] A. I. Morosov and A. S. Sigov. *Proximity effect in ferromagnet-antiferromagnet systems*. J. Magn. Magn. Mat. **258**, 388–390 (2003).
- [51] M. Kiwi, J. Mejía-López, R. D. Portugal, and R. Ramírez. *Exchange bias model for Fe/FeF₂: Role of the domains in the ferromagnet*. Europhys. Lett. **48**, 573 (1999).
- [52] M. Kiwi, J. Mejía-López, R. D. Portugal, and R. Ramírez. *Exchange bias systems with compensated interfaces*. Europhys. Lett. **75**, 3995 (1999).

- [53] M. Kiwi, J. Mejía-López, R. D. Portugal, and R. Ramírez. *Positive exchange bias model: Fe/FeF₂ and Fe/MnF₂ bilayers*. Solid State Communications **116**, 315 (2000).
- [54] J. V. Kim, R. L. Stamps, B. V. McGrath, and R. E. Camley. *Angular dependence and interfacial roughness in exchange-biased ferromagnetic/antiferromagnetic bilayers*. Phys. Rev. B **61**, 8888 (2000).
- [55] J. V. Kim and R. L. Stamps. *Theory of long-wavelength spin waves in exchange biased bilayers*. J. Appl. Phys. **89**, 7651 (2001).
- [56] J. V. Kim and R. L. Stamps. *Hysteresis from antiferromagnet domain-wall processes in exchange-biased systems*. J. Magn. Magn. Mat. **286**, 233 (2005).
- [57] J. V. Kim and R. L. Stamps. *Defect-modified exchange bias*. Appl. Phys. Lett. **79**, 2785 (2001).
- [58] J. V. Kim and R. L. Stamps. *Hysteresis from antiferromagnet domain-wall processes in exchange-biased systems: Magnetic defects and thermal effects*. Phys. Rev. B **71**, 094405 (2005).
- [59] R. L. Stamps. *Dynamic magnetic hysteresis and anomalous viscosity in exchange bias systems*. Phys. Rev. B **61**, 12174 (1999).
- [60] R. L. Stamps. *Mechanisms of exchange bias*. J. Phys. D **3**, R247 (2000).
- [61] A. Hoffmann. *Symmetry Driven Irreversibilities at Ferromagnetic-Antiferromagnetic Interfaces*. Phys. Rev. Lett. **93**, 097203 (2004).
- [62] I. S. Jacobs and J. Kouvel. *Exchange Anisotropy in Mixed Magnanites with the Hausmannite Structure*. Phys. rev. **122**, 412 (1961).
- [63] J. Kouvel. *A ferromagnetic-antiferromagnetic model for copper-magnanese and related alloys*. J. Phys. Chem. Solids **24**, 795 (1963).
- [64] E. Fulcomer and S. H. Charap. *Thermal fluctuation aftereffect model for some systems with ferromagnetic-antiferromagnetic coupling*. J. Appl. Phys. **43**, 4190 (1972).
- [65] C. Hou, H. Fujiwara, K. Zhang, A. Tanaka, and Y. Shimizu. *Temperature dependence of the exchange-bias field of ferromagnetic layers coupled with antiferromagnetic layers*. Phys. Rev. B **63**, 024411 (2001).

- [66] S. Brems, K. Temst, and C. van Haesendonck. *Origin of the training effect and assymetry of the magnetization in Polycrystalline exchange bias system*. Phys. Rev. Lett. **99**, 067201 (2007).
- [67] M. D. Stiles and R. D. McMichael. *Temperature dependence of exchange bias in polycrystalline ferromagnet-antiferromagnet bilayers*. Phys. Rev. B **60**, 12950 (1999).
- [68] M. D. Stiles and R. D. McMichael. *Model for exchange bias in polycrystalline ferromagnet-antiferromagnet bilayers*. Phys. Rev. B **59**, 3722 (1999).
- [69] N. C. Koon. *Calculations of Exchange Bias in Thin Films with Ferromagnetic/Antiferromagnetic Interfaces*. Phys. Rev. Lett. **78**, 4865 (1998).
- [70] M. Tsunoda and M. Takahashi. *Single spin ensemble model for the change of unidirectional anisotropy constant by annealing on polycrystalline ferromagnetic/antiferromagnetic bilayers*. J. Appl. Phys. **87**, 4957 (2000).
- [71] M. Tsunoda and M. Takahashi. *Exchange anisotropy of ferromagnetic/antiferromagnetic bilayers: intrinsic magnetic anisotropy of antiferromagnetic layer and single spin ensemble model*. J. Magn. Magn. Mat. **239**, 149 (2003).
- [72] J. Saha and R. H. Victora. *Large scale micromagnetic simulation for the exchange interaction between a polycrystalline antiferromagnet and a ferromagnet*. Phys. Rev. B **73**, 104433 (2006).
- [73] D. Choo, R. W. Chantrell, R. Lamberton, A. Johnston, and K. O'Grady. *A model of the magnetic properties of coupled ferromagnetic/antiferromagnetic bilayers*. J. Appl. Phys. **101**, 09E521 (2007).
- [74] D. Suess, T. Schrefl, W. Scholz, J. Kim, R. Stamps, and J. Fidler. *Micromagnetic simulation of antiferromagnetic/ferromagnetic structures*. IEEE Trans. Magn. **38**, 2397 (2002).
- [75] D. Suess, M. Kirschner, T. Schrefl, W. Scholz, R. Dittrich, H. Forster, and J. Fidler. *Micromagnetic calculations of bias field and coercivity of compensated ferromagnetic antiferromagnetic bilayers*. J. Appl. Phys. **93**, 8618 (2003).
- [76] D. Suess, M. Kirschner, T. Schrefl, J. Fidler, R. Stamps, and J. Kim. *Exchange bias of polycrystalline antiferromagnets with perfectly compensated interfaces*. Phys. Rev. B **67**, 054419 (2003).
- [77] M. Kirschner, D. Suess, T. Schrefl, J. Fidler, and J. Chapman. *Micromagnetic calculation of bias field and coercivity of polycrystalline ferromagnetic/antiferromagnetic layers*. Phys. Rev. B **39**, 2735 (2003).

- [78] H. Fujiwara, K. L. Zhang, T. Kai, and T. Zhao. *Effect of direct exchange coupling between antiferromagnetic grains on magnetic behavior of ferro/antiferromagnetic exchange coupled polycrystalline layer systems*. J. Magn. Magn. Mat. **235**, 3319 (2001).
- [79] K. Zhang, T. Zhao, and H. Fujiwara. *Training effect of exchange biased iron-oxide/ferromagnet systems*. J. Appl. Phys. **89**, 6910 (2001).
- [80] Y. Imry and S. Ma. *Random-Field Instability of the ordered state of Continuous symmetry*. Phys. Rev. Lett. **35**, 1399 (1975).
- [81] U. Nowak, K. D. Usadel, P. Miltényi, J. Keller, B. Beschoten, and G. Güntherodt. *The domain state model for exchange bias I: Theory*. Phys. Rev. B **66**, 14430 (2002).
- [82] A. P. Malozemoff. *Random-field model of exchange anisotropy at rough ferromagnetic-antiferromagnetic interfaces*. Phys. Rev. B **35**, 3679 (1987).
- [83] A. P. Malozemoff. *Mechanism of exchange anisotropy*. J. Appl. Phys. **63**, 3874 (1988).
- [84] A. P. Malozemoff. *Heisenberg-to-Ising crossover in a random-field model with uniaxial anisotropy*. Phys. Rev. B **37**, 7673 (1988).
- [85] T. C. Schulthess and W. H. Butler. *Coupling mechanisms in exchange biased films*. J. Appl. Phys. **85**, 5510 (1999).
- [86] A. L. Dantas, G. O. G. Reboucas, A. Silva, and A. Carrico. *Interface roughness effects on coercivity and exchange bias*. J. Appl. Phys. **97**, 10K105 (2005).
- [87] S. H. Tsai, D. Landau, and T. C. Schulthess. *Effect of interfacial coupling on the magnetic ordering in ferro-antiferromagnetic bilayers*. J. Appl. Phys. **93**, 8612 (2003).
- [88] D. Lederman, R. Ramírez, and M. Kiwi. *Monte-Carlo simulations of exchange bias of ferromagnetic thin films of $FeF_2(100)$* . Phys. Rev. B **70**, 184422 (2004).
- [89] C. Mitsumata, A. Sakuma, and K. Fukamichi. *Mechanism of the exchange-bias field in the ferromagnetic and antiferromagnetic bilayers*. Phys. Rev. B **68**, 014437 (2003).
- [90] P. Miltényi, M. Gierlings, J. Keller, B. Beschoten, G. Güntherodt, U. Nowak, and K. D. Usadel. *Diluted Antiferromagnets in Exchange Bias: Proof of Domain State Model*. Phys. Rev. Lett. **84**, 4224 (2000).

- [91] U. Nowak, A. Misra, and K. D. Usadel. *Modeling exchange bias microscopically*. J. Magn. Magn. Mat. **240**, 243 (2002).
- [92] A. Misra, U. Nowak, and K. D. Usadel. *Structure of domains in an exchange-bias model*. J. Appl. Phys. **95**, 1357 (2004).
- [93] A. Misra, U. Nowak, and K. D. Usadel. *Control of exchange bias by diluting the antiferromagnetic layer*. J. Appl. Phys. **93**, 6593 (2003).
- [94] T. Mewes, R. Lopusnik, J. Fassbender, B. Hillebrands, M. Jung, D. Engel, A. Ehresmann, and H. Schmoranzer. *Suppression of exchange bias by ion irradiation*. Appl. Phys. Lett. **76**, 1057 (2000).
- [95] A. Mougin, T. Mewes, M. Jung, D. Engel, A. Ehresmann, H. Schmoranzer, J. Fassbender, and B. Hillebrands. *Local manipulation and reversal of the exchange bias field by ion irradiation in FeNi/FeMn double layers*. Phys. Rev. B **63**, 60409 (2001).
- [96] B. Beckmann, U. Nowak, and K. D. Usadel. *Asymmetric reversal modes in ferromagnetic/antiferromagnetic multilayers*. Phys. Rev. Lett. **91**, 187201 (2003).
- [97] G. Scholten, K. D. Usadel, and U. Nowak. *Coercivity and exchange bias of ferromagnetic/antiferromagnetic multilayers*. Phys. Rev. B **71**, 064413 (2005).
- [98] C. Papiusoi, J. Hauch, M. Fecioru-Morariu, and G. Guntherodt. *Tuning the exchange bias of soft metallic antiferromagnets by inserting nonmagnetic defects*. J. Appl. Phys. **99**, 123902 (2006).
- [99] B. Beckmann and K. D. Usadel. *Cooling-field dependence of asymmetric reversal modes for ferromagnetic/antiferromagnetic multilayers*. Phys. Rev. B **74**, 054431 (2006).
- [100] N. A. Usov and S. A. Gudoshnikov. *Numerical simulation of magnetization process in antiferromagnetic-ferromagnetic bilayer with compensated interface*. J. Magn. Magn. Mat. **300**, 164 (2006).
- [101] K. Takano, R. H. Kodama, A. E. Berkowitz, W. Cao, and G. Thomas. *Interfacial uncompensated antiferromagnetic spins: Role in unidirectional anisotropy in polycrystalline Ni₈₁Fe₁₉/CoO bilayers*. Phys. Rev. Lett. **79**, 1130 (1997).
- [102] K. Takano, R. H. Kodama, A. E. Berkowitz, W. Cao, and G. Thomas. *Role of interfacial uncompensated antiferromagnetic spins in unidirectional anisotropy in Ni₈₁Fe₁₉/CoO bilayers*. J. Appl. Phys. **83**, 6888 (1998).

- [103] A. E. Berkowitz and K. Takano. *Exchange anisotropy - a review*. J. Magn. Magn. Mat. **200**, 552 (1999).
- [104] X. Zianni and K. N. Trohidou. *Monte Carlo simulations on the coercive behaviour of oxide coated ferromagnetic particles*. J. Phys.: Condens. Matter **10**, 7475 (1998).
- [105] E. Eftaxias and K. N. Trohidou. *Numerical study of the exchange bias effects in magnetic nanoparticles with core/shell morphology*. Phys. Rev. B **71**, 134406 (2005).
- [106] K. N. Trohidou, M. Vasilakaki, L. Bianco, D. Fiorani, and A. M. Testa. *Exchange bias in a magnetic ordered/disordered nanoparticle system: A Monte-Carlo simulation study*. J. Magn. Magn. Mat. **316**, e82 (2007).
- [107] O. Iglesias, X. Batlle, and A. Labarta. *Microscopic origin of exchange bias in core/shell nanoparticles*. Phys. Rev. B **72**, 212401 (2005).
- [108] O. Iglesias and A. Labarta. *Monte-Carlo simulation study of exchange biased hysteresis loops in nanoparticles*. Phys. B **372**, 247 (2006).
- [109] D. Givord, V. Skumryev, and J. Nogués. *Exchange coupling mechanism for magnetization reversal and thermal stability of Co nanoparticles embedded in a CoO matrix*. J. Magn. Magn. Mat. **294**, 111 (2005).
- [110] J. Mejía-López, P. Soto, and D. Altbir. *Asymmetric reversal of the hysteresis loop in exchange-biased nanodots*. Phys. Rev. B **71**, 104402 (2005).
- [111] B. D. Cullity. *Introduction to magnetic materials*. Addison-Wesley Publishing Company (1972).
- [112] J. C. Slater. *Cohesion in Monovalent Metals*. Phys. Rev. **35**, 509–529 (1930).
- [113] J. C. Slater. *Atomic Shielding Constants*. Phys. Rev. **36**, 57–64 (1930).
- [114] J. C. Slater. *The Ferromagnetism of Nickel*. Phys. Rev. **49**, 537–545 (1936).
- [115] H. A. Kramers. *L'interaction Entre les Atomes Magnétogènes dans un Cristal Paramagnétique*. Physica **1**, 182–192 (1934).
- [116] P. W. Anderson. *Antiferromagnetism. Theory of Superexchange Interaction*. Phys. Rev. **79**, 350–356 (1950).
- [117] M. A. Ruderman and C. Kittel. *Indirect Exchange Coupling of Nuclear Magnetic Moments by Conduction Electrons*. Phys. Rev. **96**, 99–102 (1954).

- [118] T. Kasuya. *A Theory of Metallic Ferro- and Antiferromagnetism on Zener's Model*. Prog. Theor. Phys. **16**, 45–57 (1956).
- [119] K. Yosida. *something*. Phys. Rev. **106**, 893 (1957).
- [120] Bruce M. Moskowitz, Institute for Rock Magnetism. *Magnetic Anisotropy-HITCHHIKER'S GUIDE TO MAGNETISM* (2009). http://www.irm.umn.edu/hg2m/hg2m_c/hg2m_c.html.
- [121] S. Ostanin, S. S. A. Razee, J. B. Staunton, B. Ginatempo, and E. Bruno. *Magneto-crystalline anisotropy and compositional order in $Fe_{0.5}Pt_{0.5}$: Calculations from an ab initio electronic model*. J. Appl. Phys. **93**, 453–457 (2003).
- [122] J. B. Staunton, S. Ostanin, S. S. A. Razee, B. L. Gyorffy, L. Szunyogh, B. Ginatempo, and E. Bruno. *Temperature Dependent Magnetic Anisotropy in Metallic Magnets from an Ab Initio Electronic Structure Theory: L1-Ordered $FePt$* . Phys. Rev. Lett. **93**, 257204 (2004).
- [123] P. Weiss. *Hypothesis of the molecular field and ferromagnetic properties*. J. phys. **258**, 661–690 (1907).
- [124] R. C. O'Handley. *Modern Magnetic Materials: Principles and Applications* (1999).
- [125] U. Nowak and K. D. Usadel. *Monte Carlo studies of slow relaxation in diluted antiferromagnets*. Phys. Rev. B **39**, 2516 (1989).
- [126] U. Nowak and K. D. Usadel. *Slow relaxation of diluted antiferromagnets*. Physica B **165**, 211 (1990).
- [127] U. Nowak and K. D. Usadel. *Nonexponential relaxation of diluted antiferromagnets*. Phys. Rev. B **43**, 851 (1991).
- [128] U. Nowak and K. D. Usadel. *Diluted antiferromagnets in a magnetic field: A fractal-domain state with spin-glass behavior*. Phys. Rev. B **44**, 7426 (1991).
- [129] W. Kleemann, A. R. King, and V. Jaccarino. *Diluted antiferromagnets in a magnetic field: A fractal-domain state with spin-glass behavior*. Phys. Rev. B **34**, 479 (1986).
- [130] C. Binek. *Training of the exchange-bias effect: A simple analytic approach*. Phys. Rev. B **70**, 014421 (2004).
- [131] L. Fernandez-Outon, G. Vallejo-Fernandez, S. Manzoor, and K. O'Grady. *Thermal instabilities in exchange biased materials*. J. Magn. Magn. Mat. **303**, 296 (2006).

- [132] F. Radu and H. Zabel. *Exchange bias effect of ferro-/antiferromagnetic heterostructures*. In H. Zabel and S. Bader (editors), *Magnetic Heterostructures: Advances and Perspectives in Spinstructures and Spintransport*, 97. Springer, Berlin Heidelberg (2008).
- [133] S. Roy, M. R. Fitzsimmons, S. Park, M. Dorn, O. Petravic, I. V. Roshchin, Z.-P. Li, X. Batlle, R. Morales, A. Misra, X. Zhang, K. Chesnel, J. B. Kortright, S. K. Sinha, and I. K. Schuller. *Depth Profile of Uncompensated Spins in an Exchange Bias System*. *Phys. Rev. Lett.* **95**, 047201 (2005).
- [134] M. R. Fitzsimmons, B. J. Kirby, S. Roy, Z.-P. Li, I. V. Roshchin, S. K. Sinha, and I. K. Schuller. *Pinned magnetization in the antiferromagnet and ferromagnet of an exchange bias system*. *Phys. Rev. B* **75**, 214412 (2007).
- [135] R. Morales, Z.-P. Li, J. Olamit, K. Liu, J. M. Alameda, and I. K. Schuller. *Role of the Antiferromagnetic Bulk Spin Structure on Exchange Bias*. *Phys. Rev. Lett.* **102**, 097201 (2009).
- [136] F. Radu, M. Etzkorn, T. Schmitte, R. Siebrecht, A. Schreyer, K. Westerholt, and H. Zabel. *Asymmetric magnetization reversal on exchange biased CoO/Co bilayers*. *J. Magn. Magn. Mat.* **240**, 251 (2002).
- [137] F. Nolting, A. Scholl, J. Stöhr, J. W. Seo, J. Fompeyrine, H. Siegwart, J.-P. Locquet, S. Anders, J. Lüning, E. E. Fullerton, M. F. Toney, M. R. Scheinfein, and H. A. Padmore. *Direct observation of the alignment of ferromagnetic spins by antiferromagnetic spins*. *Nature* **405**, 767 (2000).
- [138] F. Radu, S. K. Mishra, I. Zizak, A. I. Erko, H. A. Durr, W. Eberhardt, G. Nowak, S. Buschhorn, H. Zabel, K. Zhernenkov, M. Wolff, D. Schmitz, E. Schierle, E. Dudzik, and R. Feyerherm. *Origin of the reduced exchange bias in an epitaxial FeNi(111)/CoO(111) bilayer*. *Phys. Rev. B* **79**, 184425 (2009).
- [139] X. Qiu, D. Yang, S. Zhou, R. Chantrell, K. O'Grady, U. Nowak, J. Du, X. Bai, and L. Sun. *Rotation of the Pinning Direction in the Exchange Bias Training Effect in Polycrystalline NiFe/FeMn Bilayers*. *Phys. Rev. Lett.* **101**, 147207 (2008).
- [140] L. E. Fernandez-Outon and K. O'Grady. *Angular dependence of coercivity and exchange bias in IrMn/CoFe bilayers*. *J. Magn. Magn. Mat.* **290**, 536–539 (2005).
- [141] K. Binder and D. Heermann. *Monte Carlo Simulation in Statistical Physics*. Springer-Verlag, Berlin (1997).

BIBLIOGRAPHY

- [142] U. Nowak. *Thermally activated reversal in magnetic nanostructures*. In D. Stauffer (editor), *Annual Reviews of Computational Physics IX*, 105. World Scientific, Singapore (2001).

- [143] G. Marsaglia. *CHOOSING A POINT FROM SURFACE OF A SPHERE*. *ANNALS OF MATHEMATICAL STATISTICS* **43**, 645 (1972).